The Dissertation Committee for Alfredo J. Duarte Gomez
certifies that this is the approved version of the following dissertation:

Hydrodynamic effect of nanosecond discharge pulses in air: high fidelity models and scaling laws

Committee:

Fabrizio Bisetti, Supervisor

Laxminarayan Raja

Robert Moser

Timothy Ombrello

Philip Varghese

Thomas Underwood

Hydrodynamic effect of nanosecond discharge pulses in air: high fidelity models and scaling laws

by

Alfredo J. Duarte Gomez, B.S.

DISSERTATION

Presented to the Faculty of the Graduate School of

The University of Texas at Austin

in Partial Fulfillment

of the Requirements

for the Degree of

DOCTOR OF PHILOSOPHY

THE UNIVERSITY OF TEXAS AT AUSTIN

December 2024

Dedicated to my family.

Acknowledgments

I would like to recognize the support of several people in the development of this dissertation. First, I would like to thank my advisor Fabrizio Bisetti for his guidance throughout this journey. His passion for scientific research is reflected every week in the time that he dedicates to every one of his students, and his insight and attention to detail has been essential in the writing of this dissertation. I would also like to thank my dissertation committee members, Prof. Laxminarayan Raja, Prof. Philip Varghese, Dr. Timothy Ombrello, Prof. Thomas Underwood, and Prof. Robert Moser for the feedback that helped improve this dissertation.

I would also like to take a moment to recognize the help of my peers. Dr. Nicholas Deak played a very important role as a mentor in my early graduate studies, and his expertise and continued support made this dissertation possible. I would also like to recognize the help of Dr. Marcus Day and Dr. Lucas Esclapez for their support. I would also like to thank my fellow graduate student Aditya Vinod, and staff members Scott Messec, Annecy Liddell, and Yasmin Welch. Finally, I want to acknowledge the efforts of Priscilla Pak, Arnav Trivedi, and Colton Shepard as a test audience for this dissertation.

I also want to recognize NSF Award No. 1903775 (Program Director: Harsha Chelliah) and DOE contract DE-EE0008874 for supporting this research. I am also grateful for the generous support of the Texas Advanced Computing Center (TACC)

for providing essential computational resources throughout my graduate studies. A portion of the research was also performed using computational resources sponsored by the Department of Energy's Office of Energy Efficiency and Renewable Energy and located at the National Renewable Energy Laboratory. Finally, I want to give very special thanks to my mother, my father, my brothers and sister, and my wife for their incredible support and encouragement.

Hydrodynamic effect of nanosecond discharge pulses in air: high fidelity models and scaling laws

Publication No. _____

Alfredo J. Duarte Gomez, Ph.D.
The University of Texas at Austin, 2024

Supervisor: Fabrizio Bisetti

Nanosecond discharge pulses (NSDP) applied to air/fuel mixtures is a promising technology to improve ignition reliability and combustion stability. The understanding of physical mechanisms behind these improvements is still limited and numerical studies play a key role towards this goal. Three mechanisms of combustion enhancement are postulated: chemical/kinetic, heating, and hydrodynamic. The aim of this thesis is to develop novel numerical tools for the study of 3-D multi-pulse discharges in air and air/fuel mixtures and apply them to formulate a systematic theory for the hydrodynamic processes induced by the plasma discharges.

In the first part of this study, nanosecond discharge pulses in air with significant energy depositions are investigated using a zero dimensional isochoric and adiabatic reactor. A two-temperature model with detailed air-plasma kinetics is utilized for a variety of conditions in order to characterize the effects of nanosecond

discharges in air. A comprehensive description of the state of non-equilibrium created by a nanosecond discharge in air is provided through metrics that describe gas heating, vibrational excitation, and chemical non-equilibrium, including a novel approach using constrained equilibrium. The sensitivity of the results to the kinetics mechanism and voltage waveform is also investigated and discussed. The accuracy of the reduced mechanism is found to be adequate for the intended applications, and it is found that the common strategy of interrupting the voltage pulse instantaneously once the target energy has been deposited is likely to underestimate vibrational excitation.

In the second part, a numerical framework for the simulation of discharges in three-dimensional configurations is presented and applied to pin-to-pin discharges in air. The numerical framework is found to be suitable for high-fidelity simulations, where a variety of multi-scale physical processes are observed throughout the simulation. This includes streamer propagation, fast gas heating, shock expansion, and cold gas entrainment, reproducing behaviors observed in several experimental studies. Newly developed tools allow for the simulation of strongly coupled multi-pulse discharges with complex streamer propagation and energy depositions. The governing equations, assumptions, simplifications, limitations, and algorithms are presented and discussed in detail.

After demonstrating the capabilities of the novel numerical framework with a reference case at atmospheric conditions, the framework is used to study the hydrodynamic effect of nanosecond discharges in air systematically. The hydrodynamic effect concerns a strong induced velocity in the direction perpendicular to the gap

midplane (i.e., oriented along the axis of the pin electrodes) after the expansion of the hot gas kernel. The problem of a single pulse discharge is cast in terms of dimensionless parameters, and parametric sweeps are used to generate data suitable to further the understanding of the hydrodynamic effect under the assumption that viscous processes can be neglected. Two models are used: a simplified model with direct heating of the gas, uniform energy deposition in a cylindrical region, and no viscous/diffusive effects (Euler restriction to the Navier-Stokes equations), and the high-fidelity mathematical model developed in this work.

The simplified model is used to provide a characterization of the flow immediately after energy deposition by the discharge and to serve as a best-case scenario for scaling arguments. An initial assessment shows that the simplified model reproduces important physical processes and select qualitative behaviors when compared to the high-fidelity model. However, there remain important qualitative and quantitative differences. The solutions to the simplified model show self-similarity, linear scaling between a dimensionless energy parameter and the duration of the expansion phase. The effect of geometric parameters such as the ratio of the radius of the cylindrical kernel to its height is considered minor when compared to the effect of the dimensionless energy deposited.

Finally, the results of the high-fidelity model are presented to characterize the hydrodynamic effect and its dependence on the configuration parameters. The effects of geometric parameters is found to be heightened by the inhomogeneous spatial distribution of the energy density deposited by the discharge, which also varies for different background conditions. Agreement between self-similar solutions

under the same theory applied to the results with the simpler model remains good and provides clear insight and guidance in the design of nanosecond discharges. The duration of the acoustic phase, induced velocity, and heated kernel expansion are characterized and used to provide estimates of characteristic time scales for advection and diffusion. The results are put into context with recent experimental evidence on the existence of two different regimes with regard to the hydrodynamic processes induced by nanosecond discharges.

Table of Contents

List of Tables

List of Figures

Chapter 1

Introduction

1.1 Motivation

A significant amount of the world's energy as well as transportation relies on the combustion of fossil fuels. In recent years, climate change and threats to energy security have highlighted the need for new and more efficient combustion devices. Research groups have taken an interest to non-equilibrium plasmas for combustion ignition and control as a promising alternative to traditional technology. Despite the growing body of work on experiments using plasmas in combustion devices, the mechanisms responsible for combustion ignition and control enhancement are not understood to the extent that would enable design and optimization of plasma-based combustion systems.

The low-temperature plasmas and attending non-equilibrium gases can be created in a variety of devices and conditions. In combustion and ignition control applications, nanosecond discharge pulses (NSDP) are a particularly promising technology. Nanosecond discharge pulses are characterized by an electron temperature T_e that is much larger than the background temperature of the ions and neutral species, weakly ionized plasmas at atmospheric conditions with number densities of electrons ranging from 10^{12} to 10^{17} cm^{-3}, reduced electric fields E/N of 100-800 Td,

and voltage pulses with peak values of 5-50 kV and short durations ranging from 1 to 50 ns. An example of nanosecond discharge pulses produced in a pin-to-pin configuration is shown in Fig. 1.1, where we observe digital camera images of the corona, glow, and spark discharge regimes from the experiments by Pai et al. [7]. In this work, the emphasis will be on the *spark* regime, where the discharge deposits large amounts of energy (0.1-6 mJ) resulting in significant heating ($\mathcal{O}$(1,000 K)) of the gas.

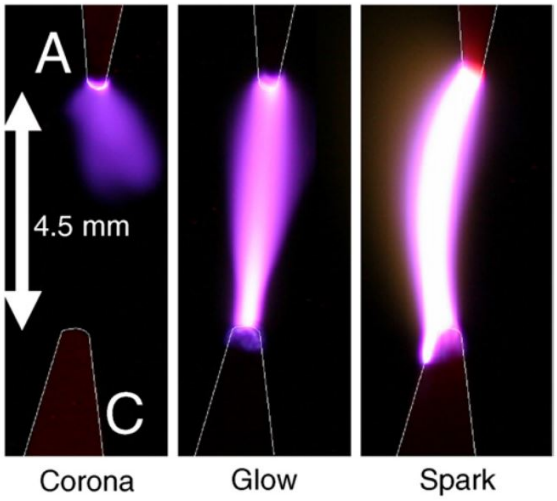

Figure 1.1: Digital camera images of the corona, glow, and spark discharge regimes reproduced from Ref. [7] for air at 1 atm, T = 1000 K, and a gap distance of 4.5 mm.

Several experimental studies demonstrated the advantages of low-temperature plasmas for combustion enhancement. In the work by Barbosa et al. [19], an experimental study was performed on the stability of an air/propane flame, where it was found that the lean extinction limit of the flame with the low temperature plasma

is four times lower than without plasma. In another experimental study by Do et al. [20], nanosecond discharge pulses were used to stabilize a flame in a supersonic cavity, where a noticeable reduction of the ignition delay time was observed when the plasma was applied. Finally, in the work by Wolk et al. [21], an experimental study of a microwave-assisted spark for methane/air mixtures demonstrated the enhancement of laminar flame development in a range of initial pressures and equivalence ratios.

Tangible benefits with the use of nanosecond discharge pulses have been established in a variety of combustion applications. However, the description of the enhancements is not quantitative. The complex physical mechanisms governing plasma assisted combustion in a pin-to-pin capacitive discharge configuration are illustrated in the experimental work by Lefkowitz et al. [8], where the dynamics of ignition using nanosecond discharge pulses in methane/air were characterized over a broad parametric range. The ignition probability was studied by varying repetition frequency, number of pulses, equivalence ratio, gap distance, and flow velocity. Three inter-pulse coupling regimes were identified based on a ratio of time scales defined by pulse frequency and flow velocity: the fully coupled regime, partially coupled regime, and the decoupled regime.

These regimes and their impact on the structure of the resulting ignition kernel are illustrated in Fig. 1.2. Examples of the ignition probabilities for a lean methane/air mixture for the three regimes are shown in Fig. 1.3. The fully coupled regime, observed at the highest repetition frequencies, consistently exhibited the largest probability of ignition. For the partially coupled and decoupled regime,

the probability of ignition was non-monotonic, as observed in Fig. 1.3. For a stoichiometric ratio of $\phi = 0.55$, the probability of ignition decreases monotonically as it moves from the fully coupled to the decoupled regime. For stoichiometric ratios of $\phi = 0.6$ and $\phi = 0.65$, the probability of ignition decreases as it enters the partially coupled regime, and then increases again as it approaches the decoupled regime. Multi-dimensional numerical modelling can undoubtedly play a key role in improving the understanding of the distinct spatial and temporal scales involved in plasma-assisted combustion and its regimes.

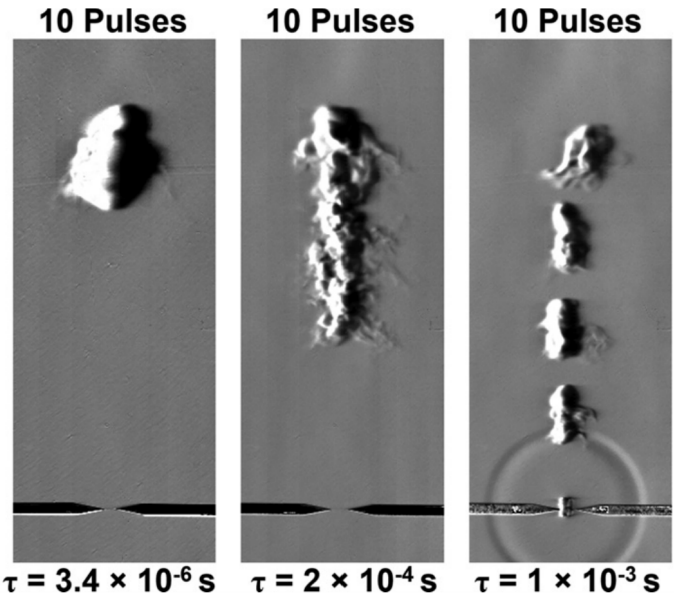

Figure 1.2: Experimental results adapted from Ref. [8] showing the impact of the discharge regime on the morphology of the ignition kernel: fully coupled (left), partially coupled (middle), and decoupled (right).

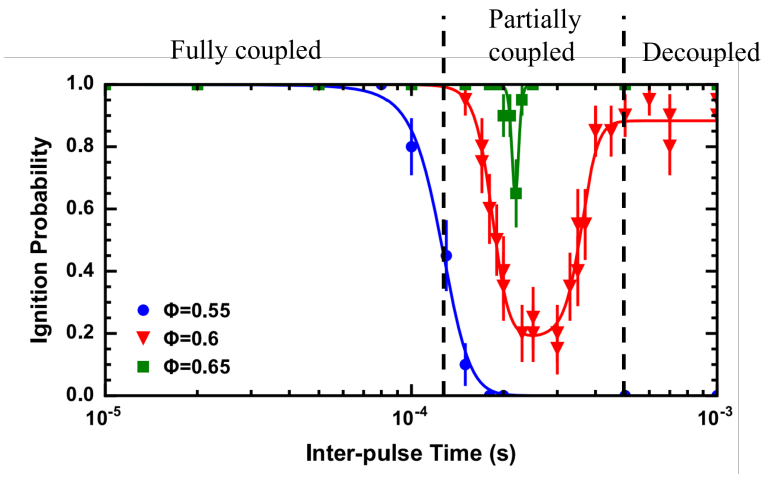

Figure 1.3: Ignition probability as a function of the interpulse time from experiments in Ref. [8], representing the transition between discharge regimes. Depending on the stoichiometry of the mixture, the probability of ignition decreases monotonically (ϕ = 0.55), or decreases and then increases (ϕ = 0.6 and ϕ = 0.65) as it transitions between the three different regimes.

1.2 Nanosecond discharges in a pin-to-pin configuration

1.2.1 Overview

Each nanosecond discharge pulse engenders several physical processes over a wide range of time scales. A brief overview of these processes is given in Fig. 1.4. Following an increase of the voltage between the two electrodes, the large electric fields at the pin tips lead to the formation of ionization waves that propagate across the gap, establishing a conducting channel. During the remainder of the voltage pulse, energies ranging from 0.1 to 6 mJ are deposited over a very short interval $\mathcal{O}$(1-10 ns). Energy deposition over such a short period of time leads to an increase in temperature and pressure of the gas at nearly constant density (see Fig. 1.4(a)). Over

the next few microseconds, the hot pressurized kernel expands outwards, inducing weak shocks into the surrounding gas and leaving behind a region of low-density gas at elevated temperature (see Fig. 1.4(b)), eventually relaxing back to the original background pressure. The propagation of the outward expansion wave and the low-density regions may set the fluid in motion over longer time scales (see Fig. 1.4(c)), while the electrodes act as no-slip boundary conditions and sources of thermal losses due to conduction.

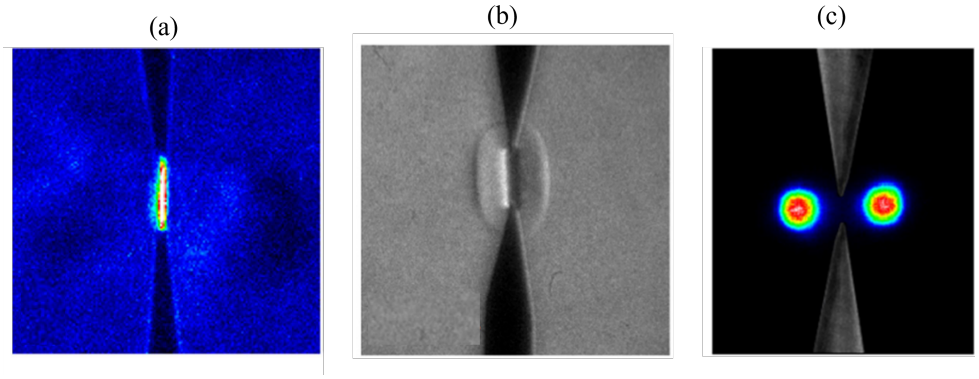

Figure 1.4: (a) Early heating and (b) expansion observed from Schlieren imaging of nanosecond discharges, adapted from the experimental results presented in Refs. [9; 10]. (c) OH-PLIF visualization for nanosecond discharge in air adapted from Ref. [11], showing the fluid motion induced by the discharge.

Three general mechanisms for combustion enhancement have been discussed in the literature: ultrafast heating [22], kinetic pathways [2], and induced hydrodynamics [11]. In nanosecond discharge pulses, the mixture is heated at sub-acoustic time scales, usually referred to as ultrafast heating. Higher temperatures lead to increased reactivity that can be beneficial to combustion when compared to traditional sparks, where the mixture is heated over time scales of several microseconds.

The large electron temperatures induced by nanosecond discharges can also lead to alternative kinetic pathways, such as dissociation, generation of radicals, vibrational excitation, and electronic excitation amongst others. An overview of the fractional power dissipated by electrons for different mixtures and values of the reduced electric field E/N was provided by Starikovskiy et al. [23]. The kinetic effect was explored in detail in the numerical study by Deak et al. [24] for methane/air and ethylene/air mixtures in a zero dimensional reactor. With a two-temperature model, the energy was deposited selectively to either the gas (direct heating) or electrons (larger electron temperature) over similar time scales, allowing to distinguish between enhancement provided by pure heating or alternate kinetic pathways. Finally, the expansion process following sub-acoustic heating can also induce a strong hydrodynamic effect that may redistribute energy and combustion radicals over a larger volume than a traditional spark, as shown in the work by Stepanyan et al. [10].

Based on the overview and complex physical processes presented thus far, it is apparent that the high-fidelity multidimensional modelling of NSDPs poses significant challenges brought by the interaction of disparate physical processes spread across time scales spanning several orders of magnitude. Over time scales of $\mathcal{O}(10$ ns) we observe streamer discharge and energy deposition, followed by the relaxation of electronically excited species, weak shock expansion and relaxation of vibrationally excited species $\mathcal{O}(1$ μs), hydrodynamics and mixing $\mathcal{O}(10$ μs), and ultimately the ignition of hydrocarbon/air mixtures. There exists also broad separation between spatial scales governing streamer propagation $\mathcal{O}(1$ μm) and NSDP device geometries $\mathcal{O}(10$ mm).

1.2.2 Hydrodynamic effect

The current work focuses primarily on the hydrodynamic effect induced by nanosecond discharge pulses, as illustrated in Fig. 1.4(c). Elevated axial velocities induced by the expansion of the pressurized kernel have been observed in a variety of experimental and numerical studies. In some cases pertaining to the ignition produced by pin-to-pin discharges, such hydrodynamic effect has been highlighted as the most prominent combustion enhancing mechanism [25]. The detailed understanding of this hydrodynamic effect and its dependence on configuration parameters is a key component towards the quantitative understanding of the spatial and temporal scales governing plasma assisted combustion.

Detailed experimental observations were provided by the work from Stepanyan et al. [10; 11]. In their work, Stepanyan et al. [10] showed that the initially thin hot channel shown in Fig. 1.4 expands rapidly, setting the fluid into motion towards the axial midplane and creating a torus. For the data shown in their study, nanosecond discharges were able to excite a volume more than two times larger than that created by a conventional spark, even when the energy deposited by the nanosecond discharge was lower. The recirculation effect produced by nanosecond discharges also contributed to redistribute active species over a wider region. These results were complemented by synchronized diagnostics of Schlieren imaging, OH-PLIF, and electrical measurements of deposited energy in Ref. [11]. It was confirmed that the recirculation phenomenom described occurs only above a certain energy threshold, and that it provided a helpful way to deposit energy and continuously expand the active volume when compared to a conventional spark.

The hydrodynamic behavior of nanosecond discharges was also studied by Dumitrache et al. [12] using experimental data and simplified numerical models. Two regimes were identified based on the strength of the hydrodynamic effect as shown in Fig. 1.5. In the *toroidal* regime, the induced hydrodynamic effect is strong enough to cause the collapse of the cylindrical kernel into a symmetric torus (see Fig. 1.5(a)). In the *diffusive regime*, the hydrodynamic effect is limited, and the cylindrical structure of the kernel persists (see Fig. 1.5(b)). The ocurrence of one regime over the other was linked to the amount of energy deposited and length of the gap. Short gaps ($d < 3$ mm) favor the toroidal regime, whereas long gaps ($d > 3$ mm) favor the diffusive regime. The underlying physical mechanism governing this effect was attributed to vorticity generation produced by baroclinic torque. A dimensionless parameter was also proposed to help predict the transition from one regime to the other and will be further discussed in Section 7.1.

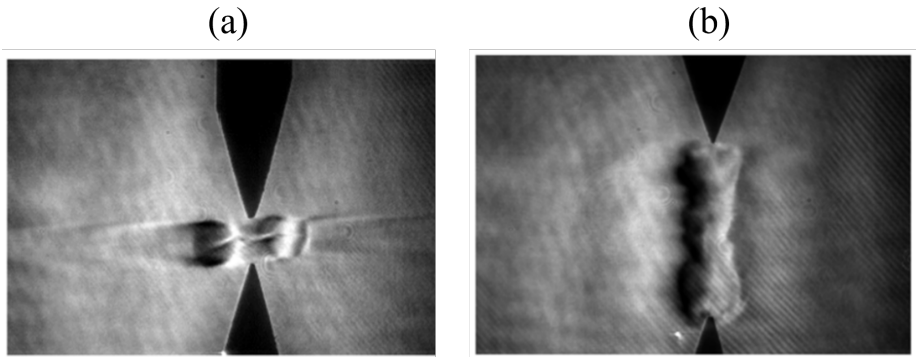

Figure 1.5: Schlieren images adapted from the experimental work by Dumitrache et al. [12] showing (a) the toroidal regime (gap length $d = 1$ mm) with a strong hydrodynamic effect and (b) the diffusive regime (gap length $d = 4$ mm) with a limited hydrodynamic effect.

In recent work, the cumulative hydrodynamic effect of successive multiple pulses and its impact on a potential ignition event has been studied in experimental configurations. In the work by Lovascio et al. [25], the hydrodynamic effect was identified as the driving mechanism behind the ignition of a lean propane/air flame. The instabilities generated by successive pulses triggered a jetting motion that allowed the formation of a flame kernel far from the inter-electrode region. In the work by Opacich et al. [26], the development of a methane/air ignition kernel was studied in a cross-flow environment. The jetting behavior was observed for a gap length of 2 mm, which aided in extending the reactive region produced by nanosecond discharges. In the experimental work by Shcherbanev et al. [27], this jetting motion was characterized in quiescent air at atmospheric conditions. The authors were able to identify a dependence between the number of required pulses to trigger the jetting motion, and parameters such as gap length and energy deposited per pulse.

1.3 Numerical Modeling

To accurately model the physics described in the previous section, we require a plasma-fluid model that introduces stringent requirements on the resolution of all pertinent time and length scales. For example, accurately modeling the streamer propagation and energy deposition at atmospheric pressure and temperature requires resolutions of $\mathcal{O}$(1-5 μm) and time step limitations as small as a tenth of a picosecond. These stand in stark contrast to the length and time scales encountered in combustion devices, which can range from 10 to 100 mm and times of $\mathcal{O}$(0.1 - 1 ms). Additionally, high-fidelity models require plasma kinetics models that are not always available and

that can be much involved and computationally expensive [28; 4; 29].

The complexities associated with numerical modeling of plasma-fluid processes have led to a hierarchy of modelling approaches. We refer to the first class of approaches as *empirical models*, which neglect plasma discharge and energy deposition altogether. In this class of models, the pressure and temperature profiles resulting from the isochoric energy deposition are prescribed and often informed by experimental observations. For example, in the work by Dumitrache et al. [12] (shown in Fig. 1.6), the hydrodynamic effect induced by nanosecond discharge pulses was studied using an empirical model informed by experimental measurements of NS-DPs in air. With a similar approach, Bane et al. [30] studied the effect of different electrode geometries on the ignition of hydrogen/air mixtures. The greatest advantage of *empirical models* is their simplicity and numerical efficiency, which allows the user to sidestep the discharge phase and plasma-fluid processes, and to rely on well established compressible solvers. The main disadvantages are the inability to model the impact of more complex discharge processes such as vibrational excitation, relying on detailed experimental measurements that may not be available, issues associated with spatially inhomogeneous energy deposition, and the additional difficulties to model more than a single pulse.

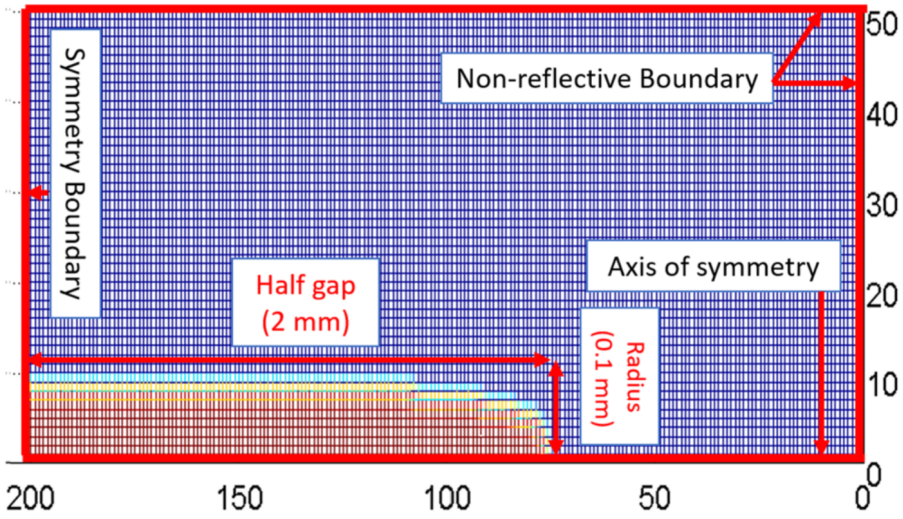

Figure 1.6: Example of the empirical approach adapted from Dumitrache et al. [12] to model the energy deposition of a nanosecond discharge. Here, we observe a smoothed cylindrical uniform energy density (in red) with a specified gap length and radius. Energies and radii measured from experimental configurations are used to initialize a kernel of hot gas.

A second class of modeling approaches, termed *phenomenological models*, aims for a balance between cost and efficiency [13; 31]. Again, the discharge phase is not simulated, focusing instead on prescribing distinct energy contributions that are known to occur in nanosecond discharge pulses. Typically, three energy contributions are postulated and modeled as shown in Fig. 1.7: fast heating, vibrational excitation, and chemical effects. With a known energy deposition and/or power, the user allocates fractions of the total to each of these energy channels leveraging expert knowledge from experiments or numerical studies in zero-dimensional reactors. For ultrafast heating, the energy fraction is allocated and leads to an increase in the sensible enthalpy of the mixture, reproducing the effect of heating. The second

fraction is used to initialize an energy density variable that represents the energy stored in overpopulated vibrational states, typically decreasing over time scales of several microseconds. The final fraction is used to reproduce applicable chemical effects consistent with the specified energy balance, typically dissociation and formation of combustion radicals. This approach allows the modelling of the chemical and heating effects to a higher degree of fidelity without incurring the full cost of two-way coupling between plasma discharge and background gas. The greatest disadvantage of this class of approaches is the need to specify the spatial distribution of the energy density at the onset of the simulation, often assumed to be spatially inhomogeneous within a cylindrical region and constant from pulse to pulse.

The first example of this class of models was presented by Castela et al. [13], where it was employed to study a sequence of discharge pulses in air and methane/air mixtures. This study showed that vibrational excitation has only a minor impact on mixture ignition and highlighted the importance of the production of O radicals in hastening ignition. The model was also used to study the impact of gas flow recirculation and its effect on species and temperature around the discharge zone for a methane/air mixture [32]. More recent studies have built on the work of Castela et al. in order to improve the fidelity of the model. For example, Barleon et al. [31] developed the PACMIND code in order to provide a more general framework for incorporating detailed kinetic models and to inform the selection of energy fractions depending on discharge conditions. Significant improvements in model fidelity were reported compared to the work by Castela et al. A similar open-source tool was developed by Shao et al. [33] in order to integrate tools used in the plasma and

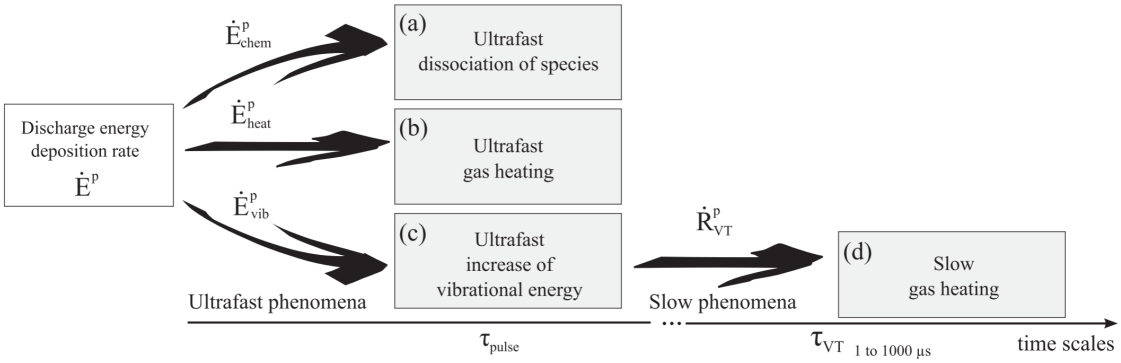

Figure 1.7: Overview of the phenomenological model for nanosecond discharge pulses adapted from Castela et al. [13].

combustion communities more seamlessly.

The use of phenomenological models to describe and inform complex plasma-assisted combustion phenomena has grown considerably. In the work by Taneja et al. [34; 35], large-eddy simulation (LES) with a phenomenological model was used to explain the experimental observations as reported in Ref. [8]. Based on their simulations, the authors attribute the observed decrease of the ignition probability in the partially coupled regime to a convective heat loss mechanism due to the weak induced shock, which reduces the kernel volume significantly and leads to a destructive effect between pulses. In recent work by Male et al. [36] and Impagnatiello et al. [37], LES with the phenomenological model from Ref. [38] was employed to study the effects of NSDPs on thermoacoustic instabilities in a sequential combustor and compare simulation results to experimental data. The results in Ref. [36] showed a significant decrease of the acoustic energy production when the NSDP was active. In Ref. [37], the simulations demonstrated that NSDPs initiate reacting kernels upstream that

interact with the acoustic field and with the main flame brush, inducing a drastic reduction in the fluctuations of heat release in the second stage of the combustor.

Finally, recent modelling approaches have pursued a full coupling between discharge processes and background gas dynamics [14; 39; 38]. Fully coupled approaches model the streamer phase, energy deposition, and ensuing transport processes. These models are similar to the simulation framework pursued in our work and attending high-fidelity models. The fully coupled approach offers the most fidelity, while also incurring the largest computational cost and model complexity. In addition to the complex physical processes and resolution of the widely separated spatial and temporal time scales as discussed, fully coupled models require more complex chemical kinetic mechanisms that feature significantly more species than traditional combustion mechanisms.

In the work by Mao et al. [14], the ignition of preheated air/hydrogen gaseous mixtures was explored for a variety of conditions. Their results show that any enhancement to ignition is sensitive to electrode shape, diameter, and gap size. In Refs. [38; 39], the effect of the pulsing frequency on the ignition of preheated methane/air and hydrogen/air mixtures was explored. Barleon et al. [38] found that the induced shock wave produced by high-energy discharges can lead to quenching of the ignition kernel, while weaker and more frequent pulses reduce this effect by depositing energy more homogeneously. Similarly, Mao et al. [39] found that two sequential pulses, in the partially coupled and decoupled regimes, failed to produce ignition even when the total energy deposited is above the minimum ignition energy of a single pulse. In the fully-coupled regime, the pulses succeeded to produce a successful ignition even

when the total energy deposited was below the reported minimum ignition energy of the single pulse. The enhancement was attributed to the overlap of the OH radical pool and increased heating due to the higher reduced electric field. While these studies present a significant advancement in the modelling of single and multi-pulse discharges, they have been limited to axisymmetric configurations. In the case of Ref. [38], multi-pulse discharges were confined to the diffusive regime, where the path of the discharge is predictable and gives rise to a diffuse plasma channel and hot gas kernel.

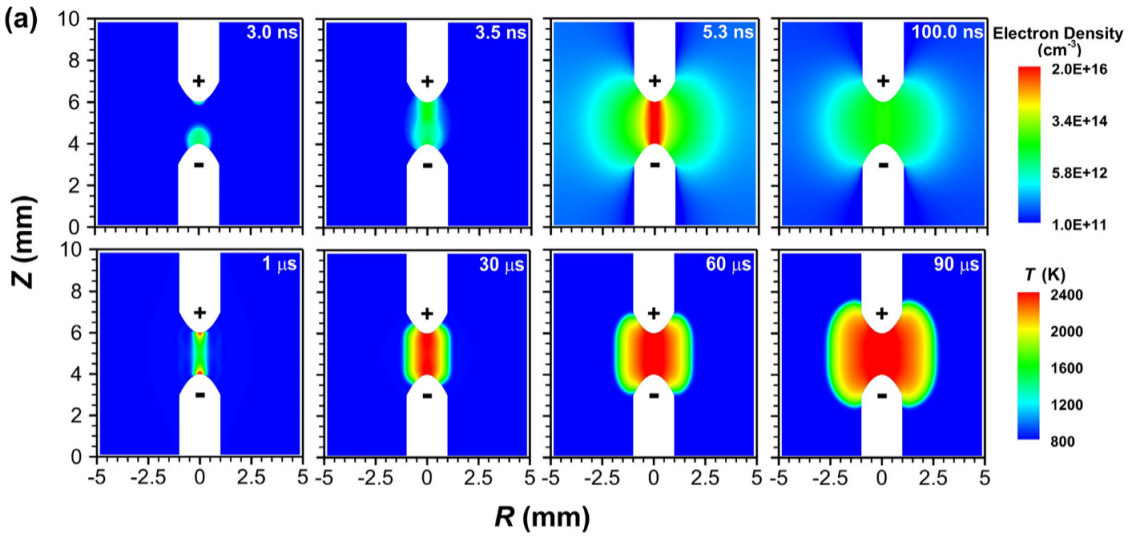

Figure 1.8: High-fidelity modelling of the ignition of a preheated air/hydrogen mixture adapted from Ref. [14]. Results show streamer propagation on nanosecond time scales and the ignition of the mixture between 1 to 100 μs.

1.4 Summary of key contributions

Despite progress in the multi-dimensional modelling of plasma assisted combustion in a pin-to-pin configuration, a quantitative and systematic understanding of the induced hydrodynamic effect is not available. The work by Dumitrache et al. [12] is one of the few numerical studies that explore strong hydrodynamic effects. While useful, the theory advanced by Dumitrache et al. [12] model to predict toroidal collapse is limited to a binary classification, with no information regarding timescales or length scales involved. Additionally, the study assumed uniform energy depositions and did not consider electrode geometry.

Fully coupled solvers to investigate pin-to-pin discharges have not been applied to a regime where the hydrodynamic effect is significant and leads to toroidal collapse. Numerical studies with fully-coupled models [14; 39; 38] focused on preheated mixtures and/or longer gaps, where the diffusive regime is prevalent. The focus of these numerical studies has been on cumulative kinetic and heating effects from multiple discharges rather than hydrodynamics. In this work, we employ a fully coupled model with detailed plasma kinetics to study the hydrodynamic effect induced by nanosecond discharges in pin-to-pin configurations. The newly developed framework allows for the efficient simulation of three-dimensional coupled discharges up to hundreds of microseconds. Key contributions are summarized below:

- Characterization of the non-equilibrium generated by nanosecond discharge pulses in air under different conditions relevant to applications. Commentary and discussion regarding the consequences of common energy deposition strate-

gies in numerical modelling.

- Development and validation of a high-fidelity numerical framework for the simulation of the multi-physics and multi-scale phenomena encountered in nanosecond discharges. Examples are provided for efficient three-dimensional simulations of multi-pulse discharges in air and air/fuel mixtures.

- Detailed characterization of single pulse discharges in air including: streamer propagation, establishment of the conducting channel and energy deposition, electrical properties of the conducting channel, heated kernel expansion with mass and energy losses, and induced hydrodynamic effect causing toroidal collapse. An example of the simulation of multiple pulses illustrates the effects of inter-pulse coupling on the spatial profiles of the energy deposition and subsequent hydrodynamic effect.

- Quantitative analysis, scaling arguments, and characterization of single pulse discharges in air at a variety of thermodynamic conditions. These include: spatial energy deposition profile, duration of the acoustic phase, velocity induced in the axial direction, and width of the hot kernel following expansion. Such characterization is then utilized to investigate the competition between diffusive and convective physical processes and to propose a regime diagram to guide future numerical and experimental studies.

This dissertation is organized as follows. In Chapter 2, we explore non-equilibrium effects of nanosecond discharges in air using a two-temperature isochoric

and adiabatic zero-dimensional reactor. In Chapter 3, the impact of different parameters on the nanosecond discharges is explored, including different energy depositions and voltage waveforms. In Chapter 4, we present governing equations, closures, assumptions, simplifications, and numerical algorithms used to model nanosecond discharge pulses in air. In Chapter 5, we provide a detailed overview of the physical processes involved in discharges in air by using a reference case at atmospheric conditions. Finally, in Chapters 6 and 7, the hydrodynamic effect is explored in detail using a simplified model, and high-fidelity simulations with the newly developed framework. Summary and conclusions follow in Chapter 8.

1.4.1 Summary of Published Work

Journal Publications

- **Duarte Gomez, A.**, Deak, N., Esclapez, L., Day, M., Bisetti, F. "Mathematical models and numerical methods for high-fidelity simulation of ignition of reactive mixtures by nanosecond plasma discharges in realistic configurations" *Combustion Theory and Modelling*, (under review, submitted September 2024)

- Rekkas-Ventiris, G., **Duarte Gomez, A.**, Deak, N., Kincaid, N., Pepiot, P., Bisetti, F., Bellemans, A. "A novel machine learning based lumping approach for the reduction of large kinetic mechanisms for plasma-assisted combustion applications" *Combustion and Flame*, Volume 260, 2024, 113252, `https://doi.org/10.1016/j.combustflame.2023.113252`

- **Duarte Gomez, A.**, Deak, N., Bisetti, F., "Jacobian-free Newton–Krylov

method for the simulation of non-thermal plasma discharges with high-order time integration and physics-based preconditioning" *Journal of Computational Physics*, Volume 480, 2023, 112007,
https://doi.org/10.1016/j.jcp.2023.112007

Conference Proceedings

- **Duarte Gomez, A.**, Deak, N., Esclapez, L., Day, M., Bisetti, F., "Verification and Validation of a fully-coupled three-dimensional low-temperature plasma and reactive Navier-Stokes solver" presented at AIAA SciTech 2024, Orlando, FL
https://doi.org/10.2514/6.2024-1820.

- **Duarte Gomez, A.**, Deak, N., Bisetti, F., "Direct Numerical Simulation of expansion, hydrodynamic mixing, and heat transfer to electrodes during low-temperature plasma discharges in atmospheric air" presented at the APS 76th Annual Meeting of the Division of Fluid Dynamics (DFD), Washington, DC.

- **Duarte Gomez, A.**, Deak, N., Bisetti, F., "Effect of Multiple pulses on Nanosecond Discharges" presented at AIAA SciTech 2023, National Harbor, MD,
https://doi.org/10.2514/6.2023-0569.

- **Duarte Gomez, A.**, Deak, N., Bisetti, F., "Efficient preconditioning for the simulation of nanosecond discharges using Jacobian-free Newton Krylov Meth-

ods" presented at the 75th Annual Gaseous Electronics Conference (GEC), Sendai, Japan.

Chapter 2

Non-equilibrium discharges: Overview

The understanding of the hydrodynamic effect of nanosecond discharge pulses begins with the understanding of fast-gas heating and kinetic effects. With a higher level of non-equilibrium, more energy is stored in excited or dissociated states, leading to a lower increase in the temperature and pressure of the mixture. The voltage applied during a nanosecond discharge pulse leads to heating over time scales of nanoseconds and a corresponding rise in pressure due to the isochoric nature of the process. During the subsequent expansion of the pressurized channel, significant hydrodynamic effects ensue, such as the recirculation effect described in Chapter 1. This fast-gas heating on sub-acoustic time scales is one of the key differences between non-equilibrium discharges and thermal discharges that heat the gas over much longer periods of time ($\mathcal{O}$ (1 μs)) [40].

In addition to fast-gas heating, other important energy channels include vibrational excitation and the dissociation of N_2 and O_2. Detailed kinetic simulations are the only reliable manner of accurately capturing the redistribution of electrical energy among those channels at different thermodynamic conditions and for different voltage pulses. A two-temperature model is used to describe the non-thermal plasma generated by a large voltage pulse that produces electron temperatures that

are significantly higher than those of neutral particles and ions. We begin by presenting zero-dimensional reactor simulations with significant heating and identifying the mechanisms/reactions responsible for heating using a detailed kinetics mechanism. A description of the resulting non-equilibrium is also presented.

The objectives are as follows:

- Identify processes and reactions responsible for fast gas heating and slow gas heating as typically observed in non-equilibrium discharges in air.
- Characterize the degree of vibrational non-equilibrium during and after the discharge.
- Provide an analysis of the non-equilibrium state of the gas and its dependence from operating parameters in order to guide the interpretation of non-equilibrium effects in multi-dimensional discharge configurations.

2.1 Two-temperature reactor governing equations

The mathematical model consists of a set of ordinary differential equations (ODEs) that describe the evolution of the thermodynamic state of an ensemble of M species. The approach described below is identical to the two-temperature model used by Deak et al. in Ref. [41] and it will only be briefly described here. The number density of each particle class is n_i, the internal energy density of the electrons is u_e, and u is the internal energy density of the ensemble of all other particles. The system

of $M+2$ nonlinear ODEs reads

$$\frac{dn_i}{dt} = \omega_i \quad i = 1, \ldots, M, \tag{2.1}$$

$$\frac{du_e}{dt} = Q_e \qquad \frac{du}{dt} = Q. \tag{2.2}$$

In the equations above, ω_i is the net rate of formation of particle i and Q_e and Q are the rate of energy gain for the electrons and all other particles. The electron energy source term reads

$$Q_e = 3k_B \left(\sum_{i=1,\, i\neq e}^{M} \nu_i^{el} \frac{m_e}{m_i} \right) n_e (T_e - T) - \sum_{j=1}^{R} \delta\varepsilon_j \omega_e^j + Q_E(t). \tag{2.3}$$

The first and second terms in Eq. (2.3) represent energy transfers from electrons to other particles via elastic and inelastic collisions, respectively. m_i and m_e are the masses of species i and electron mass, ν_i^{el} is the elastic collision frequency between species i and the electron, T_e and T are the temperature of the electron and that of all other particles. $\delta\varepsilon_j$ is the energy lost by the electron in inelastic collision j occurring at a rate ω_e^j. The third term in Eq. (2.3), $Q_E(t)$, represents the energy acquired by electrons from the electric field during each pulse. The internal energy source term for the ensemble of particles other than the electrons is $Q = -Q_e + Q_E(t)$.

Thermodynamic properties and rate coefficients for all plasma processes and conventional combustion chemistry reactions are stored in CHEMKIN format and evaluated using the two-temperature extension of the CHEMKIN library [42]. More details about the kinetic model are provided below in Section 2.2. Time integration

of the system of ODEs is performed efficiently with a variable time step and variable order Backward Differentiation Formula (BDF) implicit method as implemented in the CVODE solver [43].

2.2 Kinetics Mechanism

The kinetic mechanism developed in [41] (adapted from [44]) is used in this study and summarized briefly. The set of plasma kinetics includes electron impact processes with O_2, N_2, and O resulting in excitation, dissociation, and ionization. Vibrational excitation is included only for N_2, with the first 8 vibrational levels along with electronically excited states for O_2, N_2, O, and N. Thermodynamic properties of excited states are calculated using the approach described in Ref. [1], avoiding the common issue of *double-counting* vibrational states. For more information regarding cross-section data, rate coefficients and its functional form, and discussions about the range of validity of the mechanism, the reader is referred to Refs. [44; 41]. The detailed list of species included in the mechanism is listed in Tab. 2.1.

2.3 Overview of the plasma discharge at ambient conditions

We consider air (79% N_2 and 21% O_2 by volume) at atmospheric conditions, 1.0 atm and initial temperature $T_0 = 300$ K. A positive voltage is applied at the anode while the cathode is grounded. The voltage bias is described by the sigmoid

Table 2.1: Species included in the detailed air/plasma kinetics model grouped in three categories: neutral and charged species in thermal equilibrium (groups 1 and 2) and neutral species in thermal non-equilibrium (group 3). Symbol $N_2(v = 0)$ represents the vibrational ground state of diatomic nitrogen and symbols $N_2(v = 1, \ldots, 8)$ represent states in the first eight vibrational bands above ground for which thermodynamic properties are computed as in Ref. [1] (see Appendix B for details).

Group	Species
1. Equilibrium	O, N, NO, O_2, O_3
2. Charged	E, $O_2{}^+$, $N_2{}^+$
3. Non-equilibrium	$N_2(v = 0)$, $N_2(v = 1)$, $N_2(v = 2)$, $N_2(v = 3)$, $N_2(v = 4)$, $N_2(v = 5)$, $N_2(v = 6)$, $N_2(v = 7)$, $N_2(v = 8)$, $N_2(A^3\Sigma_u^+)$, $N_2(B^3\Pi_g)$, $N_2(B'^3\Sigma_u^-)$, $N_2(W^3\Delta_u)$, $N_2(a^1\Pi_g)$, $N_2(a'^1\Sigma_u^-)$, $N_2(a''^1\Sigma_g^+)$, $N_2(w^1\Delta_u)$, $N_2(C^3\Pi_u)$, $N_2(E^3\Sigma_g^+)$ $O_2(a^1\Delta_g)$, $O_2(b^1\Sigma_g^+)$, $O(^1D)$, $O(^1S)$, $N(^2D)$, $N(^2P)$

function

$$V(t) = V_{\max}\left[f(t-\delta,\lambda) + f(t-\delta-t_r-t_p,-\lambda) - 1\right], \tag{2.4}$$

$$f(t,\lambda) = \frac{1}{1+\exp\left(-\lambda t\right)}, \tag{2.5}$$

where the delay $\delta = 3.0$ ns, rise time $t_r = 5$ ns, $\lambda = 8/t_r$, and plateau time $t_p = 55$ ns are constants. The maximum voltage $V_{\max}$ is specified for a maximum reduced electric field of 200 Td and a maximum volumetric energy deposition of 2.4 mJ/mm^3, which corresponds roughly to an energy per pulse of 1 to 2.5 mJ (assuming a discharge radius of 250 μm and gap length between 1 and 2.5 mm). This volumetric energy deposition results in heating of the gas to around 2000 K, which is within the range of temperatures observed in nanosecond discharge pulses. If the maximum volumetric energy deposition is reached before the voltage pulse is over, the voltage is instantaneously set to zero and no more energy is deposited into the mixture. The

resulting temperature and E/N profiles from the start of the discharge up to 5 ms are presented in Fig. 2.1.

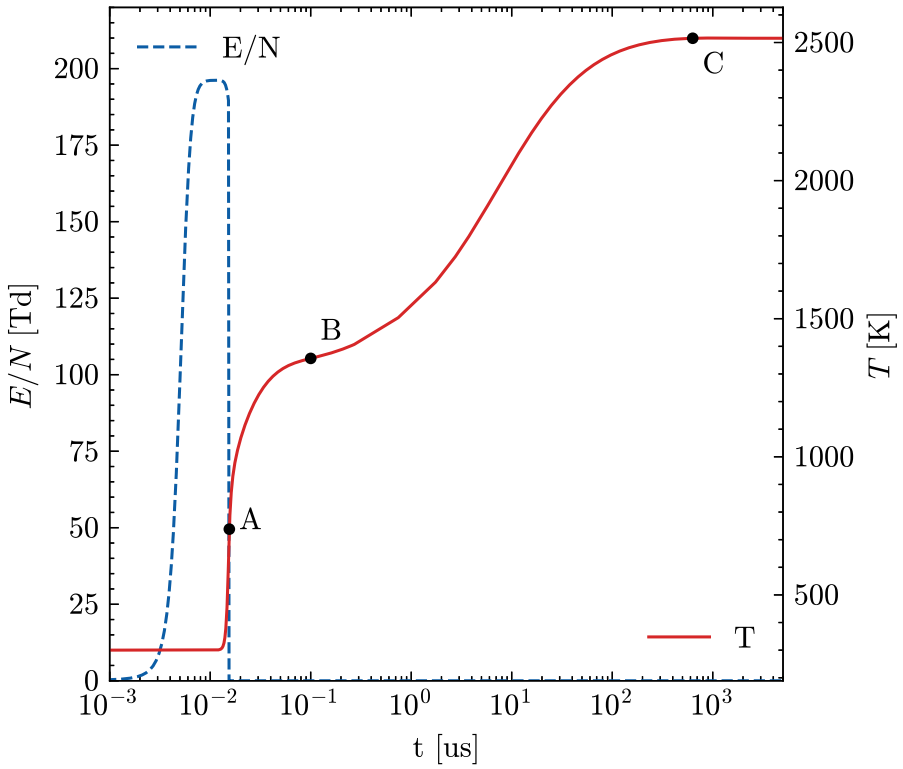

Figure 2.1: Overview of the temperature (solid red line) and reduced electric field E/N (dashed blue line) for a volumetric energy deposition of 2.4 mJ/mm^3. Important events are labeled:"A" marks the end of the energy deposition, "B" marks the end of the first stage of heating, and "C" marks the end of the second stage of heating.

From Fig. 2.1, we identify several important features in the temporal evolution of the temperature associated with all particles other than electrons. From the beginning of the simulation up to instant A, we observe the rise of the reduced electric field until E/N reaches a plateau value around 200 Td, depositing all the energy before being turned off at around 15 ns. While the voltage pulse is active,

the temperature rises by about 500 K and when the voltage is off, the temperature continues rising by about 600 K more. Instant B in Fig. 2.1 at 100 ns marks the end of the first stage of heating, the so-called "fast" gas heating [22] associated with sub-acoustic time scales. The second stage of heating, or the so-called slow-heating, takes place over the longer interval of about 100 μs between instants B and C in Fig. 2.1 and corresponds to a temperature rise of 1200 K in this case.

In order to evaluate the impact of the various kinetic processes on the observed temperature rise, more specific metrics are required. We define the rate of change in temperature associated with each reaction k by using the net volumetric rate of reaction q_k [kmol/m^3-s], energy lost by electrons and gained by the gas ϵ [J/kmol], change in the internal energy associated with the reaction at a given temperature Δu [J/kmol], and the volumetric heat capacity at constant volume $c_v C$ [J/K-m^3]

$$\frac{dT_k}{dt} = q_k \frac{\epsilon - \Delta u(T)}{c_v C}. \tag{2.6}$$

The metric above provides a quantitative measure of the contribution of each reaction towards the rise in temperature of the gas at a given instant. Let's illustrate this quantity with the impact dissociation reaction

$$\mathrm{E} + \mathrm{N_2} \rightarrow 2\mathrm{N} + \mathrm{E}. \tag{2.7}$$

At reference conditions (T = 298.15 K), the reaction has an ϵ value of 1.25 $\times 10^3$ J/kmol, and a $\Delta u(T)$ value of 0.944 $\times 10^3$ J/kmol, used to calculate the value of the numerator in Eq. (2.6) of 0.31 $\times 10^3$ J/kmol. The integral dT_k/dt of this metric over a select time interval also provides the overall temperature change associated with

each reaction. The integral

$$\int_{t_A}^{t_B} \frac{dT_k}{dt} dt, \tag{2.8}$$

is computed for all reactions and its absolute value used to rank the reactions. The 20 largest contributions during the "fast heating" stage are shown in Fig. 2.2.

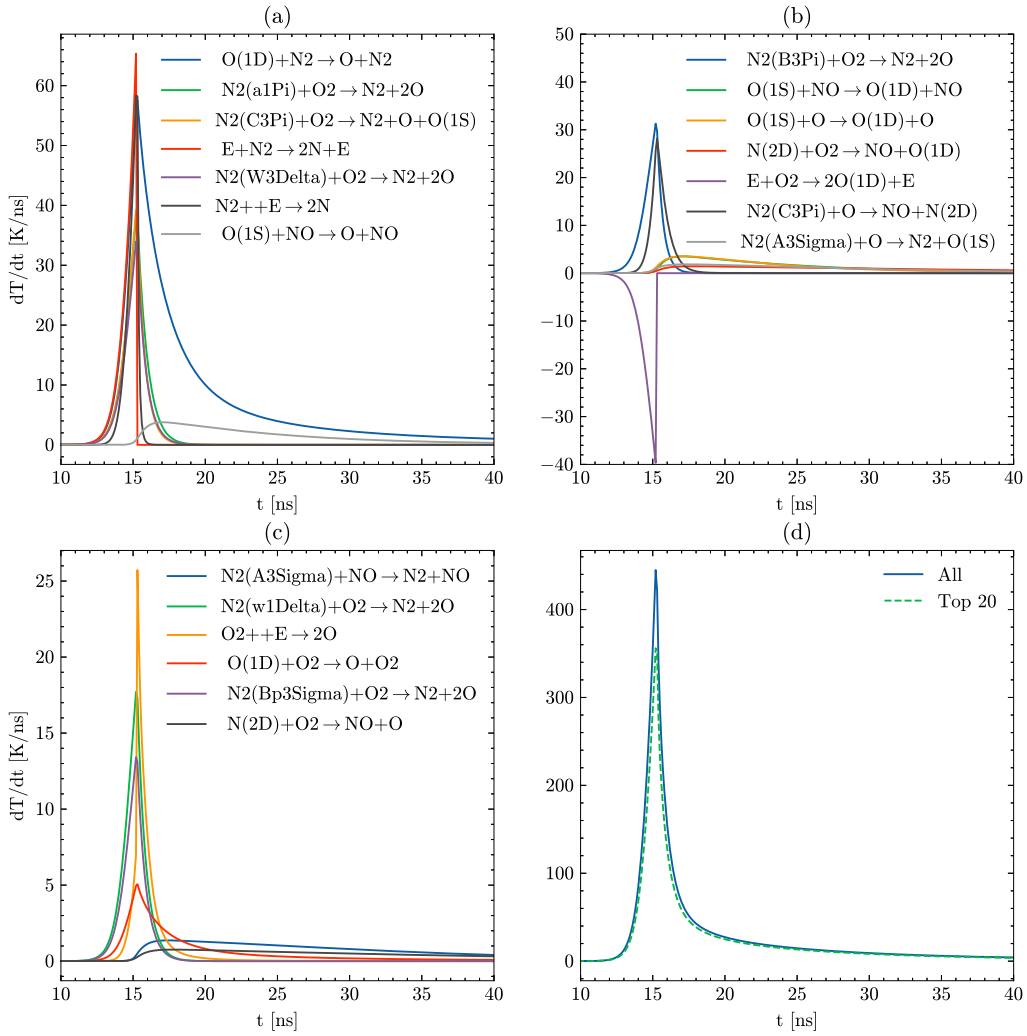

Figure 2.2: (a), (b), and (c) dT/dt for each of the top 20 ranked reactions based on the integral in Eq. (2.8) with $t_A = 0$ and $t_B = 100$ ns. (d) Contribution of the top 20 reactions to the total heating rate of the gas. Time interval spans the first stage of heating $0 \leq t \leq 100$ ns.

The top 20 reactions account for about 80-90% of the total heating rate observed during the first stage. From the reactions shown in Fig. 2.2, it is clear that

four classes of reactions dominate the first stage of heating: dissociative quenching of electronically excited N_2 states (e.g., $N_2(B^3\Pi) + O_2 \rightarrow N_2 + 2O$), electron impact dissociation of N_2 or O_2 (e.g., $N_2 + E \rightarrow 2N + E$), dissociative recombination of N_2^+ or O_2^+ (e.g., $N_2{}^+ + E \rightarrow 2N$), and quenching of electronically excited O atoms (e.g., $O(^1D) + N_2 \rightarrow O + N_2$). The contribution of the quenching of electronically excited N molecules, while present, is very small compared to the contribution of other reactions.

The same methodology is applied during the second stage of heating between instants B and C in Fig. 2.1 in order to determine the reactions with the largest contribution. The top 20 reactions and their contribution towards gas heating during the second stage is shown in Fig. 2.3.

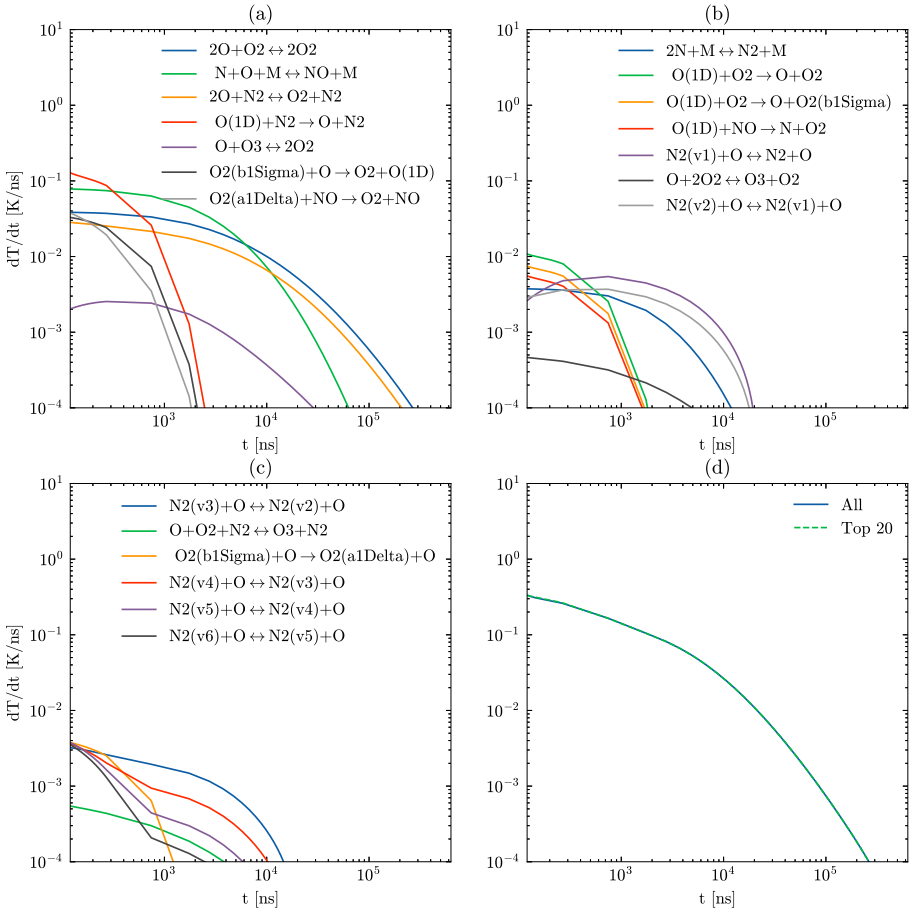

Figure 2.3: (a), (b), and (c) dT/dt for each of the top 20 ranked reactions based on the integral in Eq. (2.8) with $t_A = 100$ ns and t_B the end of the simulation. (d) Contribution of the top 20 reactions to the total heating rate of the gas. Time interval spans the second stage of heating 100 ns $\leq t \leq t_{\text{end}}$.

The second stage of heating lasts longer than the first stage and is also characterized by contributions of different classes of reactions. Among the many reactions contributing to mixture heating over long time scales, it is worth highlighting the following processes: the recombination of O and N molecules throughout the time inter-

val (eg., $2O+O_2 \leftrightarrow 2O_2+$ and $2N+M \leftrightarrow N_2+M$), quenching of the $O(^1D)$ atom (e.g., $O(^1D)+N_2 \rightarrow O+N_2$) and excited O_2 molecules (e.g., $O_2(B^1\Sigma)+O \rightarrow O_2+O(^1D)$) during the early stages (0.1 to 1 μs), and the relaxation of vibrationally excited N_2 molecules (e.g., $N_2(v_1)+O \leftrightarrow N_2+O$) between 1 and 10 μs. The reactions identified in this analysis are summarized and organized in categories in Tab. 2.2 for the first heating stage and in Tab. 2.3 for the second heating stage.

The same approach is now employed to understand the processes responsible for heating throughout the entire discharge and following the relaxation phase. The contribution of all reactions in a specific category are summed together and the total change in temperature associated with the reaction category is computed by integrating Eq. (2.6) in time. The comparison of the two metrics is shown in Fig. 2.4. Notice that reactions labeled as "O quenching" in both tables are combined.

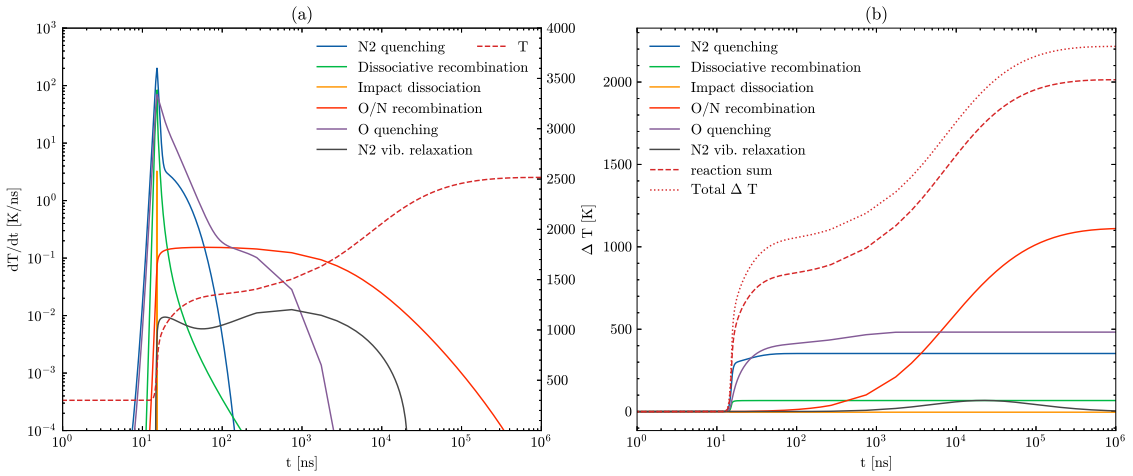

Figure 2.4: (a) Contribution of each reaction category to the mixture heating rate and (b) total temperature associated with the reaction category throughout the entire process. In (a), the temperture is shown on the vertical axis on the right.

Table 2.2: Summary of reactions with the largest contribution towards gas heating during the first stage, $0 \leq t \leq 100$ ns.

No.	Reaction equation
	Quenching of electronically excited N_2
1	$N_2(a^1\Pi_g) + O_2 \rightarrow N_2 + O_2$
2	$N_2(C^3\Pi_u) + O_2 \rightarrow N_2 + O + O(^1S)$
3	$N_2(W^3\Delta_u) + O_2 \rightarrow N_2 + 2O$
4	$N_2(B^3\Pi_g) + O_2 \rightarrow N_2 + 2O$
5	$N_2(C^3\Pi_u) + O \rightarrow NO + N(^2D)$
6	$N_2(A^3\Sigma_u^+) + O \rightarrow N_2 + O(^1S)$
7	$N_2(A^3\Sigma_u^+) + NO \rightarrow N_2 + NO$
8	$N_2(B^3\Sigma_u^+) + O_2 \rightarrow N_2 + 2O$
	Dissociative recombination
9	${N_2}^+ + E \rightarrow 2N$
10	${O_2}^+ + E \rightarrow 2O$
	Impact Dissociation
11	$N_2 + E \rightarrow 2N + E$
12	$O_2 + E \rightarrow 2O + E$
13	$O_2 + E \rightarrow 2O(^1D) + E$
	Quenching of electronically excited O
14	$O(^1D) + N_2 \rightarrow O + N_2$
15	$O(^1S) + NO \rightarrow O + NO$
16	$O(^1S) + NO \rightarrow O(^1D) + NO$
17	$O(^1S) + O \rightarrow O(^1D) + O$
18	$O(^1D) + O_2 \rightarrow O + O_2$

Table 2.3: Summary of reactions with the largest contribution towards gas heating during the second stage heating, $t \geq 100$ ns.

No.	Reaction equation
	Atomic oxygen and nitrogen recombination
1	$2O + O_2 \leftrightarrow 2O_2+$
2	$N + O + M \leftrightarrow NO + M$
3	$2O + N_2 \leftrightarrow O_2 + N_2$
4	$O + O_3 \leftrightarrow 2O_2$
5	$O + 2O_2 \leftrightarrow O_3 + O_2$
6	$2N + M \leftrightarrow N_2 + M$
7	$O + O_2 + N_2 \leftrightarrow O_3 + N_2$
	Oxygen quenching
8	$O(^1D) + N_2 \rightarrow O + N_2$
9	$O(^1D) + O_2 \rightarrow O + O_2$
10	$O(^1D) + O_2 \rightarrow O + O_2(b^1\Sigma_g^+)$
11	$O(^1D) + NO \rightarrow N + O_2$
12	$O_2(b^1\Sigma_g^+) + O \rightarrow O_2 + O(^1D)$
13	$O_2(a^1\Delta_g) + NO \rightarrow O_2 + NO$
14	$O_2(b^1\Sigma_g^+) + O \rightarrow O_2(a^1\Delta_g) + O$
	Vibrational relaxation
15	$N_2(v_1) + O \leftrightarrow N_2 + O$
16	$N_2(v_2) + O \leftrightarrow N_2(v_1) + O$
17	$N_2(v_3) + O \leftrightarrow N_2(v_2) + O$
18	$N_2(v_4) + O \leftrightarrow N_2(v_3) + O$
19	$N_2(v_5) + O \leftrightarrow N_2(v_4) + O$
20	$N_2(v_6) + O \leftrightarrow N_2(v_5) + O$

Figure 2.4 confirms some of our earlier observations. At the earliest stage of the discharge and shortly thereafter, heating is dominated by quenching of electronically excited N_2 molecules and electronically excited O atoms. The role played by the dissociation of oxygen by excited N_2 quenching is well known and highlighted in the detailed experimental measurements by Rusterholtz et al. [22]. This observation is also supported by the review in Popov et al. [45], where the quenching of excited N_2 and electronically excited states of O were highlighted as the main sources of fast gas heating in the near afterglow phase following discharges with reduced electric field strengths $150 \leq E/N \leq 250$. The contribution of dissociative recombination reactions is noticeable, but significantly smaller than that of quenching reactions. While the peak value of dT/dt associated with individual impact dissociation reactions is high (see Fig. 2.2), their overall contribution to the temperature rise of the mixture is minor. During the second heating stage, the heating process is dominated by O and N recombination with smaller contributions from vibrational relaxation and O quenching. Overall, considering only 38 reactions and 6 categories of reactions, we were able to account for 90% of gas heating (as measured by the overall increase in the mixture temperature).

At this point, it is important to recall the limitations associated with the use of an isochoric-adiabatic zero dimensional reactor for the simulation of plasma discharges. In nanosecond discharges operating near atmospheric pressure, we expect the gas to undergo an isochoric process during the first 50 to 100 ns. However, this early phase is followed by the expansion of the pressurized channel, which leads to a rapid decrease in temperature and pressure, in addition to mass, momentum,

and energy transport. The implications of those important simplifications on the dynamics of chemical non-equilibrium are obviously challenging to predict a priori. A more comprehensive analysis of the robustness of the conclusions advanced in this Chapter is presented in Chapter 3 (see section 3.2).

2.4 Vibrational non-equilibrium

Describing accurately the increase in the mixture temperature is an important aspect of simulating nanosecond discharge pulses, yet it does not represent the whole non-equilibrium processes engendered by the discharge. In typical discharges near or at atmospheric pressures, anywhere between 10% and 30% is thought to be stored in overpopulated vibrational degrees of freedom [22; 31]. Next, we present an analysis that seeks to quantify the temporal evolution of vibrationally excited diatomic nitrogen.

We defined particles representing nitrogen in its vibrational ground state ($N_2(v = 0)$) and an additional 8 particles representing nitrogen in vibrational states 1 through 8. Each of those particles is associated with the energy of the vibrational band origin. In Fig. 2.5, we observe the fraction of each band of vibrationally excited nitrogen as a function of the energy of the vibrational band origin at different times during the discharge. The slope of the relative populations for $v = (0, 1)$ is much larger than for $v = 2-8$ at early stages following the discharge, indicating that the vibrational temperature of the "first level" is considerably lower than the temperature of the higher vibrational states ($v = 2, \ldots, 8$). In Ref. [46], it is explained that the electron impact processes during the discharge produce overpopulated vibrational

states for $v \geq 2$, yielding temperatures that are comparable to those of electrons and much larger than the temperature associated with populations in levels 0 and 1.

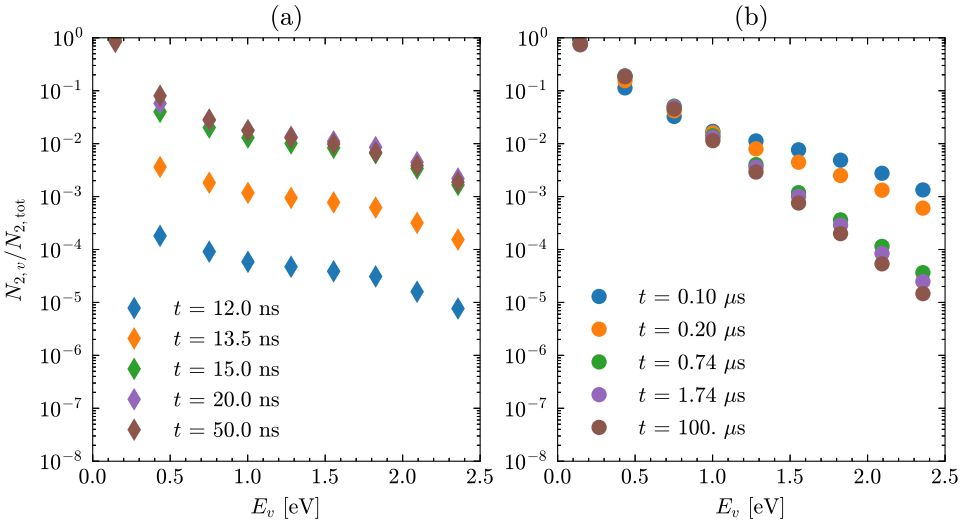

Figure 2.5: Fraction of vibrationally excited nitrogen as a function of the energy of the vibrational band origin at (a) early and (b) later stages of the discharge.

This type of non-equilibrium energy distribution has been observed in previous experimental work [47; 48], where it has been parameterized by three temperatures: T_{v01} is calculated from the relative populations of particles in vibrational levels $v = 1$ and $v = 0$, and T_{v1v} is calculated from the relative population of particles in vibrational states $v > 1$, in addition to the gas temperature T, which can be taken to represent a translational temperature also equal, by construction of the thermodynamic model, to the rotational temperature. A visual representation of these three temperatures along with relative populations is shown in Fig. 2.6 at different times during the discharge.

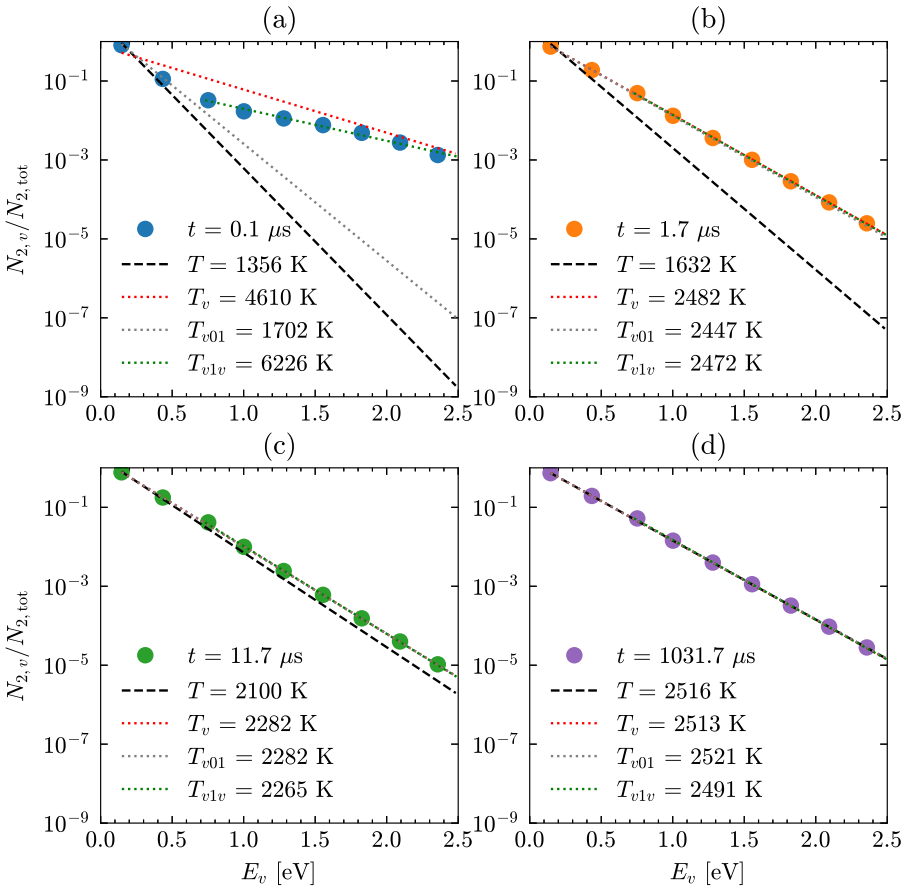

Figure 2.6: Relative populations of vibrationally excited nitrogen particles, Boltzmann temperature of vibrationally excited species ($v = 0, \ldots, 8$) T_v, Boltzmann fit temperature using only the first two vibrational levels ($v = 0, 1$) T_{v01}, and Boltzmann fit temperature of vibrational levels ($v = 2, \ldots, 8$) T_{v1v} at different times.

At early times ($t < 50$ ns), the three temperature model is inadequate to describe the vibrational energy distribution (not shown), which displays a sharp "kink" beginning at $v = 7$. Following the discharge ($t = 0.1$ μs), the three temperature model becomes adequate and the three temperatures differ one from the other. At later stages, the distribution is accurately represented by a single vibrational temperature

T_v, which is found to be significantly larger than the background temperature until about 10 μs. Eventually, the populations of nitrogen in the various vibrational states reach a state of equilibrium at the gas temperature. The three temperatures as a function of time are shown in Fig. 2.7 for $t > 100$ ns.

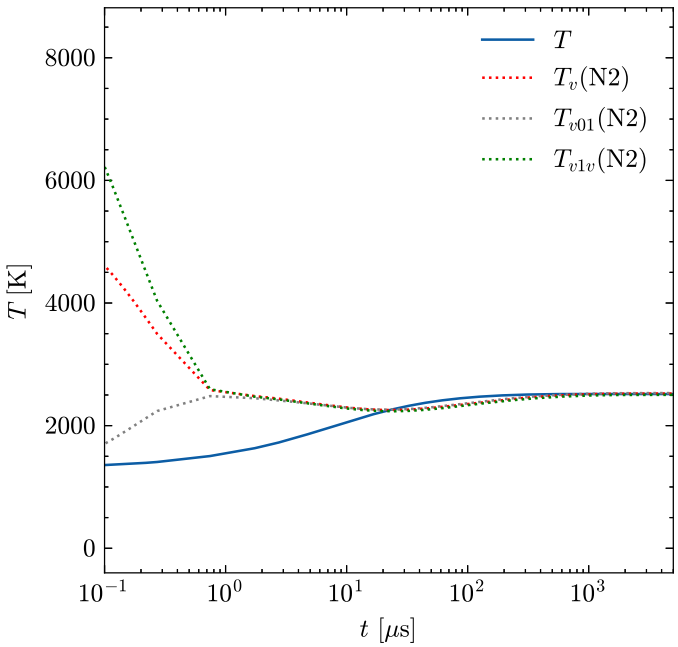

Figure 2.7: Gas temperature T, Boltzmann fit temperature using vibrational levels $v = (0, \ldots, 8)$ T_v, vibrational temperature T_{v01}, and T_{v1v} as a function of time. See Figure 2.6 for more details.

The discharge generates vibrational non-equilibrium associated with vibrational temperatures of up to 6000 K for the higher vibrational states. At 1 μs, the vibrational states approach a Boltzmann distribution and the vibrational non-equilibrium can be described by a single vibrational temperature T_v as seen from the overlap of the various vibrational temperatures in Fig. 2.7. For a brief period of

time, the vibrational temperature drops slightly below the gas temperature, likely a minor nonphysical effect due to the numerical model. Finally, thermal equilibrium is reached by about 500 μs. The magnitude and trends observed for the various vibrational temperatures presented above are comparable to those found in experimental studies of vibrational non-equilibrium in air [46; 47; 48].

2.5 Phenomenological Description

The simulation of fully coupled nanosecond discharges in air or air/fuel mixtures are numerically demanding. The time step sizes and spatial resolution required are much more stringent than those for Large-Eddy simulation, and the number of species and reactions required to accurately describe kinetics are significantly larger. In order to overcome this challenge, recent studies focused on developing a phenomenological description of the discharge [31; 33; 34] (see Chapter 1 for a detailed discussion). The objective of this class of approaches is to capture the most important effects of the non-equilibrium discharge, without incurring the cost and complexity associated with multidimensional modelling of plasma discharges.

The most popular approach involves splitting the discharge power $\dot{E}^p$ [W] into three components

$$\dot{E}^p = \dot{E}^p_{\text{chem}} + \dot{E}^p_{\text{heat}} + \dot{E}^p_{\text{vib}}, \tag{2.9}$$

where $\dot{E}^p_{\text{chem}}$ represents chemical effects (mainly dissociation), $\dot{E}^p_{\text{heat}}$ represents fast gas heating, and $\dot{E}^p_{\text{vib}}$ non-equilibrium vibrational excitation.

The power corresponding to fast gas heating $\dot{E}^p_{\text{heat}}$ is added directly as a

source term to the energy transport equation. The non-equilibrium vibrational energy density is removed from the mixture energy and modeled through a separate vibrational energy transport equation, where the vibrational power $\dot{E}^p_{\text{vib}}$ is added as a source term. Finally, chemical species production terms $\dot{\omega}_k$ associated with species k are added as source terms to the species conservation equations in a manner that is consistent with $\dot{E}^p_{\text{chem}} = \sum_k u_k \dot{\omega}_k$, where u_k is the internal energy of species k, and typically results in the dissociation of nitrogen and oxygen. The computation of these chemical source terms is outside the scope of this work, and the reader is directed to Refs. [31; 13] for more details. In the context of these models, however, it is important to explore the values taken by the coefficients α_{chem}, α_{heat}, and α_{vib} that represent corresponding energy fractions such that $\sum \alpha_j = 1$.

In this work we follow the approach outlined in Ref. [31] to calculate the coefficients, which are obtained by postprocessing simulations of plasma discharges in zero-dimensional isochoric and adiabatic reactors. The various energy contributions are computed starting from the internal energy u_k of the kth species [J/kmol], which is split into four parts

$$u_k = u_{k,\text{chem}} + u_{k,\text{vib}} + u_{k,\text{exc}} + u_{k,\text{ion}}. \tag{2.10}$$

For details and a discussion on how the internal energy u_k is split into the above 4 contributions for each species, the reader is referred to Appendix A.

The discharge energy density is similarly divided into different energy density channels e^p_{i} [J/m^3], which are computed as

$$e^p_{\text{i}} = \sum_k^N \int_t \dot{\omega}^p_k u_{k,i} dt, \tag{2.11}$$

where $i = \text{chem}, \text{vib}, \text{exc}, \text{ion}$, represents the energy channel, N is the number of species and $\dot{\omega}_k^p$ [kmol/m^3-s] is the net reaction rate of species k associated with a particular energy density channel e_i^p. Finally, heating is computed as

$$e_{\text{heat}}^p = \int_t \sum_j^P q_j[\epsilon - \Delta u(T)]dt, \tag{2.12}$$

where q_j is the net reaction rate associated with reaction j, and P is the total number of reactions. The discharge energy fractions are then determined using

$$\alpha_{\text{chem}} = e_{\text{chem}}^p/e^p,\ \alpha_{\text{heat}} = (e_{\text{heat}}^p + e_{\text{ion}}^p + e_{\text{exc}}^p)/e^p, \alpha_{\text{vib}} = e_{\text{vib}}^p/e^p, \tag{2.13}$$

where e^p [J/m^3] is the known volumetric energy deposited into the mixture.

The three coefficients are plotted in Fig. 2.8 along with the reduced electric field for the reference case. In the earliest stages of the discharge when the voltage is increasing, most of the energy is deposited into vibrational excitation. This trend quickly changes after the voltage plateau is reached, when there is a significant decrease in vibrational excitation and a corresponding increase in the heating coefficient (which includes the contribution associated with electronically excited and ionized species) and in the chemical energy coefficient.

Finally, there is another significant change after the voltage is turned off at 15 ns, where some of the "heat" energy goes into "chemical" energy. This is likely the result of dissociative quenching of electronically excited N_2 and quenching of electronically excited O immediately after the discharge. After this inversion of the contributions, the coefficients reach a plateau that last for tens of nanoseconds. Since the aim of phenomenological models is to avoid simulating the discharge phase, the

asymptotic values of the coefficients at 100 ns are adopted to initialize hydrodynamic simulations in these kind of approaches. The computed values are in good quantitative agreement with those reported for air at 200 Td from Ref. [23].

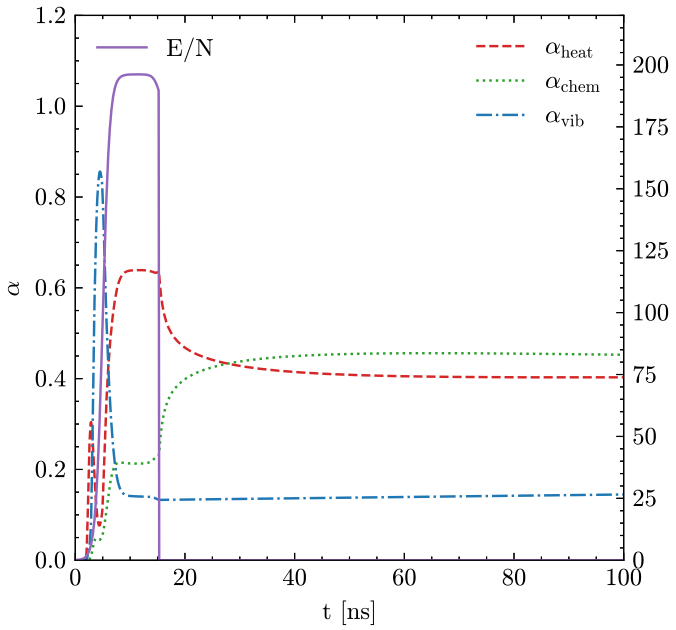

Figure 2.8: Energy deposition coefficients for heating, chemical energy, and vibrational excitation as a function of time calculated as discussed in Section 2.5.

2.6 Constrained equilibrium

In this section, we also explore and present an alternative description of the state of non-equilibrium generated by the nanosecond discharge pulse. This description is based on the theory of constrained equilibrium as presented by Pope et al. [49], which allows for the calculation of thermodynamic equilibrium under constraints on the moles of select species.

The reasoning behind the constrained equilibrium approach to the characterization of non-equilibrium induced by the plasma discharge is as follows. A nanosecond discharge pulse deposits energy in a matter of nanoseconds as described in Section 2.3. Only a fraction of the energy heats the gas directly, with the remaining energy stored in vibrational and electronic non-equilibrium, or dissociated nitrogen and oxygen. The energy stored in non-equilibrium decreases leading to an increase in gas temperature over two stages, as described in Section 2.3. Specific species are closely associated with particular relaxation processes, which provide insight about the nature of non-equilibrium generated by the discharge.

The process is summarized as follows. Species are categorized and associated with a particular type of energy or class of non-equilibrium. An equilibrium temperature is calculated assuming constant enthalpy and pressure with no constraints. Such equilibrium temperature is taken to represent the final temperature that the non-equilibrium gas would attain if it were allowed to relax at constant pressure and without heat losses. Additional equilibrium temperatures are calculated by constraining select species. While unconstrained species are allowed to relax to equilibrium, the number of moles of the constrained species stays constant and equal to the initial. As the mixture reaches a constrained equilibrium, the temperature increases, and this rise in temperature is interpreted as due to the unconstrained species relaxing to equilibrium. The various categories and associated species are outlined in Tab. 2.4.

Table 2.4: Unconstrained species per group as defined in the constrained equilibrium calculations. N_2^*, O_2^*, O^*, N^* represents all electronically excited states of diatomic nitrogen and oxygen, and atomic nitrogen and oxygen, respectively (see Ref. [2]).

Group	Unconstrained Species
Vibrational	N_2, $N_2(v \geq 1)$
Vibrational + electronic	N_2,O_2, $N_2(v \geq 1)$, N_2^*, O_2^*, O^*, N^*
Vibrational +electronic + charges	N_2,O_2, $N_2(v \geq 1)$, N_2^*, O_2^*, O^*, N^* N_2^+, O_2^+, E
Vibrational +electronic + charges + chemistry	N_2,O_2, $N_2(v \geq 1)$, N_2^*, O_2^*, O^*, N^* N_2^+, O_2^+, E, O, N, NO

The details of non-equilibrium as described by the constrained equilibrium analysis is provided in Fig. 2.9. When interpreting the curves in Fig. 2.9(b), one should keep in mind that the difference between the curves is indicative of the contribution of the species that are constrained in one case and unconstrained in the other. At the end of the discharge, we observe the potential for about 1500 K of non-equilibrium, where roughly 200 K are due to vibrational non-equilibrium, 800 K to electronic/charge non-equilibrium, and 500 K to chemical energy (dissociation) in the ground state. It is then clear that the importance of specific classes of non-equilibrium is associated with the potential for significant increases in the temperature of the gas should the mixture be brought to thermal and chemical equilibrium.

By 100 ns, the contribution of electronic/charge has disappeared as indicated by $T_{\text{vib+elec+charge}}$ being equal to T_{vib}. The sole remaining contribution to non-equilibrium other than the overpopulation of vibrational states is that associated with

"chemical" energy, i.e., the presence of atomic O and N due to dissociation of N_2 and O_2 molecules. The contribution of vibrational non-equilibrium decreases slowly until it disappears by 10 μs, and the energy stored in dissociated species decreases steadily until 100 μs when the mixture reaches thermal and chemical equilibrium, consistent with the conclusions presented in Sections 2.3 and 2.5.

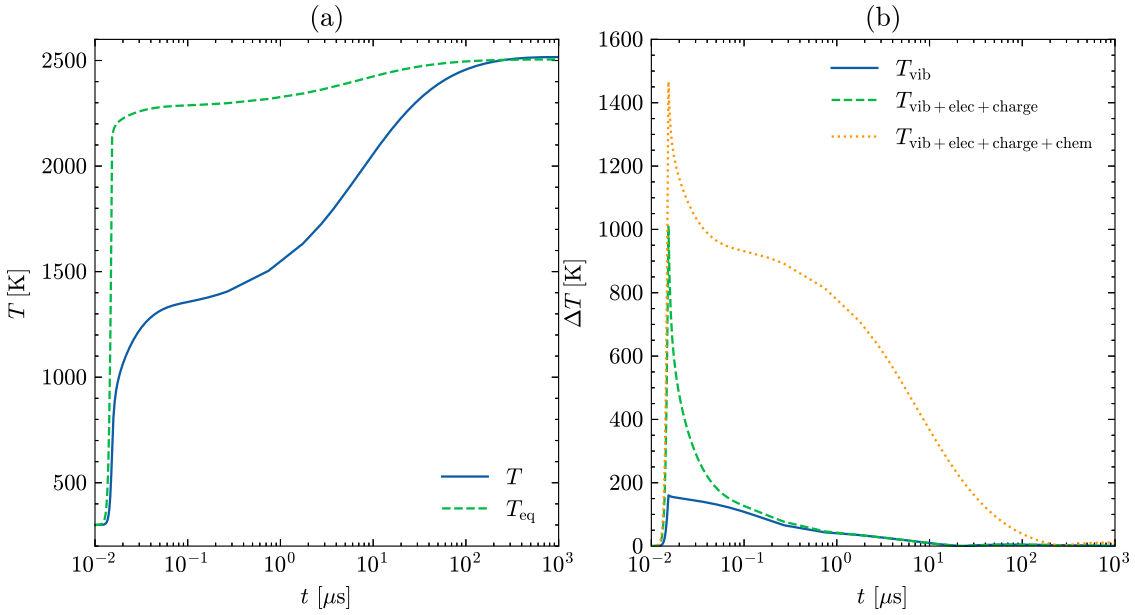

Figure 2.9: (a) Temperature T and calculated equilibrium temperature T_{eq} assuming constant enthalpy and pressure, and (b) temperature difference between mixture temperature T and equilibrium temperatures calculated assuming constant enthalpy and pressure and additional constraints as specified in Tab. 2.4

Chapter 3

Non-equilibrium discharges: Parametric Studies

In Chapter 2, we discussed the state of thermal non-equilibrium brought by a typical nanosecond discharge pulse in air, including an analysis that identified reactions responsible for gas heating, a detailed description of vibrational non-equilibrium, and quantitative metrics to characterize the nature of the non-equilibrium. In this Chapter, a similar study is performed in order to quantify how the extent and nature of non-equilibrium vary as a function of various governing parameters, including energy deposited per unit volume and voltage pulse waveforms. Finally, the reduced kinetics mechanism employed for high-fidelity simulations is presented and its accuracy assessed by comparisons against the detailed one.

The objectives are summarized below

- Characterize the effect of the energy deposited per unit volume on the evolution of the state of thermal non-equilibrium and the process of mixture thermalization.
- Quantify the effect of the pulse waveform and details of the energy deposition process on thermal non-equilibrium.
- Validate the reduced mechanism against the detailed one at conditions relevant

to high-fidelity simulations of nanosecond plasma discharges.

3.1 Parametric study: energy deposited per unit volume

In the previous section, gas heating was shown to occur over two different stages: a first stage of heating occurred on sub-acoustic time scales with a total duration of ≈ 100 ns and a second stage of heating was shown to take place afterward. In this section, the effect of varying the energy deposited per unit volume is explored and its impact on the two heating stages quantified. As it will be discussed at length in the reminder of this work, this dependence is important in the context of nanosecond discharge pulses and when scaling the hydrodynamic effect.

Early in the evolution of the thermochemical state of the gaseous mixture following energy deposition by a nanosecond pulse, gas expansion occurs as two strong spherical shocks propagate outwards from the pin tips, and a weaker cylindrical shock propagates outwards near the axial midplane in between the electrodes. The maximum pressure, temperature, and relative strength of the shocks are all related to the local thermodynamic state of the gas in the small region of the gap where energy was deposited by the discharge. At each location in the gap region, the thermodynamic state of the gas is related to both the local density of the energy deposited as well as to the degree of thermal non-equilibrium shortly after the discharge and afterglow phase. Therefore, understanding the impact of the energy deposited per unit volume on fast and slow gas heating is important in order to characterize non-equilibrium in the plasma channel, and anticipate modifications to the hydrodynamic effects brought by the discharge as the energy per pulse changes.

The energy deposited per unit volume is varied over the range $0.5 - 4.0$ mJ/mm^3 and results are shown in Fig. 3.1, where the increase in temperature brought by the discharge ranges from 500 to 3,000 K. From the temporal evolution of the temperature, it is apparent that a first rapid rise in temperature (ultra-fast and fast heating) is followed by much slower rise (or a plateau for the lowest values of energy considered), which is then followed by a second increase in temperature on longer time scales (slow heating). Note that the temporal scale is logarithmic. We also observe the temperature change ΔT normalized by the final temperature change ΔT_{f} for each volumetric energy deposition. Two trends are clear: as the energy per unit volume increases, the heating becomes faster during both stages, and the relative proportion of fast to slow gas heating increases also.

In other words, the more energy is deposited per unit volume, the greater the increase in temperature occurring on the fastest time scales (first stage heating) relative to the total increase.

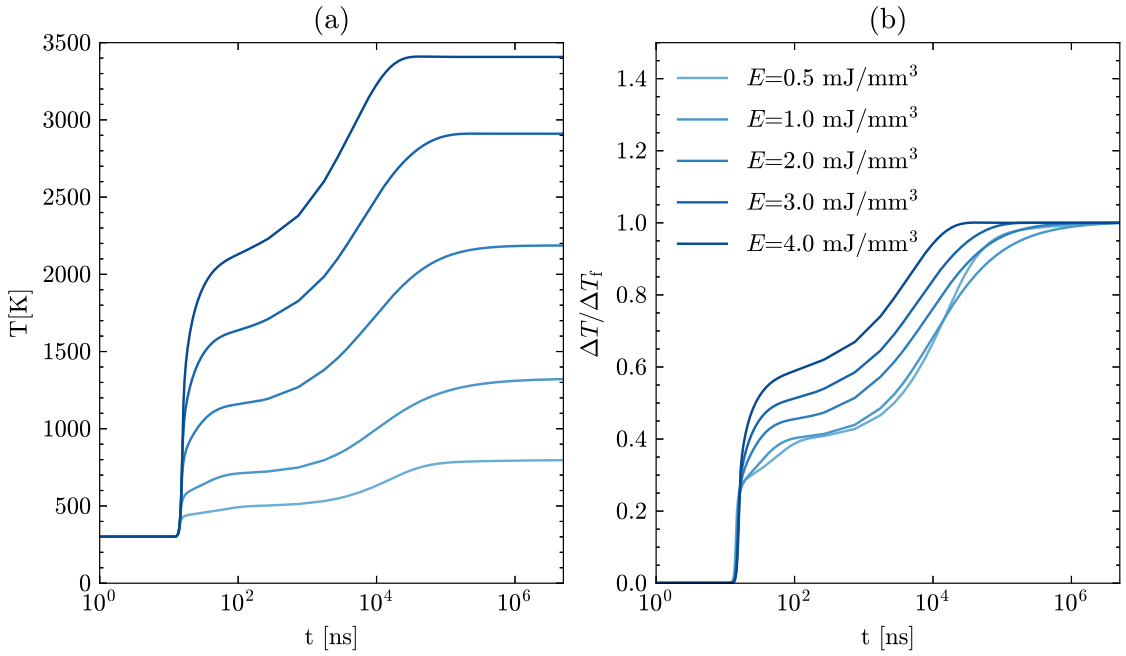

Figure 3.1: Effect of the energy deposited per unit volume on (a) the temporal evolution of temperature and (b) normalized increase in temperature as a function of time. All simulations are for air at 300 K and 1 atm.

The trends discussed above are examined in more detail by considering the various classes of reactions that contribute to gas heating and energy coefficients defined and discussed in depth in Chapter 2. Figure 3.2(a) shows the relative contributions of classes of plasma kinetic processes to the overall increase in temperature (see Section 2.3 for a detailed definition). In Fig. 3.2(b), the distribution of the plasma energy in three postulated channels [13; 31] is described by the energy coefficients (see Section 2.5 for a definition).

Both sets of data reflect cumulative contributions over long time scales, since the simulations conclude by 0.2 ms or so (see Fig. 3.1). A detailed discussion on the

implications of the length of the evolution of the zero-dimensional isochoric reactor is provided later in this Section.

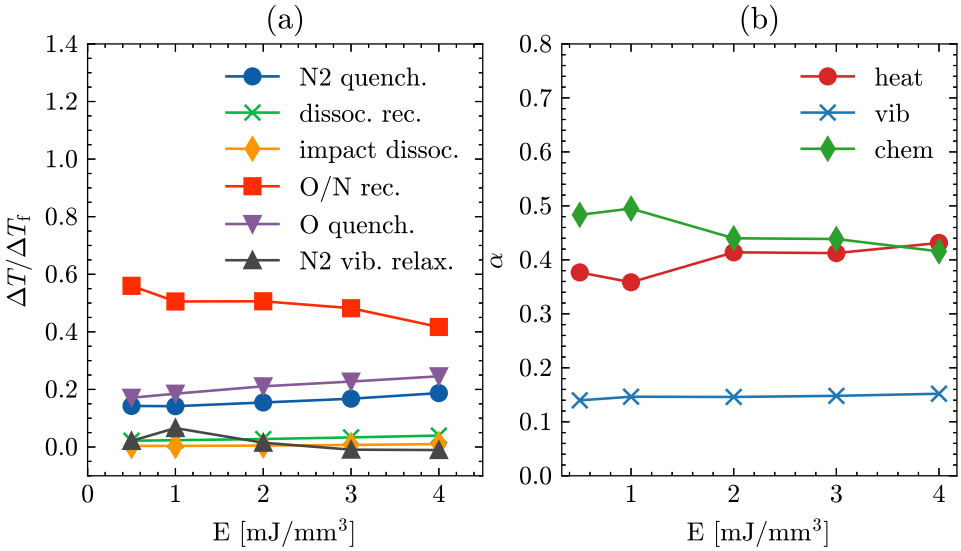

Figure 3.2: (a) Fraction of overall temperature increase associated with various classes of plasma kinetics (see Section 2.3 for the definition) and (b) energy coefficients (see Section 2.5 for the definition) as a function of the energy deposited per unit volume.

From the data in Fig. 3.2(a), it is apparent that most of the overall gas heating (between 40% and 60%) is attributed to the recombination of O and N atoms, which are formed during the discharge, while quenching of excited O and N_2 contribute equally in reason of $\approx$ 20%. The thermalization of vibrationally excited N_2, dissociative recombination, and impact dissociation contribute the remaining fraction and are minor overall contributions.

The contributions are relatively insensitive to the energy deposited, although it is apparent that, as the energy increases, the contribution of recombination de-

creases while that of quenching increases.

As far as the data in Fig. 3.2(b) are concerned, the same conclusions apply in that "heat" (reflecting the contribution of fast heating due to quenching of excited particles) and "chemical" (reflecting recombination of dissociated oxygen and nitrogen) are the greatest energy fractions and increasing energy favors the "heat" fraction over the "chemical" one. The fraction of energy that leads to vibrational excitation of N_2 is the smallest (around 15%) and is mostly insensitive to the energy deposited.

In an attempt to explain the effects brought by changes in the energy deposited during the discharge to the characteristics of thermal non-equilibrium, the mean electron energy (ϵ) and energy deposition time history are considered and shown in Fig. 3.3. It is observed that during most of the discharge, ϵ is unchanged by the amount of energy deposited for about 80% of the pulse duration, with minor variations during the interval when most of the energy is deposited towards the end of the pulse. For the largest values of the energy deposited, variations are observed in reason of 5 - 15% , which might have an impact on the energy branching of the discharge, i.e., on the fraction of electrical energy that leads to ionization, excitation, heating, and vibrational excitation. Yet, the differences in the temporal evolution of ϵ are somewhat minor and unlikely to be responsible for the changes in the nature of non-equilibrium as detailed in Fig. 3.3.

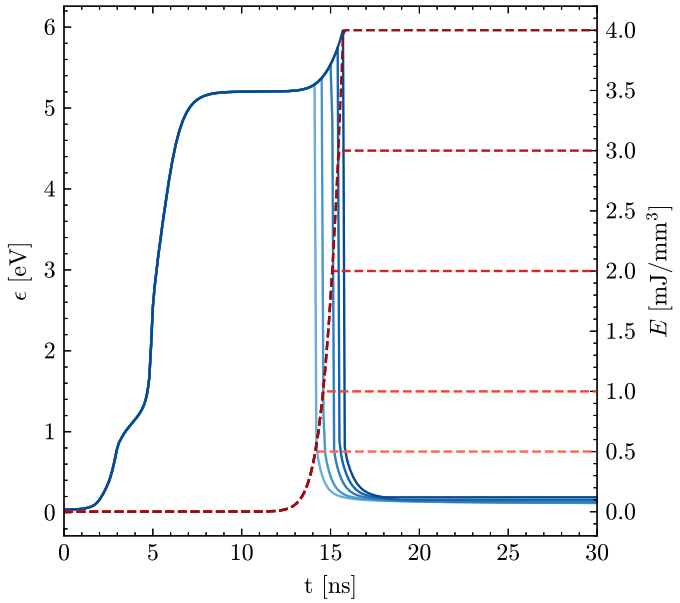

Figure 3.3: Effect of the energy deposited per unit volume on the temporal evolution of the mean electron energy (solid blue lines) and that of the cumulative energy density deposited by the discharge (dashed red lines). Darker colors correspond to higher energy deposited. See also Fig. 3.1 for the legend to the data shown. All simulations are for air at 300 K and 1 atm.

When judging the applicability of the results and data discussed thus far in this Chapter to a nanosecond discharge in between electrodes, it is important to be reminded of the limitations of the zero-dimensional iso-choric and adiabatic reactor model. Recall that the analysis presented above employ data that extend to 5 ms with temperatures that rise beyond 2,500 K (see Fig. 3.1) for the highest energy considered.

In an actual discharge between two pin electrodes, the plasma channel depressurizes and cools off in the process by $\mathcal{O}(0.5 - 5\,\mu\text{s})$ from the high-voltage pulse.

Furthermore mass and heat transport away from the kernel are active and contribute to the evolution of temperature, composition, and pressure, so that the reactor model is an inaccurate representation of the processes in the discharge channel much past $\mathcal{O}(0.5 - 5\,\mu\text{s})$ and certainly at 5 ms.

For example, note how for very high energy depositions, the vibrational relaxation leads to a "negative" ΔT (see Fig. 3.2), which is not a physically relevant result and is related to the fact that, as the reactor approaches very high temperatures near the characteristic vibrational temperature of N_2 ($\theta_v = 3521$ K), vibrational states become more populated and the vibrational excitation process becomes a sink of translational and rotational energy, which are indexed by the reactor temperature T.

In an effort to better understand these processes on more realistic time scales, we study the sensitivity of various contributions to $\Delta T/\Delta T_f$ with respect to the final time, which constrains both ΔT_f as well as the temporal interval of integration to recover the value of ΔT (see Section 2.3 for details). The results of the analysis are shown in Fig. 3.4 for an energy deposited per unit volume of $E = 4$ mJ/mm^3, which is relevant to the nanosecond discharges considered in this work.

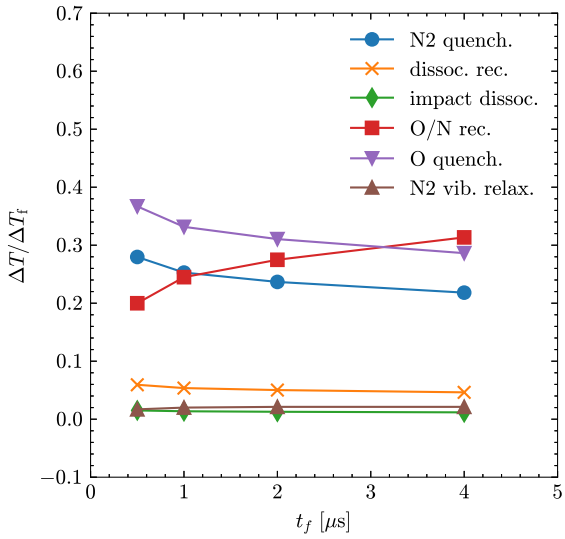

Figure 3.4: Sensitivity of the heating fraction to the final time at which the fraction is measured for the most energetic case $E = 4$ mJ/mm^3(see Section 2.3 for more details).

The data shown in Fig. 3.4 demonstrates that when the analysis is restricted to short times, e.g., $t_f = 0.5$ μs, quenching of excited O and N_2 contribute the most to heating, while as t_f increases, the cumulative contribution of quenching processes decreases monotonically in favor of the contribution of the recombination of O and N. Thus, the data shown in Fig. 3.4 recover the known features of non-equilibrium and thermalization brought by nanosecond discharges, whereby on short time scales, quenching of electronically excited particles dominates heating, while on longer time scales, recombination of atoms becomes more important to heating. Finally, we note that for all values of $t_f \leq 5$ μs explored, the contribution of vibrational relaxation is negligible (less than 2% at most) and the only noticeable contribution is that of dissociative recombination, which decreases with increasing t_f from about 6% down

to 4%.

The relative importance of the contributions of the various classes of plasma kinetics is most sensitive to t_f for small values of t_f in the range 0.5 to 2 μs, which corresponds to conventional durations of expansion of the energized plasma channels in atmospheric nanosecond discharges. In other words, our analysis confirms that the plasma kinetic processes responsible for gas heating and those associated with mass, momentum, and energy transport engendered by the discharge have significant temporal overlap, providing the opportunity for important non-linear interactions. A more definitive analysis is then possible only by considering the interaction of plasma kinetics and transport in unsteady and multi-dimensional simulations plasma assisted ignition processes with high-fidelity mathematical models.

Finally, the sensitivity of vibrational non-equilibrium with respect to the energy deposited in the isochoric reactor is explored by leveraging the metrics developed in Section 2.4. The data are shown in Fig. 3.5.

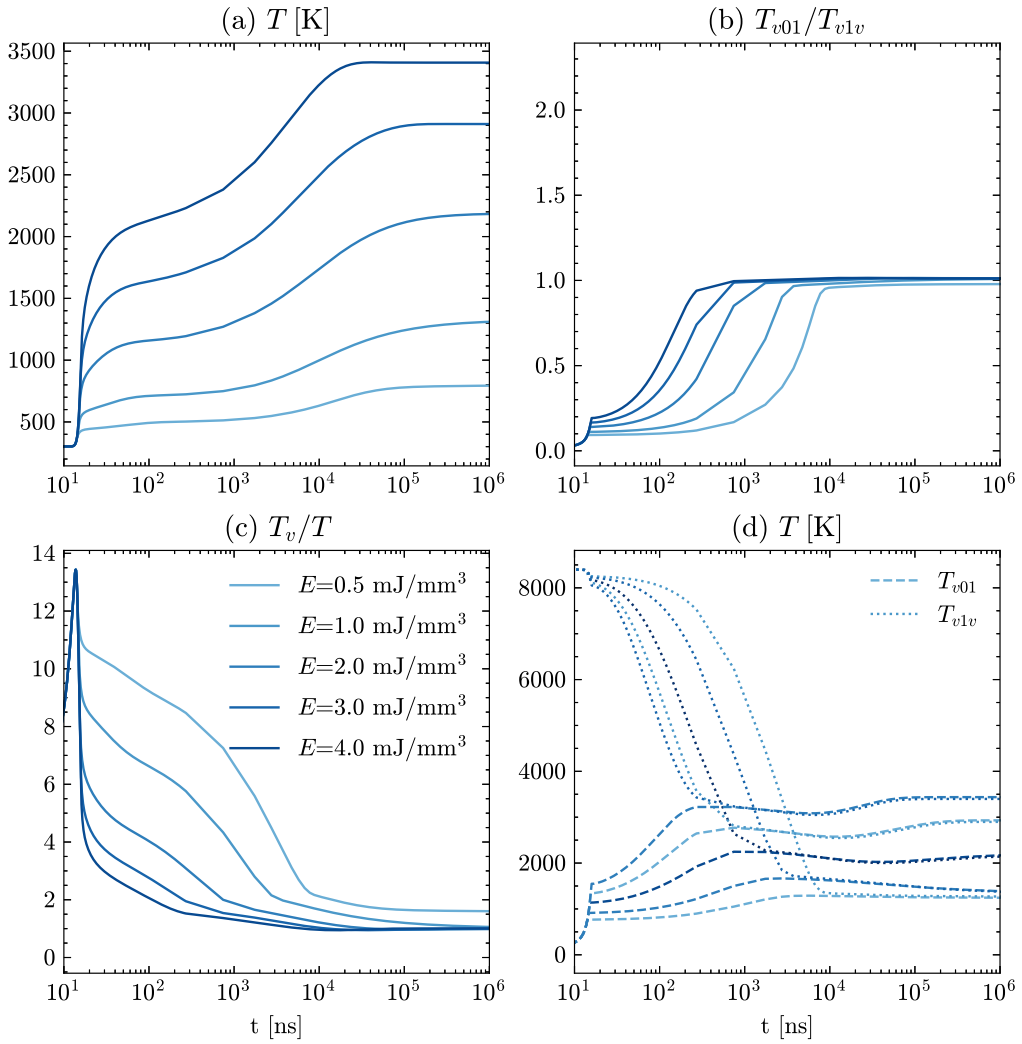

Figure 3.5: Effect of the volumetric energy deposition on the vibrational temperatures as a function of time calculated using the methodology described in Sec. 2.4.

The relaxation of the excess population of N_2 in high-energy vibrational states is studied by considering two temperature ratios: T_{v01}/T_{v1v}, which quantifies the degree of overpopulation of vibrational states $v > 1$ relative to that in the first two states, and T_v/T, which characterizes the vibrational temperature relative to the

translational/rotational one. The temporal evolution of temperatures T_{v01} and T_{v1v} is also presented.

From the data in Fig. 3.5(b) and Fig. 3.5(d), we conclude that the vibrational energy distribution converges to a Boltzmann distribution between 0.5 μs and 10 μs, depending on the energy deposited. Higher values of energy deposited per unit volume bring about a faster transition to a Boltzmann distribution. As shown in Fig. 3.5(d), temperature T_{v01} lies between 500 K and 3,000 K, while T_{v1v} is significantly higher early in the evolution of the non-equilibrium gas, reaching values as high as 8,000 K.

Even though the vibrational energy distribution relaxes to a Bolzmann distribution with a well-defined temperature, T_v/T tends to unity slowly. For example, for an energy deposition of 4 mJ/mm^3, we find that 300 ns are required for T_v/T to decrease below 1.5 and 3 μs for it to decrease below 1.1. As the energy decreases fourfold to 1 mJ/mm^3, the times taken increase to 20 μs and 200 μs, respectively.

The results discussed above are somewhat confounding in that one might expect that higher values of energy correspond to more significant degree of non-equilibrium (including the vibrational one) persisting for longer. Conversely, the results and attending analysis indicate that the opposite is true. Some further comments are in order.

We begin by remarking that the dependence of the degree of vibrational non-equilibrium on the energy deposited per unit volume is robust in time. In other words, higher values of energy lead to faster relaxation of the vibrational non-equilibrium at

all times as shown in Fig. 3.5. This observation leads us to conclude that although the relevance of the zero-dimensional isochoric reactor model past $\mathcal{O}(1\,\mu\text{s})$ is limited, the data are likely indicative of realistic physical processes on temporal scales up to about 100 to 500 ns when channel expansion and attending transport processes have not taken place.

Further analysis reveals that the observed trends are due to the fact that, as the energy deposited increases, so does the pressure in the reactor, so that vibrational relaxation occurs on shorter time scales due to the higher pressures. Thus, we conclude that the trends observed are likely to be physically sound and readily applicable to local vibrational relaxation processes in pressurized plasma channels formed by nanosecond pin-to-pin discharges.

3.2 Voltage pulse waveform

When simulating a capacitive plasma discharge, the waveform of the voltage bias applied across the two electrodes controls the electric field strength across the gap as well as the amount of electrical energy transferred to the plasma gas. Despite its importance, the effect of varying the voltage waveform on the plasma discharge, especially when simulated with multi-dimensional modeling approaches, has not been thoroughly investigated.

In this Section, the dependence of the plasma discharge and ensuing thermal non-equilibrium with respect to the voltage waveform is investigated with the aid of the zero-dimensional isochoric reactor model.

The simplest approach consists of prescribing a voltage waveform according to simple parametrizations such as a Gaussian or a sigmoid pulse whereby peak voltage and pulse duration are set to values similar to those observed experimentally [2; 29; 50; 51]. In order to understand the challenges brought by this approach, it is important to note that when a voltage waveform is prescribed, the simulated state of the plasma determines the current drawn, and consequently, the amount of energy deposited instantaneously. Since plasma models have a significant degree of uncertainty, inaccuracies in the plasma models lead to inaccuracies in the energy deposited.

Due to the large computational expense associated with multidimensional NSPD simulations, this approach is ill-suited to spatially resolved simulations of discharges. The amount of energy deposited by the discharge into the gas is very sensitive to parameters such as the pulse duration and maximum applied voltage, which can easily lead to excessive amounts of energy being deposited that are either unrealistic, inconsistent with experiments, or push the thermochemical state of the gaseous mixture outside the temperature bounds for which the thermodynamic mixture model is valid. Adjusting the waveform in order to achieve a target amount of energy known from experiments requires a trial and error approach that is not often possible when simulating multidimensional configurations.

An alternative approach consists of specifying voltage waveforms as measured from experiments [52; 53]. While such an approach seeks to better align simulations to experiments and enable more meaningful and accurate comparisons, the same challenges related to energy deposition remain since the applied voltage is indepen-

dent of current in this case also. There are additional issues too as most numerical approaches use boundary conditions that prevent the cathode fall region from forming altogether, while such voltage fall is obviously present at the cathode. In closing, we remark that the coupling between voltage and current must be modeled for the two to be consistent and such modeling task is nearly impossible without a complete characterization of the electrical circuits driving the discharge. Thus, it remains very challenging to match experimental waveforms and energy depositions even when high-fidelity numerical models are being used.

Recently, an alternative approach, which is the one employed in our work, has found widespread use, whereby a prescribed voltage waveform is applied and instantaneously (or very rapidly) reduced when a target amount of energy has been deposited [14; 38]. In this section, the discharge and non-equilibrium state of the gas are explored when such a modeling approach, which we shall refer to as "energy cutoff," is employed compared to an approach whereby a sigmoid profile is applied and its duration adjusted by trial and error until the target energy is deposited. We call this second approach "full waveform." This second approach is possible only with zero-dimensional reactor as it requires repeated simulations with adjustments to the voltage waveform. In Fig. 3.6 the reduced electric field strength E/N, gas temperature T, and mean electron energy ϵ are shown as a function of time.

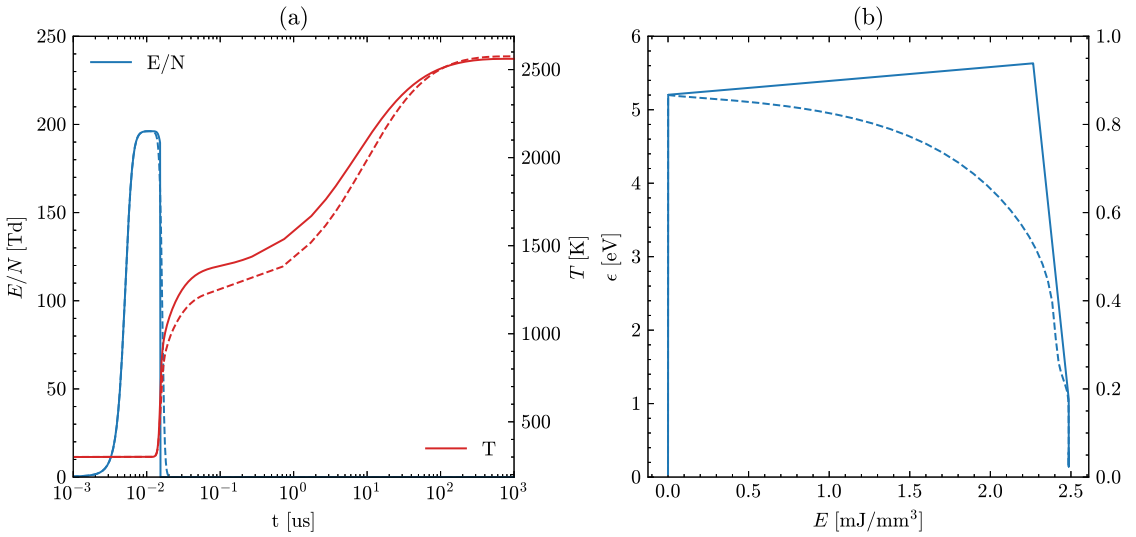

Figure 3.6: Comparison between the "energy cutoff" (solid) and "full waveform" (dashed) approaches, showing (a) the reduced electric field strength E/N and gas temperature T as a function of time, and (b) mean electron energy ϵ as a function of the cumulative energy deposited per unit volume E during the discharge. For each variable, solid lines indicate results obtained with the "energy cutoff" method and dashed lines indicate those with the "full waveform" method.

The data presented in Fig. 3.6 indicate that the manner in which the voltage waveform is applied to reach the same target energy has an effect on the gas temperature immediately after the discharge and up to about 10 μs, with a larger fraction of energy leading to fast heating for the "energy cutoff" voltage approach. This conclusion is consistent with the temporal evolution of the mean electron energy when plotted against the cumulative energy deposited. It is apparent that the "cutoff energy" method leads to a higher mean electron energy for the same amount of energy deposited (average of 5.4 eV vs 3.2 eV). Higher values of ϵ favor processes such as electronic excitation that lead to more fast heating [23]. The same mecha-

nism is made apparent by comparing the energy coefficients computed from the two sets of data, which are shown in Fig. 3.7.

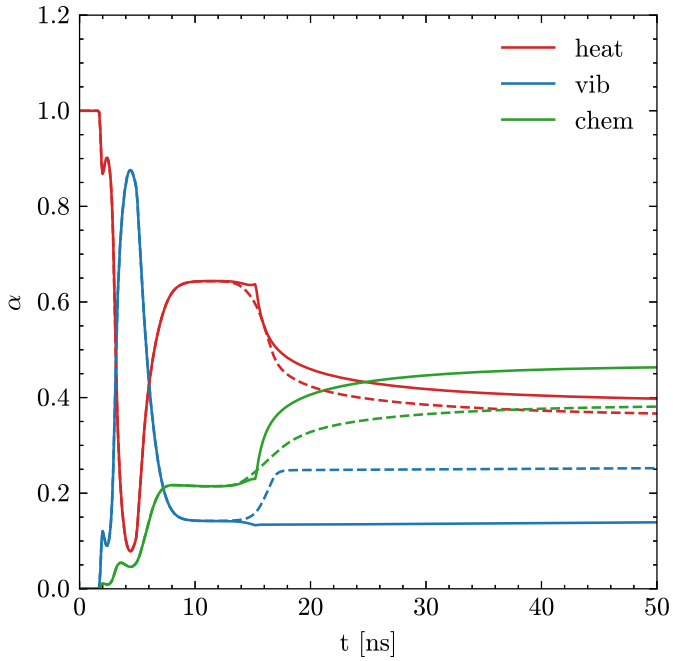

Figure 3.7: Calculated phenomenological coefficients as described in Section 2.5 showing the comparison between the "energy cuttoff" (solid) and "full waveform" (dashed) approaches.

In Fig. 3.7, particular attention should be paid to the data at time equal to 14 ns, when the energy coefficients from the two datasets diverge one from the other. It is apparent from the data that, when the "full waveform" approach is employed, α_{vib} increases during the later stages of energy deposition and such trend is absent from the data obtained with the "energy cutoff' on the account that an electron cooling phase towards the end of the discharge is absent. This difference is also reflected in the lower value of the coefficients α_{chem} and α_{heat}, and emphasizes the importance

of the mean electron energy during energy deposition. In summary, we find that there is a noticeable effect of the voltage waveform and the "energy cutoff" method is most likely underestimating vibrational excitation and overestimating the energy associated with fast heating and chemical effects, i.e., dissociation.

3.3 Reduced mechanism

Detailed kinetics mechanisms for plasma and plasma assisted combustion applications contain numerous species and reactions in an effort to provide a physically accurate and comprehensive model. However, such detailed kinetics mechanisms are impractical for the simulation of unsteady multi-dimensional plasma discharges in realistic geometries. In previous work, a detailed mechanism for the simulation of plasma assisted ignition of ethylene/air and methane/air mixtures was reduced using the Direct Relation Graph with Error Propagation with plasma specific targets [4] (P-DRGEP). Tight error tolerances for the electron energy branching during the discharge are specified, in addition to more conventional combustion targets and metrics [4]. Throughout this reduction process, the energy lost to ionization, vibrational excitation, and electronic excitation was monitored to ensure that the reduced mechanism reproduces those energy paths within an acceptable error threshold. Simulations at same nominal conditions explored prior in this Chapter are executed with the reduced kinetics mechanism and the results compared to those with the detailed one.

Table 3.1: Species included in the reduced kinetics model used in this section and grouped in three categories: neutral and charged species in thermal equilibrium (groups 1 and 2) and neutral species in thermal non-equilibrium (group 3). Symbol $N_2(v = 0)$ represents the vibrational ground state of diatomic nitrogen and symbols $N_2(v = 1, \ldots, 5)$ represent states in the first five vibrational bands above ground for which thermodynamic properties are computed as in Ref. [1] (see Appendix B for details).

Group	Species
1. Equilibrium	O, N, NO, O_2
2. Charged	E, O_2^+, N_2^+
3. Non-equilibrium	$N_2(v = 0)$, $N_2(v = 1)$, $N_2(v = 2)$, $N_2(v = 3)$, $N_2(v = 4)$, $N_2(v = 5)$, $N_2(A^3\Sigma_u^+)$, $N_2(B^3\Pi_g)$, $N_2(C^3\Pi_u)$, $O_2(a^1\Delta_g)$, $O_2(b^1\Sigma_g^+)$, $O(^1D)$

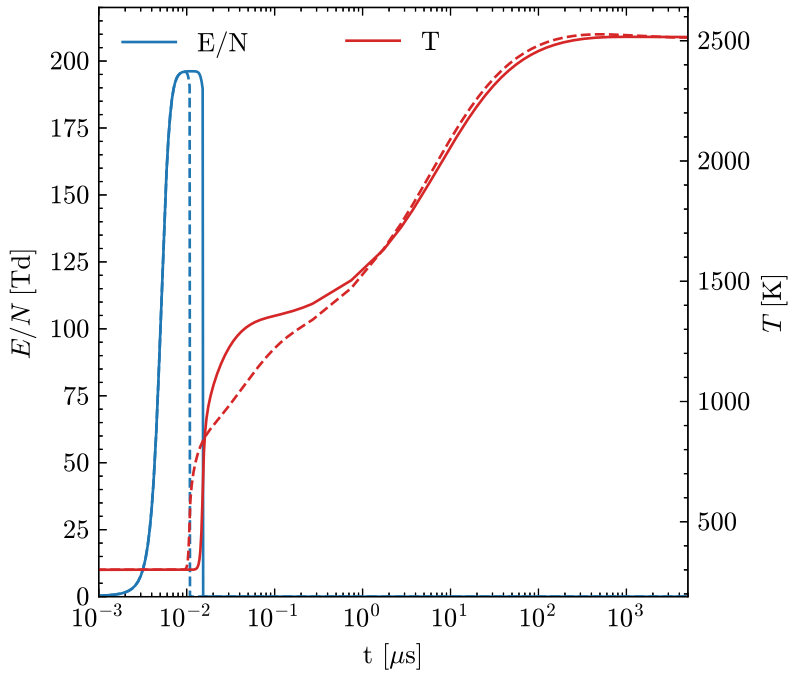

Figure 3.8: Comparison of the reduced electric field E/N (blue lines) and gas temperature (red lines) for a discharge simulated in the isochoric reactor with conditions: 1 atm, 300 K, and 4 mJ/mm^3 (see Section 2.3 for more details). Data are shown for simulations that employ the detailed (solid) and reduced (dashed) kinetics mechanisms.

The data in Fig. 3.8 demonstrate broad agreement in the temperature and E/N for simulations with the reduced and detailed mechanisms, although differences are apparent in that the discharge and energy deposition are shorter for the reduced mechanism. Furthermore, the temperature increase observed between the energy deposition and 1 μs is slower for the reduced mechanism. After 1 μs, results from the two mechanisms are nearly identical.

As mentioned in Section 2.3, the processes that control heating in nanosecond discharges include N_2 and $O(^1D)$ quenching, vibrational relaxation, and N and O recombination. The concentration of species relevant to these processes are compared in Fig. 3.9.

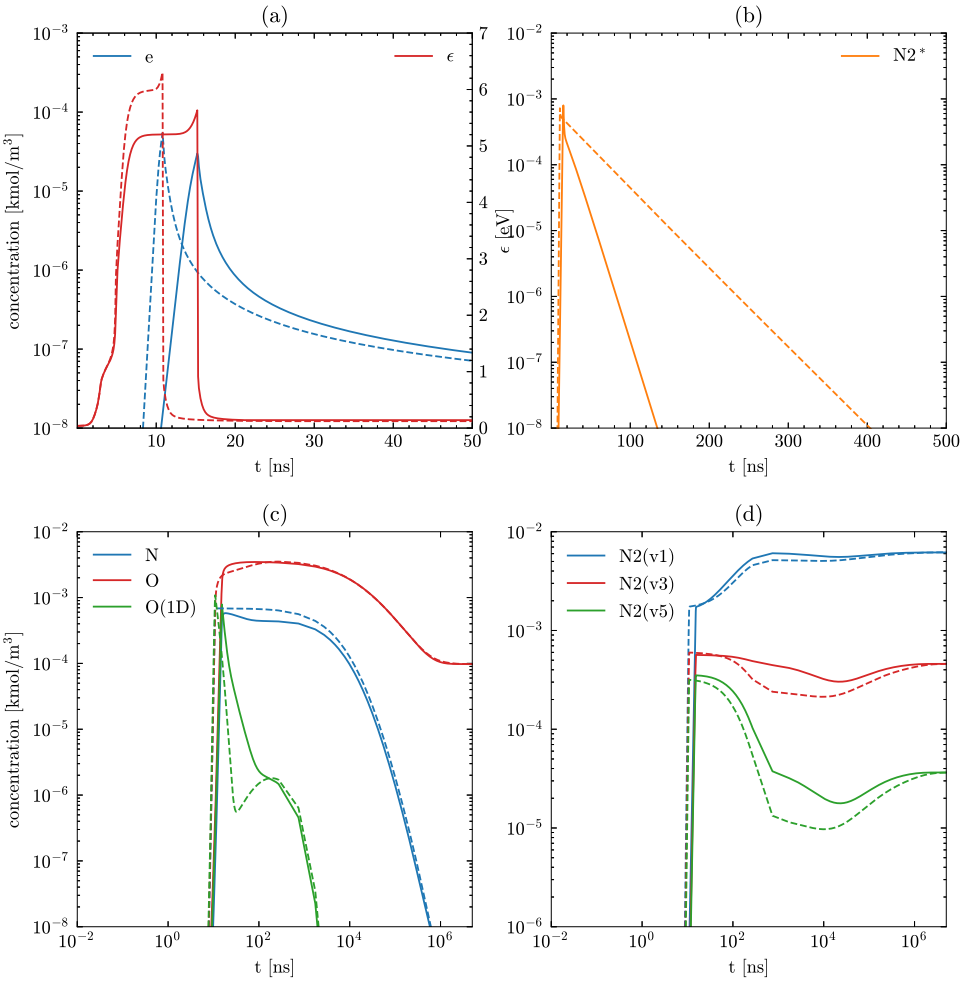

Figure 3.9: (a) Concentration of electrons and mean electron energy, (b) sum of concentrations of all excited N_2 species, (c) concentrations of dissociated nitrogen and oxygen, and (d) concentrations of select populations of vibrationally excited N_2. Data are shown for detailed (solid) and reduced (dashed) mechanisms.

The data show that a faster increase in the number density of electrons accelerates the observed energy deposition and leads to a higher mean electron energy. Because of the exponential growth of the density of the electrons, small differences in

the ionization rate will result in appreciable changes. The most prominent difference between the two sets of data lies in the temporal decay of electronically excited N_2, likely explaining the slower heating immediately after the discharge for the reduced mechanism. The concentration of $O(^1D)$ and those of higher vibrational states of N_2 are also slightly underestimated between 0.1 and 10 μs. The processes of oxygen/nitrogen dissociation and recombination is reproduced accurately by simulations with the reduced mechanism as demonstrated by the concentrations of O and N.

Finally, the normalized increase in temperature due to the processes listed in Tab. 2.2 and 2.3, and the energy coefficients are extracted over the first 100 ns of the discharge and presented in Fig. 3.10 as a function of the energy deposited per unit volume.

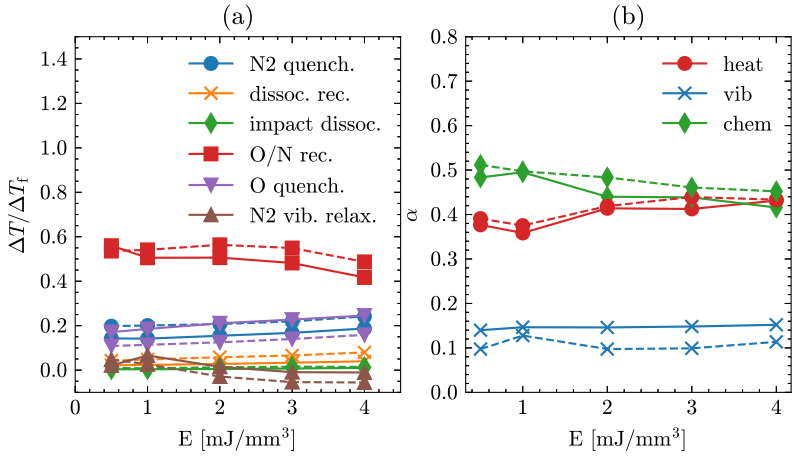

Figure 3.10: (a) Normalized increment in temperature due to the class of processes listed in Tabs. 2.2 and 2.3 as computed from simulations that employ the detailed (solid) and reduced (dashed) mechanisms. (b) Energy coefficients. The data considers the first 100 ns of the simulation.

Generally, a very good agreement for all processes across the energy deposi-

tions is observed, with errors of 8% or less. We also observe that the energy coefficients are reproduced accurately by the reduced kinetics mechanism for all energy depositions, although underpredictions of vibrational excitation and overprediction of chemical energy are apparent.

Chapter 4

Multidimensional discharges: Models and Methods

In this Chapter, we present in detail the governing equations used to model multidimensional nanosecond discharges in air as well as the subsequent transport of mass, momentum, and energy on much longer time scales. In Section 4.1, transport equations, closures, thermodynamic properties, and treatment of non-thermal electrons are discussed. In Section 4.2, the numerical methods used to solve the system of nonlinear partial differential equations are explained. The simulation framework builds upon the AMReX library, plasma discharge solver PeleCPeX, compressible solver PeleC, and low-Mach solver PeleLMeX. These tools are then extended and combined in order to enable efficient simulations of single and multi-pulse discharges in air. The objectives of this chapter are summarized below:

- Provide a comprehensive overview of the plasma-fluid model, applicable closures, assumptions, and other relevant information required to assess modeling assumptions and limitations.
- Present information on algorithms, software capabilities and limitations, boundary conditions specific to the configuration of interest, and estimates for computational costs.

- Discuss example applications to elucidate requirements for parallel computing and limitations to the maximum size of time steps allowed by accuracy and stability.

4.1 Mathematical model

The governing equations for plasma and reactive gaseous mixture constitute a system of coupled non-linear partial differential equations enforcing conservation of mass, momentum, and energy in the continuum regime. The differential equations are complemented by closures for all relevant fluxes, thermodynamic and transport properties of all particles, and rate coefficients of plasma and combustion reactions and energy exchanges among excited states.

In this Section, we present the governing equations first in Section 4.1.1, followed by closures in Sections 4.1.2 through 4.1.8. A discussion on the assumptions implicit in the governing equations and closures and on their applicability to the simulation of ignition by nanosecond discharges is given in Section 4.1.9 with additional commentary and supporting data in the Supplementary material and Appendices.

4.1.1 Transport equations

The gaseous system describing air plasmas for plasma-assisted ignition applications consists of neutrals, electrons, and ions listed in Tab. 4.1. Particle classes are indexed by $k = 1, \ldots, K$ and the index of the electrons is e. In what follows, all variables are a function of position $\boldsymbol{x}$ and time t unless otherwise noted. Partial differential equations for the conservation of mass, momentum, and energy of the

Table 4.1: Species included in the thermodynamic model of air grouped in three categories: neutral and charged species in thermal equilibrium (groups 1 and 2) and neutral species in thermal non-equilibrium (group 3). Symbol $N_2(v = 0)$ represents the vibrational ground state of diatomic nitrogen and symbols $N_2(v = 1, \ldots, 5)$ represent states in the first five vibrational bands above ground for which thermodynamic properties are computed as in Ref. [1] (see Section 4.1.4 for details).

Group	Species
1. Equilibrium	O, N, NO, O_2
2. Charged	E, ${O_2}^+$, ${N_2}^+$, ${O_2}^-$, O^-
3. Non-equilibrium	$N_2(v = 0)$[a], $N_2(v = 1)$, $N_2(v = 2)$, $N_2(v = 3)$, $N_2(v = 4)$, $N_2(v = 5)$, $N_2(A^3\Sigma_u^+)$, $N_2(B^3\Pi_g)$, $N_2(C^3\Pi_u)$, $O_2(a^1\Delta_g)$, $O_2(b^1\Sigma_g^+)$, $O(^1D)$

thermodynamic system are formulated in the continuum regime within the confines of the Chapman–Enskog theory for dilute gases.

The mass density of particles of class k is $\rho_k = m_k n_k$, where m_k is the particle mass and n_k the number density of the particle class. The mass density of the gaseous mixture is

$$\rho = \sum_{k=1}^{K} \rho_k = \sum_{k=1}^{K} m_k n_k, \tag{4.1}$$

where the summation includes electrons.

The conservation equation for mass density ρ_k reads

$$\frac{\partial \rho_k}{\partial t} = -\nabla \cdot (\rho_k \boldsymbol{u}_k) + \rho \omega_k, \qquad k = 1, \ldots, K, \tag{4.2}$$

where $\boldsymbol{u}_k$ is the mean velocity of particles of class k and the product $\rho\omega_k$ represents the net rate of production of mass of species k per unit volume due to reactions. The mean velocity $\boldsymbol{u}_k$ requires closure, which is discussed in Section 4.1.2.

The *mass-averaged bulk velocity* [54] is defined as

$$\boldsymbol{u} = \sum_{k=1}^{K} Y_k \boldsymbol{u}_k, \tag{4.3}$$

where $Y_k = \rho_k/\rho$ is the mass fraction of particles of class k and summation of Eq. (4.2) over all particle classes yields the mass conservation equation

$$\frac{\partial \rho}{\partial t} = -\nabla \cdot (\rho \boldsymbol{u}), \tag{4.4}$$

since

$$\sum_{k=1}^{K} \omega_k = 0 \tag{4.5}$$

as the total mass of the gaseous system is unchanged by reactions.

The conservation equation for the momentum per unit volume of the gaseous system comprising all particle classes reads

$$\frac{\partial \rho \boldsymbol{u}}{\partial t} = -\nabla \cdot (\rho\, \boldsymbol{u} \otimes \boldsymbol{u}) + \nabla \cdot \boldsymbol{\sigma}, \tag{4.6}$$

where $\boldsymbol{u} \otimes \boldsymbol{u}$ is the convective flux tensor and $\boldsymbol{\sigma}$ is the stress tensor (see Section 4.1.2).

Note that the contribution of electrohydrodynamic forces [55] is neglected in Eq. (4.6). In general, electrodynamic forces contribute to fluid acceleration in the presence of charged particles and electric fields and are confined to non-neutral regions of the discharge [55]. In the nanosecond discharges under consideration, the electrodynamic force is active only in very small volumes, i.e. in the non-neutral plasma sheaths and at the head of streamers, and only for the very short discharge duration $\mathcal{O}(1 - 20$ ns).

The conservation equation for energy per unit volume of the gaseous system comprising all particle classes reads

$$\frac{\partial \rho \mathcal{E}}{\partial t} = -\nabla \cdot (\rho \mathcal{E} \boldsymbol{u}) - \nabla \cdot \boldsymbol{\mathcal{Q}} + \mathcal{P}_\sigma + \mathcal{P}_\mathrm{J}, \tag{4.7}$$

where $\rho\,\mathcal{E} = U + \rho|\boldsymbol{u}|^2/2$ is the total energy per unit volume with U the internal energy and $\rho|\boldsymbol{u}|^2/2$ the kinetic energy, both per unit volume. Both internal and kinetic energy include the contribution of electrons. The heat flux vector is $\boldsymbol{\mathcal{Q}}$, $\mathcal{P}_\sigma$ is a source term due to the interaction of stresses and bulk velocity, and $\mathcal{P}_\mathrm{J}$ is a source term representing Joule (resistive) heating. Closures for $\boldsymbol{\mathcal{Q}}$ and source terms $\mathcal{P}_\sigma$ and $\mathcal{P}_\mathrm{J}$ are presented in Section 4.1.2.

In the plasma regime of interest, the electric field vector $\boldsymbol{E}$ is related to the electrostatic potential ϕ as

$$\boldsymbol{E} = -\nabla\phi \tag{4.8}$$

and the Poisson equation for ϕ reads

$$-\nabla^2\phi = \varrho/\epsilon_0, \tag{4.9}$$

where ϵ_0 is the vacuum permittivity (permittivity of free space) and ϱ is the space charge density

$$\varrho = \sum_{k=1}^{K} q_k n_k, \tag{4.10}$$

defined as the net charge per unit volume with $q_k = \mathrm{e}z_k$ the charge of a particle of class k, z_k its charge number, and e the elementary charge.

4.1.2 Closures

Closure for $\boldsymbol{u}_k$, the mean velocity of particles of class k, is based on a drift-diffusion model for the mean velocity of the particles relative to the mass-averaged bulk velocity $\boldsymbol{u}$:

$$\boldsymbol{u}_k = \boldsymbol{u} + \boldsymbol{V}_k, \tag{4.11}$$

$$\boldsymbol{V}_k = \boldsymbol{V}_k^{\mu} + \boldsymbol{V}_k^{\mathcal{D}} + \boldsymbol{u}_c, \tag{4.12}$$

where $\boldsymbol{V}_k^{\mu}$ is the (electrical) *drift velocity*, $\boldsymbol{V}_k^{\mathcal{D}}$ is the *diffusion velocity*, and $\boldsymbol{u}_c$ is the *correction velocity* [56]. Drift and diffusion velocities are defined as

$$\boldsymbol{V}_k^{\mu} = z_k \mu_k^{\mathrm{e}} \boldsymbol{E} \tag{4.13}$$

and

$$\boldsymbol{V}_k^{\mathcal{D}} = -\mathcal{D}_k \frac{\nabla X_k}{X_k}, \tag{4.14}$$

respectively, where μ_k^{e} is the electrical mobility of the particle, $\mathcal{D}_k$ its mass diffusion coefficient, and X_k the mole fraction of particle class k. Note that $z_k = 0$ and $\boldsymbol{V}_k^{\mu} = 0$ for neutral species. As written in Eq. (4.14), closure for the diffusion velocity is formulated according to the Hirschfelder and Curtiss approximation [e.g. see Ref. 54, p. 14]. Models for electrical mobility and mass diffusion coefficient are discussed in Section 4.1.5.

The expression for the correction velocity reads [56]

$$\boldsymbol{u}_c = -\sum_{k=1}^{K} Y_k \boldsymbol{V}_k^{\mathcal{D}}. \tag{4.15}$$

The definition in Eq. (4.15) is convenient as it does not require any modifications to the numerical methods implemented in PeleC (see Section 4.2) for the species conservation equations. However, the definition of the correction velocity in Eq. (4.15) implies that

$$\sum_{k=1}^{K} Y_k \boldsymbol{V}_k = Y_k \boldsymbol{V}_k^{\mu} \approx 0, \tag{4.16}$$

which introduces a negligible discrepancy in mass conservation. This discrepancy is present only during the discharge when $\boldsymbol{V}_k^{\mu} \neq 0$, i.e., up to 50 ns or so, and its impact is negligible on the account that the plasma is weakly ionized. In the plasma discharges considered in our work, the degree of ionization does not exceed 10^{-3} and its spatially and temporally averaged value is in fact much lower than its peak value.

Closure for the stress tensor reads

$$\boldsymbol{\sigma} = -p\boldsymbol{\mathcal{I}} + \boldsymbol{\tau}, \tag{4.17}$$

where p is pressure, $\boldsymbol{\mathcal{I}}$ the identity tensor, and $\boldsymbol{\tau}$ is the viscous stress tensor for which we adopt the Newtonian fluid closure:

$$\boldsymbol{\tau} = -\frac{2\mu}{3}(\nabla \cdot \boldsymbol{u})\,\boldsymbol{\mathcal{I}} + 2\mu\,\boldsymbol{\mathcal{S}}, \tag{4.18}$$

where $\boldsymbol{\mathcal{S}}$ is the rate of strain tensor and μ the dynamic viscosity. A model for the dynamic viscosity is discussed in Section 4.1.5.

As defined, pressure is proportional to the trace of the stress tensor

$$p = -\frac{1}{3}\mathrm{Tr}(\boldsymbol{\sigma}) \tag{4.19}$$

since $\mathrm{Tr}(\boldsymbol{\tau}) = 0$. Further, pressure is related to the other properties under the assumption that the gaseous system consists of ideal gases in thermal equilibrium at temperature T:

$$p = k_{\mathrm{B}} T N, \tag{4.20}$$

$$N = \sum_{k=1}^{K} n_k, \tag{4.21}$$

$$U = \sum_{k=1}^{K} \hat{u}_k n_k, \tag{4.22}$$

where summations are carried out over all particle classes, including electrons, k_{B} is the Boltzmann constant, N is the number density of the gaseous system, and $\hat{u}_k = \hat{u}_k(T)$ is the mean internal energy of particles of class k at temperature T. Thus, temperature is recovered by inverting Eq. (4.22) given the internal energy of the gaseous system U, particle densities $n_1, \ldots, n_K$, and a model for the internal energy of each particle class as a function of temperature T.

At this point, it is important to note that the definitions of pressure p and temperature T associated with Eq. (4.20), Eq. (4.21), and Eq. (4.22) apply formally only to mixtures of ideal gases in *thermal equilibrium* at a common temperature. A discussion on the applicability of the above closures in the presence of non-thermal electrons characteristic of nanosecond plasma discharges of the kind considered in this work is given in Section 4.1.9.

Closure for the heat flux vector reads

$$\boldsymbol{\mathcal{Q}} = -\Lambda \nabla T + \rho \sum_{k=1}^{K} h_k Y_k \boldsymbol{V}_k, \tag{4.23}$$

where Λ is the thermal conductivity of the gaseous mixture, $h_k = h_k(T)$ the enthalpy per unit mass of species k evaluated at temperature T, and $\boldsymbol{V}_k$ is defined as in Eq. (4.12). A model for Λ is discussed in Section 4.1.5.

The source term accounting for changes in the energy of the gaseous system due to the interaction of stresses and bulk velocity reads

$$\mathcal{P}_\sigma = -\nabla \cdot (p\boldsymbol{u}), \tag{4.24}$$

where the contribution due to viscous stresses is neglected. Joule heating reads

$$\mathcal{P}_\mathrm{J} = \mathrm{e}\, n_e \mu_e^\mathrm{e} |\boldsymbol{E}|^2, \tag{4.25}$$

where the contribution of ions is neglected due to their electrical mobility being much smaller than that of electrons.

4.1.3 Photoionization in air and ethylene/air mixtures

The rate of photoionization in mixtures of oxygen and nitrogen with or without fuel is based on a three-term approximation proposed by Bourdon et al. [3] and details are summarized below. In this section, we present the simplified model for air, and an example on how to incorporate fuel effects into the simplified model proposed in the original reference [3].

The model in Ref. [3] is an approximation of the integral model by Zhelezniak et al. [15], where the rate of photoionization at location $\boldsymbol{r}$ reads

$$S_\mathrm{ph}(\boldsymbol{r}) = \iiint \frac{I(\boldsymbol{r}')g(R)}{4\pi R^2} d\boldsymbol{r}'. \tag{4.26}$$

In the expression above, the volumetric integral is carried out over the entire domain, $R = |\boldsymbol{r} - \boldsymbol{r}'|$ is the Euclidean distance between the two locations, $I(\boldsymbol{r}')$ is an emission function discussed below, and $g(R)$ is defined as

$$\frac{g(R)}{p_{\mathrm{O}_2}} = \frac{\exp\left(-\chi_{\min} p_{\mathrm{O}_2} R\right) - \exp\left(-\chi_{\max} p_{\mathrm{O}_2} R\right)}{p_{\mathrm{O}_2} R \ln\left(\chi_{\max}/\chi_{\min}\right)}, \tag{4.27}$$

where p_{O_2} is the partial pressure of oxygen, $\chi_{\min} = 0.035$ Torr^{-1} cm^{-1} and $\chi_{\max} = 2$ Torr^{-1} cm^{-1}. The emission function $I(\boldsymbol{r}')$ assumes that the radiation emitted is proportional to the local ionization rate $S_i(\boldsymbol{r}')$ by electron impact and reads

$$I(\boldsymbol{r}') = \frac{p_q}{p + p_q} \xi S_i(\boldsymbol{r}'), \tag{4.28}$$

where p is pressure, p_q is the quenching pressure, and ξ is a dimensionless efficiency factor. Experimental measurements in air show that $p_q \approx 30 - 60$ Torr [57], although the presence of a hydrocarbon molecule lowers p_q to about 10 Torr [58]. The efficiency factor is a weak function of the reduced electric field and constant values $0.02 - 0.05$ are commonly assumed [57; 58]. In this work, we let $p_q = 30$ Torr and $\xi = 0.02$ for both air and ethylene/air mixtures.

Since the calculation of the rate of photoionization with the Zhelenzyak model is computationally prohibitive, requiring one volume integral over the entire domain for each finite volume cell, we adopt the modeling approach by Bourdon et al. [3], where the function $g(R)/p_{\mathrm{O}_2}$ is approximated by

$$\frac{g(R)}{p_{\mathrm{O}_2}} = (p_{\mathrm{O}_2} R) \sum_j A_j \exp\left(-\lambda_j p_{\mathrm{O}_2} R\right). \tag{4.29}$$

Constants A_j and λ_j are fitting parameters chosen to best approximate $g(R)/p_{\mathrm{O}_2}$ as in Eq. (4.27).

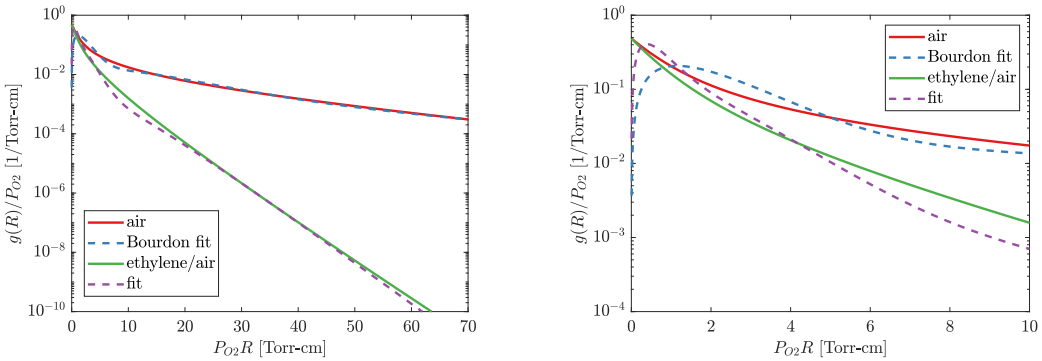

(a) (b)

Figure 4.1: Function $g(R)/P_{\mathrm{O_2}}$ as in Eq. (4.27) [15] and fit as in Eq. (4.29) [3] for air (300 K and 1 atm) and a stoichiometric ethylene/air mixture (600 K and 0.5 atm) calculated as presented in Naidis [16]. (a) data in the 0 to 70 Torr-cm range and (b) detailed view of the same data in the 0 to 10 Torr-cm range.

The rate of photoionization is then approximated by the sum

$$S_{\mathrm{ph}} = \sum_{j=1}^{3} S_{\mathrm{ph}}^{(j)}. \tag{4.30}$$

Each term $S_{\mathrm{ph}}^{(j)}(\boldsymbol{r})$ is the solution to the following Helmholtz equation:

$$\nabla^2 S_{\mathrm{ph}}^{(j)} - (\lambda_j p_{\mathrm{O_2}})^2 S_{\mathrm{ph}}^{(j)} = -A_j p_{\mathrm{O_2}}^2 I(\boldsymbol{r}). \tag{4.31}$$

Compared to pure air, hydrocarbons lower photoionization efficiency and the correction discussed in Ref. [16] is adopted together with a cross-section for photon absorption by ethylene equal to 4.5×10^{-17} cm^2 at 100 nm [59] and background number density equal to 4×10^{23} m^{-3}, consistent with stoichiometric ethylene/air at 600 K and 0.5 atm.

Function $g(R)/p_{\mathrm{O_2}}$ and its fits for air at 300 K and 1 atm and stoichiometric

Table 4.2: Parameters in the three-term exponential fit Eq. (4.29) for atmospheric air (300 K and 1 atm) taken from Ref. [3] and for stoichiometric ethylene/air at 600 K and 0.5 atm as calculated in this work.

Air (300 K and 1 atm)		
j	A_j [cm^{-2} Torr^{-2}]	λ_j [cm^{-1} Torr^{-1}]
1	1.986×10^{-4}	5.530×10^{-2}
2	0.0051	0.146
3	0.4886	0.89
Air/ethylene (600 K, 0.5 atm, $\phi = 1.0$)		
j	A_j [cm^{-2} Torr^{-2}]	λ_j [cm^{-1} Torr^{-1}]
1	2.659	2.887
2	2.676×10^{-1}	1.003
3	1.674×10^{-3}	3.354×10^{-1}

ethylene/air at 600 K and 0.5 atm are shown in Fig. 4.1 as a function of $p_{O_2}R$. Parameters A_j and λ_j are provided in Tab. 4.2.

4.1.4 Thermodynamic properties

Thermodynamic properties such as enthalpy, entropy, and specific heat at constant pressure are prescribed for all particles included in the gaseous system as listed in Tab. 4.1.

The thermodynamic properties of all species for which excited states are not considered are prescribed as those of an ideal gas as in any other combustion mechanism, i.e. each species represents an ensemble of particles populating all available energy levels according to thermal equilibrium at a given temperature. Then, enthalpy and entropy are obtained from the partition function associated with the quantum mechanical model of the particle [60].

In addition to conventional species in thermal equilibrium, the gaseous sys-

tem includes particles modeling vibrationally excited states of N_2 and electronically excited states of N_2, O_2, and O (see Tab. 4.1).

The thermodynamic properties of particles representing molecular nitrogen in states associated with specific vibrational bands are computed using the approach and supporting software tool in Ref. [1] in order to ensure a consistent thermodynamic model. Briefly, the approach proposed by Hazenberg et al. [1] avoids *double counting* energy levels by ensuring that the contribution of each energy level is included in the partition function of one particle class only. This is particularly important for the lowest lying vibrational states of an abundant species such as N_2, which account for a large fraction of nitrogen's internal energy and for which significant populations ensue during the discharge as well as when the gaseous mixture is in thermal and chemical equilibrium at practical combustion temperatures $\mathcal{O}(1500 - 2500\ \mathrm{K})$.

In practice, 6 particles with symbols $N_2(v = 0)$ and $N_2(v = 1, \ldots, 5)$ are defined. These 6 particles represent quantum mechanical structures comprising all rotational and electronic energy levels in the vibrational ground state of diatomic nitrogen and in each of the first five vibrational bands above ground, respectively. In this manner, the correct Boltzmann distribution of particles in all energy levels is recovered in the limit of thermal equilibrium at a given temperature. With reference to the notation established in Ref. [1], particle $N_2(v = 0)$ corresponds to "$N_2(\mathrm{a}, 0, \mathrm{a})$" and particle $N_2(v = i)$ corresponds to "$N_2(\mathrm{a}, i, \mathrm{a})$" for $i = 1, \ldots, 5$. The reference enthalpy of particles $N_2(v = 0)$ and $N_2(v = 1, \ldots, 5)$ is given in Tab. 4.3 at 298.15 K.

The thermodynamic properties of select electronic states of N_2, O_2 and O included in the thermodynamic model (see Tab. 4.1) are obtained by shifting the

Table 4.3: Enthalpy of select species at reference temperature 298.15 K. H_0 represents the species enthalpy on a molar basis, while $\hat{h}_0$ is the species enthalpy for a single particle.

Species	H_0 (MJ kmol^{-1})	$\hat{h}_0$ (eV)
$N_2(v=0)$	0.0	0.0
$N_2(v=1)$	27.87	0.2889
$N_2(v=2)$	55.40	0.5742
$N_2(v=3)$	82.59	0.8560
$N_2(v=4)$	109.4	1.134
$N_2(v=5)$	135.9	1.409
$N_2(A^3\Sigma_u^+)$	595.3	6.170
$N_2(B^3\Pi_g)$	709.2	7.350
$N_2(C^3\Pi_u)$	1064	11.03
O_2	0.0	0.0
$O_2(a^1\Delta_g)$	94.55	0.980
$O_2(b^1\Sigma_g^+)$	157.3	1.630
O	249.2	2.583
$O(^1D)$	439.3	4.553

enthalpy of formation of the corresponding equilibrium species in order to account for the energy of the electronic state relative to the ground state. While such an approach does lead to counting electronic states in the excited state species and in the equilibrium species twice when both are constituents of the gaseous mixture, the contribution of electronic states to the equilibrium species at temperatures $\mathcal{O}(300-5000\text{ K})$ considered in our work is negligible since the associated levels are scarcely populated. Thus, such an approach does not induce any significant error in the thermodynamic properties of the mixture. The reference enthalpy of particles representing select electronically excited states of N_2, O_2 and O included in the thermodynamic model is given in Tab. 4.3 at 298.15 K.

The thermodynamic model adopted here is consistent in the sense as defined

in Ref. [1] as the adiabatic and isobaric equilibrium temperature of fuel/air mixtures reproduces those that were obtained with a conventional combustion mechanism, i.e. one that features equilibrium species only. In other words, the thermodynamic model employed in our work yields the correct temperature when the system is in thermal and chemical equilibrium.

A validation of the thermodynamic properties of all particles included in the gaseous system is included in Appendix B for ethylene/air mixtures, a thermodynamics data file in the NASA format used by CHEMKIN [61] and pertinent references is provided as Supplementary material.

4.1.5 Transport properties

A mixture-average model [54] is adopted for the mass diffusion coefficient $\mathcal{D}_k$ of all particles other than electrons. The mixture-average model requires binary diffusion coefficients, which are calculated based on collision integrals that employ the Stockmayer potential. Thus, the binary diffusion coefficients of ion-neutral pairs are calculated with the Stockmayer potential also, although it is known that such potential is not well suited for ion-neutral interactions and the $(n, 6, 4)$ potential is preferable on theoretical grounds [e.g, see 62]. Nonetheless, usage of the Stockmayer potential with optimized parameters for ions is deemed sufficiently accurate for the present objectives.

The electrical mobility of all ions is set to be consistent with a normalized mobility of $\mu_i^{\mathrm{e}} N = 6.7 \times 10^{21}$ m^{-1} V^{-1} s^{-1}. This corresponds to a mobility of $\mu_i^{\mathrm{e}} = 2.7 \times 10^{-4}$ m^2 V^{-1} s^{-1} for air at 1 atm and 300 K. For discharges at different

thermodynamic conditions, the background number density is calculated to adjust the mobility.

The dynamic viscosity μ and thermal conductivity Λ of the gaseous mixture are computed with a mixture-average model also under the same simplifying assumptions, i.e. that the gaseous system consists of ideal gases in thermal equilibrium.

Closures for electrical mobility and mass diffusion coefficient of non-thermal electrons account for non-thermal effects and are discussed in detail in Sections 4.1.6 and 4.1.7.

4.1.6 Non-thermal electrons

During the discharge when the voltage is elevated and shortly thereafter, electrons are not in thermal equilibrium with the other particles, rather they attain much higher temperature

$$T_e = \frac{2\langle\epsilon\rangle}{3k_\mathrm{B}}, \tag{4.32}$$

where $\langle\epsilon\rangle = U_e/n_e$ is the mean electron energy, k_B the Boltzmann constant, U_e the energy of the electrons per unit volume, and n_e their number density.

When non-thermal electrons are present, it is necessary to account for their temperature (or their mean energy) because the cross-sections for electron impact processes depend on the energy of the colliding electron and, consequently, the rate coefficients depend on the electron energy distribution function (EEDF), of which the mean electron energy is the first moment. Similarly, the electron mobility and diffusivity change depending on the EEDF.

In this work, we adopt the widely used Local Field Approximation (LFA) [63; 64], whereby the mean electron energy and related electron temperature are taken to be functions of the local *reduced electric field strength* E/N ($E = |\boldsymbol{E}|$ is the magnitude of the electric field vector and N is the number density of the gaseous mixture) and of the composition and temperature of the gas.

The functional dependence of T_e from E/N is obtained from multiple solutions to the two-term approximation to the Boltzmann kinetic equation in air and ethylene/air stoichiometric mixture at prescribed temperature under the simplifying assumption that effects related to changes in composition and temperature of the background gas are secondary. Similarly, electron-electron interactions are neglected, which is a valid assumption for weakly ionized plasmas. Solutions are calculated with the software BOLSIG+ [65].

Prior to the simulation of plasma discharges, BOLSIG+ [65] is executed for varying values of E/N and air at 300 K and an ethylene/air stoichiometric mixture at 600 K. The electron temperature is computed from the mean electron energy and stored in a table available as Supplementary material. Evaluation of $T_e = T_e(E/N)$ when needed is carried out by linear interpolation of the values stored in the table.

The normalized electron mobility $\mu_e^{\mathrm{e}} N$, consisting of the product of the electrical mobility μ_e^{e} and number density N, and the normalized electron diffusivity $\mathcal{D}_e N$, where D_e is the electron mass diffusion coefficient, are also functions of E/N.

Data from BOLSIG+ are fit to the following functions

$$\mu_e^{\mathrm{e}} N = A \exp\left\{ \sum_{n=0}^{8} b_n^{\mu} (\ln T_e)^n \right\}, \tag{4.33}$$

$$\mathcal{D}_e N = A \exp\left\{ \sum_{n=0}^{8} b_n^{\mathcal{D}} (\ln T_e)^n \right\}. \tag{4.34}$$

The functional fits are evaluated as needed during the simulation and then divided by the total gas number density N in order to recover μ_e^{e} and $\mathcal{D}_e$. The coefficients b_n^{μ} and $b_n^{\mathcal{D}}$ are provided in Appendix D.

Because tabulated values of T_e, $\mu_e^{\mathrm{e}} N$, and $\mathcal{D}_e N$ pertain to a specific gas mixture and temperature, changes to those electron properties due to changes in the background gas composition and temperature are neglected in our modeling approach. Auxiliary simulations with varying mixture fuel/air stoichiometry (equivalence ratios between 0.6 and 1.4, including pure air) and temperature (300 K $\leq T \leq$ 3000 K) yielded only relative differences within 5% for the mean electron energy $\langle \epsilon \rangle$ and $\mu_e^{\mathrm{e}} N$, and within 10% for $\mathcal{D}_e N$ across all cases at $E/N \geq 10$ Td. Although more significant differences appear for $E/N < 10$ Td, relevant values of E/N during the nanosecond pulse range from 50 to 800 Td.

More detailed comparisons and discussion are provided in Appendix C. A file containing the cross sections downloaded from the LXCat online database [66] and used with BOLSIG+ for both air and ethylene/air mixtures is provided as Supplementary material.

4.1.7 Transport properties in the ambipolar diffusion limit

During the nanosecond voltage pulse, high electric fields lead to ionization, large electron and ion number densities, and to the propagation of streamers that require detailed modelling of charge transport as outlined in Section 4.1.2. During this early phase, there exist a tight coupling between space charge and the electric field that requires the solution of a Poisson equation for the electrostatic potential.

After the voltage pulse, significant populations of charged particles persist in select regions of the gap and, in the absence of an applied electric field, the higher diffusion coefficient of electrons induces charge separation, which in turn induces an electric field. The electric field is observed across scales comparable to the Debye length, resulting in a reduction of the flux of electrons and an increase in that of positive ions, with the total charge flux being nearly zero [67]. Consequently, regions of neutral plasma remain neutral. In other words, fluxes of electrons and ions are coupled together and the regime is often referred to as the *ambipolar diffusion limit* [67]. Under the assumption that the total charge flux is zero, one derives expressions for modified diffusion velocities of charged species.

In this work, the ambipolar model discussed in Prager et al. [67] is adopted, yielding the following expression for the ambipolar diffusion velocity of species k

$$\boldsymbol{V}_k^{A,D} = \boldsymbol{V}_k^{\mathcal{D}} - \beta_k \sum_{j=1}^{K} \frac{z_j M_k}{z_k M_j} \boldsymbol{V}_j^{\mathcal{D}}, \tag{4.35}$$

where $\boldsymbol{V}_k^{\mathcal{D}}$ denotes the diffusion velocity as in Eq. (4.14), M_k denotes the molar mass

of species k, and β_k is the mole fraction X_k weighted by the diffusion coefficient

$$\beta_k = \frac{z_k^2 \mathcal{D}_k X_k}{\sum_{j=1}^{K} z_j^2 \mathcal{D}_j X_j}. \tag{4.36}$$

In practical terms, it is apparent from Eq. (4.35) that the modification to the diffusion velocity pertains to charged species only ($z_k \neq 0$) and that charged species compensate for the non-vanishing charge flux according to their ability to diffuse as measured by β_k. Then we set

$$\boldsymbol{V}_k = \boldsymbol{V}_k^{A,D} + \boldsymbol{u}_c, \tag{4.37}$$

and consistently

$$\boldsymbol{u}_c = -\sum_{k=1}^{K} Y_k \boldsymbol{V}_k^{A,D}. \tag{4.38}$$

This approach is computationally advantageous for two reasons. Firstly, the assumption that the total charge flux is zero provides an equation for the electric field, which dispenses with solving for the electrostatic potential and alleviates the restrictive dielectric relaxation constraint on the maximum time step size allowed. Secondly, under the ambipolar diffusion velocity model, the mass fluxes of electrons are comparable in magnitdue to those of ions, which removes the taxing constraints on the maximum stable time step size brought by electron drift and diffusion fluxes.

Further discussion on the transition from the drift-diffusion model for the transport of charged species in Section 4.1.2 to the ambipolar diffusion velocity closure discussed here is provided in Section 4.2.

4.1.8 Kinetics for plasma, non-equilibrium, and combustion processes

There exist four classes of elementary reactions in the model employed here: *(i)* plasma processes and reactions that involve electrons with rate coefficients that depend on the electron temperature T_e; *(ii)* reactions involving charged species that depend on the gaseous mixture temperature, e.g., charge transfer and recombination; *(iii)* reactions that describe the formation and loss of particles representing excited states due to energy exchanges and relaxation (thermalization); and *(iv)* elementary combustion reactions with rate coefficients in Arrhenius form that depend on the temperature of the gaseous mixture in thermal equilibrium.

Starting from a detailed mechanism for air plasmas proposed by Eckert [44], a detailed mechanism consisting of 163 species and 1167 reactions comprising all four classes above was assembled in Ref. [2] to simulate the ignition of methane/air and ethylene/air mixtures by nanosecond discharges in zero-dimensional isochoric reactors. The detailed mechanism was then reduced by employing the reduction methodology P-DRGEP [4], which retains accurate electron energy branching ratios during the discharge in addition to more conventional combustion targets and metrics.

In this work, we adopt the reduced mechanism first presented in Ref. [4] as a starting point. The mechanism is extended to include negative ions O_2^- and O^- together with related reactions for electron attachment and detachment and charge recombination [68; 69; 70; 71; 72]. These newly added reactions are listed in Tab. 4.4 together with pertinent references and their functional form and related parameters are provided in Appendix E. After such a modification, the mechanism comprises

Table 4.4: Summary of reactions involving negative ions, including electron attachment, electron detachment and charge recombination, which are added to those already included in the model proposed in Ref. [4]. The functional form and related parameters of those reactions are provided in the Supplementary material.

No.	Reaction	Fit type	Ref.
	Electron attachment		
R1	$E + O_2 + M \rightarrow {O_2}^- + M$	$f(T_e)$	[71]
R2	$E + O_2 \rightarrow O + O^-$	FIT1	[72]
R3	$E + O_2(a^1\Delta) \rightarrow O + O^-$	FIT1	[72]
R4	$E + O_2(b^1\Sigma) \rightarrow O + O^-$	FIT1	[72]
	Charge transfer and electron detachment		
R5	$O^- + O_2 \rightarrow O + {O_2}^-$	Janev	[70]
R6	${O_2}^- + O_2 \rightarrow E + 2O_2$	FIT1	[70]
R7	$O^- + O_2 \rightarrow E + O_2 + O$	FIT1	[70]
R8	$O^- + N_2 \rightarrow E + N_2 + O$	FIT1	[70]
	Electron-ion and ion-ion recombination		
R9	${O_2}^- + {O_2}^+ + M \rightarrow 2O_2 + M$	Arr.	[71]
R10	$O^- + {O_2}^+ + M \rightarrow O + O_2 + M$	Arr.	[71]
R11	${O_2}^- + {N_2}^+ + M \rightarrow O_2 + N_2 + M$	Arr.	[71]
R12	$O^- + {N_2}^+ + M \rightarrow O + N_2 + M$	Arr.	[71]

57 species and 243 reactions, which is further reduced for air discharges by removing species containing either H or C atoms to 21 species and 87 reactions. Comparisons between the detailed and reduced mechanisms are provided in Chapter 2.

Thermodynamic properties for species $N_2(v = 0, \ldots, 5)$ are computed as discussed in Section 4.1.4 and substituted to the ones in Ref. [4].

4.1.9 Simplifications associated with non-thermal electrons

During the capacitive discharge and shortly thereafter, electrons attain temperatures that are much higher than those associated with all other particles. Further, select atoms and molecules are brought in thermal non-equilibrium by electron

impact, leading to a hierarchy of energy exchanges as the system relaxes towards thermal equilibrium. Finally, the gaseous system is in chemical non-equilibrium.

Except for the transport properties of electrons and the rate coefficients of select reactions that involve energetic electrons, the mathematical models and closures discussed thusfar and presented in Sections 4.1.1 and 4.1.2 treat the gaseous system as one in thermal equilibrium at a common temperature. Electronic and vibrational non-equilibrium effects are modelled by particles that account for subsets of electronic and vibrational energy states with all other degrees of freedom in thermal equilibrium at the temperature of the gaseous system. While our treatment of non-equilibrium atoms and molecules is established and deemed accurate for the present purpose [73], the implications associated with the presence of non-thermal electrons require additional discussion and consideration.

The models and closures adopted in our work are valid for plasma regimes whereby the energy gained by the electrons during the plasma discharge is small compared to that gained by the gaseous system as a whole, i.e., comprising all particles and including electrons. In other words, if we let ΔU represent the gain in the internal energy of the entire collection of particles and similarly let the gain in the electron energy be ΔU_e, the proposed models and closures apply for $\Delta U \gg \Delta U_e$. In this limit, computing the (thermal) equilibrium temperature T from Eq. (4.22) and pressure p as in Eq. (4.20) is adequate since the contribution of the energy stored by the population of electrons to the internal energy of the entire gaseous system (and associated random motion and related peculiar velocities and pressure [74]) is negligible. During plasma discharges pertinent to applications for which our novel

simulation framework is proposed, we find that $\Delta U \gg \Delta U_e$ and our models and closures are applicable.

A comprehensive discussion and validation of our treatment of the system's temperature and pressure in the presence of non-thermal electrons, including a posteriori estimates based on data from simulations with a two-temperature zero-dimensional reactor [2], are included in Appendix F.

4.1.10 Boundary conditions for charged particles and electrostatic potential at electrode surfaces

Boundary conditions for all fields other than the mass density ρ_k of charged particles are prescribed as commonly done for reactive compressible Navier-Stokes [75; 76] or their low Mach number restriction [77], e.g., no-slip surfaces, inlets and outlets, impermeable surfaces, and isothermal or adiabatic surfaces.

Numerical boundary conditions for the mass density of electrons and ions at electrode surfaces follows the theory in Gorin et al. [78] and are applicable in the limit of the *two-stream approximation* [79; 80], which considers both a particle flux directed from the plasma to the electrode surface and a flux directed from the electrode to the plasma.

The resulting expression for the electron flux normal to the electrode surface ($\Gamma_{e,n}$, directed from the plasma into the electrode) reads

$$\Gamma_{e,n} = \frac{n_e}{2} v_e^{\mathrm{th}} - 2\gamma\Gamma_{i,n}, \quad v_e^{\mathrm{th}} = \sqrt{\frac{8k_{\mathrm{B}}T_e}{\pi m_e}}, \tag{4.39}$$

where v_e^{th} is the electron thermal velocity, calculated using the electron temperature and mass (T_e and m_e). The flux is positive when directed away from the plasma and

into the electrode, and negative when directed away from the electrode and into the plasma. Thus, electrons are lost to the electrode due to the electron thermal velocity term, and are emitted from the electrode due to secondary electron emission, which depends on the flux of ions to the electrode $\Gamma_{i,n}$ and the secondary electron emission coefficient γ (SEEC), and is negative.

These modeling choices represent a departure from the boundary fluxes traditionally used in similar numerical studies, as an extra factor of two is applied to both terms in Eq. (4.39). The modeling of boundary conditions for plasma fluid models remains an open question, due in large part to the inherent complexity of describing processes at the boundary, which require a particle-based model and the electron energy distribution function for a high degree of accuracy. In our previous study [81], we demonstrated that in the cathode plasma sheath, which is the region most impacted by modeling choices at the electrode surface, the sensitivity of the solution to the secondary emission coefficient γ is relatively small compared to most other modeling choices, indicating only a modest impact of the additional factor of 2.

In the case of ions in the limit of a *strong electric field*, the electric drift flux dominates over the thermal one and the flux of positive ions reads

$$\Gamma^{+}_{i,n} = \begin{cases} n_i \mu^{\mathrm{e}}_i E_n, & E_n > 0 \\ 0, & \text{otherwise,} \end{cases} \tag{4.40}$$

where $E_n = \boldsymbol{E} \cdot \boldsymbol{n}$ is the component of the electric field normal to the electrode surface, positive when the electric field points from the plasma into the electrode, resulting in a flux of positive ions into the electrode. The flux for negative ions

employs the same approach and reads

$$\Gamma_{i,n}^{-} = \begin{cases} -n_i \mu_i^{\mathrm{e}} E_n, & E_n < 0 \\ 0, & \text{otherwise,} \end{cases} . \tag{4.41}$$

resulting again in a positive flux of ions into the electrode. On all surfaces other than those of the electrodes, homogeneous Neumann conditions are applied to the mass density of all charged particles, e.g. on far-field domain boundaries.

Finally, the electrostatic potential obeys Dirichlet boundary conditions at electrode surfaces and homogeneous Neumann on all other surfaces, including on far-field domain boundaries.

Application of Eq. (4.39), Eq. (4.40), and Eq. (4.41) with a secondary emission coefficient $0.001 \leq \gamma \leq 0.05$ results in the formation of plasma sheaths at the cathode and anode [81]. Conversely, setting homogeneous Neumann conditions on the mass density fields of all charged particles on the electrode surfaces prevents the formation of sheaths altogether. Because the absence of plasma sheaths results in significant computational savings, it is a widely adopted simplification [e.g., see 82]. Boundary conditions that support the formation of plasma sheaths are employed depending on the objectives of the simulation, e.g. in cases when the accurate description of the electrical properties of the plasma and of the voltage fall across the cathode sheath are required.

In previous work by Deak [41], simulations that allow for the formation of sheaths were performed for a similar configuration, where sheath thickness between 0.03 to 0.08 mm was observed depending on the value prescribed for the secondary emission coefficient. The sheath is then expected occupy around 1-4% of the domain,

while the voltage fall effect is effectively accounted for through an equivalent voltage that causes breakdown in the gap. By using the simplified boundary conditions, a solution that is accurate the bulk of the plasma conducting channel (up to 96-99% of the domain) is obtained.

4.2 Numerical methods

Solutions to the governing partial differential equations and related closures and physical models presented in Section 4.1 are obtained with the finite volume method as implemented by two parallel solvers available within the Cartesian adaptive mesh refinement library AMReX and one novel plasma discharge solver built anew for the present purposes.

Our approach to the numerical integration of the system of non-linear equations reflects challenges brought by the many coupled physical processes and the broad dynamic ranges of spatial and temporal scale involved in the ignition of a mixture of hydrocarbon fuel and air by NRP discharges across pin electrodes.

4.2.1 The AMReX library and Navier-Stokes solvers

AMReX is an open-source software library comprising data structures, functions, and linear and non-linear solvers that support the implementation of the finite volume method for the multi-component reactive Navier-Stokes equations. The library implements adaptive mesh refinement (AMR) on Cartesian meshes and employs the Embedded Boundary (EB) method [83] to address complex geometries with a state redistribution approach, which addresses time step restrictions due to small

cut cells.

AMReX is part of the Exascale Computing Project (ECP) [84] and benefits from support by the U.S. Department of Energy (DOE) with the goal of improving its performance for use on next-generation high-performance computing (HPC) platforms.

Two solvers for the multi-component reactive Navier-Stokes based on AMReX are readily available and actively developed and maintained: "PeleC" and "PeleLMeX."

PeleC implements an AMR-based solver suitable for use in flows dominated by compressibility effects, including those with shocks. The governing equations are solved in conservative form using Riemann solvers for the evaluation of the fluxes on the surfaces bounding control volumes. A second-order method of lines (MOL) is used for temporal integration and features a predictor-corrector algorithm to segregate transport, which is treated explicitly, from chemical reactions, which are integrated via an implicit backward differentiation formula (BDF) method at each control volume independently of transport.

On the account of the explicit nature of the time integration method, PeleC is best suited for the simulation of compressible reactive flows with modest stiffness, whereby the temporal scales of the flow dynamics of interest are not much larger compared to the time step size limitations brought by stability, whether based on convective or diffusive processes. More details on PeleC are discussed in Ref. [85].

PeleLMeX implements an AMR-based solver suitable for use in low speed

reactive flows that feature variable density. PeleLMeX solves the so-called *low Mach number* restriction to the Navier-Stokes equations [86; 87], in which density is approximated as a function of a spatially uniform pressure, itself distinct from the hydrodynamic pressure appearing in the momentum equation. The approach involves solving a Poisson equation for a scalar field required to enforce mass conservation (continuity). Time integration is achieved via time-implicit methods in order to overcome severe restrictions brought by diffusive and viscous terms. The temporal integration of the chemical source terms is carried out for each control volume independently of transport. The segregated integration methods are combined with a spectral deferred correction (SDC) approach to ensure accurate coupling between chemical reactions, convective and diffusive transport, all the while ensuring mass conservation. On the account of the low Mach restriction to the governing equations as well as the implicit time integration method and SDC, PeleLMeX delivers most efficiently solutions for low speed flow configurations, allowing for large time step sizes and overcoming the stiffness associated with chemical kinetics and diffusive fluxes on high-resolution meshes typical of Direct Numerical Simulation (DNS). More details on PeleLMeX are discussed in Ref. [88].

4.2.2 PeleCPeX – An AMR solver for plasma discharges

The existing solver PeleC is extended to implement models required to simulate nanosecond plasma discharges and non-thermal plasmas, including energy deposition and afterglow phases. The physical models employed are discussed in detail in Section 4.1.

The extended plasma discharge solver is referred to as "PeleCPeX" and implements the following features: *(i)* drift-diffusion closure for the mean flux of charged particles (Eq. (4.13)); *(ii)* framework for the solution to the Poisson equation for the electrostatic potential (Eq. (4.9)); *(iii)* Joule heating term (Eq. (4.25)) in the transport equation for the total energy; and *(iv)* provisions for the modeling of non-thermal electrons, including accounting for the dependence of transport properties and rate coefficients of selected reactions on the electron temperature (see Section 4.1.6).

The transport of non-thermal electrons and the addition of the electrostatic potential bring significant numerical challenges to the solution of the governing equations. Firstly, the electron drift velocity imposes stringent stability requirements on the time step size due to its high value associated with the mobile electron. Secondly, the electron diffusion coefficient is also much higher than that of all other particles, bringing tight stability constraints on the time step size also, this time due to the diffusive term in the electron conservation equation. Thirdly, there exist a strong coupling between the electrostatic potential and charge transport as the electric field induces charge fluxes, which alter the space charge locally. In turn, changes in the space charge induce changes in the electrostatic potential and electric field. Such two-way coupling occurs on time scales proportional to the dielectric relaxation time scale, which must be resolved.

The numerical challenges discussed above are addressed through several numerical approaches, which are discussed below. Further details on the numerical methods implemented in PeleCPeX are given in Refs. [89; 81] and a validation study against known benchmarks for the simulation of plasma streamers is presented in

Ref. [90].

The time-integration algorithm implemented in PeleC is summarized first and further details are available in Ref. [6]. Next, extensions to the algorithm to accommodate the advancement of the governing equations for plasma fluid model are discussed. The reactive Navier-Stokes equations are integrated in PeleC using a finite-volume, second-order method-of-lines (MOL) approach. The advective terms are discretized spatially using a Godunov scheme with characteristic-based extrapolation to cell faces and a Riemann solver [91]. Diffusive terms are discretized using a second-order centered scheme.

In what follows, let $\boldsymbol{U} = (\rho, \rho\boldsymbol{u}, \rho\ \mathcal{E}, \rho_k)$ indicate the vector of conserved variables, which are advanced from time t_n to time $t_{n+1} = t_n + \delta t$. Superscript $(\cdot)^n$ indicates that a quantity is available at time t_n and similarly for $(\cdot)^{n+1}$. A predictor-corrector approach is employed, whereby the advective and diffusive terms $\boldsymbol{S}_{AD}$ are calculated multiple times during one step in order to construct an approximation $\boldsymbol{U}^{**}$ to the state variable $\boldsymbol{U}^{n+1}$:

$$\boldsymbol{S}_{AD}^{n} = A(\boldsymbol{U}^{n}) + D(\boldsymbol{U}^{n}) \tag{4.42}$$

$$\boldsymbol{U}^{*} = \boldsymbol{U}^{n} + \delta t(\boldsymbol{S}_{AD}^{n} + \boldsymbol{\omega}_{r}^{n}) \tag{4.43}$$

$$\boldsymbol{S}_{AD}^{n+1} = A(\boldsymbol{U}^{*}) + D(\boldsymbol{U}^{*}) \tag{4.44}$$

$$\boldsymbol{U}^{**} = (\boldsymbol{U}^{n} + \boldsymbol{U}^{*})/2 + (\delta t/2)\,(\boldsymbol{S}_{AD}^{n+1} + \boldsymbol{\omega}_{r}^{n}), \tag{4.45}$$

where A and D represent advective and diffusive operators, while $\boldsymbol{\omega}_r^n$ is a time-lagged reactive source discussed below. Then, an advective/diffusive forcing term is

calculated

$$\boldsymbol{F}_{AD} = (\boldsymbol{U}^{**} - \boldsymbol{u}^n)/\delta t - \boldsymbol{\omega}_r^n, \tag{4.46}$$

after which the solution at the next time step is obtained by integrating $\boldsymbol{U}^n$ with $\boldsymbol{F}_{AD}$ and the (non-linear) chemical sources at each cell from t_n to t_{n+1} using the stiff ODE solver implemented in CVODE [43]. The time-lagged reactive source term is then updated for use during the next time step

$$\boldsymbol{\omega}_r^{n+1} = (\boldsymbol{U}^{n+1} - \boldsymbol{U}^n)/\delta t - \boldsymbol{F}_{AD}. \tag{4.47}$$

In order to integrate the governing equations in the plasma fluid model, a novel time-integration scheme is developed as summarized in Algorithm 1. Key additions to the original PeleC scheme include: a semi-implicit solver for the electrostatic potential [92], calculation of the photoionization term as outlined in Section 4.1.3, boundary conditions for charged species as discussed in Section 4.1.10, computation of the Joule heating term, and calculation of reaction rates as a function of the electron temperature.

Due to the time-explicit integration of convection and diffusion, there exist well-known constraints to the step size. In addition, the dielectric relaxation time scale associated with tight coupling between changes in electron number density and electric field must be considered in order to maintain stability of the numerical solution. During the discharge phase, the time step size is calculated as

$$\delta t = \min\{0.3\,\delta t_A, \alpha_E\,\delta t_E, 0.3\,\delta t_D\}, \tag{4.48}$$

$$\delta t_A = \min\left\{\Delta/|\boldsymbol{V}_e^{\mu}|\right\}, \tag{4.49}$$

Algorithm 1 PeleCPeX time-integration approach

procedure ADVANCE($\boldsymbol{U}$ from t_n to $t_{n+1} = t_n + \delta t$)
  $\boldsymbol{E}^{n+1} = -\nabla\phi^{n+1}$ ▷ ϕ computed with semi-implicit approach
  $S^n_{\text{ph}} = S_{\text{ph}}(\boldsymbol{U}^n)$ ▷ Computed with 3-term Helmholtz approximation
  $\boldsymbol{S}^* = AD(\boldsymbol{U}^n, \boldsymbol{E}^{n+1})$ ▷ Advective/diffusive sources and boundary fluxes
    $S^* \leftarrow S^* + S_{\text{J}}(\boldsymbol{U}^n, \boldsymbol{E}^{n+1})$ ▷ Joule heating added to energy density source
  $\boldsymbol{U}^* = \boldsymbol{U}^n + \delta t(\boldsymbol{S}^* + \boldsymbol{\omega}_r^n)$
  $\boldsymbol{S}^{n+1} = AD(\boldsymbol{U}^*, \boldsymbol{E}^{n+1})$
    $S^{n+1} \leftarrow S^{n+1} + S_{\text{J}}(\boldsymbol{U}^*, \boldsymbol{E}^{n+1})$
  $\boldsymbol{U}^{**} = (\boldsymbol{U}^n + \boldsymbol{U}^*)/2 + (\delta t/2)\,(\boldsymbol{S}^{n+1} + \boldsymbol{\omega}_r^n)$
  $\boldsymbol{F}_{AD} = (\boldsymbol{U}^{**} - \boldsymbol{U}^n)/\delta t - \boldsymbol{\omega}_r^n + S^n_{\text{ph}}$ ▷ Advective/diffusive forcing term
  $\boldsymbol{U}^{n+1}$ at each cell ▷ Integrated from $\boldsymbol{U}^n$ with $\boldsymbol{F}_{AD}$, and non-linear $\boldsymbol{\omega}_r$
  $\boldsymbol{\omega}_r^{n+1} = (\boldsymbol{U}^{n+1} - \boldsymbol{U}^n)/\delta t - \boldsymbol{F}_{AD}$.
end procedure

$$\delta t_E = \min\left\{\epsilon_0/(\mathrm{e}\mu_e^{\mathrm{e}} n_e)\right\}, \tag{4.50}$$

$$\delta t_D = \min\left\{\Delta^2/\mathcal{D}_e\right\}, \tag{4.51}$$

where Δ is the length of the cubic cell side, δt_A, δt_E, and δt_D represent the maximum time step size due to electron drift, dielectric relaxation, and electron diffusion processes. Minimization occurs across all cells and all AMR levels. The user-defined safety factor 0.3 used for the electron drift constraint is a consequence of the method of lines. The factor α_E that multiplies δt_E is set equal to either 10 or 20 depending on the phase of the plasma discharge (see discussion in Section 4.2.3 below and related figures) and is made possible by the semi-implicit treatment of the coupling between space charge and electric field [92] and is set based on numerical experiments. Finally, a maximum time step size of 50 ps is imposed to ensure accuracy during the initial transient when the voltage increases from low values. For all configurations and resolutions employed in this study, electron drift and the dielectric relaxation

constraints result in the most stringent limitation to the time step size.

4.2.3 Solution framework

In this Section, the solution framework used to simulate ignition by one or more nanosecond pulse discharges with high-fidelity elementary physical models is presented with each framework component discussed in the same sequence as that of the physical processes leading to ignition: discharge, afterglow, shocks and expansion, hydrodynamics and mixing, and ignition.

For the sake of clarity, the framework is discussed for the case of the ignition of a stoichiometric ethylene/air mixture at scramjet conditions by a single nanosecond pulse. This configuration presents additional complexities due to ignition phenomena and is further discussed in Ref. [5]. Nonetheless, it is easily applicable to single- and multi-pulse discharges in air also, which is the main focus of this dissertation. The extension of the approach to repetitively pulsed discharges is discussed as appropriate.

Figure 4.2 summarizes the solution framework, which leverages three separate solvers: PeleCPeX, PeleC, and PeleLMeX. The solvers implement mathematical models and numerical methods tailored to the physical processes most relevant to each specific phase, thereby ensuring computational efficiency.

The *plasma discharge* phase lasts from the start of the simulation to the instant when the applied voltage bias is set to zero (event "A" in Fig. 4.2) and is characterized by elevated electric fields, significant ionization, the propagation of streamers towards the electrodes followed by energy deposition in a conducting

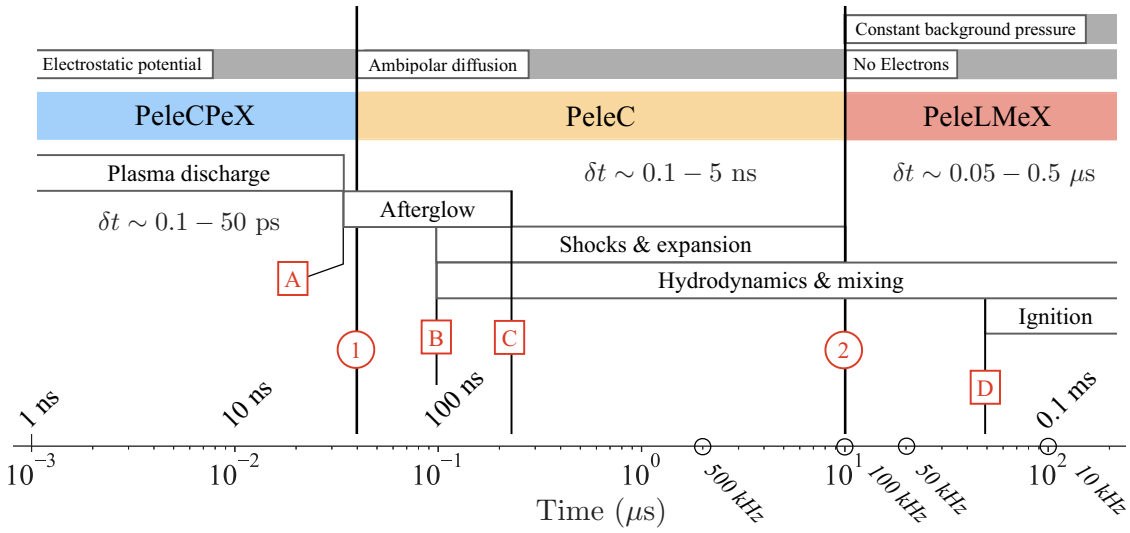

Figure 4.2: Solution framework utilized for the simulation of plasma assisted ignition of ethylene/air mixtures at 600 K and 0.5 atm (see Ref. [5]). The framework leverages three separate solvers, i.e., PeleCPeX, PeleC, and PeleLMeX, which implement mathematical models and numerical methods tailored to the physical processes most relevant to each specific phase, thereby ensuring computational efficiency. Labels "1" and "2" mark the physical time corresponding to the transition from one solver to the next. For each solver, a range of time step sizes δt is provided and additional data are shown in Fig. 4.3. Labels "A" through "D" indicate the time when specific physical processes of interest are most relevant as discussed in the commentary. Also marked are the intervals between pulses for repetition frequencies from 10 kHz to 500 kHz (open circles on the time axis).

channel bridging the gap. The discharge phase terminates when a user-prescribed amount of energy is deposited into the gas and the voltage difference across the electrodes is set to zero.

The discharge phase requires the solution of the unsteady electric potential accounting for space charge effects, transport of charged species due to electric fields, and plasma reactions that depend on elevated mean electron energies. It also requires solving for the evolution of the thermochemical state of the gaseous mixture, which attains elevated temperature and pressure and significant thermal non-equilibrium.

The discharge phase is simulated using PeleCPeX and the elementary models and closures implemented therein. The time step sizes range from 0.1 to 50 ps as shown in Fig. 4.3, where we observe distinct features. Up to marker "I," the time step size decreases steadily due to the restriction associated with electron drift and is inversely proportional to the increase in the maximum value of the electric field strength due to the applied voltage. After marker "I," significant shielding at the electrodes occurs, which decreases the maximum electric field and leads to a relaxation of the electron drift time scale. Shortly after the conducting channel is established, a steady increase in the number density of electrons ensues and the dielectric time scale restriction ($\alpha_E = 10$) overtakes that due to electron drift. The time step size continues to decrease, reaching its minimum over the entire numerical simulation at marker "II." Later in the evolution of the conducting channel, a constant time step of 0.5 ps is imposed, roughly equivalent to a safety factor of $\alpha_E = 20$, which is found to yield a stable solution at reduced computational costs.

At time instant "A" when the electric field due to the voltage bias becomes

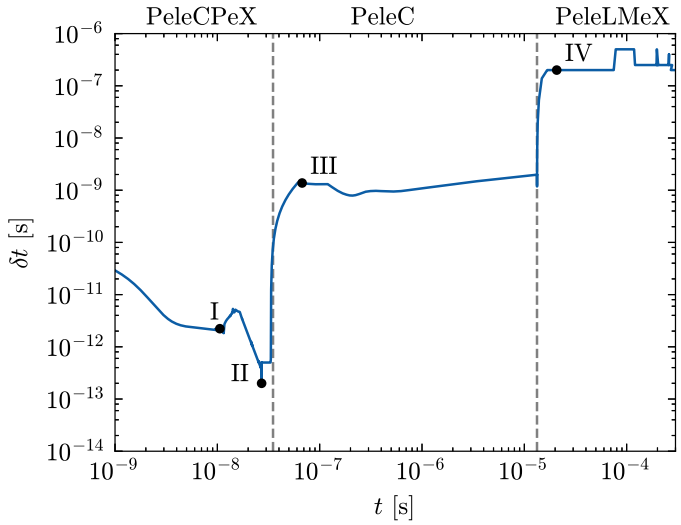

Figure 4.3: Time step size δt during the simulation of plasma assisted ignition of ethylene/air mixtures at 600 K and 0.5 atm (see Ref. [5]). Vertical dashed gray lines represent instants when the solver changes from PeleCPeX to PeleC and from PeleC to PeleLMeX, respectively. Markers "I" through "IV" correspond to events discussed in the commentary in Section 4.2.3.

zero instantaneously, only the electric field associated with the space charge remains, inducing significant charge drift fluxes. The ensuing rapid transport of charges acts to reduce the space charge engendering neutrality in the plasma. During this short-lived transient, the same mathematical models and numerical methods employed during the discharge phase are used and the simulation continues with PeleCPeX until the maximum electric field strength anywhere in the domain decreases below a user-defined threshold indicating that the plasma is quasi-neutral to a reasonable approximation.

Once the plasma is quasi-neutral (label "1" in Fig. 4.2), the solver changes from PeleCPeX to PeleC with the ambipolar diffusion closure for the mass flux of charges. Thus, the Poisson equation for the electrostatic potential is not solved any longer. PeleC is employed to simulate the evolution of the gas during the *afterglow* phase, which is characterized by charge transfers and recombination reactions as well as kinetic processes that accompany the fast and slow return of the gaseous system to thermal equilibrium. In the simulations discussed later in this work, the threshold is set to 50 Td.

Use of PeleC equipped with the ambipolar diffusion model for charges during the afterglow phase is of paramount importance for the simulation of multiple nanosecond pulses since the spatial distribution of charges immediately prior to a discharge controls the propagation of streamers and influences the location where the conducting channel forms. In the absence of the ambipolar diffusion model, plasma neutrality is not preserved, rather unphysical charge separation appears. On the contrary, in the case of a single nanosecond pulse, use of the ambipolar diffusion

model is not strictly necessary since charges do not take part in the subsequent physical processes, which involve the formation of weak shocks, hydrodynamic mixing, and possibly ignition. Thus, any unphysical space charge distribution and lack of plasma neutrality resulting from inaccurate closures for the mass flux of charges is inconsequential.

As time progresses during the afterglow phase, the pressurized channel expands by way of a system of weak shocks that propagate outwards away from the pin tips and the center of the electrode gap. The onset of those processes marks the beginning of the *shocks and expansion* phase (see Fig. 4.2), which commences when the density anywhere in the domain decreases by more than 5% with respect to its far field value (event "B" in Fig. 4.2). The system of shocks emanating from the pin tips and the gap sets the fluid in motion also, commencing the *hydrodynamics and mixing* phase, whereby surrounding fluid is entrained into the electrode gap and mixed with the hot gases produced by the discharge. During the early portion of the shock, expansion, hydrodynamic, and mixing phases, the afterglow phase ends when the maximum temperature in the computational domain reaches its peak value as fast gas heating associated with the relaxation of electronically excited states concludes (event "C" in Fig. 4.2).

The time step sizes during integration with PeleC range from 0.1 ns to ≈ 5 ns as shown in Fig. 4.3. At the onset, a transition period between markers "II" and "III" occurs as the time step size increases steadily. By marker "III," the maximum time step size reaches a value due to conventional limitations brought by acoustic speeds in compressible explicit solvers. Past marker "III," the time step size remains

constant during the early phases of the kernel expansion and then grows slowly up to 5 ns until the transition to the PeleLMeX solver.

The expansion continues until pressure relaxes back to its value prior to the nanosecond discharge. In practice, there remain small spatial fluctuations in pressure associated with low speed fluid motion. When the pressure within a radial distance equal to 4 times the electrode gap is within 5% of its value at the onset of the simulation, the *shocks and expansion* phase concludes (label "2" in Fig. 4.2) and the simulation continues with PeleLMeX, which solves the low Mach number restriction of the Navier-Stokes equations.

The importance of compressibility effects should be assessed in the context of the application, with the strategy described above being adequate for discharges in quiescent air. In some cases, the interaction of the outward propagating pressure waves with flow elements further away from the gap may be important, delaying the transition or requiring a reevaluation of the criterion. In the most limiting scenario, transition to the low Mach approximation may be prevented altogether, leading to an increase in the overall computational costs as discussed in this section.

Past instant "2," low speed hydrodynamic and mixing processes driven by density gradients continue and interact with chemical reactions possibly engendering ignition of the reactive mixture. Maximum temperature and heat release decrease steadily between events "C" and "D" shown in Fig. 4.2. At the instant marked with "D," this trend reverses and a sharp increase in the heat release rate is observed, immediately followed by an increase in the maximum temperature. Later, over an interval of duration $\mathcal{O}(10-100\,\mu\text{s})$, an expanding premixed flame front is established,

indicating that an ignition event has taken place.

The time step sizes taken by PeleLMeX range from 0.05 to 0.5 μs as shown in Fig. 4.3. An early transition is apparent as PeleLMeX starts. After marker "IV," time steps of approximately 0.5 μs are employed until ignition takes place. Challenges with accuracy and stability due to high gradients in temperature across thin thermal layers enveloping the embedded boundaries representing the electrodes force a reduction in the time step size at times. In order to avoid gross inaccuracies leading to unphysical results, constant time step sizes are set, which explains the observed "staircase" pattern in Fig. 4.3.

Figure 4.2 shows the interval between subsequent pulses for repetition frequencies between 10 kHz (corresponding to 0.1 ms) and 500 kHz (corresponding to 2 μs). It is apparent that in the case of repeated pulses, the interval duration determines whether the simulation should continue with the low Mach number solver PeleLMeX or a new plasma discharge should be simulated directly with PeleCPeX starting from the shocks and expansion phase simulated with PeleC. For example, in the case of repetition frequencies $\geq$ 100 kHz, it most efficient to simply alternate between PeleCPeX and PeleC, while for frequencies below 50 kHz, PeleLMeX should be employed after PeleC and prior to switching back to PeleCPeX to simulate a new plasma discharge.

Practical details such as the need to convert solutions produced by the compressible reactive Navier-Stokes solver PeleC into a format suitable for the low Mach number reactive flow solver PeleLMeX might make solver switching inconvenient and cumbersome for repetition frequencies only slightly lower than 100 kHz, so that

Table 4.5: Range of time step sizes, minimum and maximum overall number of cells (summed across all AMR levels), number of AMR levels, number of processors, and computational cost measured as wall-clock time for each of the three solvers employed during the corresponding phases shown in Fig. 4.2 for the simulation of the single-pulse ignition of an ethylene/air stoichiometric mixture at scramjet conditions (see Ref. [5]).

Solver	δt (ns)	# Cells	AMR levels	# Processors	Wall-clock time [hrs]
PeleCPeX	$10^{-4} - 0.05$	$30 - 35$ M	5	7,168	100
PeleC	$0.1 - 5$	$10 - 15$ M	4	3,584	40
PeleLMeX	$50 - 500$	$10 - 15$ M	4	1,792	12

one might simply extend the use of PeleC slightly past the instant labelled as "2" although compressibility effects are no longer relevant.

Finally, we note that, even if only PeleCPeX and PeleC are employed for repetition frequencies $\geq$ 100 kHz, simulations of ignition require integration to $\mathcal{O}(0.5 - 1\,\text{ms})$, which is most efficiently accomplished with PeleLMeX once nanosecond plasma discharges terminate.

A summary of the minimum and maximum time step size, minimum and maximum overall number of control volumes (summed across all AMR levels), number of AMR levels, number of processors, and computational cost measured as wall-clock time is provided in Tab. 4.5 for the simulation of the single-pulse ignition of an ethylene/air stoichiometric mixture at scramjet conditions (see Ref. [5]). It is apparent that most of the computational cost is associated with the simulation of the discharge phase with PeleCPeX, when the dielectric time scale restricts time step sizes down to $\mathcal{O}(0.1$ ps) during energy deposition in the conducting channel and 5 levels are required to resolve all relevant spatial features.

4.3 Summary and Overview

A comprehensive numerical framework for the high-fidelity simulation of nanosecond discharge pulses was developed and presented. Important approximations include a simplified voltage waveform, reduced kinetics model, local field approximation, and simplified boundary conditions. The simplified waveform facilitates the energy deposition and the simulation of the afterglow phase in the absence of a circuit model, which would ensure a close coupling between volage and current. In the process, vibrational excitation is underestimated slightly and the temporal scales of the discharge process are shortened. The local field approximation, which does not require an additional equation for the electron energy density, was considered sufficiently accurate for the current purposes as discussed in Appendix F. With simplified boundary conditions that avoid the formation of plasma sheaths, emphasis is placed on the simulation of plasma dynamics in the bulk of the conducting channel, while the effect of the voltage fall is addressed through an equivalent voltage that causes breakdown.

Effective strategies were proposed and utilized to overcome commonly encountered complicating factors in the simulation of nanosecond discharges. The tight coupling between electric field and space charge during the energy deposition was addressed through a semi-implicit scheme, while electron transport is treated explicitly in time. The large separation of spatial scales was addressed with the use of adaptive mesh refinement (AMR) algorithms and an embedded boundary method was used to represent complex geometries. The need to model three-dimensional configurations over a wide range of time scales relevant to plasma assisted combus-

tion was addressed using a hierarchy of massively parallel solvers (PeleCPeX, PeleC, and PeleLMeX). Finally, detailed plasma kinetics and limiting time scales associated with chemical kinetics were overcome using fractional steps and pointwise implicit solvers as described in this chapter.

Chapter 5

Pin-to-pin discharges: Overview

In this Chapter, detailed simulations are leveraged to present a comprehensive description of single and multi-pulse plasma discharges in atmospheric air, which are of paramount importance in the modeling of realistic ignition systems that use NRP discharges. Two axisymmetric pin electrodes are considered, which is a common configuration in experimental and numerical studies alike [50; 27; 93].

First, we consider a single pulse, which deposits 800 μJ of energy and results in the formation of a hot kernel of gases. The discharge is dominated by various physical processes taking place across a wide range of time scales, which we split into the discharge phase, acoustic (or expansion) phase, and hydrodynamic phase, respectively. Subsequently, the kernel of hot gases left behind by the discharge undergoes toroidal collapse as described by Dumitrache et al. [12]. In the second case study, a second plasma discharge occurs at 200 μs after the first (corresponding to a 5 kHz repetition frequency). This second pulse deposits an additional 800 μJ of energy in a conducting plasma channel, which is established away from the axis and toward the pocket of hot air left behind by the first pulse following toroidal collapse. This behavior matches qualitatively experimental observations by Adams et al. [94], who reported that the path taken by a second plasma discharge depends

on the interval between the two pulses.

Together, the results discussed in this Chapter demonstrate the capability of the proposed framework to simulate single and multi-pulse nanosecond plasma discharges for ignition of air/fuel mixtures, providing quantitative information on computational complexity and costs. Furthermore, the simulations provide unprecedented insight into multiple processes that lead to heat and mass transport in the electrode gap following a single or multiple nanosecond pulse discharges. The objectives of this chapter are as follows:

- Provide a detailed overview of the physical processes engendered by single pin-to-pin discharge including: streamer propagation, energy deposition, shock propagation and gas expansion, and finally, cold gas entrainment.
- Discuss and define processes, metrics and features, and quantities of interest that will be leveraged in order to support a quantitative analysis in later chapters.

5.1 Configuration

The geometry arrangement of the pin-to-pin configuration is shown in Fig. 5.1(a). The computational domain is a cube of side equal to 10 mm arranged as in Fig. 5.1(b), which shows the electrode assembly also. The two pins are separated by a gap $d = 2.5$ mm, measured from the tip of one electrode to the other. The electrode geometry consists of a cylindrical shaft and parabolic end with tip having radius of curvature $r_c = 250$ μm (corresponding to $r_c/d = 0.1$). The parabolic section of the

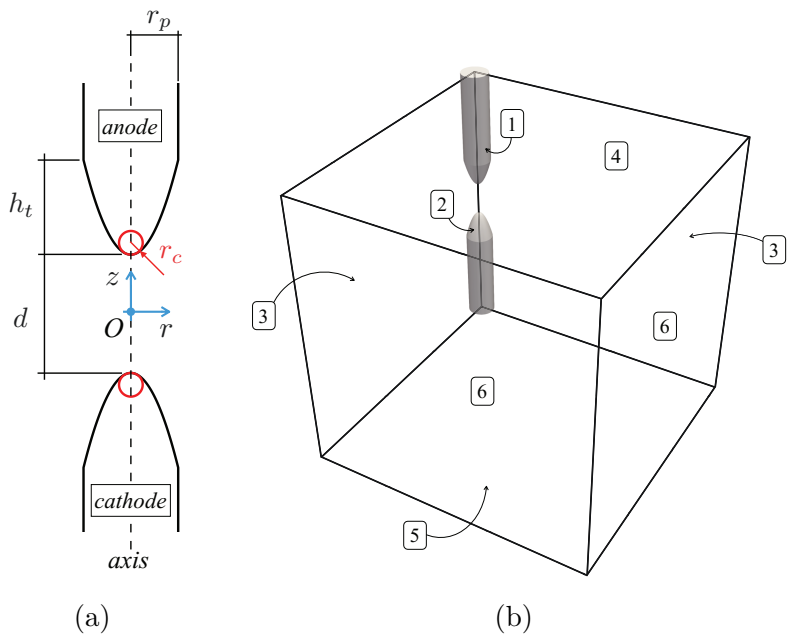

Figure 5.1: (a) Geometry of the two pin electrodes with cylindrical coordinate system. The electrode gap is $d = 2.5$ mm, the paraboloid tips have radius of curvature $r_c = 250$ μm and height $h_t = 2$ mm, and the cylindrical shafts have radius $r_p = 1$ mm. The origin of the coordinate system is located at the mid-point of the gap along the axis of the electrodes. (b) Cubic computational domain of side 10 mm with each bounding surface labelled as in Tab. 5.2 and pin electrodes shown in gray. The pin electrodes are modeled with the Embedded Boundary (EB) method available in the library AMReX.

electrodes extends away from the tip for $h_t = 2$ mm until the radius r_p is equal to 1 mm, which is the radius of the cylindrical shaft. Overall, each pin extends 3.75 mm from the top and bottom surfaces of the cubic domain. The geometry of the electrodes shown in Fig. 5.1(a) reproduces that in experimental studies of pin-to-pin discharges [10; 27].

The choice of a parabolic pin tip shape is a convenient approach to impose a radius of curvature at the tip and a smooth transition where the tip merges with the cylindrical base of the pin as in experimental configurations. In reality, electrodes are commonly manufactured as sharp cones with a specified angle, with the pin tip curvature measured during the experimental campaign or sharpened as desired. By specifying pin base radius and pin tip curvature that match those reported from experiments, the sloped section of the pin can be expected to be reasonably close to that of the manufactured cone. The difference is likely negligible for discharges in quiescent air, explored in this work, where the pin tip curvature is expected to be the dominant parameter. An increased sensitivity to the sloping section of the pin may be observed for high-speed cross-flow configurations, although such effects are outside the scope of this work and unclear at present.

The simulations are executed in a Cartesian quarter-periodic cubic domain and suitable boundary conditions at the bounding surfaces are chosen to enforce the quarter periodic geometry. When post-processed, fields are treated as axisymmetric, parametrized by a cylindrical coordinate system as a function of axial coordinate z and radial distance from the axis r. The cylindrical coordinate system and its origin in the middle of the gap on the axis of the pin electrodes are shown in Fig. 5.1(a).

The computational domain is discretized by cubic control volumes and the AMR capabilities of the solvers are leveraged to add resolution only where needed. The base mesh (AMR level 0) consists of 64^3 control volumes across a cube of side 10 mm, yielding a base resolution $\Delta_0 = 10$ mm$/64 \approx 160$ μm. Up to 5 additional levels of refinement are used for select phases of the simulation, yielding the finest resolution of $\Delta_5 = \Delta_0/2^5 \approx 5$ μm (AMR level 5) as the cubic control volume size decreases by a factor of two with each level. Past the discharge phase, the finest resolution is relaxed to $\Delta_4 = \Delta_0/2^4 \approx 10$ μm by setting the maximum number of AMR levels to 4.

Electrodes are represented by the Embedded Boundary (EB) method [83]. In order to improve the accuracy and robustness of the numerical boundary conditions as well as that of the solution near the electrodes, the finest AMR level is employed for cells cutting through the surfaces of the electrodes. When PeleCPeX is used to simulate the plasma discharge, cells on the electrode surfaces have the finest resolution Δ_5 (AMR level 5, corresponding to $\Delta_5 \approx 5$ μm), while past the discharge phase when PeleC is used, resolution is relaxed to Δ_4 (AMR level 4, corresponding to $\Delta_4 \approx 10$ μm).

During the simulations, local refinement is driven by criteria that are specific to each solver and phase as detailed in Tab. 5.1. The selection of the minimum resolution is a compromise between accuracy and computational efficiency. Resolution of the streamer front and the region at the electrode boundaries is the most demanding and typical cell sizes range from 3 μm to 10 μm as employed in plasma streamer simulations [38; 14; 95; 52]. In this work, a resolution of 5 μm is selected

Table 5.1: Threshold values that control adaptive mesh refinement for each of the three solvers. $\max \Delta$ represents the absolute value of the maximum difference between field values across any two adjacent cells. The spatial resolution associated with AMR level ℓ is $\Delta_\ell = \Delta_0/2^\ell$ where $\Delta_0 = 10$ mm$/64 \approx 160$ μm is the size of cells in the base mesh.

Field	$\max \Delta$	AMR levels	PeleCPeX	PeleC	PeleLMeX
E/N	5 Td	5	✓		
T	20 K	4	✓	✓	✓
p	2500 Pa	3	✓	✓	

as a compromise between accuracy and efficiency. In previous work the gradient of the reduced electric field was shown to be a sensible criterion to refine the streamer structure [90] for which a maximum difference of 5 Td across adjacent cells is imposed. Another important solution feature driving refinement is the hot kernel of gases formed during energy deposition, for which a conservative criterion of maximum temperature difference of 20 K across adjacent cells was imposed. Finally, expansion of the pressurized gas induces weak shocks and outward waves. When the shock location coincides with the boundary of the hot gas kernel at the initial stages of the expansion, the temperature criterion enforces a resolution of 10 μm. As the pressure fronts move outward and weaken, they are resolved by imposing a criterion allowing for a maximum pressure difference of 2500 Pa across adjacent cells resulting in a spatial resolution of 20 μm. The pressure threshold corresponds to 2% of the background pressure for the atmospheric case. In a study involving similar expansion processes [12], a sensitivity study indicates that a spatial resolution of 15 μm is sufficient. In the same study [12], smaller kernel radii and stronger shocks are observed compared to the ones encountered in this study.

At the onset of the simulation, the fluid is quiescent and its spatially ho-

Table 5.2: Boundary conditions on each of the bounding surfaces labeled in Fig. 5.1(b). †: a *symmetry* boundary condition is implemented as homogeneous Neumann conditions on the field. ‡: see the PeleC documentation [6] for a description of the *outflow* boundary condition.

Surface	Description	Navier-Stokes	Electrostatic potential	Charge densities
1	Anode	No-slip, isothermal, solid wall	Dirichlet $V(t)$	Homog. Neumann
2	Cathode	No-slip, isothermal, solid wall	Homog. Dirichlet	Homog. Neumann
3	Symmetry plane	Symmetry†	Symmetry†	Symmetry†
4	Top plane	No-slip, adiabatic, solid wall	Dirichlet $V(t)$	Homog. Neumann
5	Bottom plane	No-slip, adiabatic, solid wall	Homog. Dirichlet	Homog. Neumann
6	Far-field	Outflow‡	Homog. Neumann	Homog. Neumann

mogeneous thermochemical state is equal to that of air at 300 K and 1 atm. Air is modelled as a mixture of oxygen (21% by volume) and nitrogen. The gaseous mixture is mildly pre-ionized into a neutral plasma by letting the number density of electrons and that of $O_2{}^+$ ions equal to 10^9 m^{-3} (or 10^3 cm^{-3}) everywhere in the domain. The simulations feature 21 species and 87 reactions. The species consist of all species listed in Tab. 4.1.

The boundary conditions on each of the six bounding surfaces labeled in Fig. 5.1(b) are summarized in Tab. 5.2. As far as the Navier-Stokes equations are concerned, the surfaces of the two pin electrodes are treated as no-slip, isothermal, and solid boundaries (the mass flux of neutral particles is zero). In particular, no-slip surfaces allow for the development of velocity boundary layers on the surface of the

electrodes. Such boundary layers form during fluid entrainment following discharges with significant energy deposition.

Electrodes are made of metal (e.g., tungsten [96; 93]) with large thermal diffusion coefficients that result in the surface of the solid electrode remaining near its initial temperature even when exposed to hot gases generated by nanosecond pulses. Thus, the temperature on the surface of both electrodes is held constant and equal to the initial air temperature (300 K), bringing about the development of thermal boundary layers and energy loss by conduction.

The top and bottom planar surfaces are treated as no-slip, adiabatic, and solid surfaces. Since the top and bottom surfaces are sufficiently far away from the active region around the electrode gap, shocks and acoustic waves attenuate prior to reflecting off those surfaces, so that such reflections do not affect the processes near the gap. The far-field boundary surfaces are treated as outflow surfaces as they are also placed sufficiently far away from the region of interest. The outflow conditions implemented in PeleC are employed and correspond to extrapolations from inside the domain (see Ref. [6]). In practical terms, at the end time considered in the numerical simulations considered, acoustic waves have not yet reached the far field surfaces so that the actual boundary conditions do not have any impact on the solution. Provisions exist in PeleC to specify subsonic inflows and outflows that take into account local characteristics as needed.

On the anode and top planar surfaces, the electrostatic potential obeys Dirichlet boundary conditions and is set equal to a prescribed time-varying voltage bias $V(t)$. The cathode and bottom planar surfaces are grounded so that the potential

is set to zero, corresponding to homogeneous Dirichlet boundary conditions. On the far-field bounding surfaces, the electrostatic potential obeys homogeneous Neumann boundary conditions.

On the two planar surfaces labeled *symmetry plane*, homogeneous Neumann conditions are imposed for all fields in order to obtain solutions that are quarter-periodic (symmetry condition).

Boundary conditions for the mass density of electrons and ions on the surface of the electrodes as well as on the top and bottom surfaces differ from those of all other (neutral) particles. Depending on the application and fidelity desired, the boundary conditions for charged particles on electrodes take select functional forms (see Section 4.1.10 for a comprehensive discussion of boundary conditions for charged particles). For the application discussed in this Chapter, homogeneous Neumann boundary conditions are applied to the mass density of all charged species as also done in Barléon et al. [38], thereby preventing the formation of plasma sheaths [97], which would require even higher spatial resolution than the one employed.

It is important to note that plasma sheaths result in large voltage falls from the cathode to the plasma bulk, so that the voltage bias applied to the electrodes is greater than that acting across the plasma, making the accurate modeling of plasma sheaths necessary for quantitative comparisons between experiments and simulations. Consequently, sheaths are not essential to the objectives of our study and the homogeneous Neumann conditions applied to the densities of charged particles prevent sheath formation and lower resolution requirements and computational costs.

The positive voltage bias applied to anode and top bounding surface is described by the following sigmoid function:

$$V(t) = V_{\max}\left[f(t-\delta,\lambda) + f(t-\delta-t_r-t_p,-\lambda) - 1\right], \tag{5.1}$$

$$f(t,c) = \frac{1}{1+\exp\left(-ct\right)}, \tag{5.2}$$

where δ, t_r, $\lambda = 8/t_r$, and t_p are constants that control the voltage rise and pulse duration, and $V_{\max}$ is the peak voltage. In this work, for all configurations, we use δ = 3 ns, t_r = 4 ns, and t_p = 50 ns, while $V_{\max}$ is selected to obtain a nominal value of the reduced electric field E/N = 204 Td regardless of thermodynamic conditions. The same approach as in Refs. [14; 38] is adopted here, whereby the voltage is set to zero when a prescribed amount of energy has been deposited. The effect of this modeling approach on the plasma discharge and on the ensuing non-equilibrium gas was investigated and explained in Chapter 3 (see Section 3.2). The energy deposited is monitored in time by integrating the total energy density $\rho\,\mathcal{E}$ over the entire computational domain.

5.2 Discharge phase

Streamer propagation during nanosecond discharges in the pin-to-pin electrode configuration have been studied and discussed extensively in previous studies [41; 97; 50; 98; 93]. In the following discussion, we provide only a brief summary of streamer propagation and focus instead on the stages immediately following the establishment of the conducting channel that enables large energy deposition into the gaseous mixture.

It is well established that the curvature at the pin tips induces large electric fields that lead to localized ionization and the accumulation of charged species as the applied voltage increases. Eventually, this leads to the "ignition" and propagation of an ionization wave, as seen in Fig. 5.2. A negative streamer, characterized by negative space charge at the head, propagates from the cathode in the direction of the anode, while a positive streamer, characterized by positive space charge at the head, propagates from the anode in the direction of the cathode (see Fig. 5.3). The two streamers are characterized by different electron densities, but both induce a strong electric field at the head and a near zero electric field in their wake. Streamer propagation and connection lasts a matter of nanoseconds, after which a conducting channel is established and the plasma channel is characterized by a nearly uniform reduced electric field strength.

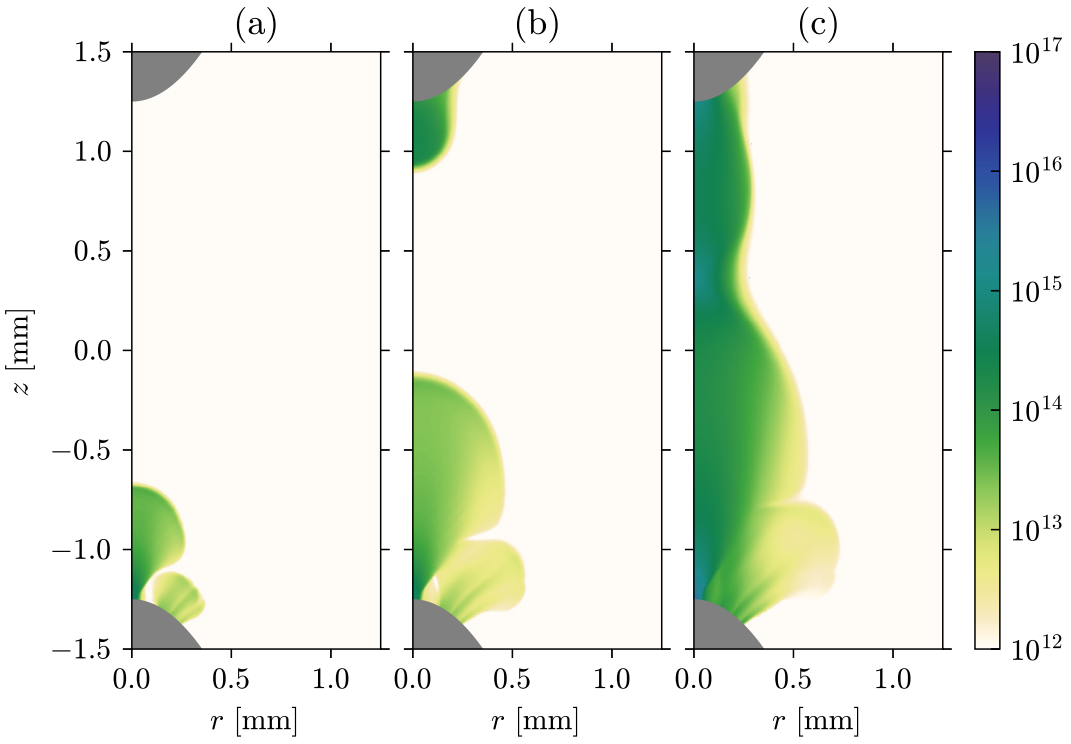

Figure 5.2: Number density of electrons [cm^{-3}] at (a) 4.1 ns, (b) 4.9 ns, and (c) 5.7 ns, showing the ignition and propagation of the positive streamer (from cathode at the bottom to anode at the top), negative streamer (from anode at the top to cathode at the bottom) and streamer connection, respectively.

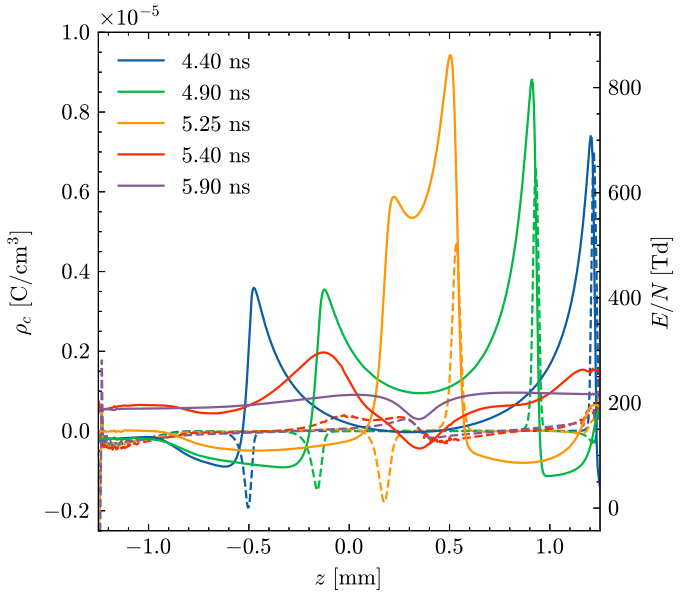

Figure 5.3: Reduced electric field streangth E/N (solid lines) and space charge density ρ_c (dashed lines) as a function of the axial coordinate z, illustrating the differences between the positive and negative streamer during propagation.

As far as the electrical aspects of a nanosecond capacitive discharge are concerned, the transition from streamer propagation to the formation of a conductive channel is very consequential. Initially, when charges are absent between the electrodes, the load is capacitive as current flows to the electrodes. When the plasma channel is established, the number density of electrons increases rapidly, which also increases the conductivity of the channel, allowing large currents to flow across the electrodes [99]. At this point, the load becomes resistive, and allows for significant energy deposition into the gaseous mixture.

Since the load resistance is a function of the instantaneous plasma state in the conducting plasma channel, there exist a strong coupling between the driving

circuit, current, and voltage. For example, the sudden increase in conductivity and current is accompanied by a rapid voltage drop. In this work, we do not consider the coupling between the incoming voltage pulse and plasma, rather we provide detailed electrical properties of the conducting channel as the plasma evolves in time during energy deposition, which concludes by 8 ns when 800 μJ are deposited into the gas. The temporal evolution of the number density of electrons and reduced electric field along the axis of symmetry ($r = 0$) and as a function of the distance on the midplane ($z = 0$) are presented after streamer connection in Fig. 5.4. The number density of electrons increases by an order of magnitude growing up to 10^{16} cm^{-3} by 8 ns, while the radius of the channel also increases significantly, until it reaches a value of roughly 200 to 250 μm by the end of the energy deposition. In experimental work by Xu et al. [9] and Rusterholtz et al. [22] at atmospheric conditions, discharge radii of 200 μm and 225 μm were reported in the middle of the gap. The space charge distribution induces an electric field that results in an overall electric field (applied field plus field induced by the space charge) that is nearly spatially uniform throughout the channel, offsetting the very high value of the applied electric field near the pin tips.

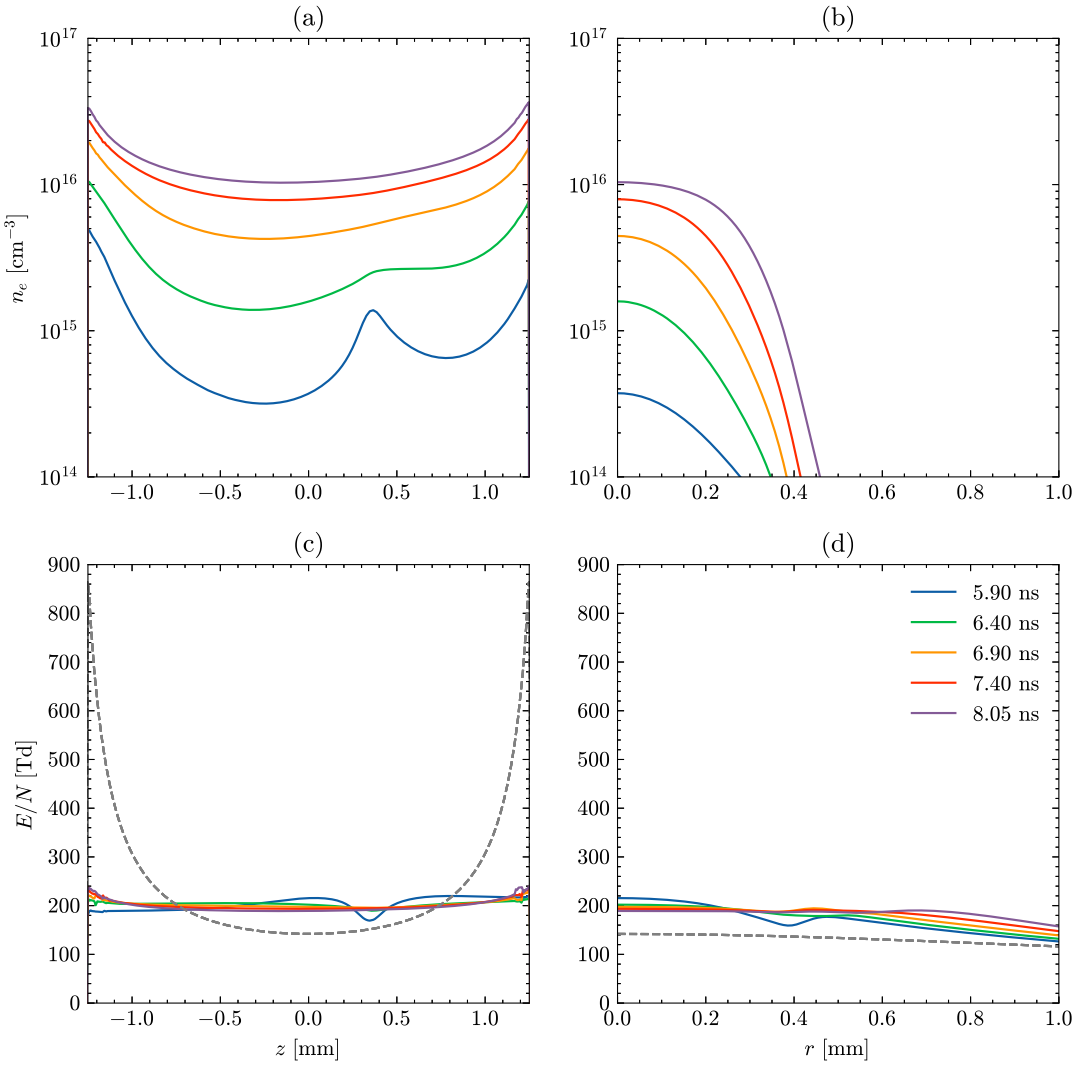

Figure 5.4: Number density of electrons n_e after streamer connection as a function of (a) axial coordinate along the axis and (b) radial coordinate at the midplane, illustrating growth by an order of magnitude, as well as an increase in the radius of the conducting channel. Reduced electric field as a function of (c) axial coordinate along the axis and (d) radial coordinate at the midplane shows a large induced electric field near the pin tips that offsets the applied electric field (gray dashed line). The resulting reduced electric field is nearly spatially uniform throughout the plasma channel.

Complementary plasma properties are presented in Fig. 5.5, where the mean electron energy is shown to increase up to 5 eV by 8 ns. The mean electron energy is radially uniform on the midplane up to a distance of about 600 μm when it starts decreasing, taking the value of 4 eV in the fringes at 1 mm from the axis.

The plasma conductivity peaks at 70 S/m by 8 ns on the axis of the plasma channel, rapidly decreasing to 10 S/m at a radial distance of 350 μm from the axis. Again, note that the plasma conductivity increases very rapidly through the energy deposition phase past streamer connection $5.9 \leq t \leq 8$ ns. The fact that the mean electron energy is nearly uniform in a large portion of the conducting channel suggests that similar energy branching is expected throughout the discharge channel for this particular configuration.

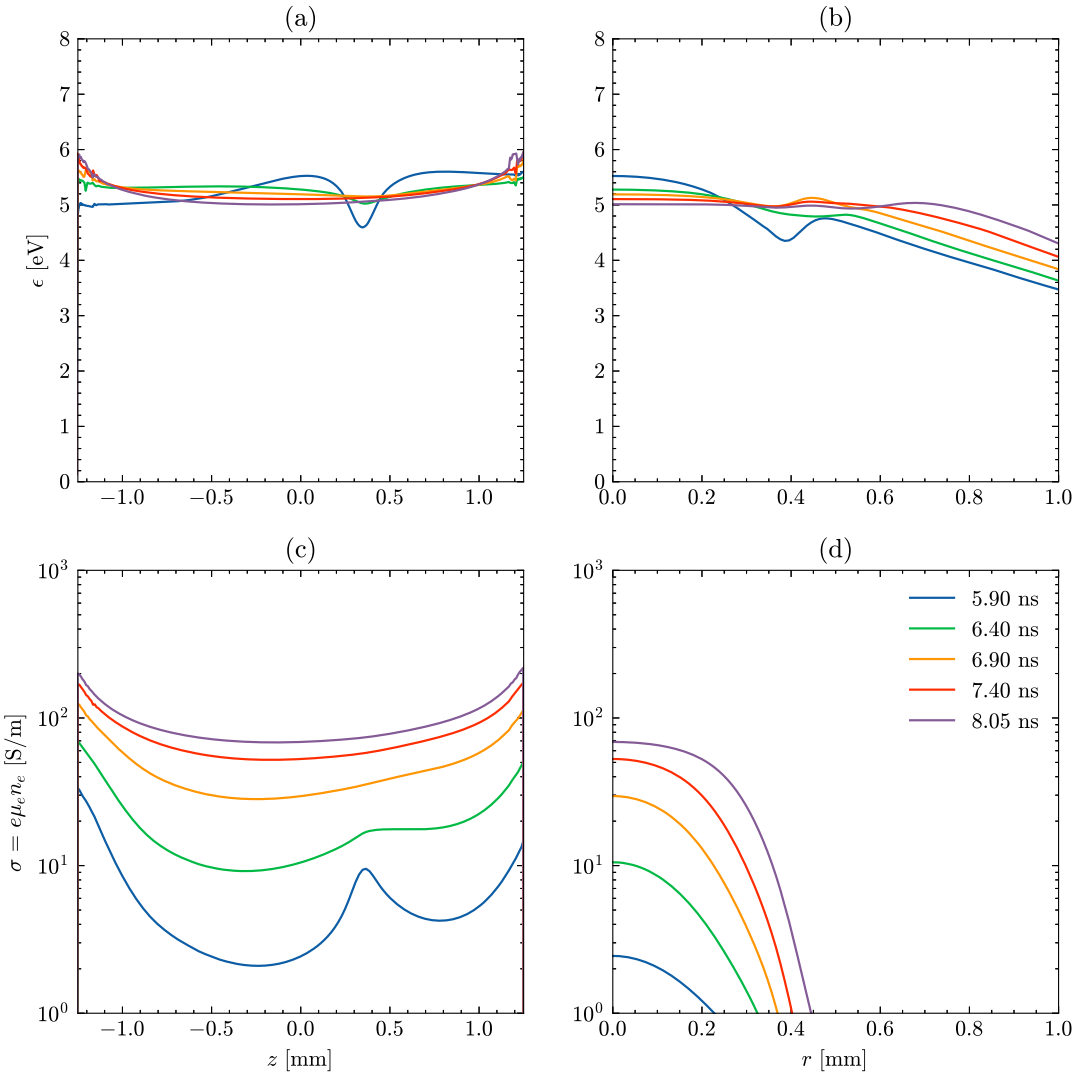

Figure 5.5: Mean electron energy ϵ as a function of (a) the axial coordinate along the axis and (b) radial coordinate at the midplane, ranging from 5 to 7 eV and consistent with the reduced electric field strength according to the local-field approximation. The conductivity is shown as a function of (c) the axial coordinate along the axis and (d) the radial coordinate at the midplane. Conductivity shows an increase proportional to the number density of electrons and highlights a significant change in the resistance offered by the plasma on nanosecond time scales, complicating the analysis of voltage and current waveforms.

A summary of the temporal evolution of the maximum values of electron density and reduced electric field strength as well as of their values on the axis at the midpoint of the electrode gap is provided in Fig. 5.6. In Fig. 5.6, we observe the rapid increase in the number density and reduced electric field as the applied voltage increases until the negative streamer "ignites" and begins propagating at time instant "A". The positive streamer "ignites" and propagates at time instant "B", and this process is accompanied by a plateau in the electron density. Streamer connection at time instant "C" is accompanied by a sudden increase in the peak E/N, which then decreases rapidly. Significant differences in the electrical properties of the plasma channel before and after connection as well as in the very fast timescales of energy deposition are well illustrated by the following observation pertaining to the data in Fig. 5.6. After 1.5 ns from streamer connection at instant "C," 10% of the total energy (or 80 μJ) has been deposited (time instant "D"). By time instant "E," the fraction has increased to 50% (or 400 μJ), so that an additional 40% (or 320 μJ) have been deposited in about 0.75 ns. Even more remarkable is the fact that the remaining 50% of energy is then deposited in 0.5 ns between instant "E" at 7.5 ns, and 8 ns when the energy target of 800 μJ is attained and the voltage is turned off.

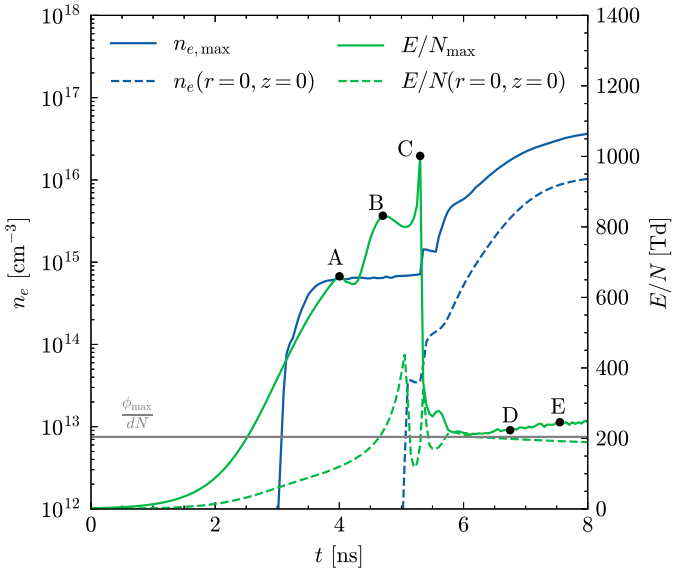

Figure 5.6: Overview of the discharge, including streamer propagation and energy deposition, showing the maximum electron density and maximum reduced electric field, along with the electron density and reduced electric field in axis in the middle of the gap as a function of time. Important events are highlighted throughout the discharge including "A" onset of the propagation of the negative streamer, "B" the onset of the propagation of the positive streamer, and "C" streamer connection. Event "D" denotes instant when 10% of the total energy has been deposited, and "E" denotes the deposition of 50% of the total energy. Notice the decreasing time required to deposit energy due to the rapidly increasing number density of electrons in the plasma channel.

The final state of the plasma channel is described by the spatial distributions of the number density of electrons, reduced electric field, and internal energy density when energy deposition ends at $t = 8.05$ ns. Data are presented in Fig. 5.7. The number density of electrons has grown by an order of magnitude with respect to streamer propagation (see Fig. 5.2), and is characterized by a nearly uniform reduced electric field, although the region where the electric field is uniform extends radially

outwards farther than that where the electron density is nearly uniform. The final internal energy density distribution shows a much larger energy density near the pin tips compared to the middle of the channel.

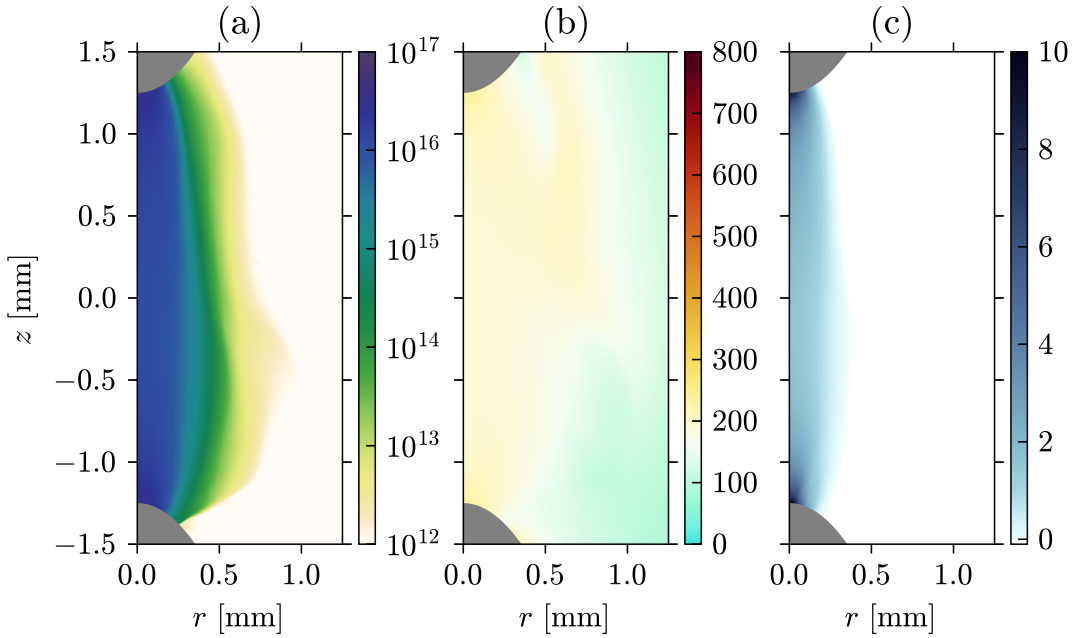

Figure 5.7: Spatial distribution of (a) number density of electrons [cm^{-3}], (b) reduced electric field [Td], and (c) internal energy density [J/mm^{-3}] at $t = 8.05$ ns. In this configuration, 800 μJ of energy have been deposited in the gaseous mixture.

The distribution of the energy density after the application of the nanosecond pulse is an important piece of information for when considering the evolution of the non-equilibrium gaseous mixture. In phenomenological models, for simplicity, it is commonly assumed that the energy distribution is only a function of the radius r [31; 13]. In Fig. 5.8, the normalized energy density is shown as a function of the axial coordinate along the axis and of the radial coordinate at three axial locations,

i.e., at the midplane and near the two electrode tips. The total energy density is normalized by $(\rho\mathcal{E})_{\text{ref}} = Q/V$, where Q is the known deposited energy (800 μJ) and V is a volume selected such that $\int_V (\rho\mathcal{E})/(\rho\mathcal{E})_{\text{ref}} dV = 1.0$. The initial energy density of the mixture is very small, and the total energy density can be interpreted as the overall energy density gain.

In this work, we calculated the cylindrical reference volume $V = d\pi r^2 = 0.12$ mm^3, using the gap length $d_{\text{gap}} = 2.5$ mm and a reference radius $r = 124$ μm. As shown in Fig. 5.8, the spatial distribution of $(\rho\mathcal{E})/(\rho\mathcal{E})_{\text{ref}}$ is highly inhomogeneous with significant axial and radial dependence. Near the pin tips, the energy density is about 5 times greater than that encountered in the middle of the gap (see Fig. 5.8(a)). Furthermore, the internal energy is distributed more narrowly near the pin tips compared to the middle of the gap, where the width of the energetic kernel is wider (see Fig. 5.8(b)). The role played by an inhomogeneous energy distribution compared to a uniform one will be further explored in later chapters.

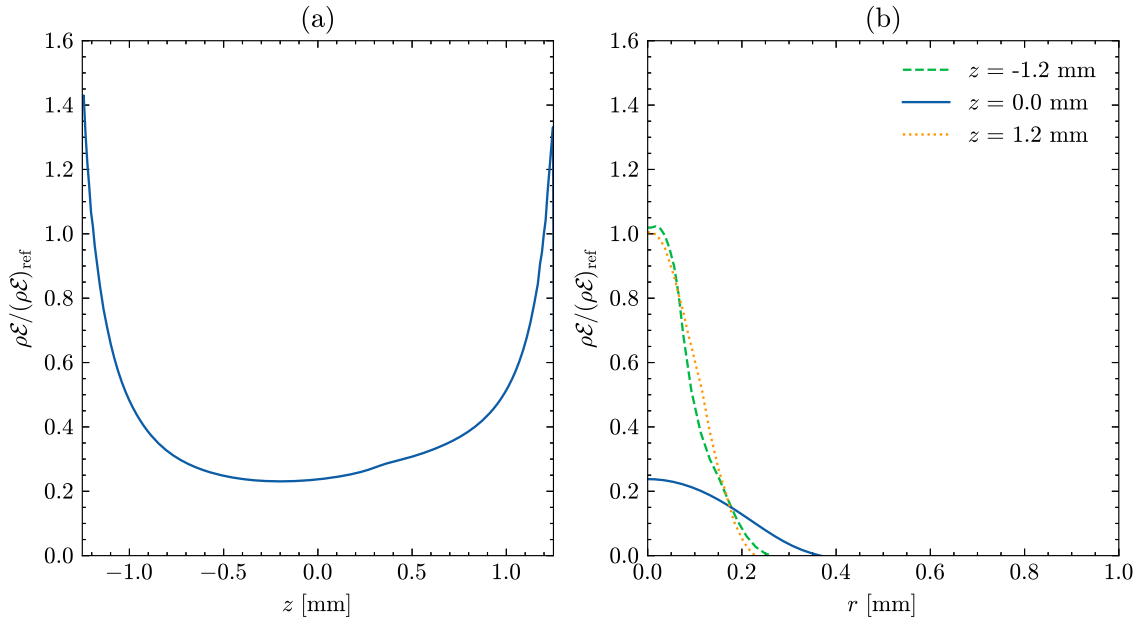

Figure 5.8: Normalized energy density $(\rho\mathcal{E})/(\rho\mathcal{E})_{\text{ref}}$ as a function of (a) the axial coordinate along the axis and (b) the radial coordinate at three different axial locations. The reference volume is selected such that the normalized energy density integrates to unity. The normalized internal energy distribution exhibits a significant dependence with respect to both radial and axial coordinates, with higher energy densities near the electrode tips. All data is shown at t =8.05 ns.

Next, an analysis of the state of non-equilibrium shortly after the discharge at time 8.05 ns is presented and data are shown in Fig. 5.9. The state of non-equilibrium is described by the equilibrium temperature and various other temperature metrics based on constrained equilibrium, which were introduced and discussed in Section 2.6 when applied to data from reactor simulations. Based on the spatial distribution of the gaseous mixture temperature and its equilibrium temperature (computed at constant enthalpy and pressure), the middle of the gap is characterized by a higher degree of non-equilibrium compared to near the pins. In other words, the state of

non-equilibrium is spatially inhomogeneous with the gas in the middle of the gap further away from thermal equilibrium. This is apparent in Fig. 5.9, where the translational/rotational temperature of the mixture is nearly 800 K lower than the equilibrium temperature ($T = 1000$ K compared to $T_{\rm eq} = 1700$ K), while at an axial distance of 0.05 mm away from the tips of anode and cathode, the temperature is only lower by 500 K ($T = 3700$ K compared to $T_{\rm eq} = 4200$ K). Moreover, it is also evident that the state of thermal non-equilibrium extends radially further at the midplane ($z = 0$) than near the pin tips. This spatial dependence is also consistent with that of the energy density shown in Fig. 5.8. The fact that the translational/rotational temperature is lower than the equilibrium one has important consequences for the value attained by pressure, as the overpressure engendered by the discharge drives the expansion process and attending hydrodynamics as discussed later in this Chapter.

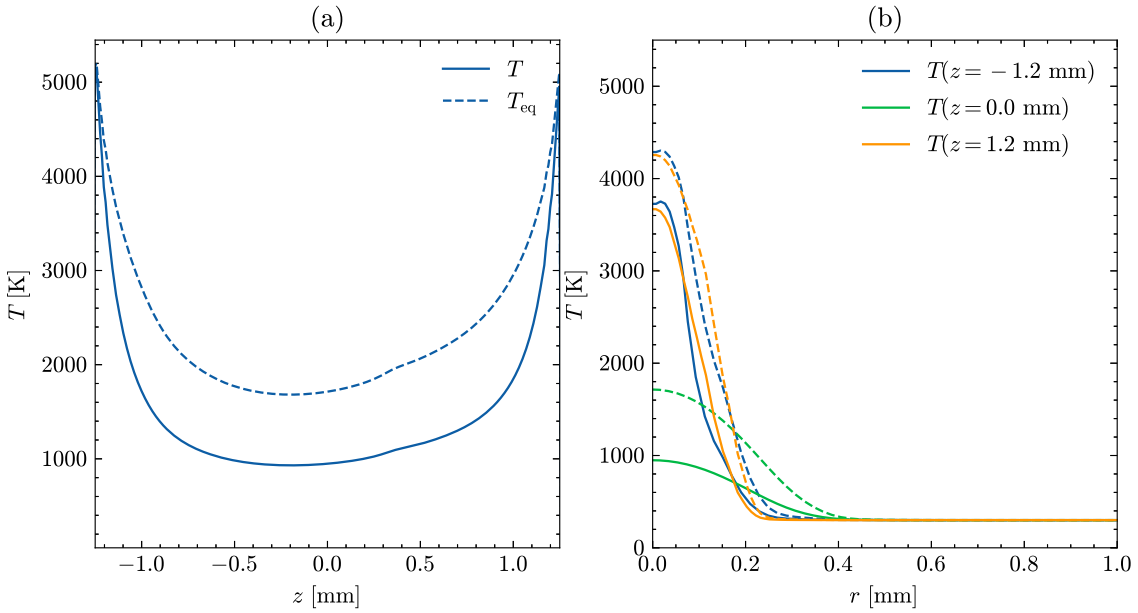

Figure 5.9: Temperature T (solid lines) and equilibrium temperature T_{eq} (dashed lines) assuming constant enthalpy/pressure as a function of (a) the axial coordinate along the axis and (b) the radial coordinate at three axial locations. Higher levels of non-equilibrium are observed in the middle of the gap compared to the region near the pin tips. All data shown at 8.05 ns.

5.3 Acoustic Phase

In the previous section, the isochoric energy deposition process was characterized and discussed in depth. Recall that the discharge deposited 800 μJ over a period of 8.05 ns. This process creates a kernel of non-equilibrium gases at an elevated pressure and temperature that proceeds to expand, as weak shock waves propagate into quiescent air. In Fig. 5.10, the spatial distribution of pressure throughout the initial stages of the expansion process is shown from 60 to 600 ns. At the earliest instant considered, pressure is consistent with the internal energy deposition as explored in

detail in the previous section, although masked in Fig. 5.10(a) due to the saturation of the colorscale. By 360 ns a shock structure consisting of stronger spherical shocks emanating from the pin tips and a weaker cylindrical shock emanating from the middle of the channel is apparent (see Fig. 5.10(b)). It is apparent that, following the outward propagation of the spherical shocks at the pin tips, a region of low pressure forms across the electrode gap. By 600 ns, pressure has decreased down to 0.25 atm at select locations across the gap as a consequence of the transient expansion. The corresponding local Mach number of the fluid at the same times is reported in Fig. 5.11, showing a similar structure, where the observed Mach number, based on the local velocity magnitude and temperature of the mixture, ranges from 0 to 1.2.

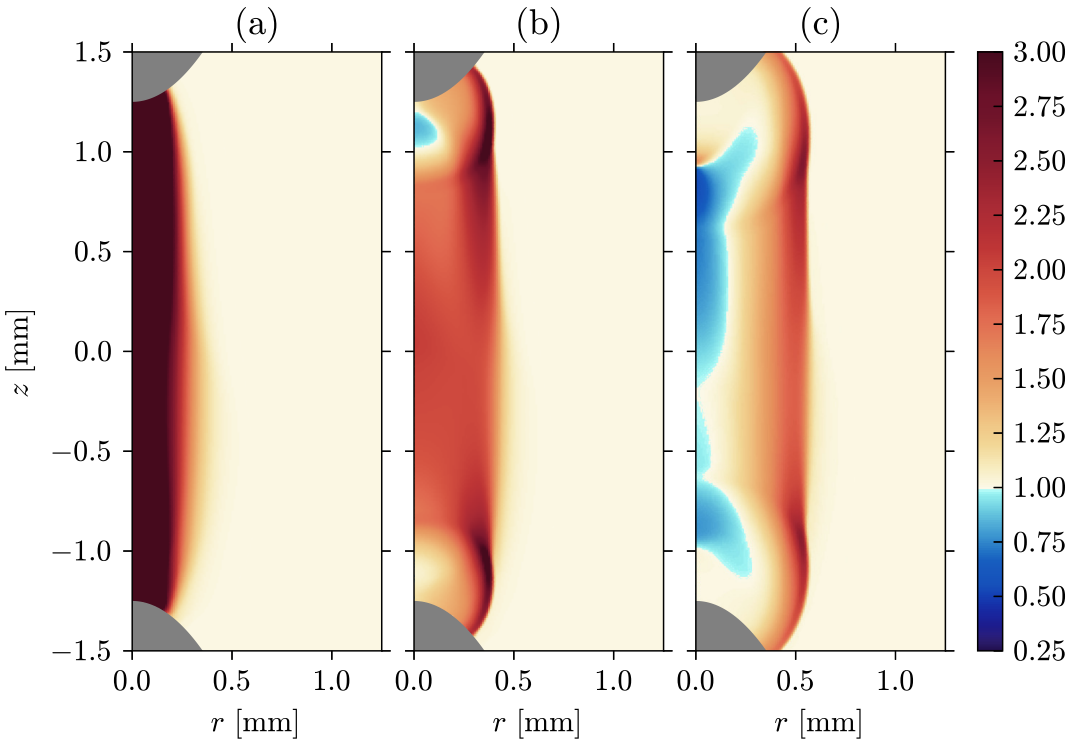

Figure 5.10: Spatial distribution of pressure [atm] during gas expansion at (a) 60 ns, (b) 360 ns, and (c) 600 ns. The shock structure consists of stronger spherical shocks emanating from the pin tips, and a weaker cylindrical shock emanating from the middle of the channel. Pressure in (a) is saturated by the colorscale.

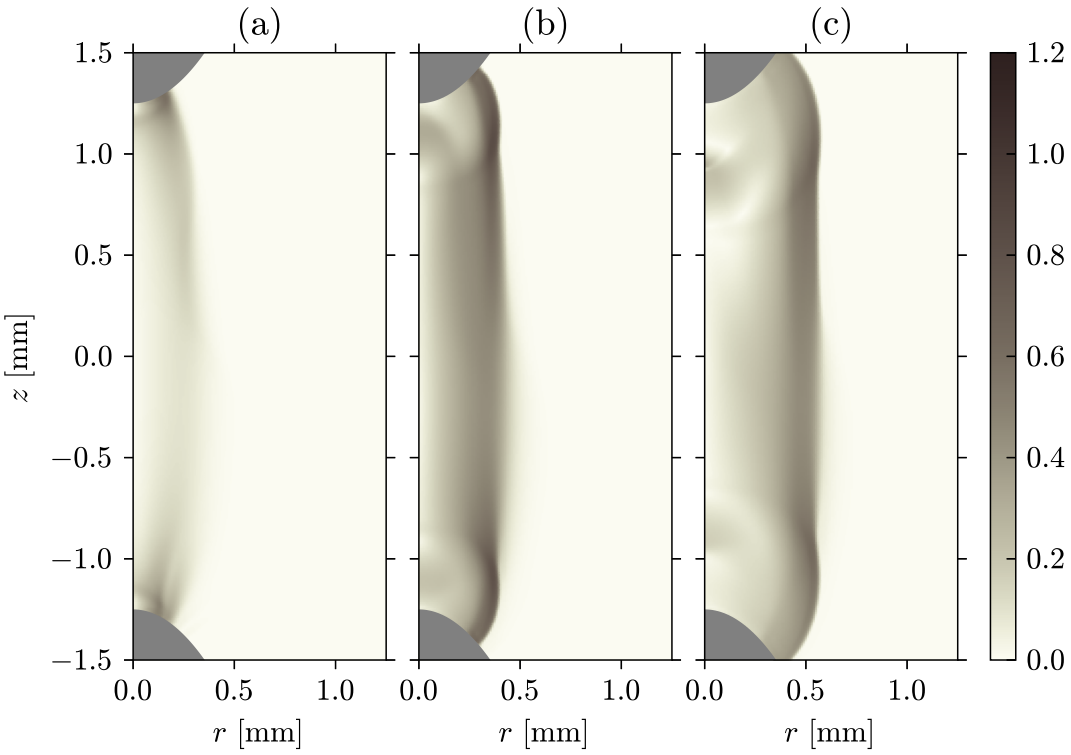

Figure 5.11: Local flow Mach number during the hot gas expansion process at (a) 60 ns, (b) 360 ns, and (c) 600 ns. The shock structure consists of stronger spherical shocks emanating from the pin tips, and a weaker cylindrical shock emanating from the middle of the channel.

More details on the expansion process are presented in Fig. 5.12, where the temperature, density, pressure and radial component of velocity are shown as function of the radial coordinate at the midplane ($z = 0$). At 0.06 μs, the density field is mostly uniform and pressure is equal to 4 atm in the middle of the gap, the maximum temperature is 1200 K and the radial component of velocity peaks at 50 m/s. From 0.06 μs to 0.6 μs the expansion process changes the structure of the heated channel rapidly. Initially, the heated channel expands along with the

shock, until the outward propagating cylindrical shock detaches around 0.6 μs. This process is quantified by radii r_A and r_B, which correspond to the radial location where the temperature increment relative to the background gas temperature T_0 is $0.607(T_{\max} - T_0)$, corresponding to the inflection point of a Gaussian kernel profile in the radial direction. The expansion process leads to the kernel growing in width from 0.19 mm at 0.06 μs to 0.33 mm at 0.6 μs, which corresponds to an increase by a factor of 3 of the heated cylindrical kernel volume. Thereafter, the width of the heated gas kernel does not change significantly over the following 1.4 μs, illustrating the role of convective transport engendered by the expansion process at this early phase compared to diffusive processes, which occur over longer time scales. By the end of the expansion, the density in the middle of the channel has decreased by a factor of 4 compared to the background one, and pressure is now slightly lower than that of the background gas. At 1.98 μs, the shock is located at a radial distance of about 1.15 mm from the axis as it continues to move outwards.

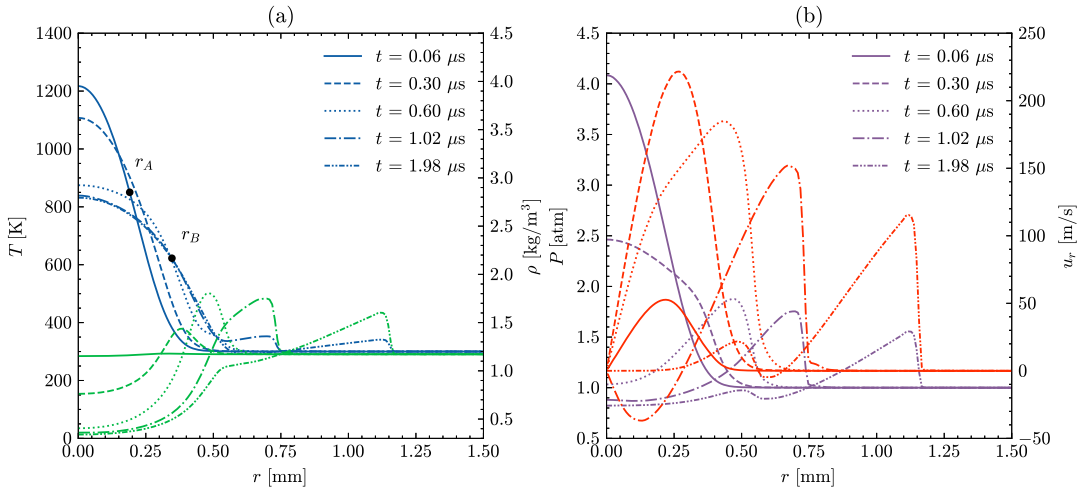

Figure 5.12: (a) Temperature (blue color line) and density (green color line), and (b) pressure (purple color line) and radial velocity (red color line) as a function of the radial coordinate in the middle of the electrode gap ($z = 0.0$ mm) from 0.06 μs to 1.98 μs. The measured radii $r_A = 0.19$ mm and $r_B = 0.33$ mm show the location where the temperature increment is $0.607(T_{\max} - T_0)$ at 0.06 μs and 1.02 μs respectively, illustrating the growth of the heated channel brought by gas expansion.

The early stages of the expansion are also significant. In the analysis that follows, constrained equilibrium is used as explained in detail in Section 2.6 in order to gain more insight into non-equilibrium following the plasma discharge. The constrained equilibrium approach summarizes the state of non-equilibrium, which requires a vector comprising the concentration of 21 species, with a set of 4 temperature increments. Fig. 5.13 reports the radial distribution of the 4 relevant temperatures at the midplane at 4 instants in time during the expansion process. In order to aid the reader in interpreting the temperature metrics, 4 temperature increments are marked in Fig. 5.13(a). ΔT_H denotes the difference between the background temperature and the translational/rotational temperature, and a measure of gas heating.

ΔT_V is the difference between the initial gas temperature and the constrained equilibrium temperature T_{vib}, obtained allowing only the vibrational states of N_2 to relax to equilibrium, and is nearly proportional to the energy stored in vibrationally excited states. Similarly, temperature increments ΔT_E and ΔT_C represents the energy stored in electronic and chemical (e.g., associated with dissociated O and N) non-equilibrium, respectively.

Immediately after energy deposition at 8.05 ns (see Fig. 5.13(a)) the peak equilibrium temperature on the gap midplane is equal to 1,700 K, i.e., 1400 K higher than the 300 K in the far-field. Of those 1,400 K, 650 K are reflected in the translational/rotational temperature, 100 K are associated with vibrational excitation, 500 K with electronic excitation, and 150 K with chemical non-equilibrium (dissociated O and N). By 60 ns, as shown in Fig. 5.13(b), the equilibrium temperature has increased by 50 K, which is due to energy transport from the regions near the pin tips towards the midplane. However, ΔT_H and ΔT_C have increased significantly, while ΔT_E has decreased during the afterglow phase, indicating that energy stored in electronically excited states has been transferred to heating (as reflected by the translational/rotational temperature of the gas) and dissociated molecules, in agreement with the analysis on data from isochoric reactor simulations presented in Chapter 2 and Ref. [31]. By the end of the expansion, the equilibrium temperature has decreased to 1400 K due to expansion and the translational/rotational temperature is 850 K, with further decrease of the energy stored in electronically excited states. The energy stored in vibrational excitation accounts for 100 K and the remaining 450 K are due to dissociated O and N.

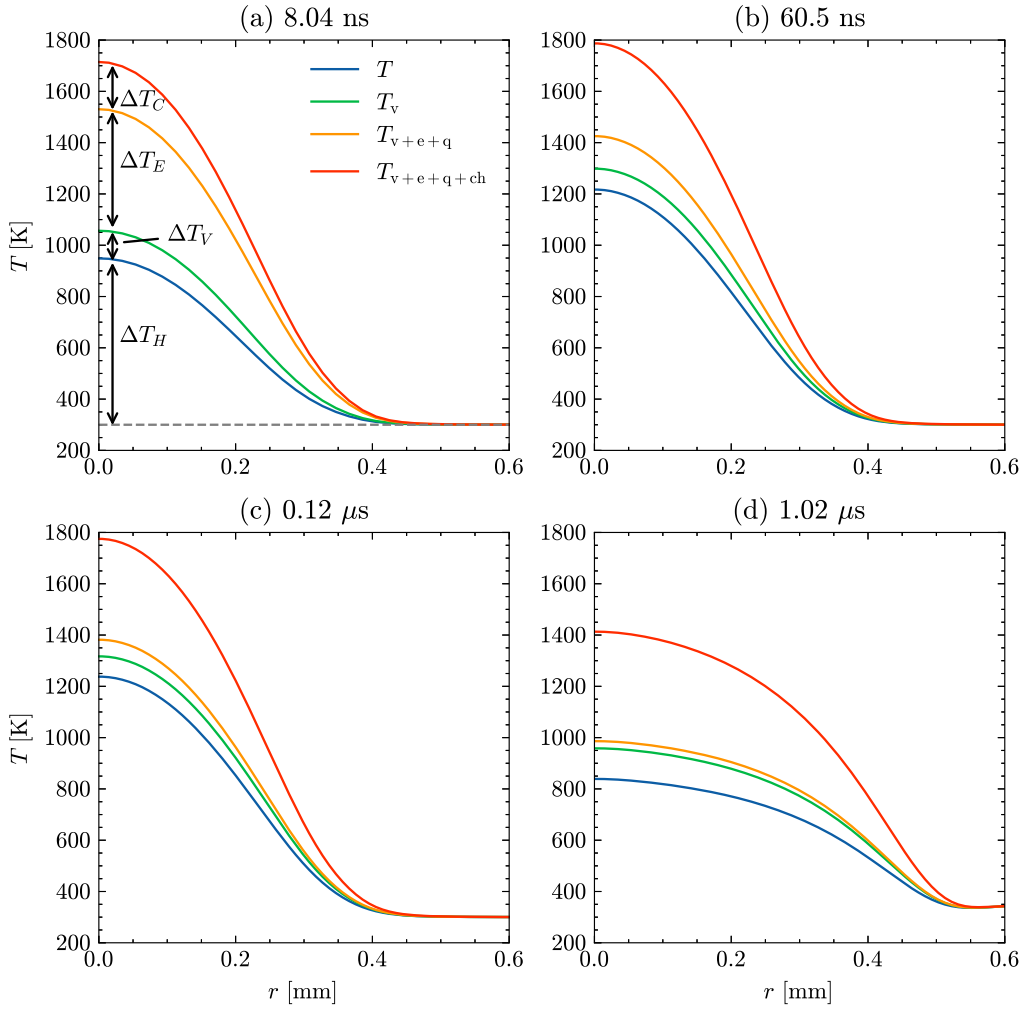

Figure 5.13: Constrained equilibrium temperature metrics as a function of the radial coordinate at the midplane ($z = 0$) calculated using the approach discussed in Section 2.6. $\Delta T_C, \Delta T_E, \Delta T_V, \Delta T_H$ represent temperature differences that can be mapped to energy stored in dissociated species (chemical non-equilibrium), electronically excited species, vibrationally excited species, and heating, respectively.

A more comprehensive picture of the state of non-equilibrium is provided by Fig. 5.14, where the four constrained equilibrium temperatures are shown as a

function of the axial location along the axis at two instants.

The data in Fig. 5.14(a) indicate that at 120 ns, the state of non-equilibrium of the gas near the pin tips is rather different from that on the midplane since the relative contributions to the equilibrium temperature by vibrational excitation, electronic excitation, and chemical non-equilibrium vary significantly depending on the axial coordinate. For example, close to the pins, the translational/rotational gas temperature T is highest (about 3600 K) and only 350 K below equilibrium. Furthermore, energy is solely stored in electronic excitation and charge dissociation. Conversely, on the midplane, the gas temperature is 1200 K and the equilibrium temperature is 1750 K, i.e., there is a potential for an increase in temperature by 550 K should the gas relax to thermal and chemical equilibrium. Moreover, based on the analysis, 400 K of such increase are due to chemical non-equilibrium (i.e., dissociated O and N), while the remaining 150 K are divided nearly equally among the other types of non-equilibrium.

After expansion at 1.02 μs (see Fig. 5.14(b)), the state of non-equilibrium is more spatially homogeneous across the gap. Note that very little energy is stored in vibrational modes (providing between 150 K and 250 K to the equilibrium temperature depending on axial location) and most of the non-equilibrium is chemical and due to dissociated O and N (responsible for 850 K at the pin tips and 450 K in the middle of the gap). Finally, notice that the equilibrium temperature is highest at the pin tips (about 3000 K compared to the gas temperature of 1850 K) and lowest on the midplane (about 1350 K compared to the gas temperature of 800 K).

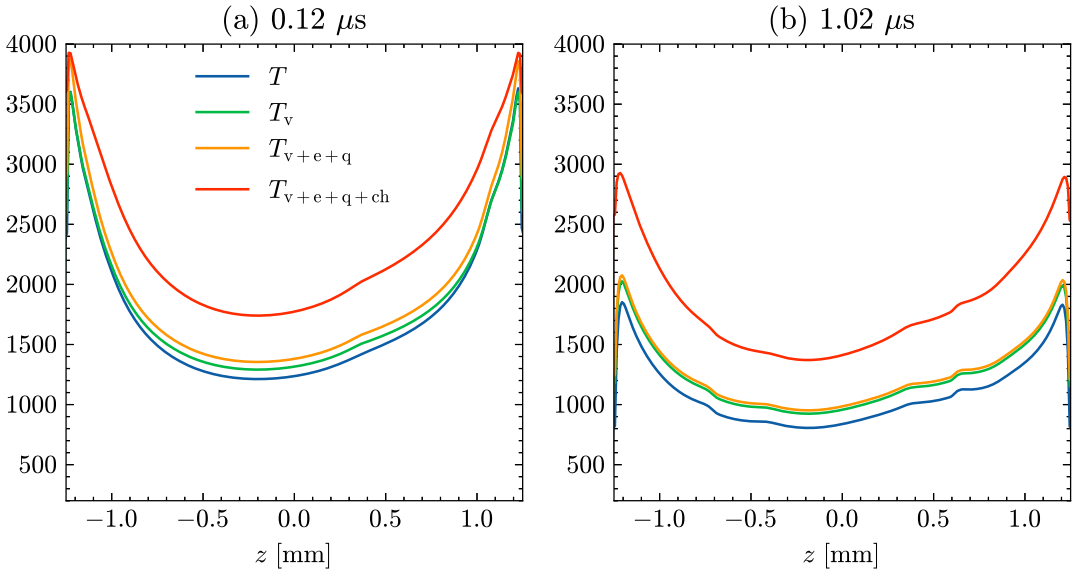

Figure 5.14: Constrained equilibrium temperature metrics along the axis as a function of the axial coordinate, calculated using the approach discussed in Section 2.6. The nature of non-equilibrium of the gas changes significantly before and after the hot gas kernel expansion.

The analysis presented thus far in this Chapter focused on energy deposition, expansion of the hot gas kernel, and its immediate aftermath. Following the expansion, a hot low-density kernel is left across the electrode gap. Cold gas entrainment and mass transfer ensue to fill the void left by the expanding fluid, eventually settling into two opposing jets that form a stagnation flow directed towards the axial midplane as seen in Fig. 5.15(a). As shown in Fig. 5.15(b), at 2 μs, the axial component of velocity is positive on the anode side and negative on the cathode side, indicating that fluid is moving away from the midplane towards the electrodes. Such a velocity distribution is entirely consistent with the late stages of the expansion process. At this instant, the pressure in the middle of the gap is equal to about 0.8 atm (see

Fig. 5.12(b)), i.e., still slightly below the background pressure of 1 atm. Such pressure distribution is a vestige of the earlier expansion process bringing pressures as low as 0.25 atm (see Fig. 5.10(c) where the pressure distribution is shown at 0.6 μs).

Conversely, shortly after, the pressure in the middle of the gap becomes equal to 1 atm and, sometime between 3 and 4 μs, the direction of the flow changes and cold gas flows from the region surrounding the pins towards the middle of the gap, giving rise to entrainment. During this second stage, the fluid velocity is dominated by low Mach number flow processes in that the low density region in the middle of the gap drives fluid flow. The axial velocity peaks at 6 μs, with maximum velocities of 35 m/s. At this stage in time, a thermal boundary layer around the electrode surfaces becomes apparent as shown in Fig. 5.15(b). By 8 μs, the thickness of the thermal boundary layer has grown to 0.25 mm (comparable to the radius of curvature of the pin tips) from about 0.05 mm at 2 μs when measured along the axis at the electrode tips. Note that during this interval, the temperature on the midplane increases by about 100 K from 850 K.

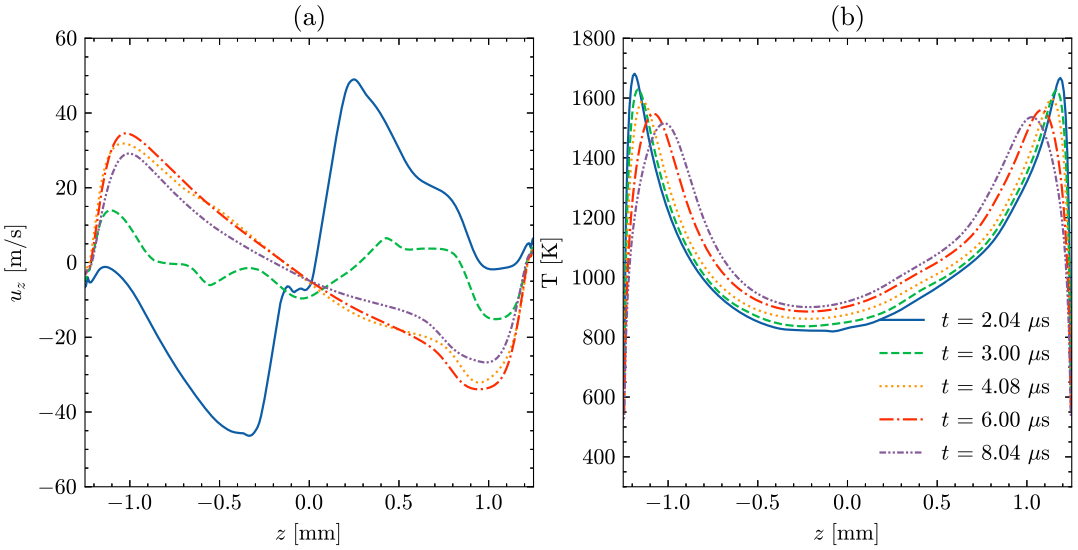

Figure 5.15: Spatial distribution of (a) axial component of velocity and (b) temperature along the axis as a function of the axial coordinate after the gas expansion. After the gap pressurizes, the flow eventually settles into opposing jets directed towards the middle of the gap.

The state of the gas once the pressure is equal to 1 atm across the entire region near the gap ($t = 8.05$ μs) is shown in Fig. 5.16, where the spatial distribution of pressure, temperature and axial component of velocity is reported. It is apparent that the gas near the pins is hotter when compared to that in the middle of the gap, as already shown in Fig. 5.15(b). Once again, we remark that numerical studies that assume cylindrical energy depositions that are solely a function of the radial coordinate, are unable to reproduce this important feature of the temperature field [12; 34; 13]. Vortical structures are present near the pin tips as studied in detail in other works [12; 100].

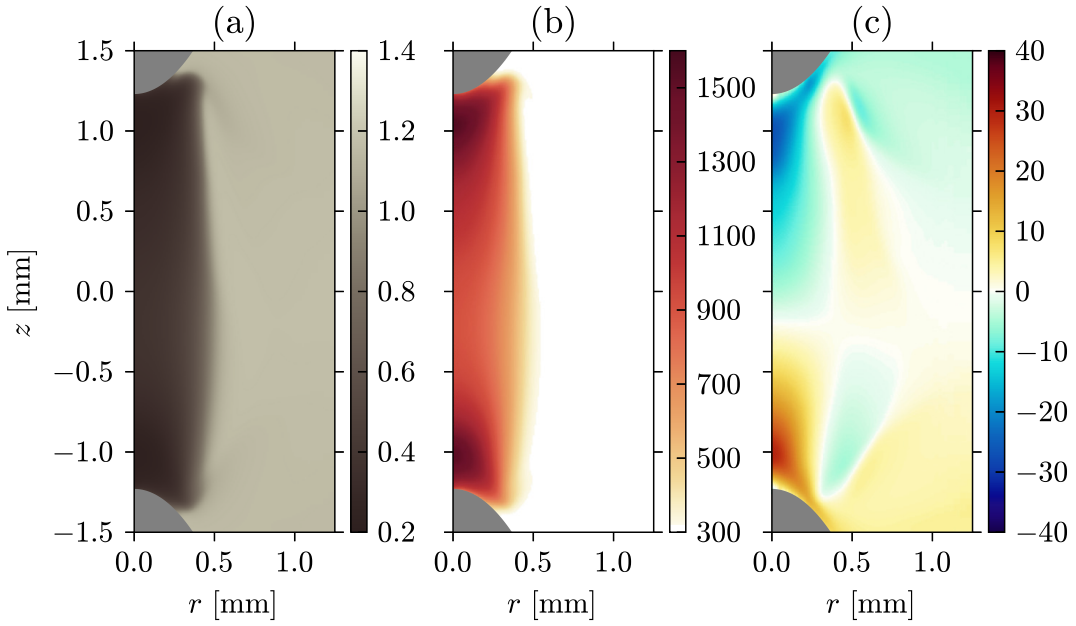

Figure 5.16: Spatial distribution of (a) density [kg/m^3], (b) temperature [K], and (c) axial component of velocity [m/s] after the pressure in the gap has returned to 1 atm at $t = 8.04$ μs. After the expansion process, the velocity field is consistent with a stagnation flow directed towards the midplane that convects top and bottom hot gas pockets from the pin tips towards the middle of the gap, leading to the so-called toroidal collapse.

5.3.1 Energy and mass losses

By the end of the expansion phase, a hot gas kernel at a high temperature, low density, and pressure equal to the original background pressure is left in the electrode gap. The thermodynamic state of the gas in the kernel implies that there is a loss of energy and mass compared to the original state immediately after the deposition of electrical energy. In this Section, a quantitative analysis of the loss of energy and mass incurred during the acoustic phase is provided.

The analysis requires the definition of two control volumes: the first control volume ("A") corresponds to the entire computational domain, and the second control volume ("B") is cylindrical in shape. The cylinder's axis is aligned with the axis of the electrodes and its height and radius are equal to 3.5 mm and 1 mm, respectively. The total energy density in these two volumes are integrated, and their values shortly after the discharge are subtracted to emphasize changes in the energy contained in the control volumes and then shown in Fig. 5.17(a). The same procedure is applied to mass by integrating the gas density.

The differential total energy contained in both control volumes is initially equal to 800 μJ, corresponding to the target deposited energy. Total energy in the domain $E_A(t)$ decreases steadily due to loss to the electrodes by conduction. By 8 μs, the losses amount to 16 μJ out of the 800 μJ deposited (or 2%). Between 2 and 6 μs, the total energy in control volume "B," which corresponds to the electrode gap area, decreases below that in the entire domain $E_A(t)$. This occurrence is due to the weak shocks moving out of control volume "B" and the difference $E_A(t) - E_B(t)$ represents the energy that is lost by the gaseous mixture in the region near the electrodes during the expansion process. By 8 μs, the difference is equal to 56 μJ (7% of the 800 μJ deposited) and is labeled as ΔE_{exp} in Fig. 5.17(a). Considering the two losses to the electrodes by conduction and to the expansion process, the total energy remaining in the electrode gap region is 742 μJ or 92% of the electrical energy deposited.

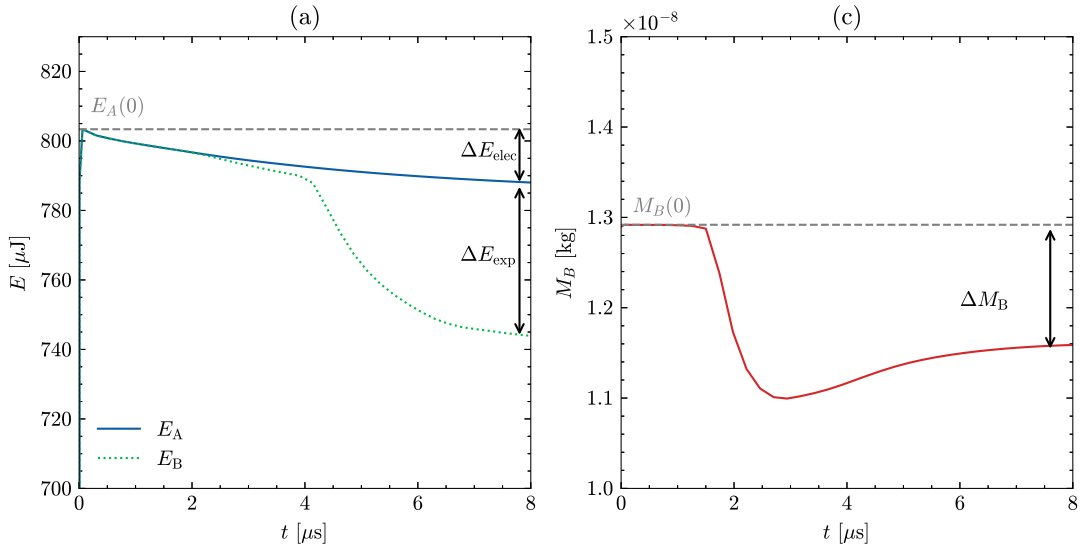

Figure 5.17: (a) Total energy in volumes "A" (full domain) and "B" (height 3.5 mm and radius 1.0 mm aligned with the electrodes' axis) showing the loss of energy to the cold electrodes $\Delta E_{\text{elec}} = 16$ μJ and to the expansion process $\Delta E_{\text{exp}} = 56$ μJ. (b) Total mass inside volume "B" showing a mass loss ΔM_B corresponding to 10% of the original mass.

Finally, Fig. 5.17(b) reports the mass inside control volume "B," representing the mass in the electrode gap region. It is apparent that the expansion process moves mass out of the gap region. Recall that by the end of the expansion, pressure returns to the background value but the temperature of the gas in the gap is higher and its density lower. It is interesting to note that the temporal evolution of $M_B(t)$ is not monotonic, rather the mass in the gap region attains a local minimum rapidly at 3 μs before increasing slowly. This behavior is consistent with the axial component of velocity shown in Fig. 5.15 and Fig. 5.16 whereby early on fluid flows away from the midplane and later fluid is entrained into the gap region.

By 3 μs the expansion process brings about a 15% mass loss and by 8 μs, the loss is back to 10% of the initial mass $M_B(0)$.

In summary, the picture that emerges from the analysis discussed above and presented in Fig. 5.17 support the conclusion that, for this particular configuration and choice of control volumes, about 11% of the total energy deposited in the electrode gap region (defined as a cylinder of height 3.5 mm and radius 1.0 mm aligned with the electodes' axis) is lost to conduction to the cold electrodes (2%) and to the expansion process (9%). Furthermore, about 10% of the mass in the same electrode gap region is lost also by 8 μs.

5.4 Toroidal collapse

As shown in Fig. 5.15(b), the temperature field presents two local maxima near the electrode tips. As time progresses, cold fluid entrained from the region around the electrodes pushes these two pockets of hot gases towards the midplane. This is shown in Fig. 5.18 from $t = 50$ μs to 200 μs. If the entrainment velocity is sufficiently high and/or the gap distance is sufficiently small, the motion of the hot pockets of gas is dominated by advective transport, eventually causing them to collapse into a toroidal structure as observed in Fig. 5.18(c). This process, which is usually referred to as "toroidal collapse" has been reported in numerical and experimental studies throughout the literature [12; 32; 101]. It has been reported that, for wider gaps and/or lower velocities, the toroidal collapse does not occur and the hot gas kernel retains its cylindrical shape as diffusive processes lead to its slow widening instead. Note also that vortical structures active off-axis near the pin tips lead

to the roll-up of the temperature field, while entrained gases flow on the surface of the electrodes towards the midplane. The phenomena and mechanisms controlling toroidal collapse have been at the center of an ongoing discussion in the literature [100; 12] and will be further addressed quantitatively in later chapters so that here only a bfrief overview is presented.

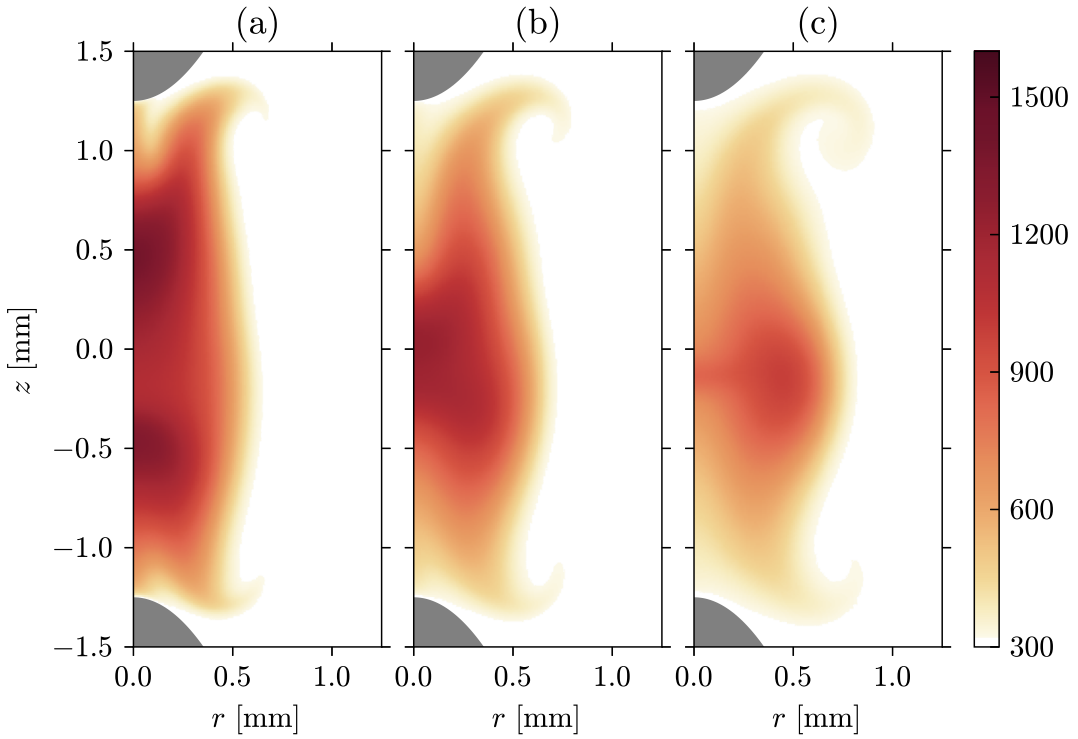

Figure 5.18: Spatial distribution of the temperature field [K] at (a) 50 μs, (b) 100 μs, and (c) 200 μs. The two pockets of hot gases near the anode and cathode tips are pushed towards the axial midplane by the stagnation flow, eventually resulting in toroidal collapse observed as shown at 200 μs.

The spatial distribution of temperature and axial component of velocity are shown as a function of the axial coordinate along the axis and of the radial coordinate

at the midplane for various instants in Fig. 5.19. The two pockets of hot gases move towards the midplane until they merge between 50 and 100 μs, as the torus forms between 100 and 150 μs. It is also apparent that the flow field is not symmetric with respect to the midplane and the stagnation point lies on the cathode side, consistent with slightly higher velocities on the anode side and more robust entrainment. By the time of the toroidal collapse at 0.2 ms, the width of the hot gas kernel at the midplane extends outwards radially by nearly 1 mm. The radial profile in Fig. 5.19(b) shows also that the temperature admits a local maximum at 0.5 mm, where it is equal to nearly 1000 K.

During the same interval, the axial component of velocity remains nearly along the axis while its magnitude decreases (see Fig. 5.19(c)). By 200 μs, the peak value of u_z has decreased to about 10 m/s. Also, the fluid is left nearly undisturbed past a radial distance of about 0.4 mm at the midplane (see Fig. 5.19(d)).

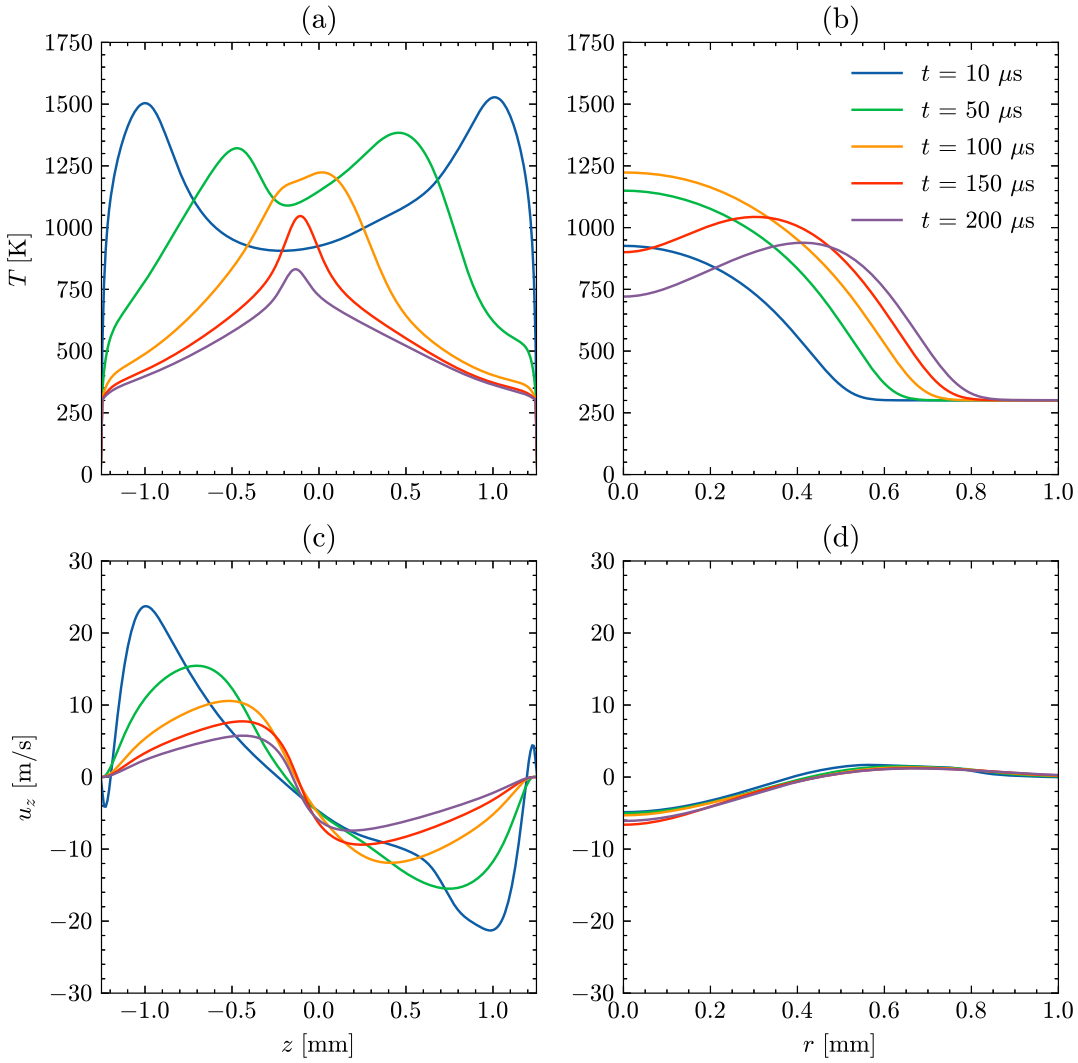

Figure 5.19: Temperature T as a function of (a) the axial coordinate along the axis and (b) the radial coordinate at the midplane ($z = 0$). Axial component of velocity u_z as a function of (c) the axial coordinate along the axis and (d) the radial coordinate at the midplane ($z = 0$).

5.5 Second pulse

The successful ignition of an air/fuel mixture using nanosecond discharges for ignition usually requires multiple pulses, with frequencies ranging from 5 to 200 kHz. In this section, a second nanosecond voltage pulse is applied after 200 μs from the first, corresponding to a pulse repetition frequency of 5 kHz. The second voltage waveform is identical to the first and 0.8 mJ of energy are deposited by 3.6 ns on the account of a faster streamer ignition and connection compared to the first pulse.

Figure 5.20(a) shows the electron density at 2.8 ns from the onset of the second pulse, as the positive and negative streamers are about to connect and establish a conducting channel. At the time of the second nanosecond discharge, a region of elevated temperature generated by the first pulse and subsequent toroidal collapse is located near the axis (see Fig. 5.18 and Fig. 5.19).

Temperature stratification is associated wih gas density inhomogeneities, which change the local reduced electric field strength. As the density decreases, the reduced electric field increases, which tends to guide streamers towards regions of low density. As shown in Fig. 5.20(b) and Fig. 5.20(c), the streamers propagate off-axis and this behavior reproduced by the numerical simulation is qualitatively consistent with experimental data by Adams et al. [94], who reported that the path taken by a second plasma discharge depends on the interval between pulses. For intermediate values of inter-pulse times, which allowed the hot kernel generated by the first pulse to move radially outwards, yet not disappear, the authors [94] reported streamers propagating off-axis around the hot kernel left behind by the previous pulse.

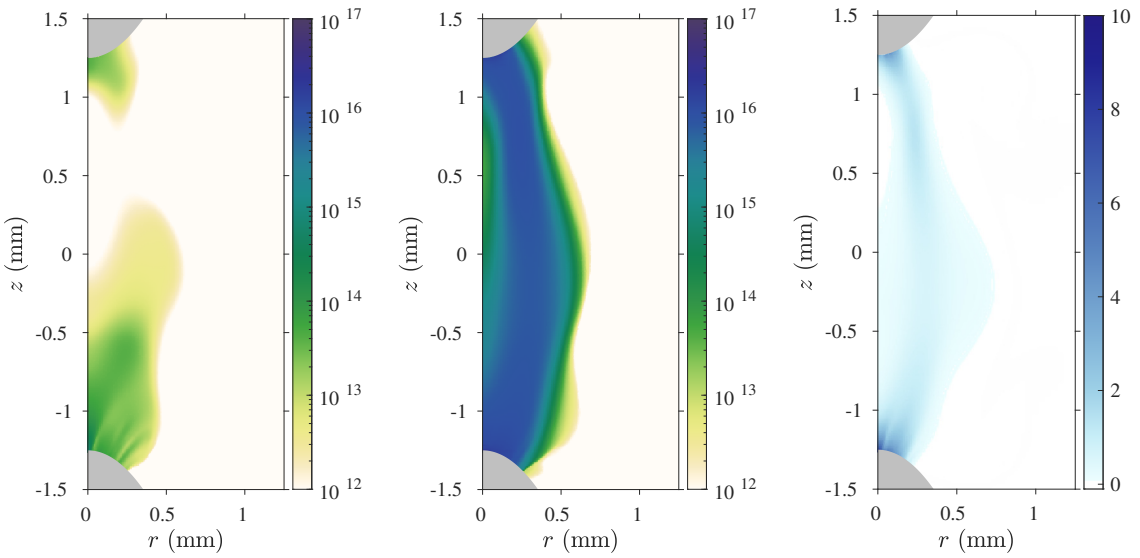

(a) n_e [cm^{-3}], 2.8 ns (b) n_e [cm^{-3}], 3.6 ns (c) U [J/cm^3], 3.6 ns

Figure 5.20: Visualization of the discharge phase of a second nanosecond voltage pulse in atmospheric air (1 atm and 300 K). (a) Number density of electrons shows off-axis propagation induced by the low-density/high temperature region created by the previous pulse. (b) The number density of electrons and (c) internal energy per unit volume at the end of energy deposition show very different energy profile compared to the first pulse, and occupy a larger volume.

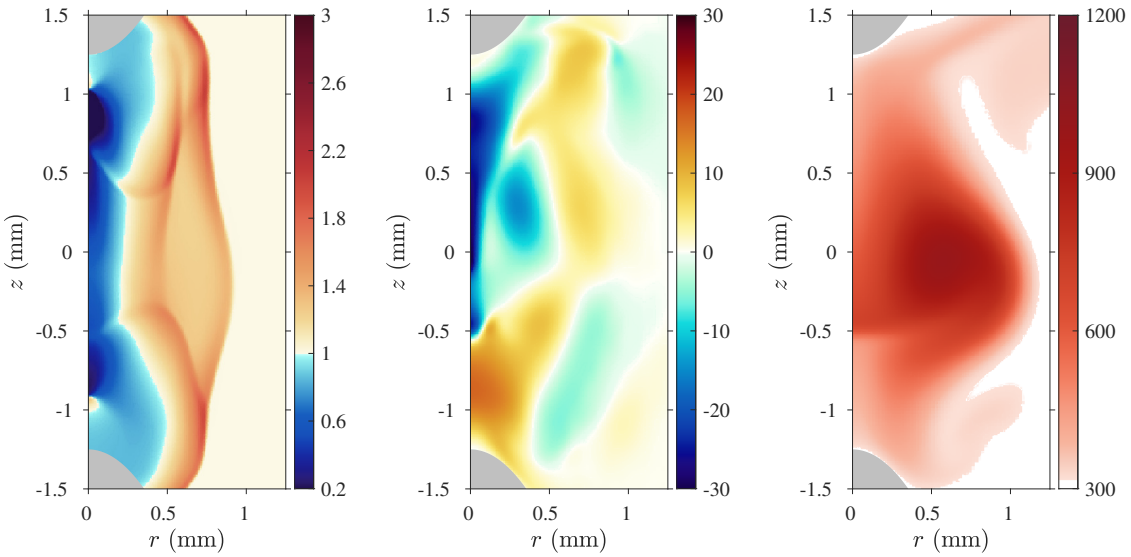

(a) p [atm], 0.75 μs (b) u_z [m/s], 25 μs (c) T [K], 200 μs

Figure 5.21: Visualization of processes following a second nanosecond voltage pulse in atmospheric air (1 atm and 300 K). (a) The pressure field at 0.75 μs shows a more complex shock system compared to the first pulse. (b) Following the depressurization of the plasma channel, a stagnation flow (shown at 25 μs) leads to the collapse of the hot gases into a second torus overlapping with the one generated by the first pulse. (c) The temperature field at 200 μs demonstrates that the second discharge pulse engenders heating of the air over a larger volume compared to the first.

Following the depressurization of the off-axis channel, which gives rise to a distinctly different expansion process compared to the first pulse (see Fig. 5.7), the ensuing stagnation flow (see Fig. 5.21) induces the collapse of the hot kernel into a compact region of hot gases, which occupies a larger volume than the first, extending radially further away from the axis as apparent comparing the temperature fields in Fig. 5.18 to that in Fig. 5.21, both shown at 200 μs from the discharge.

Energy deposition away from the axis results in the volume affected by the second nanosecond plasma discharge being significantly larger than the first by about 33% (based on the volume contained within an isosurface of temperature equal to 400 K for the first pulse, and 800 K for the second pulse). Because the same 0.8 mJ are deposited as in the first pulse, the energy density is lower in the second pulse, although the volume of heated gases is larger.

Based on the case study discussed above, it is clear that the detailed simulation of nanosecond plasma discharges, including that of the propagation of streamers, is needed in order to describe the location of energy deposition and the shape of the kernel of hot gases accurately, especially in the case of ignition by repeated discharge pulses or in the case of flows with density stratification due to turbulent mixing.

In the results presented thus far, the quarter-periodic domain and spatially uniform initial conditions facilitate the parametrization of the results as axisymmetric. Throughout the discharge, minor perturbations in the azimuthal angle direction have been observed for certain conditions, challenging the presumption of axisymmetry implied by the presentation of the results. For a second pulse, the results presented in the work by Adams et al. [94] suggest that a strong degree of axisym-

metry remains, as evidenced by the streamers creating a prolate spheroid as reported by the authors themselves [94]. As more pulses are applied, three dimensional effects become prominent [27], implying that, at some point, the quarter-periodic domain used thus far will become inadequate.

Chapter 6

Hydrodynamics: Simplified Model

In this Chapter, we present a first application of dimensional analysis to the formulation of a generalizable theory for the hydrodynamic effect induced by nanosecond discharges. The approach presented in this Chapter follows ideas proposed in Refs. [13; 31]. In this simplified configuration, the nanosecond discharge is not modeled, rather its effect is approximated by prescribing elevated pressure and temperature consistent with isochoric thermal heating. The size of the cylindrical kernel of pressurized and heated gases is generally approximated from experimental measurements. Diffusive and viscous effects in the bulk and also those associated with the presence of the pin electrodes are neglected in this Chapter as well. The objectives of the study presented in this Chapter are as follows:

- Establish similarities and differences between simplified configurations and modeling approaches (e.g., neglecting the discharge altogether) and realistic high-fidelity modeling.
- Leverage a best-case scenario to demonstrate self-similarity using proposed dimensionless parameters.
- Explore the effects of varying the dimensionless parameters and characterize

their effect on the duration of the acoustic phase and on the induced velocity at the end of kernel expansion.

6.1 Configuration

We begin by presenting the simplified configuration. The treatment of the problem is similar to the one introduced in Chapter 5, and is shown schematically in Fig. 6.1. Simulations are executed in a Cartesian cubic domain and boundary conditions chosen so that the solution is axisymmetric, and in post-processing, the axisymmetric fields are indexed in cylindrical coordinates. The base mesh of the cubic domain consists of 32^3 control volumes across a cube of side 5 mm, yielding a base resolution $\Delta_0 = 5$ mm/ $32 \approx 160$ μm. Up to 3 additional levels of refinement are used for a minimum resolution of ≈ 20 μm. Note that studies that use phenomenological models commonly use resolutions between 15 and 25 μm [12; 35; 31]. Local refinement is driven by differences between field values across two adjacent cells in temperature and pressure. A cell is refined if there is maximum difference of 2000 Pa across adjacent cells up to AMR Level 3 (≈ 20 μm), or if there is a maximum difference of 75 K across adjacent cells up to AMR Level 3 (≈ 20 μm).

Symmetry boundary conditions are applied at bounding surfaces labeled "1" to take advantage of the radial and axial symmetry of the configuration. At bounding surfaces labeled "2", we apply a non-reflective subsonic outflow boundary condition [17]. Pressure is imposed at the boundary and all other flow variables are extrapolated from the interior in order to avoid reflection of the outgoing pressure waves.

More details are presented in Fig. 6.2, where the background energy density is

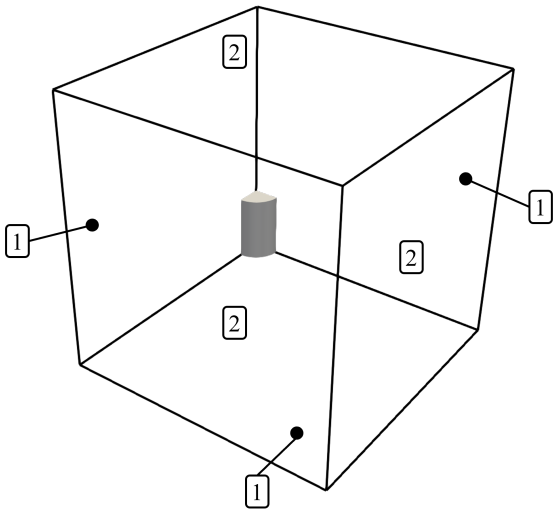

Figure 6.1: Cubic computational domain with a cylinder representing the approximate size of the hot gas kernel used to initialize the flow field in this simplified configuration. Symmetry boundary conditions are imposed on surfaces labeled "1", while non-reflective subsonic outflow boundary conditions [17] are imposed at surfaces labeled "2".

increased uniformly inside a cylindrical kernel of vertical height d, and radius r_0. We take advantage of the symmetry around the axis and the symmetry in the axial plane, with the domain representing one eighth of the full domain. We define an energy density ρe_{avg} as the energy deposited Q divided by the volume of a nominal cylindrical kernel $V = \pi r_0^2 d$, with r_0 and d being the radius and length of the cylindrical kernel, respectively. Mathematically, we define a dimensionless energy kernel function that represents deposition in a cylindrical region

$$\mathcal{F}(r,z) = \frac{1}{1+\exp\{(r-r_0)/\sigma_0\}} \frac{1}{1+\exp\{(|z|-0.475d)/\sigma_0\}}, \tag{6.1}$$

where σ_0 is a parameter that controls the thickness of the transition layers. Assuming a quiescent background gas at pressure P_0 and density ρ_0, the energy density of the background gas is $\rho e_0 = f(\rho_0, P_0, T_0)$. The initial energy density is prescribed as $\rho e(r,z) = \rho e_0 + \rho e_{\text{avg}} \mathcal{F}(r,z)$. The density remains unchanged, resulting in an isochoric increase in temperature and pressure inside the cylindrical kernel.

An example of the initialization procedure is shown in Fig. 6.2 with $r_0 = 150$ μm, $\sigma_0 = 25\mu$m, and $d = 2.5$ mm. The volumetric integral of the kernel function in Eq. (6.1) $\int_{\mathcal{V}} \mathcal{F}(r,z)\, d\mathcal{V}$ is within 2% of the volume of the cylinder on the account of the added transition layers. The energy deposited Q takes values from 0.1 to 6.0 mJ consistent with the literature [8; 11; 12; 100].

6.2 Dimensional Analysis: Simplified model

The proposed configuration is parametrized by the following variables: deposited energy Q, background density and pressure ρ_0 and P_0, cylinder height d,

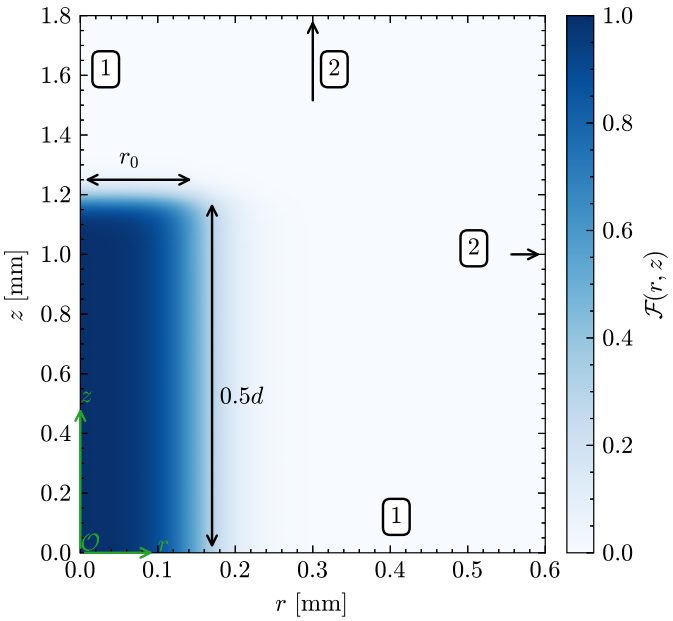

Figure 6.2: Example of the spatial distribution of the normalized energy using Eq. (6.1) with $r_0 = 150$ μm, $d = 2.5$ mm, and $\sigma_0 = 25$ μm. Bounding surfaces "1" and "2" from Fig. 6.1 are labeled relative to the normalized energy kernel.

cylinder radius r_0, and transition layer thickness σ_0. The dimensions of the parameters in the MLT class of systems of units are:

$$[Q] = ML^2T^{-2}, \tag{6.2}$$

$$[\rho_0] = ML^{-3}, \tag{6.3}$$

$$[P_0] = ML^{-1}T^{-2}, \tag{6.4}$$

$$[d] = L, \tag{6.5}$$

$$[r_0] = L, \tag{6.6}$$

$$[\sigma_0] = L. \tag{6.7}$$

In addition to the configuration parameters, we define coordinate $\boldsymbol{x}$, time t, density ρ, pressure P, and velocity $\boldsymbol{u}$ with dimensions

$$[\boldsymbol{x}] = L, \tag{6.8}$$

$$[t] = T, \tag{6.9}$$

$$[\rho] = ML^{-3}, \tag{6.10}$$

$$[P] = ML^{-1}T^{-2}, \tag{6.11}$$

$$[\boldsymbol{u}] = LT^{-1}. \tag{6.12}$$

Configuration parameters ρ_0, r_0, d, and Q are used to define reference scales

$$\mathcal{M} = \rho_0 r_0^2 d, \tag{6.13}$$

$$\mathcal{L} = d, \tag{6.14}$$

$$\mathcal{T} = r_0^2 \sqrt{\frac{\rho_0 d}{Q}}. \tag{6.15}$$

Finally, the reference scales are used to obtain the dimensionless input parameters

$$\hat{Q} = \left(\frac{r_0}{d}\right)^2 = \Pi_1^2, \tag{6.16}$$

$$\hat{\rho}_0 = \left(\frac{d}{r_0}\right)^2 = \Pi_1^{-2}, \tag{6.17}$$

$$\hat{P}_0 = \frac{P_0 r_0^2 d}{Q} = \Pi_2^{-1}, \tag{6.18}$$

$$\hat{d} = 1, \tag{6.19}$$

$$\hat{r}_0 = r_0/d = \Pi_1, \tag{6.20}$$

$$\hat{\sigma}_0 = \sigma_0/d = \Pi_3, \tag{6.21}$$

where $\hat{\cdot}$ indicates a dimensionless variable. The analysis outlined above identifies the dimensionless problem parameters $\Pi_1 = r_0/d$, $\Pi_2 = Q/P_0 r_0^2 d$, and $\Pi_3 = \sigma_0/d$. Reference scales are also used to make the solution fields dimensionless

$$\hat{\boldsymbol{x}} = \boldsymbol{x}/d, \tag{6.22}$$

$$\hat{t} = \frac{t}{r_0^2}\sqrt{\frac{Q}{\rho_0 d}}, \tag{6.23}$$

$$\hat{\rho} = \frac{\rho}{\rho_0}\left(\frac{d}{r_0}\right)^2, \tag{6.24}$$

$$\hat{P} = \frac{P r_0^2 d}{Q}, \tag{6.25}$$

$$\hat{\boldsymbol{u}} = \frac{\boldsymbol{u} r_0^2}{d}\sqrt{\frac{\rho_0 d}{Q}}. \tag{6.26}$$

We remark that parameter Π_2 was originally proposed by Dumitrache et al. [12]. It is also clear that the transition layer thickness σ_0 introduces a third dimensionless parameter Π_3. In practice, Π_3 could be easily removed from the analysis by

employing sharp kernel boundaries ($\sigma_0 = 0.0$). However, in the simulation of hydrodynamic effects of nanosecond plasma discharges using simplified models [13; 31], smooth functions are typically favored. Thus, we retain the transition layer, but keep Π_3 constant across all configurations.

6.3 Overview

We begin by presenting an overview of the solution with parameters $Q = 800$ μJ, $r_0 = 150$ μm, $\sigma_0 = 25$ μm, and $d = 2.5$ mm, assuming background atmospheric conditions ($P_0 = 1$ atm and $T_0 = 300$ K). Results are shown in Fig. 6.3, where we observe the temperature profile at the beginning of the simulation ($t = 0$) and at $t = 12$ μs, and the resulting axial component of the velocity field at $t = 12$ μs. Important similarities between the observed results and the realistic pin-to-pin configuration results presented in Chapter 5 are immediately apparent: the radius of the heated kernel grows significantly during the expansion, and a large axial velocity is induced towards the axial midplane.

We also note that there are important differences with respect to the expansion process discussed in Chapter 5: the lack of a pin structure and the spatially uniform energy deposition cause the fluid to be entrained at a large angle, moving the heated fluid away from the midplane. In other words, a strong vertical jet moves fluid away from the middle plane along the axis and leads to a temperature bulge protruding upwards as shown clearly in Fig. 6.3(b). The axial component of the velocity also shows important differences in its spatial distribution, with the minimum (or maximum absolute value) of the axial component of the velocity located slightly

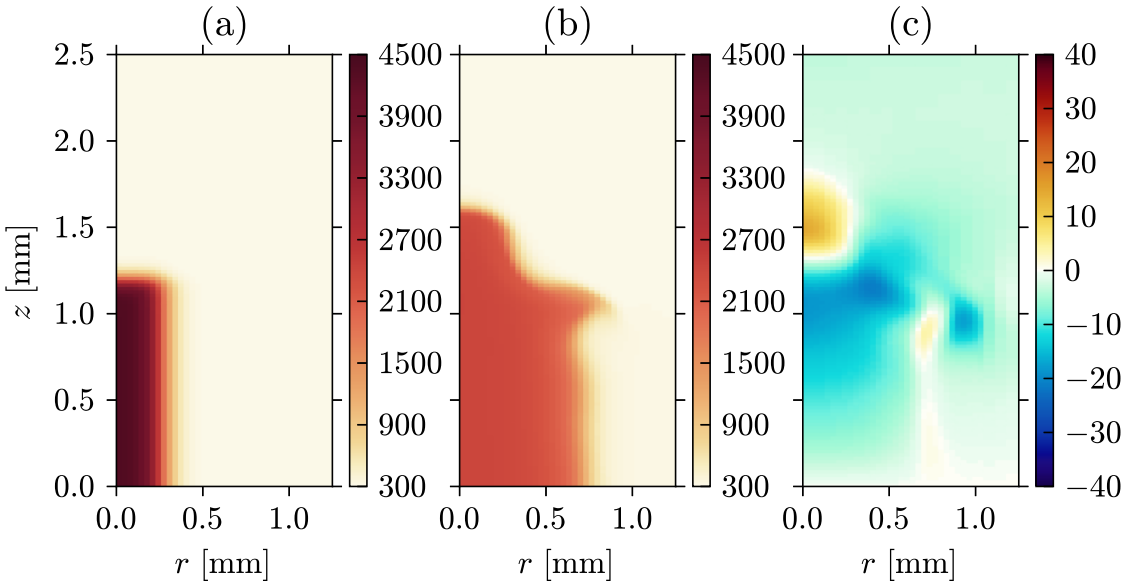

Figure 6.3: Overview of expansion with $d = 2.5$ mm, $r_0 = 150$ μm, and $Q = 800$ μJ ($\sigma_0 = 25$ μm). Temperature field [K] at (a) $t = 0$ and (b) $t = 12$ μs, and (c) axial component of velocity [m/s] at $t = 12$ μs.

off-axis. In spite of these differences, enough features are reproduced to provide a useful exploration of the hydrodynamic effect, especially as it leads to the growth of the region occupied by heated gases.

Quantitative data are provided by the spatial distribution of select fields along the axis shown in Fig. 6.4, as well as the radial direction in Fig. 6.5, at different times before, during, and after the expansion. The temperatures in the middle of the gap are significantly higher than those obtained by simulating the pin-to-pin discharge, which is explained by several factors. First, in this simplified modeling approach, non-equilibrium effects are not considered and energy goes to heating in its entirety. Second, a smaller radius of $r_0 = 150$ μm was utilized. Third, significant inhomo-

geneities in the spatial distribution of the energy deposited by the discharge are apparent as described in Chapter 5, so that the regions near the pin tips experience much higher energy density compared to that near the middle of the electrode gap. Despite the larger energy and lack of diffusive losses to the electrodes, the axial component of velocity resulting from the expansion is comparable (although smaller) to that observed from detailed simulations presented in Chapter 5. This observation suggests that the presence of the pins and an accurate spatial distribution of deposited energy are important to reproduce the induced hydrodynamic effects accurately and quantitatively, although the qualitative behavior and the order of magnitude of select variables are well-captured by a simpler modeling approach.

As just discussed, we observe a weaker hydrodynamic effect, as well as transport of energy away from the middle of the plane along the axis, a feature that was not observed in Chapter 5 or related high-fidelity simulations [14; 38]. In the simulations using the empirical model by Ref. [12], this effect is not observed either. In a recent numerical study by Taneja et al. [34; 35], the authors employed a phenomenological model with large energies and small gap as represented by the energy density distribution according to short cylinders. Similar to the feature recovered by our simulations and discussed in this Section, the results discussed in Refs. [34; 35] show a strong axial flow away from the axial midplane, inducing the separation of high-temperature lobes away from the main heated kernel.

Simplified approximations of the spatial energy deposition profile must be chosen carefully. In the case of diffusive kernels (longer gaps or lower values of deposited energy), when the velocity induced is minor and not sufficient to cause

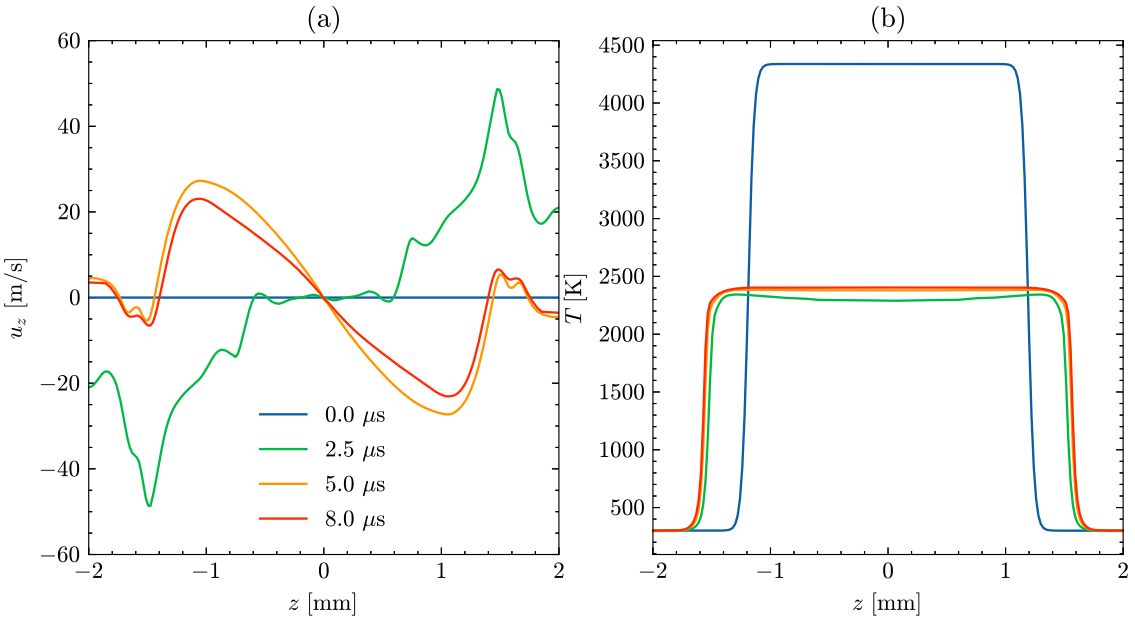

Figure 6.4: Spatial dependence of (a) axial velocity component and (b) temperature along the axis. Results from simulations with $d = 2.5$ mm, $r_0 = 150$ μm, and $Q = 800$ μJ, at initial background conditions of P_0= 1 atm and $T_0 = 300$ K.

toroidal collapse within the interval in between subsequent pulses at typical repetition frequencies (5 to 200 μs pulse interval), this is likely to be less important. However, when the hydrodynamic effect is important (short gaps and large energies), our analysis supports the conclusion that approximate energy distributions used to initialize simulations that seek to avoid the simulation of the discharge itself that can lead to (*i*) a lower induced velocity and (*ii*) additional energy losses due to nonphysical transport of energy away from the gap along the axis unobstructed by the electrodes. In summary, the choice of an adequate spatial distribution of the energy at the onset of a simulation is dependent on the application and discharge parameters.

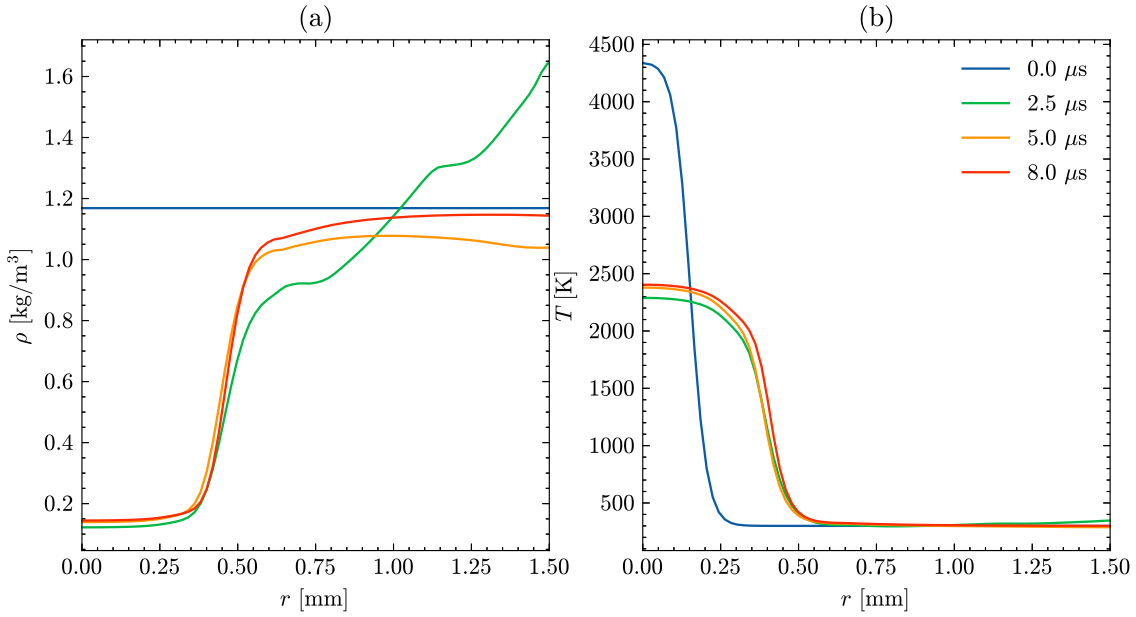

Figure 6.5: Spatial dependence of (a) density and (b) temperature along the radial coordinate in the middle of the gap ($z = 0$). Results from simulations with $d = 2.5$ mm, $r_0 = 150$ μm, and $Q = 800$ μJ, at initial background conditions $P_0 = 1$ atm and $T_0 = 300$ K.

6.4 Parametric Studies

6.4.1 Assessing self-similarity

In this Section, configuration parameters are varied judiciously in order to elicit changes in the dimensional fields and the results are processed according to the dimensional analysis discussed in Section 6.2 in order to demonstrate self-similarity when the fields are scaled appropriately. The ranges of the governing dimensionless parameters selected for the study are pertinent to pin-to-pin discharge configurations. The parameters that govern the initial conditions are summarized in Tab. 6.1 and reference scales are provided in Tab. 6.2.

Table 6.1: Summary of the parameters that govern the initial conditions and attending dimensionless parameters. A constant value $\Pi_3 = 0.01$ is adopted for all configurations.

Configuration	Q [μJ]	ρ_0 [kg/m^3]	P_0 [atm]	T_0 [K]	d [mm]	r_0 [mm]	$\Pi_2 = \hat{P_0}^{-1}$	$\Pi_1 = \hat{r}_c$
ESS-0	600	1.17	1	300	2.5	0.2	59	0.08
ESS-1	600	0.588	1	600	2.5	0.2	59	0.08
ESS-2	1200	1.17	2	600	2.5	0.2	59	0.08
ESS-3	2400	1.17	4	1200	2.5	0.2	59	0.08

Table 6.2: Summary of the reference scales $\mathcal{M}, \mathcal{L}, \mathcal{T}$ based on the parameters of each configuration.

Configuration	$\mathcal{L}$ [mm]	$\mathcal{T}$ [ns]	$\mathcal{M}/\mathcal{L}^3$ [kg/m^3]	$\mathcal{M}/\mathcal{L}\mathcal{T}^2$ [atm]	$\mathcal{L}/\mathcal{T}$ [m/s]
ESS-0	2.5	88.6	7.53 $\times 10^{-3}$	59.2	28.2 $\times 10^3$
ESS-1	2.5	62.6	3.77 $\times 10^{-3}$	59.2	39.9 $\times 10^3$
ESS-2	2.5	62.6	7.53 $\times 10^{-3}$	118.4	39.9 $\times 10^3$
ESS-3	2.5	44.3	7.53 $\times 10^{-3}$	236.8	56.4 $\times 10^3$

We begin by providing an overview of the solutions when made dimensionless as discussed. The axial component of velocity is shown in dimensionless form in Fig. 6.6 for all configurations, which share the same values for the governing dimensionless

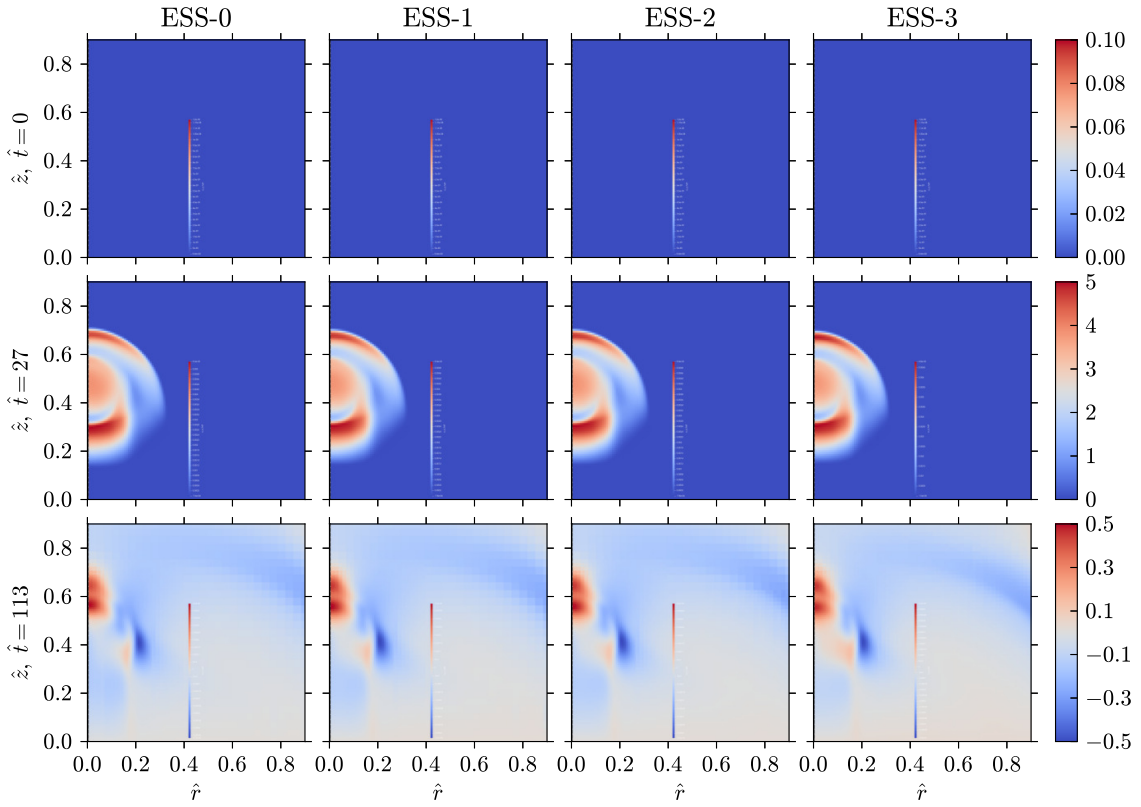

Figure 6.6: Dimensionless axial component of velocity $\hat{u}_z \times 10^3$ for the configurations presented in Tab. 6.1 at three dimensionless times. From top to bottom: before ($\hat{t} = 0$), during ($\hat{t} = 27$), and after ($\hat{t} = 113$) expansion. The dimensionless fields agree across configurations and demonstrate self-similarity.

parameters Π_1 and Π_2 as shown in Tab. 6.1. Overall, we observe very good agreement between all configurations, suggesting strong self-similarity and appropriate nondimensionalization according to the dimensional analysis presented.

Quantitative comparisons of dimensionless fields of interest are provided in Fig. 6.7 at the initial stage ($\hat{t} = 0$), during the expansion ($\hat{t} = 27$), and after the formation of the axial flow towards the midplane ($\hat{t} = 113$). We notice a discrep-

ancy in the initial pressure across configurations with different dimensional initial temperatures of the heated kernel for different initial temperatures, arising from real gas effects (i.e., a gas that is not calorically perfect). Across times, we observe very good agreement between the different configurations when comparing the three fields. There is better agreement between cases ESS-1 and ESS-2, which share the same dimensional value of temperature, than that observed among other cases, implying that the initial temperature does play a minor role that is not captured by the simplified analysis. A discrepancy of up to 10% is observed in the induced axial component of velocity, well below the differences in the velocity scale used to normalize the solution fields. These differences are ascribed minor differences in the initial dimensionless pressure across configurations at time $\hat{t} = 0$.

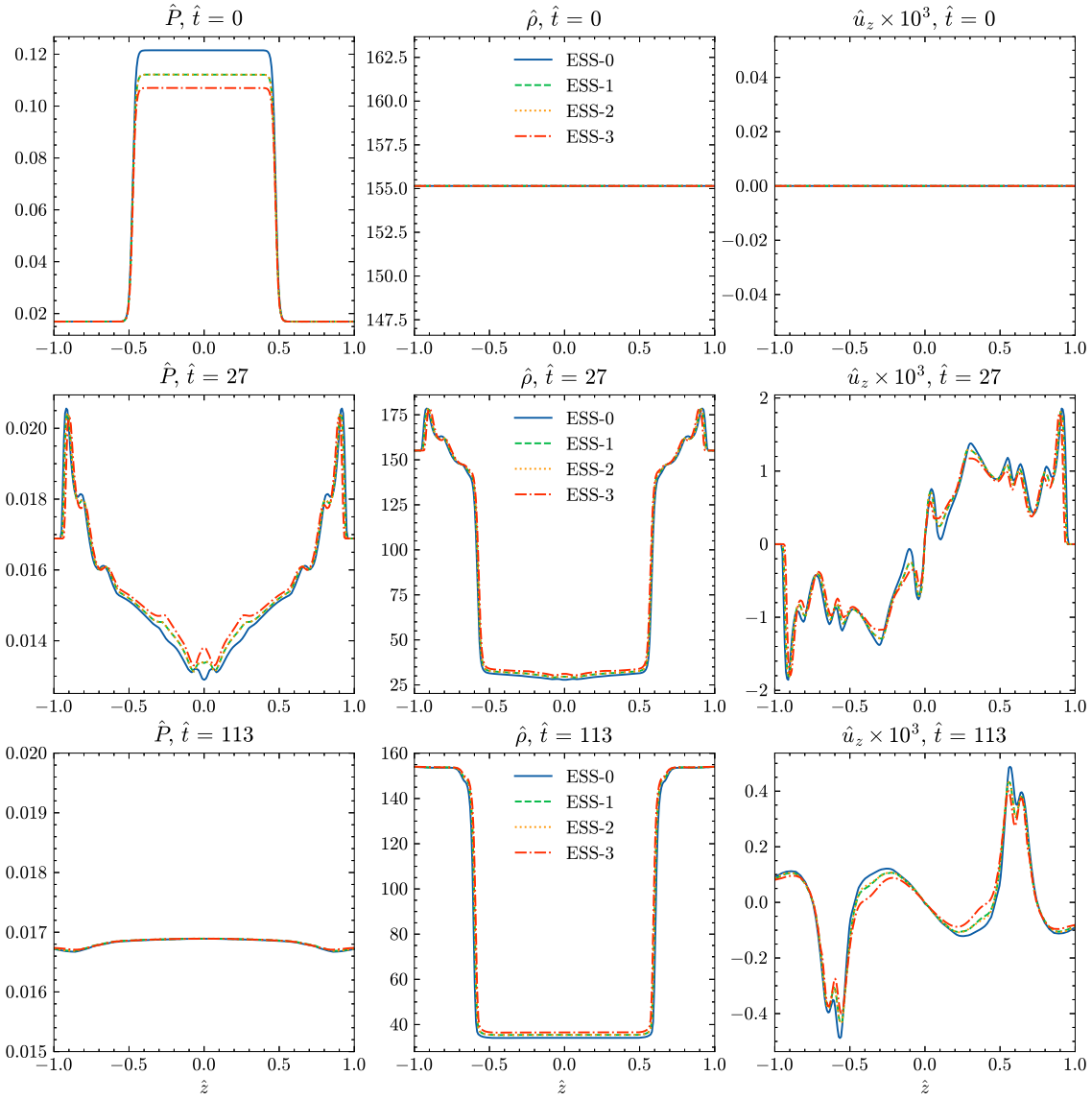

Figure 6.7: Spatial dependence across the axial coordinate along the axis ($\hat{r} = 0$) of the dimensionless pressure $\hat{P}$ (left column), density $\hat{\rho}$ (middle column), and axial velocity $\hat{u}_z$ (right column) at different dimensionless times.

6.4.2 Effect of Π_2 on the expansion process

As self-similarity for the solutions across the configurations was demonstrated, a parametric study is conducted by varying the two dimensionless governing parameters Π_1 and Π_2. In this Section we consider Π_2 and explore its effect on the expansion process over ranges of the parameter that are relevant to realistic pin-to-pin discharges. Parameters for all configurations considered in the parametric study are summarized in Tab. 6.3, where it is apparent that the energy deposited varies from 0.3 to 3.8 mJ for three different configurations: a short gap of 1.25 mm, a medium gap of 2.5 mm, and a long gap of 4.0 mm.

Table 6.3: Summary of the dimensional and dimensionless governing parameters used in the study on the dependence of the expansion process on Π_2. Constant $\Pi_3 = 0.01$ and constant background dimensional temperature of $T_0 = 300$ K is employed across all configurations.

Configuration	Q [μJ]	ρ_0 [kg/m^3]	P_0 [atm]	d [mm]	r_0 [mm]	$\Pi_2 = \hat{P}_0^{-1}$	$\Pi_1 = \hat{r}_0$
Atmospheric air, short gap							
EP2-A	150	1.17	1	1.25	0.2	29.5	0.16
EP2-B	300	1.17	1	1.25	0.2	59	0.16
EP2-C	600	1.17	1	1.25	0.2	118	0.16
EP2-D	1200	1.17	1	1.25	0.2	236	0.16
Atmospheric air, medium gap							
EP2-E	300	1.17	1	2.5	0.2	29.5	0.08
EP2-G	600	1.17	1	2.5	0.2	59	0.08
EP2-G	1200	1.17	1	2.5	0.2	118	0.08
EP2-H	2400	1.17	1	2.5	0.2	236	0.08
Atmospheric air, long gap							
EP2-I	480	1.17	1	4.0	0.2	29.5	0.05
EP2-J	960	1.17	1	4.0	0.2	59	0.05
EP2-K	1920	1.17	1	4.0	0.2	118	0.05
EP2-L	3840	1.17	1	4.0	0.2	236	0.05

In Fig. 6.8, the fields of dimensionless density $\hat{\rho}$ (top row) and dimensionless axial component of velocity $\hat{u}_z$ (bottom row) at time $\hat{t} \approx 100$ are shown for the four

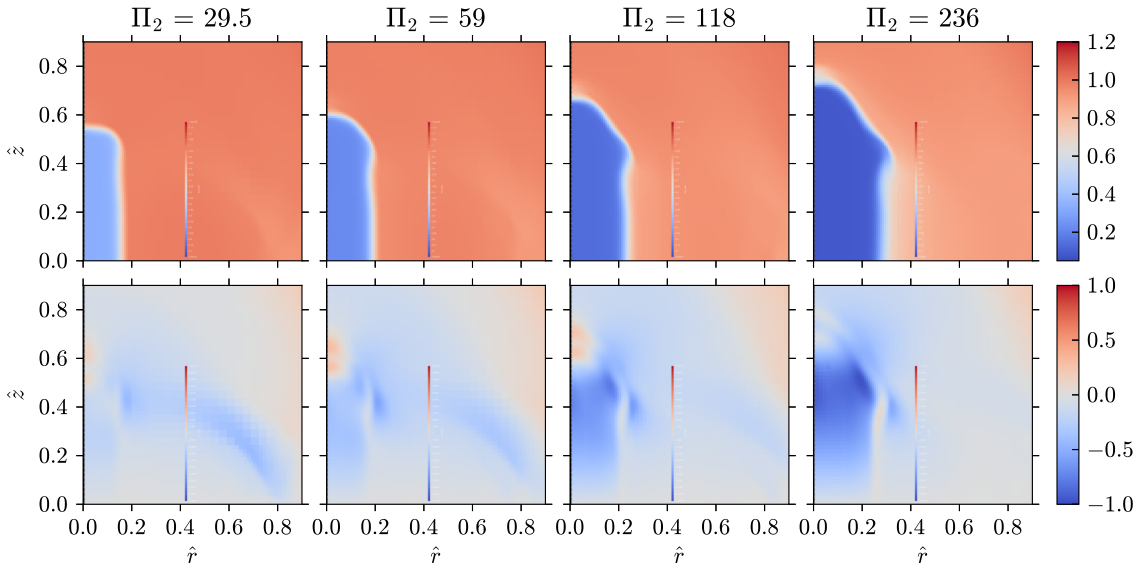

Figure 6.8: Spatial distribution of dimensionless density $\hat{\rho}$ (top row) and dimensionless axial component of velocity $\hat{u}_z$ (bottom row) at time $\hat{t} \approx 100$ for four different values of Π_2 and $\Pi_1 = 0.08$. All relevant governing parameters are given in Tab. 6.3.

different configurations with increasing values of Π_2 and equal $\Pi_1 = 0.08$ (corresponding to the medium gap case). It is apparent that higher values of Π_2 result in a larger heated region at the end of the expansion process. The shocks induced by the higher values of Π_2 move significantly faster, and are located outside the region shown by this time, but are still visible for the configuration with the lowest value of Π_2. In fact, a comparison across configurations shows how the temporal evolution is overall faster for higher values of Π_2. It is unclear whether the motion of the fluid in the direction of the positive axial coordinate would be inhibited by the presence of electrodes, or whether the observed effects would manifest themselves. Note that this fluid motion away from the midplane was not observed in the results from high-fidelity simulations discussed in Chapter 5.

Figure 6.9 shows the temporal evolution of the maximum absolute value of the axial component of velocity $|\hat{u}_{z,\max}|$ in the gap region (defined as $-1.5 < \hat{z} < 1.5$ and $\hat{r} < 0.5$) as a function of $\hat{t}$, and the maximum absolute value of the normalized pressure difference in the same gap region as a function of $\hat{t}$. It is apparent that increasing Π_2 affects the temporal evolution of the velocity field. To provide meaningful comparisons across different configurations, the duration of the expansion process $\hat{t}_{\text{end}}$ is defined as the time instant when the pressure in the gap region returns to its initial value to within 5%. Quantitatively, this occurs when

$$\max\{|P - P_0|\}/P_0 \tag{6.27}$$

decreases and remains below 0.05 for the remainder of the simulation as shown in Fig. 6.9.

Figure 6.10 shows $\hat{t}_{\text{end}}$ as a function of Π_2 for the three values of Π_1, where we observe a linear dependence of $\hat{t}_{\text{end}}$ with respect to Π_2 and a linear fit is provided using data for $\Pi_2 \leq 150$. The linear fit results in a slope of 0.81 as noted in Fig. 6.10. Thus, higher values of Π_2 associated with a more energetic discharge, all other dimensional parameters held constant, prolong the expansion proportionally. Lower values of Π_1 (associated with narrower cylindrical kernels) prolong the duration as well, although the effect is very weak compared to that of Π_2, especially at low values of Π_2.

A second quantity of interest is the maximum of the absolute value of the axial component of velocity in the gap region at the end of the expansion phase, shown in Fig. 6.10(b). From the available data, we conclude that a higher value of Π_2 increases the magnitude of the maximum value of the axial component of velocity

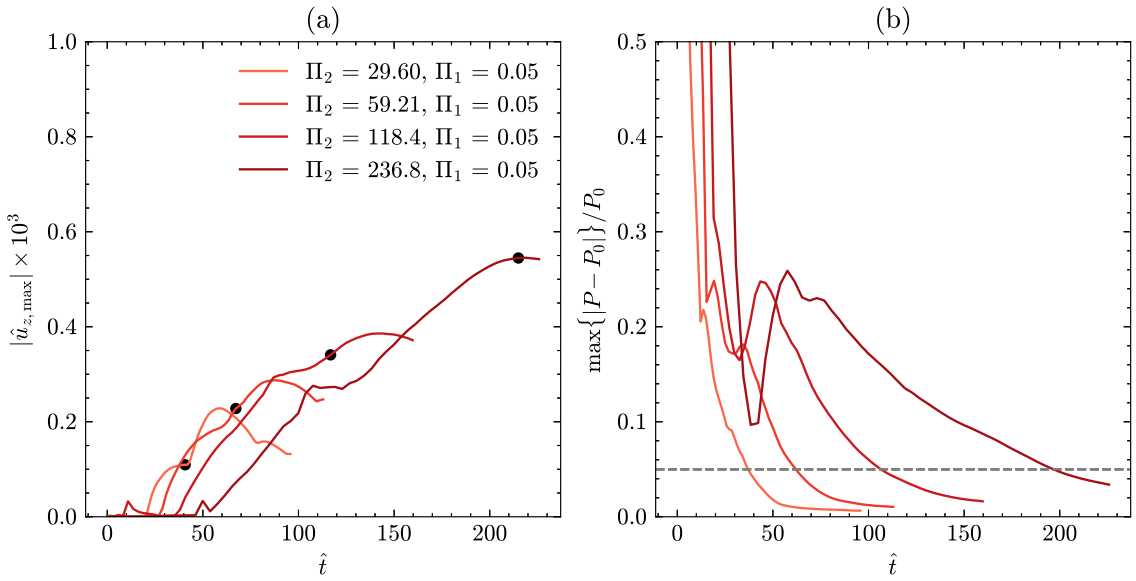

Figure 6.9: (a) Temporal evolution of the maximum absolute value of the axial component of velocity $\hat{u}_{z,\max}$ and (b) maximum value of the normalized pressure difference as a function of $\hat{t}$ for the four configurations summarized in Tab. 6.3 and constant $\Pi_1 = 0.05$. The duration of the expansion process $\hat{t}_{\text{end}}$ is calculated at the instant when $\max\{|P - P_0|\}/P_0$ drops below 0.05 (gray dotted line). This instant is annotated with black markers as shown in (a).

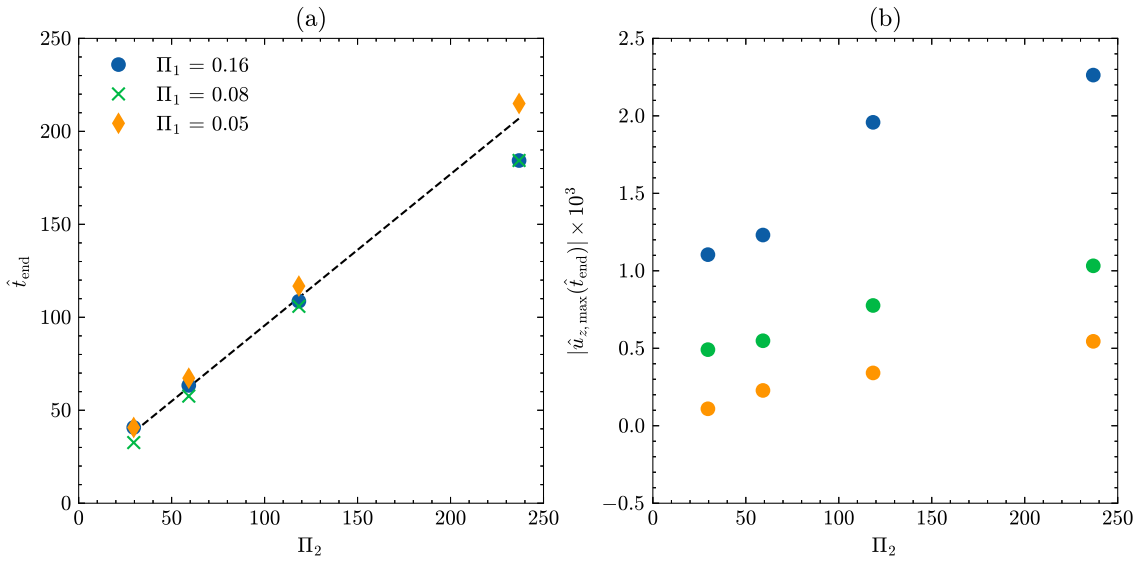

Figure 6.10: (a) Length of the acoustic phase $\hat{t}_{\mathrm{end}}$ as a function of Π_2 for various values of Π_1 along with linear best fit ($m = 0.81$ and $b = 14.18$) for all data points across values of Π_1 with $\Pi_2 < 150$, and (b) maximum of the absolute value of the axial component of velocity $|\hat{u}_{z,\max}|$ at the end of the acoustic phase as a function of Π_2 for various values of Π_1. All configuration parameters are presented in Tab. 6.3.

in the gap region by the end of the expansion phase, with a qualitative difference in the trend for very high values of energy depositions or $\Pi_2 > 50$. Contrary to $\hat{t}_{\mathrm{end}}$, $\hat{u}_{z,\max}(\hat{t}_{\mathrm{end}})$ shows a marked dependence on Π_1 for a given Π_2, with larger values of Π_1 engendering larger velocity magnitudes.

6.4.3 Effect of Π_1

In this Section, the dependence of the expansion process on the value of the dimensionless parameter Π_1 is explored. In most pin-to-pin discharge configurations, the length of the gap d varies more widely than the reported radius of the plasma channel r_0. We keep the discharge radius r_0 constant ($r_0 = 200$ μm) and vary d to bring about a change in $\Pi_1 = r_0/d$. All configuration parameters explored are shown in Tab. 6.4, where it is apparent that gap length d is varied from 1.25 mm to 4 mm, while holding Π_2 constant by adjusting the energy deposited Q.

Table 6.4: Summary of the of the dimensional and dimensionless governing parameters used in the study on the dependence of the expansion process on Π_1. Constant $\Pi_3 = 0.01$ and constant background dimensional temperature of $T_0 = 300$ K is employed across all configurations.

Configuration	Q [μJ]	ρ_0 [kg/m^3]	P_0 [atm]	d [mm]	r_0 [mm]	$\Pi_2 = \hat{P_0}^{-1}$	$\Pi_1 = \hat{r}_0$
EP1-A	300	1.17	1	1.25	0.2	59	0.16
EP1-B	432	1.17	1	1.8	0.2	59	0.11
EP1-C	600	1.17	1	2.5	0.2	59	0.08
EP1-D	960	1.17	1	4.0	0.2	59	0.05
EP1-E	600	1.17	1	1.25	0.2	118	0.16
EP1-F	864	1.17	1	1.8	0.2	118	0.11
EP1-G	1200	1.17	1	2.5	0.2	118	0.08
EP1-H	1920	1.17	1	4.0	0.2	118	0.05
EP1-I	1200	1.17	1	1.25	0.2	236	0.16
EP1-J	1728	1.17	1	1.8	0.2	236	0.11
EP1-K	2400	1.17	1	2.5	0.2	236	0.08
EP1-L	3840	1.17	1	4.0	0.2	236	0.05

Figure 6.11 shows the temporal evolution of $\hat{u}_{z,\max}$ and of the normalized pressure difference $\max\{|P - P_0|\}/P_0$ in the gap region for various values of Π_1 holding $\Pi_2 = 59.2$ constant. Compared to the data in Fig. 6.9 for $\Pi_1 = 0.05$, data from configurations with higher values of Π_1, i.e., cylindrical kernels which are wider

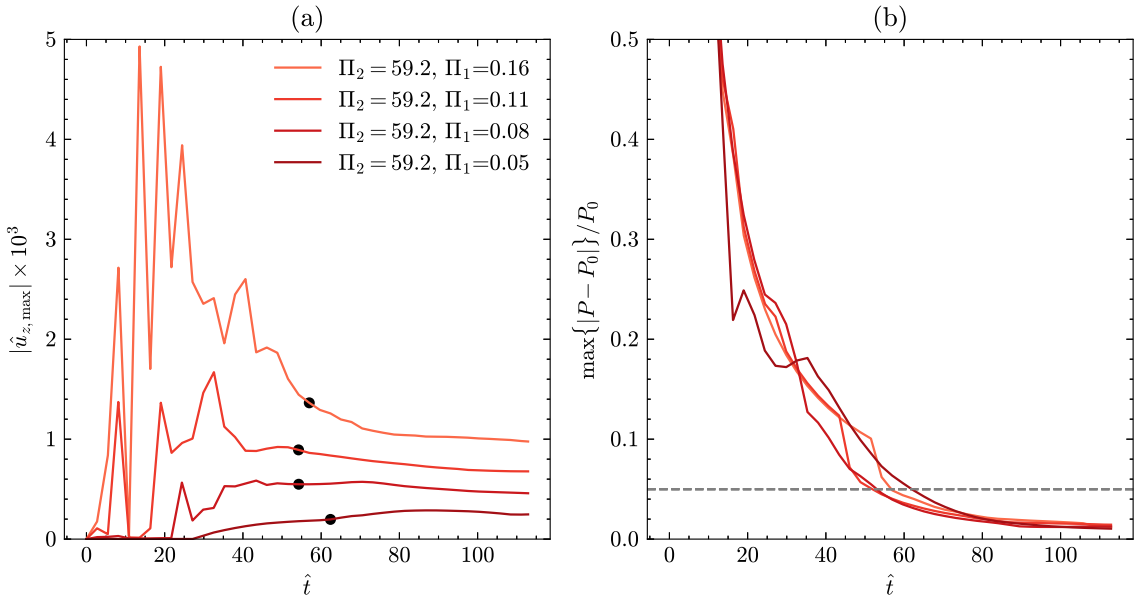

Figure 6.11: (a) Temporal evolution of the maximum absolute value of the axial component of velocity $\hat{u}_{z,\max}$ and (b) maximum absolute value of the normalized pressure difference as a function of $\hat{t}$ for the four configurations summarized in Tab. 6.4. The duration of the expansion process $\hat{t}_{\text{end}}$ is calculated at the instant when $\max\{|P - P_0|\}/P_0$ drops below 0.05 (gray dotted line). This instant is annotated with black markers as shown in (a).

in units of gap length, show a much more erratic evolution of $\hat{u}_{z,\max}$, which achieves much larger values early in the expansion phase. By $\hat{t} \geq 50$, the velocity metric appears to have achieved an asymptotic value, which is higher in magnitude the higher the value of Π_1 at least for $\Pi_2 = 59.2$. The temporal evolution of $\max\{|P - P_0|\}/P_0$ is nearly independent of Π_1 for $\Pi_2 = 59.2$ as shown in Fig. 6.11(b).

The data in Fig. 6.12 provides a comprehensive summary of the effects brought by Π_1 on the expansion process. The data show that as Π_1 increases, $\hat{t}_{\text{end}}$ decreases, although it appears that $\hat{t}_{\text{end}}$ reaches an asymptotic value, especially for the lower

values of Π_2 considered. Overall the dependence of the duration of the expansion phase on Π_1 is rather weak, especially if compared to the strong dependence on Π_2 discussed in Section 6.4.2. As far as the maximum value of the axial component of velocity at the end of the acoustic phase, it is apparent that it increases in magnitude with increasing Π_1 and the dependence is nearly linear with a proportionality constant, or slope, that increases with increasing value of Π_2.

Based on the data and commentary provided thus far, $\hat{t}_{\text{end}}$ depends linearly on Π_2 and exhibits a very weak dependence on Π_1, so that we may write

$$\hat{t}_{\text{end}} = f(\Pi_1)g(\Pi_2) \approx \hat{C}\Pi_2 + \hat{b}, \tag{6.28}$$

or

$$\frac{t}{r_0^2}\sqrt{\frac{Q}{\rho_0 d}} \approx \hat{C}\frac{Q}{r_0^2 d P_0} + b, \tag{6.29}$$

which we simplify to the following dimensional form

$$t_{\text{end}} \approx C\sqrt{\frac{Q\rho_0}{P_0^2 d}} + b. \tag{6.30}$$

Equation (6.30) establishes a linear relationship between t_{end} and $\sqrt{Q\rho_0/(P_0^2 d)}$ with a proportionality constant of $\hat{C} = 0.81$ (see caption of Fig. 6.10), which provides a reasonable approximation across all cases considered. Here the y-intercept is computed by simply scaling the dimensionless intercept ($\hat{b} = 14.18$) by the reference time, or simply $b = \mathcal{T}\hat{b}$.

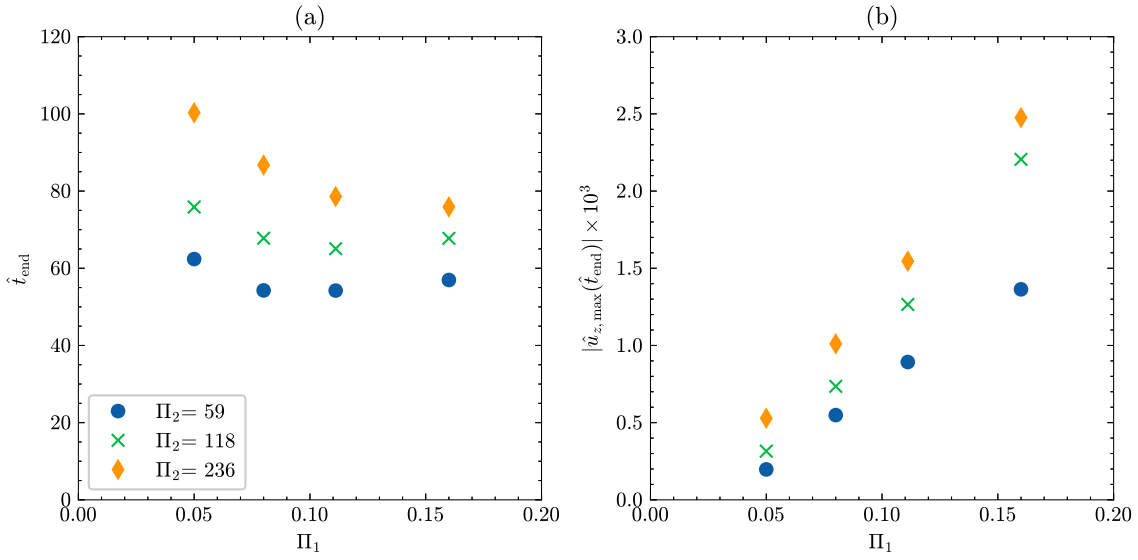

Figure 6.12: (a) Length of the acoustic phase $\hat{t}_{\mathrm{end}}$ as a function of Π_1, and (b) maximum absolute value of the axial component of velocity $\hat{u}_{z,\max}(\hat{t}_{\mathrm{end}})$ in the gap region as a function of Π_1. The configurations are described in Tab. 6.4.

Chapter 7

Hydrodynamics: High-Fidelity Models and Scaling Laws

High-fidelity fully coupled models have not been used to study the hydrodynamic effect of NSDP in air. Published studies in the literature employing fully coupled modeling approaches [14; 39; 38] are limited to the investigation of preheated air/fuel mixtures and/or longer gaps, which favor the diffusive regime, whereby hydrodynamic effects induced by the discharge are minor. In this Chapter, we present a parametric study of single pulse discharges focusing on the induced hydrodynamic effect.

The primary objective of the study discussed in this chapter is to explore dependences between electrode geometry, spatial distribution of the deposited energy, entrainment velocity, and the growth of the heated kernel due to kernel expansion. While the results from Ref. [12] put forth a systematic theory for predicting the transition between diffuse and toroidal regimes, there are important shortcomings as discussed in Section 1.2.2. Those are briefly reviewed in Section 7.1 also. In this Chapter we study the hydrodynamic effect induced by nanosecond discharges in air in a pin-to-pin configuration with a voltage pulse that brings about a nominal reduced electric field of 200 Td. The dependence of the hydrodynamic effect from

deposited energy, background conditions, and gap length are studied in detail.

The objectives are summarized below:

- Establish dependences between parameters and fields of interest relevant to the hydrodynamic effect brought about by a realistic pin-to-pin nanosecond discharge.
- Assess the degree of self-similarity between solutions and compare the effects of parameters Π_1 and Π_2 defined in Chapter 6 against the simplified configuration and models in the same Chapter.
- Establish relationships between the proposed dimensionless governing parameters and practical quantities of interest, such as the duration of the acoustic phase, the entrainment velocity ensuing from the expansion, and growth of the gas kernel energized by the plasma discharge.
- Use established relationships to propose a regime diagram that distinguishes nanosecond plasma discharge configurations dominated by advection from those dominated by diffusion.

7.1 Reevaluating Dumitrache's toroidal collapse model

As discussed in Section 1.2.2, Dumitrache et al. [12] proposed the use of a dimensionless number Π_{Tr} in order to predict whether the nanosecond discharge pulse engenders a toroidal collapse or not:

$$\Pi_{\mathrm{Tr}} = \frac{E_{\mathrm{uh}}}{P_0} \frac{1}{\pi r_0^2 d}, \tag{7.1}$$

where E_{uh} is the fraction of energy deposited going directly to heating, P_0 is the background initial pressure, πr_0^2 is the cross-section of a cylindrical kernel encompassing the region of the gap where the plasma deposits the energy (r_0 being the radius of the plasma), and d is the gap length. In its original form, the dimensionless number is challenging to use in practice, since it requires measuring the radius of the plasma kernel, a quantity that can be difficult to determine in many experimental configurations and is not necessarily well-defined. For example, in the original study by Dumitrache et al. [12], a fixed kernel radius of 100 μm was used for atmospheric discharges (as both the electrode gap and energy deposited varied), while at similar atmospheric pressure discharge conditions by Xu et al. [9] and Rusterholtz et al. [22], discharge radii of 200 μm and 225 μm were reported, respectively. In a recent study exploring hydrodynamic regimes and the implication of the regime on the ignition of a methane/air mixture at atmospheric conditions [102], the authors relied on measured radii from other similar studies in order to calculate the dimensionless parameter, even though the fuel might impact discharge characteristics. Yet, the proposed dimensionless parameter is very sensitive to changes in the plasma kernel radius, making the theory difficult to apply.

Moreover, the results presented thus far in our work are not consistent with the proposed critical value of Π_{Tr} separating the diffusive regime and that characterized by the collapse of a torus as explained by Dumitrache et al. [12], where it was concluded that discharges such that $\Pi_{\mathrm{Tr}} < 60$ give rise to hydrodynamic effects in the diffusive regime, values between 60 and 80 fall into a transition regime, and values above 80 result in the collapse of a torus, as depicted in the regime diagram

reproduced in Fig. 7.1. In Chapter 5, extensive analysis of the plasma discharge and of the temporal evolution of the heated kernel yielded a radius of 0.19 mm with energy deposition of 800 μJ. Even using the most favorable values of total energy deposition of 800 μJ and $r_0 = 190$ μm, we calculate a $\Pi_{\mathrm{Tr}} = 27.8$ that is well below the threshold value proposed by Dumitrache et al. [12]. From estimates, only about 70-85% of the deposited energy goes to ultra-fast heating (see Fig. 5.13), resulting in an even lower value of the dimensionless parameter $\Pi_{\mathrm{Tr}} = 23.7$. Yet, our detailed results show toroidal collapse ocurring between 100 μs and 200 μs from pulse initiation (see Fig. 5.18).

We also remark that, as apparent from the regime diagram in Fig. 7.1, one axis is dimensionless and the other is dimensional, pointing to the fact that the analysis is incomplete as presented in Ref. [12].

We also highlight the fact that from the results of our high-fidelity simulations, the extent of ultra-fast heating as well as the radial extent of the heated kernel depend on the axial location, which complicates the application of the theory based on the original dimensionless parameter. It is clear from this discussion that despite its simplicity, the analysis proposed by Dumitrache et al. [12] is not complete and neglects aspects worth investigating. Finally, the theory at the basis of the regime diagram presented in Fig. 7.1 leads to a binary classification and it does not provide an estimate for the time scales involved in the torus collapse.

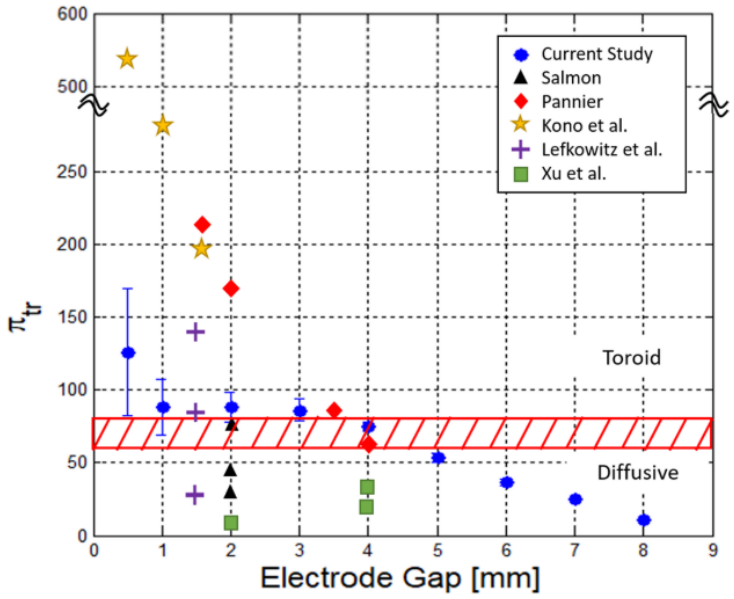

Figure 7.1: The above figure is reproduced from Ref. [12] and illustrates a regime diagram proposed by the authors. The hydrodynamic regime depends on the dimensionless parameter Π_{Tr} and gap length.

7.2 Dimensional analysis: pin-to-pin discharge

We assume that the governing problem parameters for an axisymmetric pin-to-pin discharge are the energy deposited Q, background density and pressure ρ_0 and P_0, respectively, gap d, and radius of curvature of the pin electrodes r_c, with

dimensions in the MLT class of systems of units:

$$[Q] = ML^2T^{-2}, \tag{7.2}$$

$$[\rho_0] = ML^{-3}, \tag{7.3}$$

$$[P_0] = ML^{-1}T^{-2}, \tag{7.4}$$

$$[d] = L, \tag{7.5}$$

$$[r_c] = L. \tag{7.6}$$

In addition to the parameters above, we also define position vector $\boldsymbol{x}$, time t, density ρ, pressure P, and velocity $\boldsymbol{u}$,

$$[\boldsymbol{x}] = L, \tag{7.7}$$

$$[t] = T, \tag{7.8}$$

$$[\rho] = ML^{-3}, \tag{7.9}$$

$$[P] = ML^{-1}T^{-2}, \tag{7.10}$$

$$[\boldsymbol{u}] = LT^{-1}. \tag{7.11}$$

We use the governing parameters ρ_0, r_c, d, and Q to define reference scales in a similar fashion as done in Chapter 6,

$$\mathcal{M} = \rho_0 r_c^2 d, \tag{7.12}$$

$$\mathcal{L} = d, \tag{7.13}$$

$$\mathcal{T} = r_c^2 \sqrt{\frac{\rho_0 d}{Q}}. \tag{7.14}$$

Using the reference scales above we define dimensionless input parameters

$$\hat{Q} = \left(\frac{r_c}{d}\right)^2 = \hat{r}_c^2 = \Pi_1^2, \tag{7.15}$$

$$\hat{\rho}_0 = \left(\frac{d}{r_c}\right)^2 = \hat{r}_c^{-2} = \Pi_1^{-2}, \tag{7.16}$$

$$\hat{P}_0 = \frac{P_0 r_c^2 d}{Q} = \Pi_2^{-1}, \tag{7.17}$$

$$\hat{d} = 1, \tag{7.18}$$

$$\hat{r}_c = r_c/d = \Pi_1. \tag{7.19}$$

The set of 5 dimensional parameters are reduced to 2 dimensionless ones, namely $\Pi_1 = r_c/d$ and $\Pi_2 = Q/P_0 r_c^2 d$. The reference scales are also used to make the following variables dimensionless

$$\hat{\boldsymbol{x}} = \boldsymbol{x}/d, \tag{7.20}$$

$$\hat{t} = \frac{t}{r_c^2}\sqrt{\frac{Q}{\rho_0 d}}, \tag{7.21}$$

$$\hat{\rho} = \frac{\rho}{\rho_0}\left(\frac{d}{r_c}\right)^2, \tag{7.22}$$

$$\hat{P} = \frac{P r_c^2 d}{Q}, \tag{7.23}$$

$$\hat{\boldsymbol{u}} = \frac{\boldsymbol{u} r_c^2}{d}\sqrt{\frac{\rho_0 d}{Q}}. \tag{7.24}$$

The scaling argument proposed in this dissertation is based only on the parameters Π_1 and Π_2, as in Chapter 6, where viscous and diffusive effects were neglected by solving the inviscid Euler equations. In the pin-to-pin discharge configuration and attending high-fidelity mathematical models, viscous and diffusive terms are

included, so that additional parameters are defined

$$\mathrm{Re} = \frac{\mathcal{L}(\mathcal{L}/\mathcal{T})}{\nu_0}, \tag{7.25}$$

$$\mathrm{Pr} = \frac{\nu_0}{D_0}, \tag{7.26}$$

where Re is a Reynolds number, Pr is the Prandtl number, ν_0 is the kinematic viscosity [m^2/s] of the background gas and D_0 [m^2/s] is its thermal diffusion coefficient $D_0 = \lambda_0/(\rho_0 c_p)$, λ_0 being the thermal conductivity [W/m-K], ρ_0 the density [kg/m^3], and c_p the specific heat capacity at constant pressure [J/kg-K] of the background gas. It is emphasized that the Prandtl and Reynolds numbers defined above are based on initial conditions. Within the hot gas kernel itself, a similarly defined Reynolds number based on local properties may vary by factor of ≈ 14, while local Prandtl remains very close to the background value (less than 1% change).

We reiterate that parameters Re and Pr are provided only for context and monitored, and not used directly when selecting configurations with the objective of controlling Π_1 and Π_2. Finally, we define a dimensionless parameter proportional to the inverse of a Mach number: $\hat{a}_0 = a_0/(\mathcal{L}/\mathcal{T})$, where a_0 [m/s] is the speed of sound at the conditions of the background gas

$$\hat{a}_0 = \frac{a_0 r_c^2}{d}\sqrt{\frac{\rho_0 d}{Q}}. \tag{7.27}$$

Manipulation of the above gives

$$\hat{a}_0 = \sqrt{\frac{\gamma_0 P_0}{\rho_0}}\frac{r_c^2}{d}\sqrt{\frac{\rho_0 d}{Q}} = \sqrt{\gamma_0 \frac{P_0 d r_c^2}{Q}\frac{r_c^2}{d^2}}, \tag{7.28}$$

or

$$\hat{a}_0 = \sqrt{\gamma_0 \Pi_1^2/\Pi_2} = \gamma_0^{1/2}\,\Pi_1\,\Pi_2^{-1/2}. \tag{7.29}$$

In other words, this new dimensionless parameter $\hat{a}_0$ depends solely on the two parameters Π_1 and Π_2 and on the ratio of the specific heats of the background gas.

It is apparent that the dimensional analysis discussed in this Section considers only "hydrodynamic" dimensional parameters as inputs, neglecting to include parameters pertaining to the plasma discharge or to the physical models implicit in the modeling of the plasma itself. Such a manner of proceeding is of course a gross simplification, one that requires data in order to judge its applicability and prove its utility. In other words, our analysis postulates that, even if the entirety of the discharge processes are represented only by the amount of energy deposited, the details of the hydrodynamic effect engendered by the discharge are well captured by the dimensionless parameters presented. More details are presented in Section 7.3 when the manner in which discharge parameters are chosen across configurations is explained.

The relationship among the hydrodynamic input parameters also merits a discussion. In particular, the treatment of the energy deposited Q differs in some respects from that in experimental configurations. In the treatment presented in this chapter (as well as other numerical studies), Q is a configuration parameter that is selected independently (with some physical limitations) from all other parameters. In experimental configurations, Q is a *derived* parameter, measured from the interaction of the imposed voltage waveform with the electrode capacitive circuit and the evolution of the conducting channel itself, which draws a current.

The measured energy deposited Q is also not completely independent of pressure and density. For example, faster and thicker streamers are observed at lower

pressures as reported in Ref. [103], increasing the value of the conduction current. For a more detailed discussion of the influence of pressure, density, and other relevant parameters on the measured energy, the reader is referred to Ref. [99]. In the context of this work, it suffices to say that while not completely independent, a given configuration admits a range of energies Q that can be increased or decreased by changing the voltage waveform, rise time, and amplitude. The energy ranges used in this work and discussed in the following section are within practical ranges of actual configurations.

7.3 Parametric studies

We now turn our attention to the simulation of nanosecond discharges in air leveraging the high-fidelity mathematical models and simulation framework detailed in Chapter 4. A parametric study is carried out in order to explore the effect of gap size, amount of energy deposited, and thermochemical state of the background gas on the resulting discharge and subsequent hydrodynamic effect engendered by the expansion (or acoustic) phase. Parametrization of all hydrodynamic effects and their dependences is attempted by the proposed dimensionless parameters Π_1 and Π_2. The governing parameters of all configurations considered in the study are detailed in Tab. 7.1 with gap sizes between 1 and 4 mm, background pressures between 1 and 2 atm, and background temperatures between 300 and 600 K. The pin electrode curvature r_c is kept constant and equal to 250 μm across all configurations. The selection of those dimensional governing parameters was guided by an extensive literature review as well as considerations related to computational feasibility.

For all configurations, the applied voltage parameters are as follows. The positive voltage bias applied to anode and top bounding surface is described by the following sigmoid function:

$$V(t) = V_{\max}\left[f(t-\delta,\lambda) + f(t-\delta-t_r-t_p,-\lambda) - 1\right], \tag{7.30}$$

$$f(t,c) = \frac{1}{1+\exp\left(-ct\right)}, \tag{7.31}$$

where δ, t_r, $\lambda = 8/t_r$, and t_p are constants that control the voltage rise and pulse duration, and $V_{\max}$ is the peak voltage. In this work, for all configurations, we use δ = 3 ns, t_r = 4 ns, and t_p = 50 ns. Conversely, $V_{\max}$ is scaled with respect to the base case discussed in Chapter 5 ($V_{\max}$ = 12.5 kV for discharges in air at 300 K and 1 atm and d = 2.5 mm) so that the nominal reduced electric field $E/N = (V/d)/N$ remains constant across all configurations and equal to 204 Td. This manner of scaling the applied voltage with the electrode gap and the number density of the background gas is common in the plasma literature and is adopted here in lieu of including plasma and discharge parameters in the dimensional analysis. By scaling the voltage in this fashion, we seek to normalize the hydrodynamic effect with respect to changes in the plasma discharge by keeping discharge processes unchanged across cases, albeit only approximately.

7.3.1 Spatial distribution of the energy deposited by the plasma discharge

The most consequential difference between simplified models [13; 31; 35] used in the literature and the mathematical models and computational approaches adopted in our work, is the spatial distribution of the energy deposited by the dis-

Table 7.1: List of dimensional and dimensionless parameters for all configurations considered in the study. The conditions span across four different Π_1 values and five different Π_2 values. The radius of curvature of the pin electrodes is constant $r_c = 250$ μm. The Prandtl number is constant Pr = 0.71. Across configurations with the same pair of parameters (Π_1, Π_2), the Reynolds number varies by less than a factor of 4.

Configuration	Q [μJ]	ρ_0 [kg/m^3]	P_0 [atm]	T_0 [K]	d [mm]	Π_2	Π_1	Re $\times 10^{-3}$
HF1-Q1	200	1.17	1	300	2.5	12.6	0.1	1643
HF1-Q2	300	1.17	1	300	2.5	18.9	0.1	2012
HF1-Q3	400	1.17	1	300	2.5	25.3	0.1	2324
HF1-Q4	600	1.17	1	300	2.5	37.9	0.1	2846
HF1-Q5	800	1.17	1	300	2.5	50.5	0.1	3287
HF2-Q1	100	1.17	1	300	1.25	12.6	0.2	410
HF2-Q2	150	1.17	1	300	1.25	18.9	0.2	503
HF2-Q3	200	1.17	1	300	1.25	25.3	0.2	581
HF2-Q4	300	1.17	1	300	1.25	37.9	0.2	711
HF2-Q5	400	1.17	1	300	1.25	50.5	0.2	821
HF3-Q1	200	0.588	1	600	2.5	12.6	0.1	709
HF3-Q2	300	0.588	1	600	2.5	18.9	0.1	868
HF3-Q3	400	0.588	1	600	2.5	25.3	0.1	1002
HF4-Q1	400	1.17	2	600	2.5	12.6	0.1	3287
HF4-Q2	600	1.17	2	600	2.5	18.9	0.1	4025
HF4-Q3	800	1.17	2	600	2.5	25.3	0.1	4648
HF4-Q4	1200	1.17	2	600	2.5	37.9	0.1	5693
HF5-Q3	280	1.17	1	300	1.75	25.3	0.14	1138
HF5-Q5	560	1.17	1	300	1.75	50.5	0.14	1610
HF6-Q3	640	1.17	1	300	4.0	25.3	0.0625	5950
HF6-Q5	1280	1.17	1	300	4.0	50.5	0.0625	8414

charge. Simplified models assume that the discharge energy is deposited uniformly in a region of cylindrical shape [13; 34; 35] as in Chapter 6. Conversely, results from Chapter 5 show that the energy density distribution depends markedly on the axial coordinate, with asymmetries deriving from the differences between positive and negative streamers and localized energy deposition near the pin tips compared to the middle of the gap, where the energy density is significantly lower in value. More-

over, the spatial distribution of the energy deposited depends on the density of the background gases and on the spatial inhomogeneities in the distribution of charged particles present in the gas. Both of those may change from pulse to pulse (see Fig. 5.20). In this Section, we aim to characterize the effect of geometry and background pressure and temperature on the energy distribution after a single discharge pulse into quiescent air of homogeneous pressure and temperature.

In what follows, the energy deposited by the discharge is considered immediately after the discharge deposition ends. The normalized energy density gain $(\rho e - \rho_0 e_0)/(\rho e)_{\text{avg}}$ is defined, where $(\rho e)_{\text{avg}}$ is defined as

$$(\rho e)_{\text{avg}} = Q/\pi r_c^2 d, \tag{7.32}$$

and $\rho_0 e_0$ is the energy density of the background gas. The spatial distribution of $(\rho e - \rho_0 e_0)/(\rho e)_{\text{avg}}$ is presented in Fig. 7.2. From the data shown, it is clear that as Π_1 decreases, the width of the energetic gas kernel decreases. Note that due to the choice of d as reference length scale, the dimensionless gap size remains constant and equal to unity, while the dimensionless radius of curvature of the pins decreases as Π_1 decreases. It is also apparent that, when measured in units of gap distance, the volume occupied by the energetic gas becomes smaller as the value of Π_1 decreases.

Quantitative information about the spatial distribution of the deposited energy is presented in the form of radial and axial profiles in Fig. 7.3. In Fig. 7.3(a), the radial profiles of the normalized energy density gain at $\hat{z} = 0$ are shown for every configuration in Tab. 7.1. The black markers on the curves mark the radial distance $\hat{r}^*$ where the normalized energy gain is equal to 0.607 $\max\{(\rho e - \rho_0 e_0)/(\rho e)_{\text{avg}}\}$.

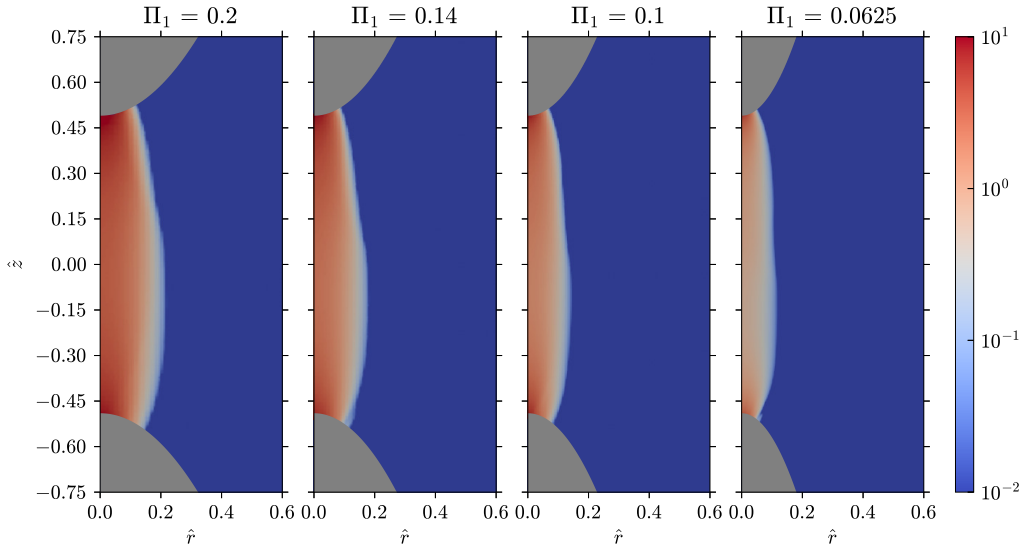

Figure 7.2: Spatial distribution of the normalized energy density gain $(\rho e - \rho_0 e_0)/\rho e_{\text{avg}}$ for four values of Π_1 and $\Pi_2 = 50.5$. The data are shown immediately after the end of the voltage pulse.

This radial coordinate corresponds to the inflection point of a Gaussian profile, and it serves as a formal measure of the width of the energized gas kernel to be compared across configurations.

Based on the data in Fig. 7.3(a), it is apparent that $\hat{r}^*$ increases as Π_1 increases. In other words, when the radius of curvature of the electrodes decreases relative to the gap, the width of the energetic gas kernel decreases (when measured in units of gap distance). Thus, the data in Fig. 7.3(a) confirms quantitatively the observations made prior based on the data shown in Fig. 7.2.

In Fig. 7.3(b), the spatial variation of the energy density shows that the energy deposition is asymmetric with more energy deposited at the anode (positive values of $\hat{z}$) than near the cathode. Note that for all configurations shown, the energy density

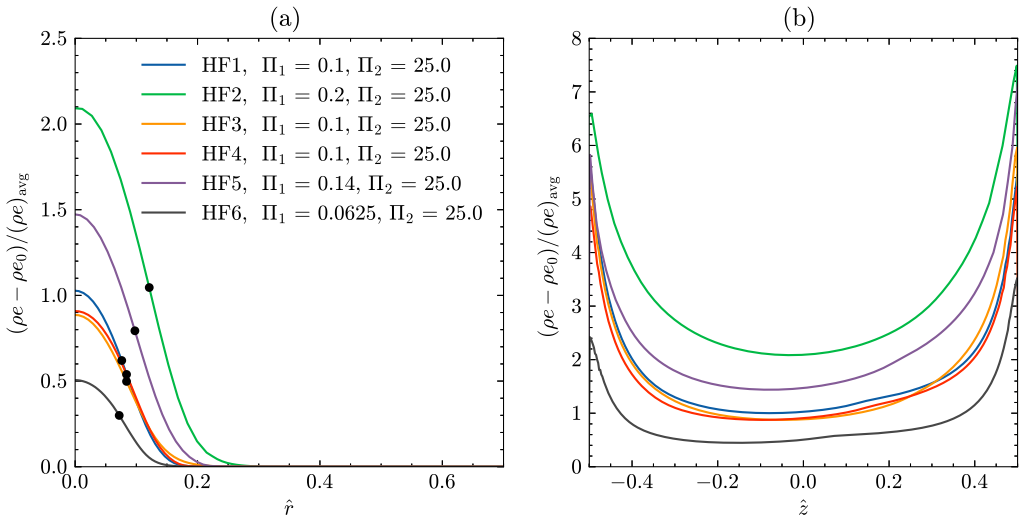

Figure 7.3: Normalized energy density gain $(\rho e - \rho_0 e_0)/(\rho e_{\text{avg}})$ along (a) the radial coordinate at the axial midplane location and (b) along the axis. In (a), black markers indicate the location of the inflection point of a Gaussian.

gain near the pin tips is severalfold times larger than the average value.

Comparing across configurations, the data suggest that the highest values of localized energy deposition at the pin tips are associated with the largest values of Π_2, although for high values of Π_2, the energy deposited in the middle of the gap increases also. We will return later to a more quantitative measure of inhomogeneity and its dependence on the geometry of the electrodes as parametrized by Π_1.

A second observation pertains to data from configurations HF1, HF3, and HF4 at $(\Pi_1, \Pi_2) = (0.1, 25.0)$ as shown in Fig. 7.3. It is apparent that, as far as the energy deposition process is concerned, the curves from the three datasets exhibit a nearly perfect collapse as expected based on dimensional analysis and inviscid scaling arguments.

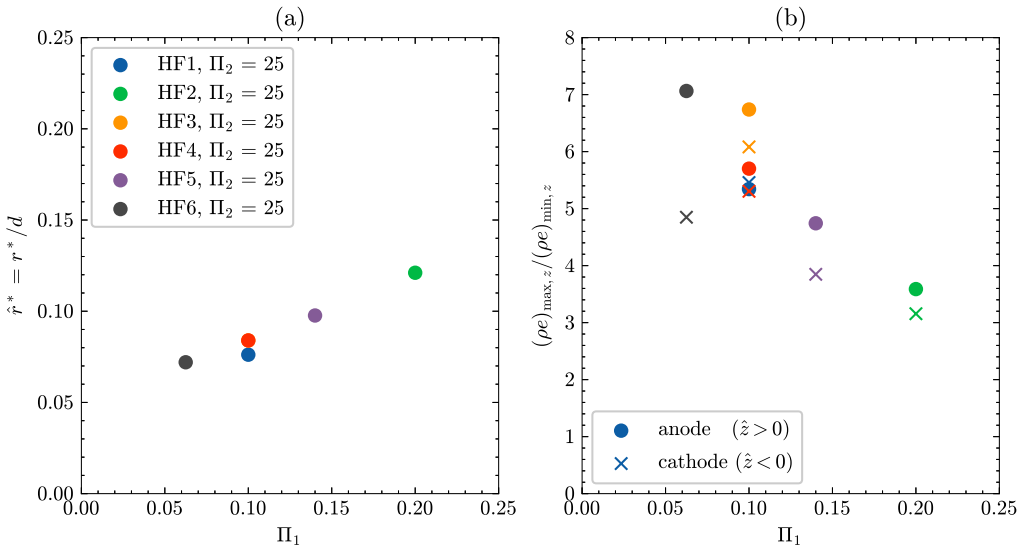

Figure 7.4: (a) $\hat{r}^*$ and (b) ratio of the maximum to minimum energy density gain along the axis on the anode ($\hat{z}$ >0) and cathode ($\hat{z}$ <0) sides. As Π_1 increases, the radius becomes larger and the inhomogeneity in the energy deposition across the gap decreases.

The trends shown in Fig. 7.3 are summarized in Fig. 7.4, where we plot $\hat{r}^*$ and the maximum ratio $(\rho e_{\max,z})/(\rho e)_{\min,z}$ along the axis on the anode side ($\hat{z} > 0$), and on the cathode side ($\hat{z} < 0$). Based on the data in Fig. 7.4(a), we conclude that as Π_2 increases, i.e., the radius of curvature of the pin electrodes increases relative to the electrode gap, the width of the energized gas kernel increases (when measured in units of gap distance). The energy density ratio decreases with increasing values of Π_2, indicating that the energy deposition is most inhomogeneous for sharp pins as expected. Furthermore, the difference between the cathode and anode regions also becomes smaller, with a higher energy density nearly always on the anode side, consistent with the observed morphology of the streamer discharge (see Fig. 5.2).

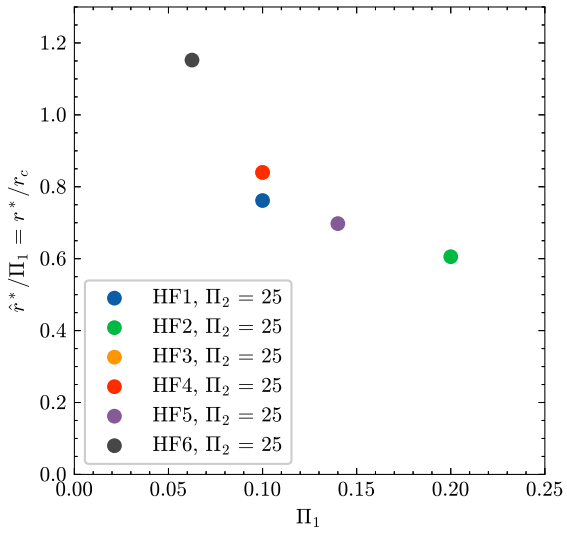

Figure 7.5: $\hat{r}^*/\Pi_1$ as a function of Π_1. The normalized variable represents the radius of the energized kernel normalized by the radius of curvature r_c.

It is often reported that the width of the plasma kernel and subsequent energized gases is related to the radius of curvature of the electrodes. In Fig. 7.5, the kernel width is shown made dimensionless by the radius of curvature $\hat{r}^*/\Pi_1 = r^*/r_c$ as a function of Π_1 at the axial midplane. When made dimensionless in this fashion, it is apparent that $r^*/r_c = \mathcal{O}(1)$, although there is a marked dependence on Π_1. As Π_1 increases, r^*/r_c decreases, indicating that, when holding the electrode gap constant and increasing the radius of curvature of the pins, the plasma channel will not grow in width as much as the radius of curvature. The inverse is also true. If the radius of curvature of the pins is made smaller by a factor, the plasma channel width will not decrease by the same factor.

Although self-similarity for configurations sharing the same values of Π_1 and Π_2 is discussed later in detail in Section 7.2, the data shown in Fig. 7.4 allow pre-

liminary considerations by comparing $\hat{r}^*$ and energy ratio $(\rho e)_{\max,z}/(\rho e)_{\min,z}$ from configurations HF1, HF3, and HF4. Across the configurations sharing Π_1 and Π_2, we observe differences with respect to the properties of the background gas, including background density, temperature, and pressure as outlined in Tab. 7.1. As explained, the dimensional analysis put forth in Section 7.3 is incomplete in that parameters related to the plasma, plasma discharge, and viscous/diffusive processes were neglected. There are a number of possible mechanisms responsible for differences between nominally self-similar configurations and those are discussed next.

First, recall that the normalized transport properties of electrons (i.e., normalized electron mobility and normalized diffusion coefficient) are functions of the reduced electric field strength E/N, which is kept constant across configurations. Since the number density of the gas N changes, so do the electron mobility and diffusion coefficient. A similar consideration holds for the ionization rate coefficient, which is also tied to E/N. Since transport properties and ionization rates are known to affect discharge morphology, it is not surprising to see only partial success in collapsing data for configurations that share parameters Π_1 and Π_2 only. Finally, we remark that at pressures higher than those considered in our work (see Tab. 7.1), it is likely that the discharge morphology will change dramatically, becoming filamentary and experiencing streamer branching (see Refs. [52; 104]). This discussion should serve as a word of caution on the broad generalizability of our conclusions beyond the conditions tested, while also recognizing the value of the high-fidelity mathematical models adopted for the study of this problem.

7.3.2 Assessing self-similarity

In this Section, the issue of self-similarity of configurations that share the same dimensionless parameters Π_1 and Π_2 is explored with respect to dimensionless density and axial component of velocity at select values of the dimensionless time $\hat{t}$. In order to achieve this goal, data from configurations HF1, HF3, and HF4 with $\Pi_1 = 0.1$ and $\Pi_2 = 25$ are considered. In Fig. 7.6, data are shown at $\hat{t} = 1$, corresponding to very early in the expansion process. At this point in time, there are slight differences among configurations throughout the gap. As far as $\hat{\rho}$ is concerned, the differences are most prominent in the middle of the gap, while for $\hat{u}_z$, the differences are most noticeable with respect to the value and axial location of peak velocity.

At this early time $\hat{t} = 1$, these minor differences are most likely related to lack of complete similarity in the discharge and attending energy deposition process. Yet, the collapse across configurations is convincing, although not as complete as for the simplified configurations discussed in Chapter 6, where the discharge was not simulated.

Figure 7.7 shows the dimensionless density $\hat{\rho}$ and axial component of velocity $\hat{u}_z$ at the end of the expansion process ($\hat{t} = 70.5$). It is apparent that the density is now lower throughout the gap and a stagnation flow has been established with fluid directed towards the center of the gap. The collapse of the data across configurations with the same values of Π_1 and Π_2 is reasonable and encouraging, although differences are apparent. Those differences are most obvious for the peak velocity and for the density in the middle of the gap and near the electrode tips, although differences do not exceed 20% of the mean across configurations for both fields.

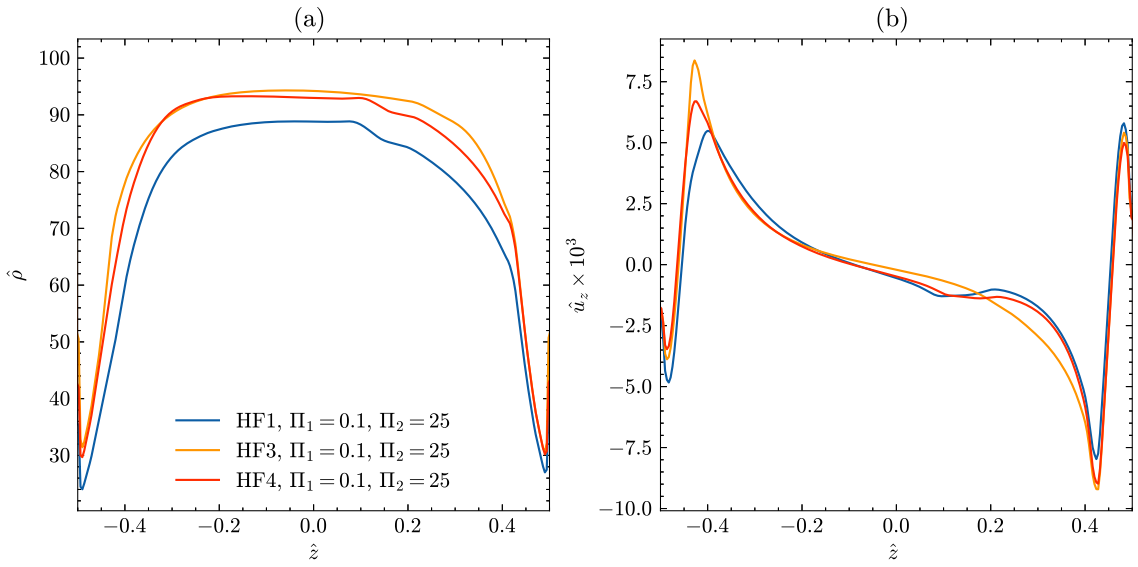

Figure 7.6: (a) Density and (b) axial component of velocity as a function of the axial coordinate along the axis at time $\hat{t} = 1$, i.e., very early on in the expansion of the hot pressurized channel.

At this point, while our data do not allow to attribute the remaining difference to any one process or mechanism that is not held constant, it is important to recall that, although the three configurations share the same values of $(\Pi_1, \Pi_2) = (0.1, 25)$, they do not share the same Reynolds number with $\mathrm{Re}/10^3 = 2324$, 1002, and 4648 for HF1, HF3, and HF4, respectively (see Tab. 7.1). In other words, HF3, HF1, and HF4 are characterized by increasing Reynolds numbers, so that one might expect viscous and diffusive processes to be less important for HF4 compared to HF3, especially over long intervals of time.

Based on the considerations above, one might expect the configuration with the lowest Reynolds number (HF3) to display more evident features tied to heat losses and viscous dissipation of momentum.

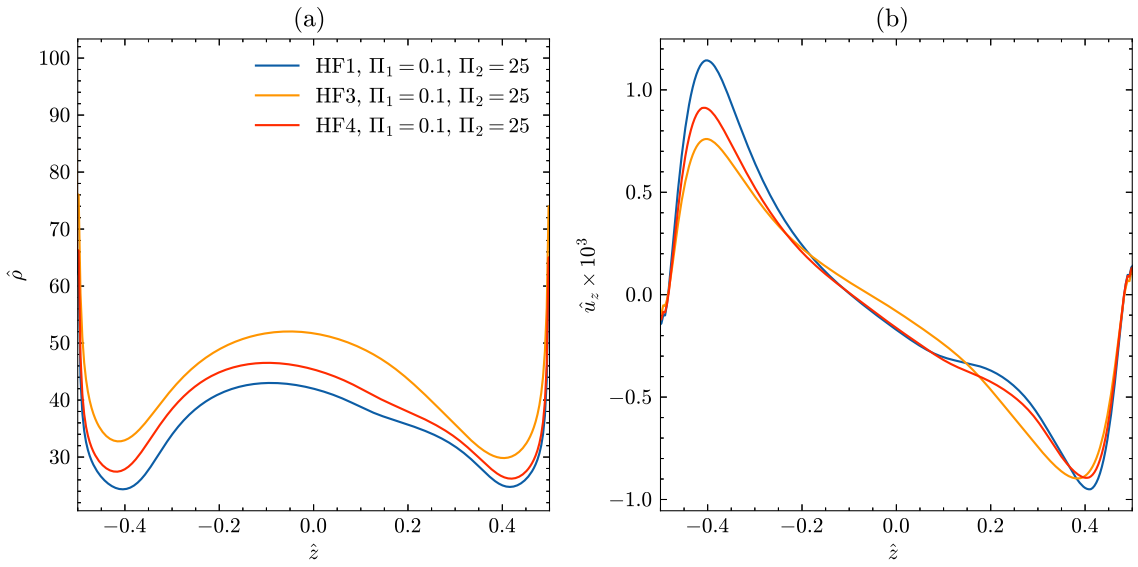

Figure 7.7: (a) Density and (b) axial component of velocity at time $\hat{t} = 70.5$, after the expansion of the hot pressurized channel. At this instant in time, a flow directed from the pin tips towards the axial midplane has developed.

A comparison across the three configurations in Fig. 7.7 does not show convincing monotonic trends with respect to the Reynolds number, although it is apparent that the density from HF3 (lowest Reynolds number) is highest (indicating lower temperatures and possibly more heat losses) and the peak value of the axial component of velocity is the lowest also (possibly indicating loss of momentum associated with viscous forces in the boundary layers formed on the electrode surfaces). As noted, the trends are not monotonic in that the data from HF4 (highest Reynolds number) lie in between those for HF3 and HF1 (intermediate Reynolds number).

We conclude by cautioning the reader that those are speculative attributions at best and only more detailed and expansive experimental and numerical studies with the high-fidelity models proposed in our work will allow to reach conclusive

attribution.

The maximum and minimum values of the dimensional pressure P, density ρ, and axial component of velocity u_z along the axis are shown in Fig. 7.8, which are compared to their dimensionless counterparts. It is apparent that, by making the variables dimensionless according to the postulates underlying the dimensional analysis and the choice of reference scales, the data from the various configurations exhibit a rather convincing collapse. As shown in Fig. 7.8, there appears to be better agreement between velocities induced near the anode (negative values) when compared to the region near the cathode (positive values). The collapse of the minimum and maximum values of $\hat{P}(\hat{t})$ is also rather convincing.

Regardless of the residual differences in the nominally self-similar solutions, the results put forth in this Section lend credibility to the postulated dimensional argument. From visual inspection of the data in Fig. 7.8, meaningful pressure fluctuations for this configuration end by $\hat{t} \approx 30$, at an instant when the self-similar solutions have not had time to diverge significantly in response to additional mechanisms not captured by the scaling arguments. Then, we argue that the solution is governed primarily by parameters Π_1 and Π_2 during the expansion phase, and to a much lesser extent by additional parameters, such as the Reynolds number. For example, we speculate that the Reynolds number will become more influential at later times when viscous and diffusive processes gain in importance.

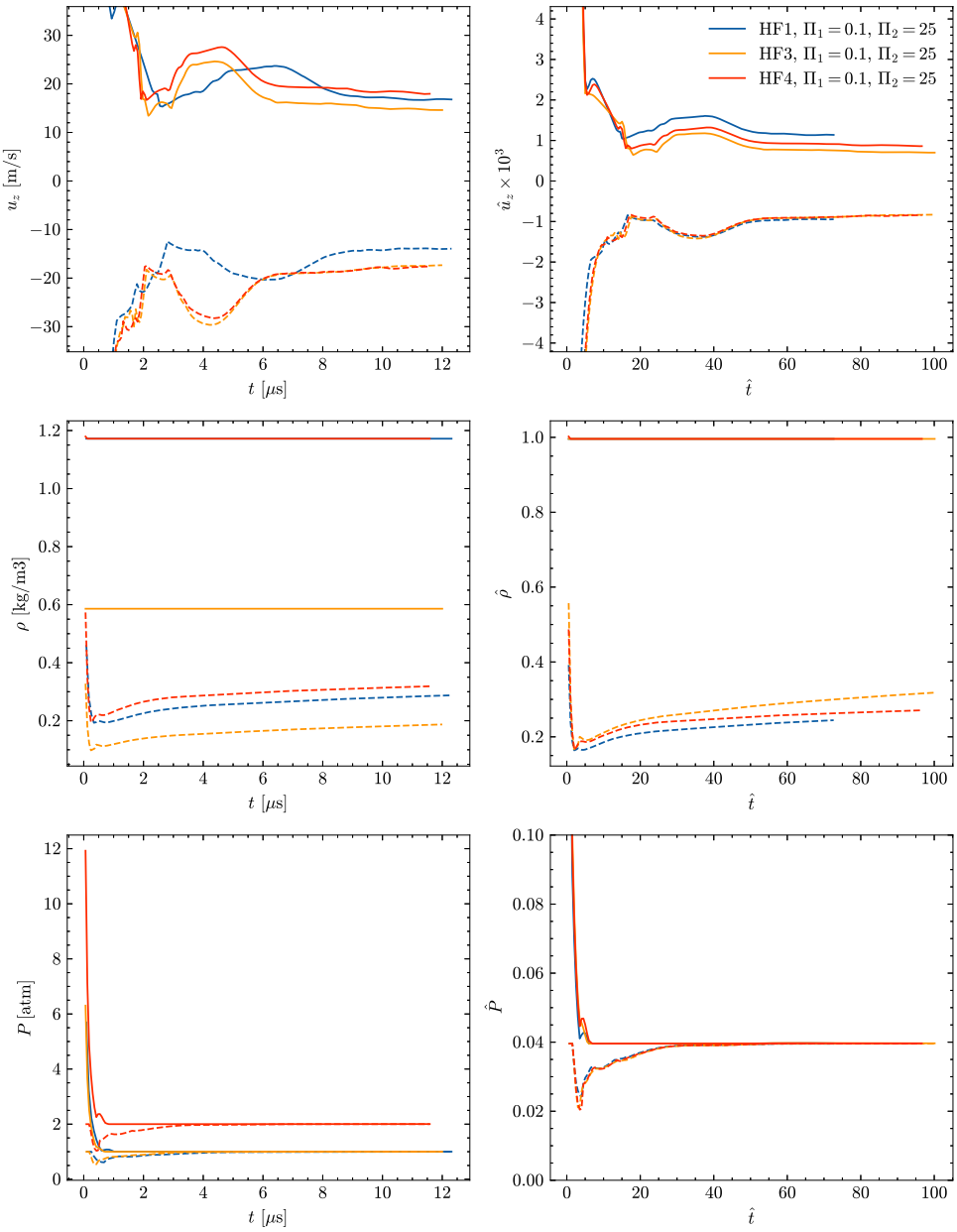

Figure 7.8: Maximum (solid) and minimum (dashed) dimensional quantities (left column) and dimensionless quantities (right column) for configurations HF1, HF3, and HF4 ($\Pi_1 = 0.1$ and $\Pi_2 = 25$). The self-similarity exhibited by the dimensionless variables is convincing, although not as successful as that observed in Chapter 6 for the simplified configurations and models.

7.3.3 Duration of the expansion phase and induced velocity

After having established a degree of self-similarity across configurations with the same pair (Π_1, Π_2), we turn our attention on the dependence of $\hat{t}_{\text{end}}$ and $\hat{u}_{z,\max}(\hat{t}_{\text{end}})$ on those two dimensionless parameters. Recall that those variables represent the dimensionless duration of the expansion phase and the peak value of the magnitude of the axial component of velocity along the axis. Note that in order to account for the asymmetry in the discharge, the maximum on the anode ($\hat{z} > 0$) and on the cathode ($\hat{z} < 0$) sides are reported separately. For details on the definition of those two variables, the reader should return to Section 6.4. The data are shown in Figs. 7.9 and 7.10, where both variables are plotted versus Π_2 for constant values of Π_1.

Values of $\hat{t}_{\text{end}}$ are in broad agreement with those discussed in Chapter 6 and shown in Fig. 6.10, as $\hat{t}_{\text{end}} = \mathcal{O}(10)$ with $\hat{t}_{\text{end}}$ increasing linearly with Π_2.

Since it is reasonable to expect that both $\hat{t}_{\text{end}}$ and $\hat{u}_{\max,z}(\hat{t}_{\text{end}})$ tend to zero as $\Pi_2 \to 0$, it is apparent that the linearity between those variables and Π_2 cannot hold near $\Pi_2 = 0$ and there is likely a non-linear dependence at even lower values of Π_2, which are not pertinent to actual discharges. In addition, the duration of the expansion phase displays a marked dependence on Π_1 with lower values of Π_1 (i.e., sharper pins) inducing higher values of $\hat{t}_{\text{end}}$ (longer durations of the expansion phase). This dependence is robust and extends across the range of Π_2 values investigated. Such dependence on Π_1 was much less pronounced for the data from simulations with the simplified configuration (e.g., see Fig. 6.10) and we attribute such heightened dependence on the interaction of the electrodes with the fluid.

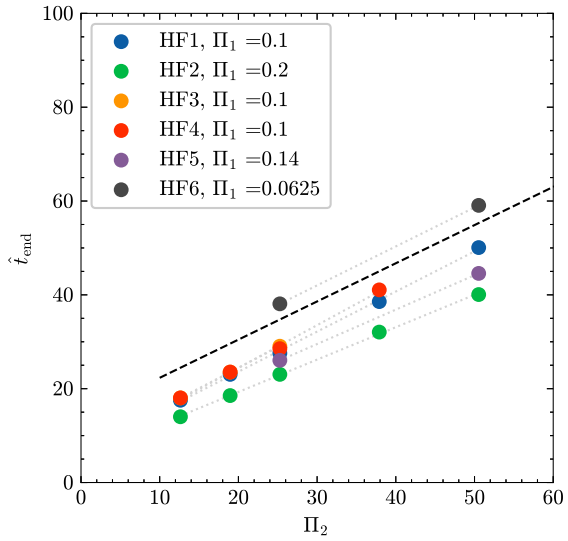

Figure 7.9: Duration of the expansion phase $\hat{t}_{\text{end}}$ as a function of Π_2 values for all configurations in Tab. 7.1. The dashed black line summarizes the results for the duration of the expansion phase from Chapter 6 and thin gray lines depict the best linear fit for each configuration. The values of the best linear fit are reported in Tab. 7.2.

The same data for $\hat{t}_{\text{end}}$ are also shown in Fig. 7.11(a) and plotted versus Π_1 for two selected values of Π_2 from the set of configurations denoted as HF1, HF2, HF5, and HF6 in Tab. 7.1. When plotted as in Fig. 7.11(a), it is apparent that as Π_1 increases, the duration $\hat{t}_{\text{end}}$ reaches a plateau, which is a behavior observed also in Fig. 6.12 pertaining to the data from the simplified configuration. Nonetheless, it seems that the data from the high-fidelity simulation retains a stronger dependence on Π_1, which is possibly due to the importance of the interaction of the flow with the electrodes as suggested above.

Linear fits employing data for a given value of Π_1 are performed and the resulting slope and intercept are reported in Tab. 7.2, where it is apparent that

while the slope is not very sensitive to Π_1, the intercept increases with decreasing values of Π_1 as already discussed. Furthermore, the R-squared value demonstrates that the dependence is very well approximated by a linear function.

Table 7.2: Values of the coefficients of the best linear fit for the duration of the expansion phase $\hat{t}_{\text{end}}$ for all configurations, based on the data presented in Fig. 7.9. The fit is of the form $y = mx + b$, with slope m and y-intercept b, with reported value of R-squared. Note that only 2 data points available for configurations HF5 and HF6.

Configuration	Π_1	m	b	R^2
HF1	0.1	0.85	6.52	0.99
HF2	0.2	0.69	5.49	0.99
HF3	0.1	0.87	7.0	0.99
HF4	0.1	0.91	6.24	0.99
HF5	0.14	0.73	7.51	-
HF6	0.0625	0.83	17.1	-

Figures 7.10(a) and 7.10(b) show the maximum of the magnitude of the axial component of velocity along the axis on the anode and cathode sides, respectively, measured at the end of the expansion process.

From the data shown, it is apparent that, for a given value of Π_1, the velocity increases with increasing Π_2 and this is a robust trend holding across all configurations. Yet, there is a marked dependence of the data on Π_1, in that as Π_1 increases, so does the magnitude of the velocity for a given value of Π_2.

For the configurations with the largest values of Π_1, the data demonstrate that the velocity reaches a plateau for sufficiently large values of Π_2. Also, the difference between the maximum magnitude of the axial component of velocity on the anode (where it is larger) and cathode sides is most pronounced for configurations with large values of Π_1.

Note that the asymmetry in the velocity field engendered by the discharge was already highlighted in Chapter 5, where it was noted that the torus forms slightly below the midplane, consistent with a larger negative velocity directed from the anode (top electrode) downwards compared to that directed from the cathode (bottom electrode) upwards. Similar observations on asymmetric flows were made in experimental studies [38,39], where it was noted that repeated nanosecond discharges brought about large scale asymmetric flows. While it is unclear whether the effects described here are cumulative over multiple pulses or not, asymmetric density and velocity fields are not accounted for in simplified modeling approaches (such as that explored in Chapter 6 in this dissertation).

A comparison of the data in Fig. 7.10 against those in Fig. 6.10 pertaining to the simplified configuration reveals that the trends are consistent between the two datasets as the velocity magnitude increases with both Π_1 and Π_2, although qualitative and quantitative differences remain. For similar values of the pair (Π_1, Π_2) for which data from both sets of simulations are available, the velocities from simulations conducted with high-fidelity models and realistic pin geometries are consistently higher by 50% or more (in certain cases, nearly double). Moreover, in the case of simulations from high-fidelity models, the velocity magnitude appears to reach a plateau, which is not apparent in the data from simplified configurations.

In the range of values of Π_2 considered, $\hat{u}_{z,\max}(\hat{t}_{\text{end}})$ reaches a plateau for $\Pi_2 \geq 30$ or so. This suggests that for a sufficiently large value of Π_2,

$$\hat{u}_{z,\max}(\hat{t}_{\text{end}}) \approx u(\Pi_1), \tag{7.33}$$

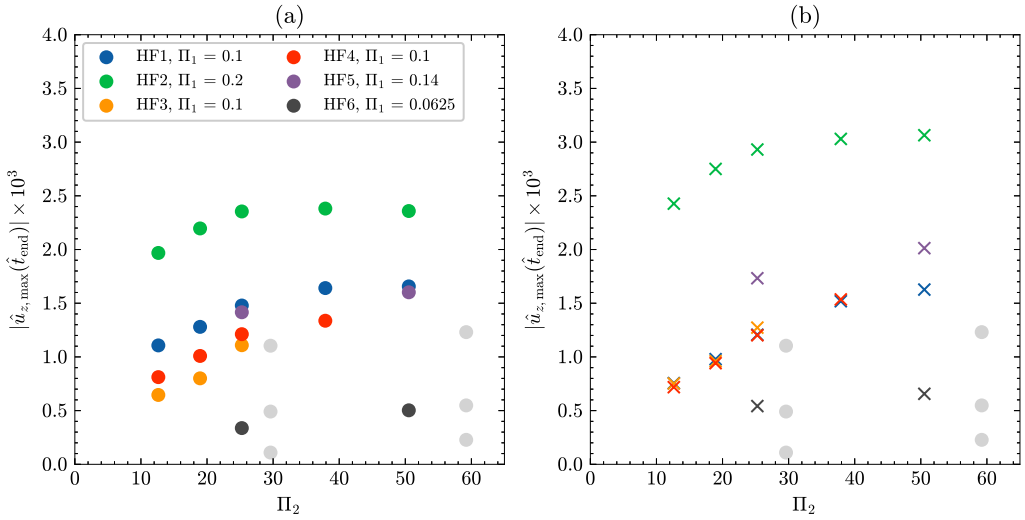

Figure 7.10: Maximum of the magnitude of the axial component of velocity at the end of the acoustic phase $u_{z,\max}(\hat{t}_{\text{end}})$ for (a) the anode side ($\hat{z} > 0$) and (b) the cathode side ($\hat{z} < 0$). Grey symbols illustrate the results from the simplified model presented in Chapter 6 for a similar Π_1 and Π_2 range (see Fig. 6.10).

where $u(\Pi_1)$ is a function that we postulate depends solely on Π_1. Then for a sufficiently large Π_2, we have

$$u_{z,\max}(t_{\text{end}}) \approx \frac{u(\Pi_1)}{r_c^2}\sqrt{Qd/\rho_0}. \tag{7.34}$$

Equation (7.34) suggests that the peak value of the axial component of velocity at the end of the gas expansion following the discharge scales as $u_{z,\max}(t_{\text{end}}) \propto \sqrt{Q}$ when holding d and r_c, i.e, the geometry of the electrode assembly, and ρ_0, i.e., the background density, constant.

7.3.4 Volumetric expansion engendered by the acoustic phase

In the final part of the study, the effect of Π_1 and Π_2 on the growth of the hot gas kernel during expansion is explored. Emphasis on this process is important

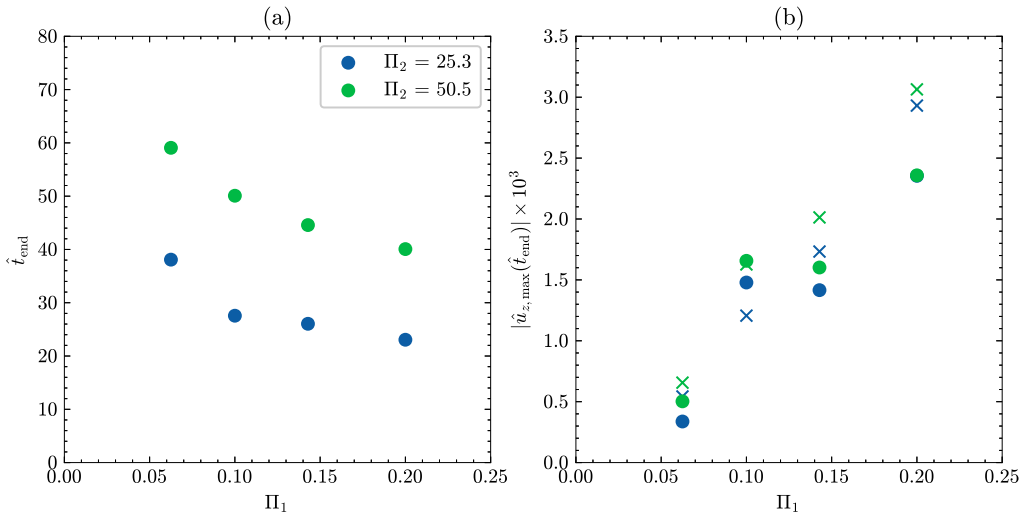

Figure 7.11: (a) Duration of the expansion phase $\hat{t}_{\mathrm{end}}$, and (b) corresponding magnitude of the axial component of velocity at the end of the expansion $\hat{u}_{z,\max}(\hat{t}_{\mathrm{end}})$ in the cathode area (circles) and anode area (crosses). The data are presented for selected Π_2 configurations from Tab. 7.1 for which simulations for all Π_1 values are available.

for ignition applications, since the probability of ignition is very sensitive to the size of the hot gas kernel as the size of the kernel governs diffusive losses over longer time scales.

The growth of the hot gas kernel is well illustrated in Fig. 7.12, where the radial distribution of the normalized temperature gain $(T - T_0)/T_0$ on the midplane of the gap ($\hat{z} = 0$) is shown immediately after energy deposition (solid lines) and at the end of the expansion process (dotted lines). Profiles are shown for different values of Π_2 for configurations in set HF1 ($\Pi_1 = 0.1$ as in Tab. 7.1). Under the reasonable assumption that the radial dependence of the normalized temperature gain is Gaussian, the width of the hot kernel is defined as the dimensionless radial distance $\hat{r}^*$ from the axis where the temperature gain is 0.607 times its peak value at the axis. Based on the data in Fig. 7.12, it is apparent that the width of the hot kernel before expansion (gray markers) is largely independent of Π_2, but the width at the end of the expansion process (black markers) varies markedly with Π_2. In other words, the expansion process brings about an important growth of the hot kernel and the resulting kernel width is a strong function of Π_2.

The data presented and discussed in Chapter 5 brought us to conclude that the spatial distribution of the normalized energy density gain is rather inhomogeneous with marked dependencies on both radial and axial coordinates. Consequently, it is natural to question the broad relevance of $\hat{r}^*$ shown in Fig. 7.12 and discussed above, as $\hat{r}^*$ measures the width of the kernel on the midplane. In order to address this issue, we also performed a similar analysis of the width of the kernel near the pin tips (not shown) and determined that the width of the hot kernel does not vary by more

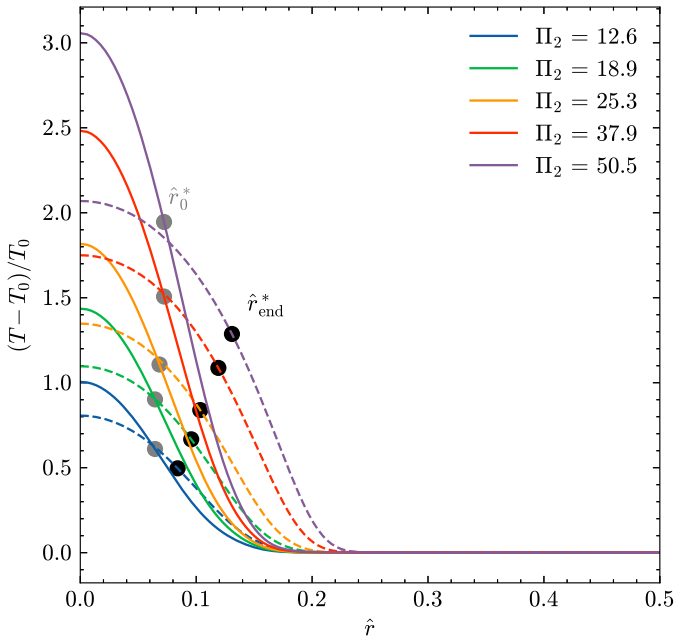

Figure 7.12: Visual depiction of the volume expansion for case HF1 ($\Pi_1 = 0.1$) and different values of Π_2. The radial profiles of $(T - T_0)/T_0$ before expansion are plotted with solid lines, and the same profiles after the expansion are plotted with dashed lines. $\hat{r}^*$ is calculated by computing the radial location of $\max 0.607(T - T_0)/T_0$, which is annotated with a gray marker before the expansion and a black marker after the expansion.

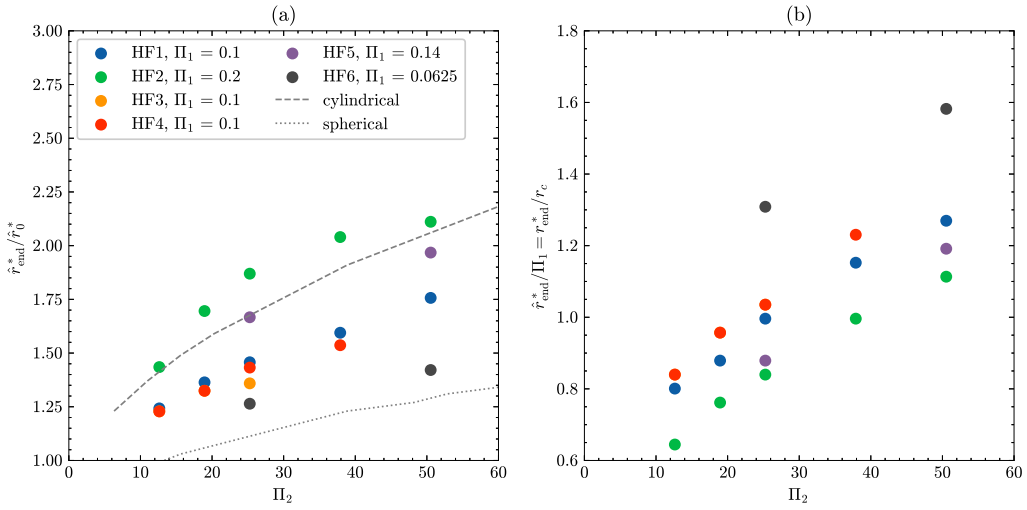

Figure 7.13: (a) Volumetric expansion of hot gas kernel during the acoustic phase measured using the kernel radius before ($\hat{r}^*_0$) and after ($\hat{r}^*_{\rm end}$) the expansion. (b) $\hat{r}^*_{\rm end}/\Pi = r^*_{\rm end}/r_c$ showing the final radius relative to the pin curvature. Results shown for all cases in Tab. 7.1. Data labeled "cylindrical" and "spherical" are calculated assuming an overpressure resulting from a uniform energy deposition with an initial radius $\hat{r}_0 = \hat{r}_c$ and a calorically perfect gas (e.g., $P/P_0 = \Pi_2(\gamma - 1)$).

than 20% along the axis, so that $\hat{r}^*$ shown in Fig. 7.12 is taken to be a well-posed measure of the kernel width, which is nearly cylindrical (although the energy density itself varies significantly along the axis).

A summary of the effect of Π_1 and Π_2 on the width of the hot kernel before ($\hat{r}^*_0$) and after expansion ($\hat{r}^*_{\rm end}$) is provided in Fig. 7.13. Those are complemented by additional data from inviscid Euler simulations for the expansion of cylindrical and spherical kernels that share the same value of Π_2 and use a calorically perfect gas model. In Fig. 7.13(a) where it is apparent that $r^*_0/r^*_{\rm end} > 1$ for all configurations as expected and that the ratio increases with increasing Π_2 for a given Π_1.

For a given value of Π_2, the ratio is larger for higher values of Π_1, indicating

that electrode geometries with "thick" pins (i.e., pins with a larger radius of curvature compared to the electrode gap distance) result in a greater increase in the width of the hot gas kernel during the expansion process. This is possibly due to the effect of increased flow confinement by the electrodes brought by the increase in the radius of curvature (in units of gap distance), leading to higher outward radial velocities.

For low values of Π_1 (i.e., "sharper" pins), it is also apparent that the dependence of r_0^*/r_{end}^* on Π_2 is nearly linear while at the highest value of $\Pi_1 = 0.2$, the functional dependence appears to saturate with a manifest non-linear dependence on Π_2.

Finally, comparison of the data against those from simulations of cylindrical and spherical kernel expansions at initial overpressures consistent with Π_2 indicate that the ratio falls between those from the two idealized configurations and that as Π_1 decreases, the ratio tends to that from spherical kernel expansions, while for increasing Π_1, the ratio is closest to the higher ratio from the cylindrical kernel, again suggesting that fluid confinement for large values of Π_1 plays a role in controlling the ratio r_0^*/r_{end}^*. Conversely, for small values of Π_1, the growth of the hot kernel is closer to that of a spherical kernel.

The data in Fig. 7.13(b) shows that the ratio r_{end}^*/r_c lies between 0.6 and 1.6 for all configurations considered and that the ratio increases with Π_2 also, yet it decreases for increasing Π_1, contrary to the observation pertaining to the data in Fig. 7.13(a). Thus, the width of the hot kernel at the end of the expansion phase is $\mathcal{O}(r_c)$, although it might differ from r_c by a factor between 0.5 and 2.0. Furthermore, in the case of "thick" pins (i.e., largest value of $\Pi_1 = 0.2$), the width of the expanded

gas kernel might be a fraction of the radius of curvature or comparable to it (at the highest values of Π_2 considered). Conversely, in the case of "pointy" electrodes (i.e., smallest value of $\Pi_1 = 0.0625$), the width of the expanded gas kernel is guaranteed to be significantly larger than the radius of curvature.

7.4 Evaluating regimes

7.4.1 Competing effects of advection and diffusion

As discussed and illustrated in Chapter 5, the expansion of the heated gas kernel engenders fluid motion. Under select circumstances, the fluid motion results in the formation of a toroidal structure of hot gases which then collapses near the midplane in between the electrodes, giving rise to a localized region of heated gases. Under other circumstances, no such toroidal structure is observed.

In this Section, we build upon the metrics and processes discussed in this Chapter as well as on the dependence of select features of the hydrodynamic state induced by the discharge on parameters Π_1 and Π_2 in order to propose a suitable parametrization of these two disparate regimes. The parametrization is formalized in a proposed regime diagram that extends that proposed by Dumitrache et al. in [12; 11]. The regime diagram is then populated with data from this study and data available from the literature and the transition between configurations that exhibit toroidal collapse and diffuse kernels is identified.

The different regimes have an impact on the successful or unsuccessful ignition, and on the morphology of the ignition kernel.

We approach the task of defining a criterion that distinguishes between the

regime of toroidal collapse and the diffusive one by defining a convective transit time τ_{transit}, which is equal to the time required by a parcel of fluid to travel a distance equal to half the gap $d/2$ when moving at a speed equal to the axial component of velocity at the end of the expansion process. One component of the transition between the toroidal collapse regime and the diffuse regime might be related to the time required for such parcel to reach the midplane. Should the transit time be very long (relative to a second scale parametrizing a competing process), toroidal collapse might be inhibited altogether. Mathematically, the transit time reads

$$\tau_{\text{transit}} = \frac{0.5d}{|u_{z,\max}(t_{\text{end}})|}. \tag{7.35}$$

In order to seek more clarity as to the dependences of τ_{transit} from relevant dimensional parameters, we approximate the velocity as dependent only on Π_1 and write

$$\tau_{\text{transit}} \approx \frac{0.5r_c^2}{u(\Pi_1)} \sqrt{\rho_0 d/Q}. \tag{7.36}$$

From Equation (7.36) the role of select dimensional parameters on the transit time is apparent and a graphical representation is provided in Fig. 7.14. First, we note the dependency on the inverse of the square root of the so-called *lineic energy* (Q/d) and also the square root of the background density ρ_0. We also note the effect of $u(\Pi_1)$. Recall that from Fig. 7.11, it is apparent that $u(\Pi_1)$ increases sharply with increasing values of Π_1, which might help explain why in experimental studies, a convenient manner of transitioning between hydrodynamic regimes (i.e. toroidal collapse vs. diffusive regime) is to adjust the electrode gap distance while keeping everything else constant, thereby changing $\Pi_1 = r_c/d$. As shown in Fig. 7.11, adjusting Π_1 in the

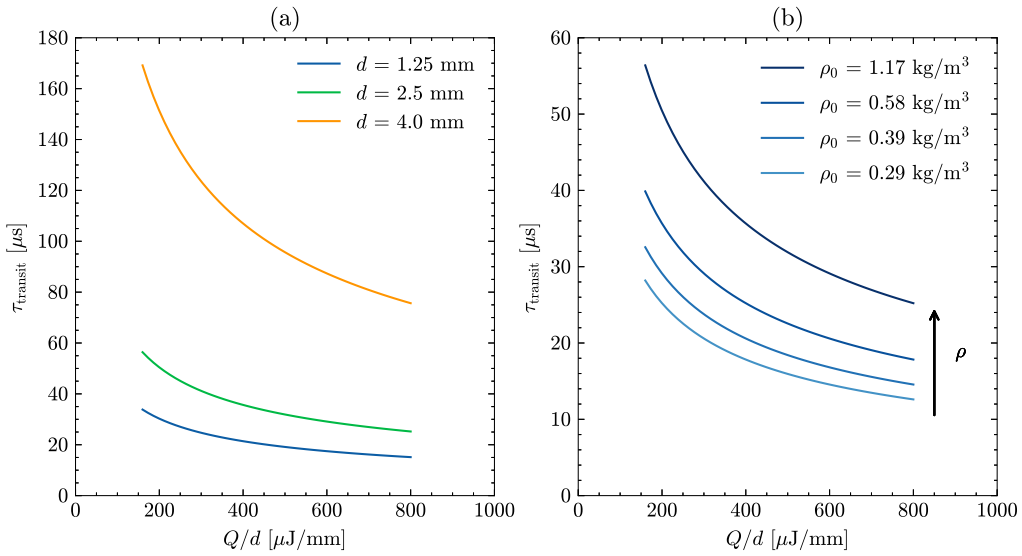

Figure 7.14: Examples of convective transit time τ_{transit} calculated using Eq. (7.36) for (a) three different gap lengths ($T_0 = 300$ K, $P_0 = 1$ atm, $\rho_0 = 1.17$ kg/m^3, and $r_c = 250$ μm) and (b) four values of background density ($d = 2.5$ mm and $r_c = 250$ μm) as a function of Q/d.

range 0.05 to 0.2 allows to change $u(\Pi_1)$ in the range 0.25 to 3, which provides the flexibility to adjust the transit time over an order of magnitude ($3/0.25 = 12 \approx 10$).

In the above discussion, we introduced the transit time, which is a convective timescale that is associated with the movement of fluid towards the midplane. In order to identify a criterion that marks a transition between the two hydrodynamic regimes of interest, i.e., one with a toroidal collapse and one without, a process competing with convective transport and inhibiting toroidal collapse must be proposed.

In what follows, we postulate that diffusion of heat radially away from the kernel's axis is in competition with the process of convective transport of energy

towards the midplane. Consequently, we define a relevant diffusive timescale τ_{diff} as

$$\tau_{\text{diff}} = \frac{r_{\text{ref}}^2}{D_0} = \frac{[f(\Pi_1, \Pi_2) r_c]^2}{D_0}, \tag{7.37}$$

where r_{ref} is a reference scale taken to be equal to the kernel width at the end of the expansion process, D_0 is the thermal diffusion coefficient $D_0 = \lambda_0/(\rho_0 c_p)$, λ_0 being the thermal conductivity [W/m-K] of the background gas, ρ_0 is the density [kg/m^3], and c_p is its specific heat capacity at constant pressure [J/kg-K]. In Eq. (7.37) above, the kernel width after the expansion relative to the radius of curvature of the pin $f(\Pi_1, \Pi_2)$ is evaluated from a surface fit to the data shown in Fig. 7.13 (a detailed discussion of the fitting procedure is provided in Appendix H). The thermal diffusion coefficient is calculated at background conditions for simplicity.

Next, a preliminary evaluation of the values taken by the ratio $\tau_{\text{transit}}/\tau_{\text{diff}}$ is presented leveraging two configurations for which high-fidelity simulation data are available. The first configuration ("A") features a 800 μJ discharge in atmospheric air at 300 K and 1 atm, while the second ("B") features a 190 μJ discharge in stoichiometric ethylene/air at 600 K and 0.5 atm, which correspond to conditions relevant to the flame holding cavity of a scramjet at a flight Mach number of 4 (see Ref. [5] for more details).

Since the minor concentration of ethylene is largely inconsequential to the hydrodynamic processes induced by the energy deposition, configurations "A" and "B" can be taken to both represent discharges in air.

Finally, the voltage pulse is adjusted between the two so that the energy deposition occurs at a common reduced electric field strength of 200 Td. In other

words, since configuration "B" features a background density that is four times lower than that in configuration "A," the peak voltage is also lower by the same factor. The configuration parameters are provided in Tab. 7.3.

Table 7.3: Summary of configuration parameters for configurations "A" and "B" (see commentary for a discussion). For both configurations $d = 2.5$ mm and $r_c = 250$ μm.

Config.	Q [μJ]	ρ_0 [kg/m^3]	P_0 [atm]	Π_2	Π_1	τ_{transit} [μs]	τ_{diff} [μs]	$\tau_{\text{transit}}/\tau_{\text{diff}}$	Collapse?
A	800	1.17	1	50.5	0.1	39.8	8000	4.99×10^{-3}	Yes
B	190	0.295	0.5	25.3	0.1	40.9	767	53.3×10^{-3}	No

Next, the transit and diffusion times are calculated based on the dimensional parameters as well as the values of Π_1 and Π_2 according to the theory explained in this Section and the values are included in Tab. 7.3 for reference.

It is apparent that both configurations share the same value of τ_{transit} since they share the same product $\rho_0 d/Q$ and we neglected the dependence of τ_{transit} on Π_2, which is lower for configuration "B." On the contrary, the diffusive time scale is much smaller for configuration "B" compared to configuration "A" on the account of the higher background gas temperature and lower pressure.

Finally, the ratios $\tau_{\text{transit}}/\tau_{\text{diff}}$ are equal to 5.0×10^3 and 53×10^3 for configuration "A" and "B," respectively.

As shown in Chapter 5, configuration "A" leads to toroidal collapse and, as shown in Ref. [5], configuration "B" does not, with the discharge leading to a diffuse kernel of hot gases. Thus, the two distinct hydrodynamic behaviors (toroidal collapse versus diffuse kernel) correlate with two very different values of the ratio $\tau_{\text{transit}}/\tau_{\text{diff}}$, whereby when the ratio is small, toroidal collapse occurs and when it is large, it does not.

We hasten to note that, at this point, there is no reason to attempt to propose a critical value of $\tau_{\text{transit}}/\tau_{\text{diff}}$ that identifies the transition between one regime and the other, rather numerical and experimental studies are required to identify a critical value for the ratio, which, of course, requires that the proposed theory be at all applicable and sensible. More analysis on the plausibility of the above theory is presented in Section 7.4.2, starting from experimental data available in the literature.

7.4.2 A proposal for a regime diagram of the hydrodynamic regime

In this Section, we first revisit select aspects of the analysis presented thus far with the objective to account for the full dependency of the transit time on both Π_1 and Π_2. Then, we manipulate the ratio $\tau_{\text{transit}}/\tau_{\text{diff}}$ in order to expose its dependence on Π_1, Π_2, Re, and Pr as defined in this Chapter. Then, the experimental data from the literature are used to ascertain whether a boundary separating the toroidal collapse regime from the diffusive regime exists in the $\Pi_1 - \Pi_2$ plane. Finally, results from the high-fidelity simulations are used to further illustrate the merits of the theory and attending regime diagram.

We begin by defining the dimensionless transit time $\hat{\tau}_{\text{transit}}$

$$\hat{\tau}_{\text{transit}} = \frac{0.5}{|\hat{u}_{z,\max}(\hat{t}_{\text{end}})|} = \frac{0.5}{v(\Pi_1, \Pi_2)}, \tag{7.38}$$

where we get $v(\Pi_1, \Pi_2)$ is represented by a surface fit to the data in Fig. 7.10 (details of the fitting procedure are discussed in Appendix H), and the dimensionless diffusive time $\hat{\tau}_{\text{diff}}$ is defined as

$$\hat{\tau}_{\text{diff}} = \frac{\tau_{\text{diff}}}{\mathcal{T}} = \frac{f(\Pi_1, \Pi_2)^2}{D_0} \frac{r_c^2}{\mathcal{L}^2} \frac{\mathcal{L}^2}{\mathcal{T}}. \tag{7.39}$$

Next, the right hand side of Eq. (7.39) is multiplied and divided by the kinematic viscosity [m^2/s] of the background gas ν_0 to obtain

$$\hat{\tau}_{\text{diff}} = \frac{\nu_0}{\nu_0} \frac{\mathcal{L}(\mathcal{L}/\mathcal{T})}{D_0} f(\Pi_1, \Pi_2)^2 \times \Pi_1^2, \tag{7.40}$$

and then rearranged

$$\hat{\tau}_{\text{diff}} = \underbrace{\frac{\nu_0}{D_0}}_{\text{Pr}} \underbrace{\frac{\mathcal{L}(\mathcal{L}/\mathcal{T})}{\nu_0}}_{\text{Re}} f(\Pi_1, \Pi_2)^2 \times \Pi_1^2. \tag{7.41}$$

Finally, we take the ratio of the dimensionless times

$$\frac{\hat{\tau}_{\text{transit}}}{\hat{\tau}_{\text{diff}}} = \frac{\tau_{\text{transit}}}{\tau_{\text{diff}}} = \frac{0.5}{\text{Pr Re}} \frac{1}{v(\Pi_1, \Pi_2)} \frac{1}{f(\Pi_1, \Pi_2)^2 \times \Pi_1^2}. \tag{7.42}$$

In Fig. 7.15, we provide a pseudocolor plot of the scaled ratio of the time scales Pr Re $\hat{\tau}_{\text{transit}}/\hat{\tau}_{\text{diff}}$ on the Π_1,Π_2 plane spanning ranges pertinent to the configurations considered in this study. We also include select contours for increasing values.

The data from the experimental work by Dumitrache et al. [12], discussed in detail in Section 7.1, is now presented in the context of our work. The reported values of the gap length, deposited energy, background pressure, and radius of curvature are used to calculate Π_1 and Π_2 as described in Section 7.2 and plotted in Fig. 7.16. The error bars in the Figure represent the uncertainty in the reported value of the radius of curvature and the markers show whether the configuration is in the diffusive (crosses) or toroidal (circles) regime. The Figure is augmented with select results from our numerical studies using high-fidelity models (enclosed by the gray dashed box). Different markers are used to represent the diffusive (filled crosses) and toroidal

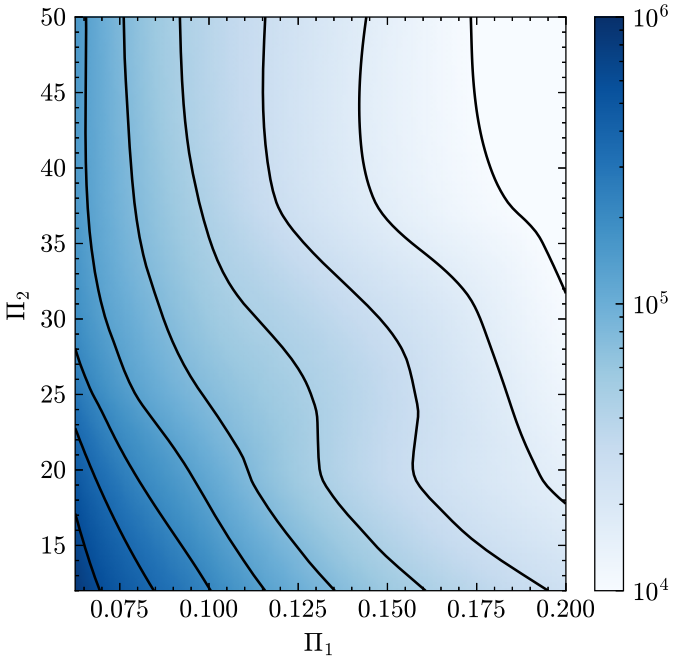

Figure 7.15: Scaled ratio of time scales Pr Re $\times \hat{\tau}_{\text{transit}}/\hat{\tau}_{\text{diff}}$ on the $\Pi_1 - \Pi_2$ plane with ranges consistent with the configurations considered in this study. Ten equally spaced contours in logarithmic space between 10^4 and 10^6 in are shown in black solid line.

(squares) regimes. Finally, the symbols are colored by the configuration Reynolds number.

The uncertainty in the radius of curvature of the electrode pin tip is a recurrent issue in the experimental study of nanosecond discharges. When operating such systems, hundreds or even thousands of discharges are produced, leading to erosion of the pin tips, which makes the radius of cuvature a somewhat ill-defined quantity. Thus, for any given configuration, a *range* of Π_1 values must be considered and the resulting uncertainties factored into the analysis of the hydrodynamic effect.

The gap lengths d used in the experimental work by Dumitrache et al. [12] range from 0.5 to 8 mm, the reported radius of curvature r_c is between 150 and 300 μm due to measurement uncertainty, and all measurements were produced at atmospheric conditions. The geometric parameters suggest significant overlap with the range of Π_1 explored in this study, with their reported values of deposited energy Q producing Π_2 values significantly higher than those explored in our work, as seen in Fig. 7.16. It also becomes clear that the parametric study by Dumitrache et al. [12] moves simultaneously across Π_1 and Π_2 space, with significant changes in the value of the Reynolds number as well. To improve the understanding of the hydrodynamic effect, future numerical studies should target larger Π_2 values produced by most experimental studies [12; 11; 101] and currently limited by the thermodynamic model.

The configurations considered in our work (enclosed by the gray box) illustrate more clearly the dependence of the hydrodynamic regime on the dimensionless parameters. Our results are broadly in agreement with those presented by Dumitrache et al. [12], where we observe the diffusive regime at low values of Π_1 and Π_2, and the

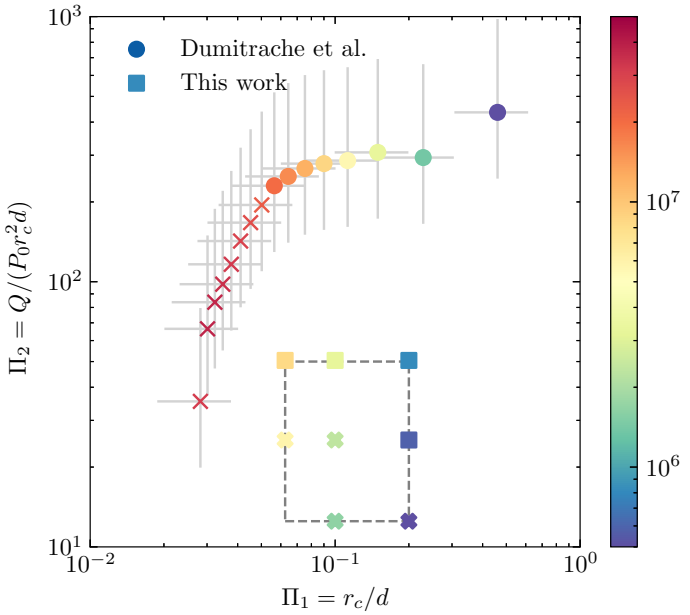

Figure 7.16: Data from Dumitrache et al. [12] and results from this work (enclosed by the gray box) plotted in the $\Pi_1 - \Pi_2$ parameter space. Error bars represent the reported uncertainty in the measured pin radius of curvature $r_c \approx$ 150-300 μm of the experimental configuration and the marker represents the diffusive regime (crosses and filled crosses) or toroidal regime (circles and squares). The Reynolds number of the configuration is represented through the colorscale. All data is at atmospheric conditions (300 K and 1 atm).

toroidal regime at high values of Π_1 and Π_2, although this was observed in a different region of the parameter space. It is also clear that the regime transition value of Π_2 may change for different Π_1 configurations, as seen in the marker sequence changing from the $\Pi_1 = 0.1$ (HF1) configuration to the $\Pi_1 = 0.2$ configuration (HF2). The results suggest that the transition occurs for $\tau_{\text{transit}}/\tau_{\text{diff}} \approx 2 \times 10^{-2}$.

The reader is also reminded that there is likely to be an important Reynolds dependence that is not captured solely by the Π_1 and Π_2 values of the configuration. For a given set of thermodynamic conditions (atmospheric in this case), the Reynolds number has a strong dependence on the Π_1 value and a weaker dependence on the value of Π_2 as seen in Fig. 7.16. The Reynolds number may also change independently of Π_1 and Π_2 depending on the thermodynamic conditions and when adjusting other configuration parameters consistently with the relationships outlined in Section 7.2. All of these effects should be considered in the study of the hydrodynamic effect of nanosecond discharges.

Chapter 8

Summary and conclusions

This dissertation presents a detailed and systematic characterization of the hydrodynamic effect induced by nanosecond discharges in air. First, the temporal evolution of atmospheric air subject to a nanosecond discharge is studied in an isochoric and adiabatic zero-dimensional reactor. The state of non-equilibrium engendered by the discharge is analyzed by identifying the kinetic processes responsible for heating, characterizing vibrational excitation, and the role of dissociated molecules. Fractions of energy stored in sensible heating, vibrational, and chemical non-equilibrium are identified based on prevailing notions in the literature, and a novel approach based on constrained equilibrium is developed and applied to characterize the extent of non-equilibrium quantitatively and aid the analysis in more complex multi-dimensional configurations.

The same detailed analysis of non-equilibrium effects is employed in a parametric study of discharges in air by varying parameters such as energy deposited per unit volume, and voltage waveform. Additional analysis compares the results of the reactor simulations to those generated with a reduced chemical kinetics mechanism to be used for multidimensional high-fidelity simulations.

In the second part of this dissertation, we develop and apply a novel frame-

work for multidimensional high-fidelity simulations of nanosecond discharges in air. The novel framework combines high-fidelity physical models with various solvers to allow for efficient simulations of multi-pulse discharges over long intervals relevant to combustion phenomena. The capabilities of the solver are demonstrated by simulating a typical nanosecond discharge in air at atmospheric conditions, where 800 μJ per pulse are deposited over two consecutive pulses. An in-depth analysis showcases the detailed insight that such simulations provide, including streamer propagation, spatially resolved electrical properties of the resulting conductive channel (e.g., the conductivity), and the spatial distribution of the energy density deposited by the electric field into the plasma gas. Energy deposition is followed by the expansion of the energized plasma channel, giving rise to mass, momentum, and energy transport in the electrode gap region. Those processes are also characterized in detail with temporal and spatial resolution for all pertinent quantities and fields. The effect of the first pulse on the propagation path of streamers and shape of the conducting channel brought by the second nanosecond pulse is also demonstrated.

Finally, simulations of two configurations are performed to investigate hydrodynamic effects brought by nanosecond discharges in air: a simplified model that assumes direct-heating and uniform energy deposition in a cylindrical region, and the novel high-fidelity modelling approach for a pin-to-pin electrode configuration. We assess the self-similarity of the solutions under scaling laws suggested by dimensional analysis under the assumption that inviscid processes dominate. We consider key quantities, such as the duration, length of the acoustic phase, mass and energy losses, and the magnitude of the velocity field at the end of the expansion phase.

All those properties have significant importance in the context of plasma assisted ignition applications as they control the subsequent ignition process.

A summary of the most important findings from each of the research topic explained in the dissertation is presented next, which is then followed by recommendations for future work.

8.1 Non-equilibrium discharges

The state of non-equilibrium generated by nanosecond discharges in air is studied using a detailed kinetics mechanism with simulations of isochoric and adiabatic reactors with a two-temperature model. Energies of $0.5 - 4$ mJ/mm^3 are deposited, resulting in equilibrium temperatures as high as 3000 K. Gas heating proceeds in two distinct stages: a first stage of heating from the start of energy deposition to about 100 ns, and a second stage from 100 ns up to about $\mathcal{O}$(10-100 μs). In the first stage, we find that heating is controlled by quenching of electronically excited N_2 molecules and O atoms and a smaller contribution from impact dissociation and dissociative recombination is also highlighted. The slower second stage is dominated by recombination of atomic nitrogen and oxygen, with smaller contributions from vibrational relaxation and further O quenching.

Vibrational non-equilibrium is characterized in detail by studying the temporal evolution of the mole fractions of 9 particles corresponding to vibrationally excited nitrogen from ground state ($v = 0$) through $v = 1, \ldots, 8$. Distinct stages of vibrational non-equilibrium are identified in the long-term evolution of the plasma gas following the discharge. During the discharge, the highest vibrational states are

heavily populated, with a temperature close to that of electrons, and the distribution across vibrational states departs markedly from a Maxwellian. By 0.1 μs (or 100 ns), the distribution settles into a functional form that is amenable to be described with a two-temperature model: a vibrational temperature for states $v = 0$ and $v = 1$, which is found to be above the translational/rotational gas temperature, and a second vibrational temperature fit to the populations in states $v = 1, \ldots, 8$, which is significantly higher than the translational/rotational gas temperature. From 1 μs onwards, the vibrational distribution is well described by a Maxwellian at a single vibrational temperature, which is slightly higher than the gas temperature. By 10 to 50 μs, the gas is fully thermalized.

Our results are put into context with published literature on non-equilibrium associated with nanosecond discharges by computing the so-called energy coefficients for heating, vibrational, and chemical non-equilibrium proposed by Castela et al. [13] and extended by Barleon et al. [31]. Further, we propose and demonstrate a new approach based on the concept of constrained equilibrium. The gas is brought to equilibrium and sets of particles are either constrained or allowed to reach equilibrium freely. A specific equilibrium temperature is associated to each set, allowing for a quantitative characterization of the contribution of each type of non-equilibrium to heating. The metrics considered, including those from the novel constrained equilibrium approach, are found to be in close agreement with studies employing zero-dimensional two-temperature plasma reactors.

Finally, the reduced kinetics mechanism employed for multidimensional studies is validated against results obtained with the detailed kinetics mechanism, as

the differences between the two sets of results are shown to be minor and largely confined to the first heating stage. The commonly adopted approach of depositing energy until a target value and then setting the voltage to zero abruptly results in underestimating slightly vibrational excitation in favor of electronic excitation and dissociation on the account that energy is not deposited by cooling electrons as in actual discharges with a decreasing voltage phase.

8.2 Multidimensional simulations: pin-to-pin configurations

A numerical framework is developed and demonstrated by simulating a nanosecond discharge in air with a gap of 2.5 mm, pin radius of curvature of 250 μm, and deposited energy of 800 μJ. The path taken by streamers as they close the electrode gap defines the spatial locations where the conducting channel is established. As the number density of electrons in the channel increases rapidly, the electrical properties of the channel also change, e.g. the conductivity increases several-fold, allowing for significant energy deposition on nanosecond time scales. The spatial distribution of the energy density from the deposition is highly inhomogeneous, with higher energy densities and smaller width of the energized channel near the electrodes. At the midplane, the energy density is up to a factor of 5 lower and the channel up to 2 times as wide.

Energy deposition on such short time scales leads to the formation of a hot pressurized channel that proceeds to expand over the next few microseconds, leading to an increase in the volume of the heated kernel by a factor of 3. The shock system consists of stronger spherical shocks emanating from the pin tips, and a weaker

cylindrical shock emanating from the middle of the gap. In a more detailed analysis of the composition of the mixture, it is found that in addition to the larger energy densities, the higher pressure near the pin tips contributes to faster heating during the afterglow, leading to an even larger difference between the overpressures. The process of expansion is also accompanied by a loss of energy and mass in the gap area compared to the immediate post-discharge state. Our estimates indicate that about 2% of the energy deposited is lost to conduction to the electrodes and additional 9% to transport away from the electrode gap region during expansion. The expansion process also induced a maximum velocity of 35 m/s in the direction of the axial midplane.

The induced hydrodynamic effect leads to the eventual collapse of the kernel into a toroidal shape between 100 and 150 μs, a process that has been observed in previous experimental studies. It is also shown that the toroidal collapse generates a maximum in temperature, which is located off-axis. This layer of hot, low density gases enhances the reduced electric field locally, redirecting streamers during the second nanosecond discharge pulse so that the conducting channel is established off-axis. This finding agrees qualitatively with the experimental studies in the literature.

Thus, it is apparent that quantitative modeling of coupling between pulses requires high-fidelity simulation of the discharge on the account of the sensitivity of discharges to spatial inhomogeneities in the density of the background gases.

8.3 Self-similarity in the inviscid limit and Scaling Laws

In an effort to develop a general theory of the hydrodynamic effect brought by nanosecond discharges, dimensional analysis is used to guide simulations and process results. Dimensional analysis is restricted to parameters that neglect the effect of viscosity and diffusivity, leading to the identification of only two governing dimensionless groups. The first group pertains to the electrode geometry and the second group parametrizes the energy deposited. The analysis is consistent with the inviscid limit of the Navier-Stokes equations and neglects chemical reactions and assumes that the gas is calorically perfect.

The validity of the dimensional analysis and ensuing parametrization is then tested against detailed simulations of two configurations and models. In the first, the energy is used to initialize a spatially uniform region of energized gas and the expansion process is simulated without electrodes. In the second, the high-fidelity model and approaches are used to simulate plasma discharge and expansion without any simplifications and with the actual geometry of the electrodes.

In what follows, recall that Q is the energy deposited, d the electrode gap distance, r_c the radius of curvature of the pin tips, P_0 and ρ_0 the pressure and density of the background air at the initial conditions, respectively. Then, the two governing dimensionless parameters are $\Pi_1 = r_c/d$ and $\Pi_2 = Q/P_0 r_c^2 d$.

The temporal evolution of all relevant quantities (e.g., velocity, density, and pressure) from simulations conducted in the simplified configuration at conditions for which the dimensional parameters differ yet the pair (Π_1, Π_2) takes the same

values demonstrate nearly perfect collapse. Such observation lends credibility to the dimensional analysis from which inviscid and diffusive processes were excluded. Despite the success in establishing self-similarity and the dependence of the solution on only two parameters, there remain qualitative differences with respect to high-fidelity simulations, including in the velocity field induced towards the axial midplane and the occurrence of entrainment of the fluid at larger angles, which, for select configurations, induces fluid motion away from the axial midplane also. These qualitative differences in the velocity field point to the need for caution when such a simplified configuration is used to simulate hydrodynamic processes as it is most often the case in studies reported in the literature.

Two parameters are defined, i.e, the dimensionless duration of the expansion phase $\hat{t}_{\text{end}}$ and the dimensionless maximum axial component of velocity at the end of the expansion phase $\hat{u}_{z,\max}(\hat{t}_{\text{end}})$. A set of numerical simulations are executed to parametrize both parameters as a function of the pair (Π_1, Π_2) over ranges of values consistent with experiments. It is shown that $\hat{t}_{\text{end}}$ depends linearly on Π_2 with a negligible dependence on Π_1, which implies that the dimensional duration of the expansion process scales as $t_{\text{end}} \propto \sqrt{Q\rho_0/(P_0^2 d)}$. $\hat{u}_{z,\max}(\hat{t}_{\text{end}})$ has a more complex dependence on both Π_1 and Π_2 although it increases with both increasing Π_2 and Π_1.

High-fidelity simulations are performed at conditions consistent with similar ranges of Π_1 and Π_2. In this set of simulations, the electrode geometry is reproduced accurately and the hydrodynamic effect studied including the simulation of nanosecond discharges, which lead to spatially inhomogeneous energy deposition. Generally,

the same trends shown by the simplified configuration hold, although the solutions differ quantitatively. In particular, the solutions display a more significant dependence on Π_1, especially with regard to the width of the discharge channel, energized gas region, and subsequent kernel of hot gases. As Π_2 increases holding Π_1 constant, the width of the hot kernel by the end of the expansion increases relative to the radius of curvature. The same is true for decreasing Π_1 ("sharper pins") holding Π_2 constant. It is also found that in the range of values of Π_2 considered, the axial component of velocity at the end of the expansion reaches a plateau for $\Pi_2 > 30$ with a value that increases with increasing Π_1. This implies that the dimensional axial component scales as $|u_{z,\max}| \propto \sqrt{Qd/\rho_0}$ and, for the same value of Π_2, configurations with higher values of Π_1 will experience higher (dimensionless) velocities.

Finally, a convective time is defined equal to the time taken by a parcel of fluid travelling at a speed equal to the axial component of velocity at the end of the expansion in order to traverse half the gap. The convective time is then compared against a diffusive time based on the width of the hot kernel of gas at the end of the expansion and the thermal diffusion coefficient of air at background conditions. The ratio of the convective to diffusive times is shown to be a function of Π_1, Π_2, and Prandtl and Reynolds numbers. It is postulated that the ratio of the convective to diffusive time parametrizes the occurrence of toroidal collapse, whereby when the convective time scale is much smaller than the diffusive one, toroidal collapse will occur. The ratio is inversely proportional to the Reynolds number. Although at present it is not possible to draw any definitive conclusion because available experimental data exist at conditions that fall outside the ranges of

dimensionless groups considered in our study, the analysis is applied to two simulated configurations, one that shows toroidal collapse and the other that does not. We show that a much lower Reynolds number for one configuration is responsible for increasing the ratio, possibly explaining the lack of toroidal collapse.

8.3.1 Considerations for operating conditions

In experimental configurations, the hydrodynamic regime plays an important role in selecting operating conditions. In the toroidal regime, the induced hydrodynamic motion can be effective in expanding the volume of gases containing elevated energy density and active species. In the diffusive regime, the compact kernel reduces mixing and may be more effective in maintaining a higher temperature over longer time scales. Given the uncertainties associated with electrode erosion and energy depositions in a realistic circuit, the gap length is the parameter that can be most reliably changed to increase or decrease the dimensionless parameters Π_1 and Π_2.

Larger values of Π_1 and Π_2 favor the toroidal regime, while lower values of Π_1 and Π_2 favor the diffusive regime. These two parameters are inversely proportional to the gap length (i.e., increasing the gap length decreases both Π_1 and Π_2), rendering gap length d as one of the most influential parameters to bring about a change in the hydrodynamic regime. This strong relationship can lead observers to the conclusion that the hydrodynamic regime is uniquely defined by the gap length, which is an incomplete interpretation. The hydrodynamic regime can also be affected by careful control of the deposited energy Q regardless of the gap length, although this parameter is more challenging to control than the gap length in an experimental

configuration.

The hydrodynamic regime can also be affected by thermodynamic conditions of the mixture. For example, let's consider a given geometric configuration (constant Π_1) that is extensively tested at atmospheric conditions. Now, it is expected that his system will "match" the observed hydrodynamic regime in the test conditions at the thermodynamic conditions of a hypersonic cavity (i.e., higher temperature and lower pressure). For a preheated mixture at low pressure, the deposited energy should decrease to match the Π_2 value, although a lower Reynolds number at these conditions will likely require a higher value of Π_2 than that used at the test conditions. This is just one example of how the results from this work can be leveraged to inform the design of nanosecond discharge systems at the desired operating conditions.

8.4 Recommendations for future work

The study presented in this dissertation can be extended following several research directions.

8.4.1 Extension of the study over a broader range of governing parameters

In this dissertation, dimensionless relationships are established at a variety of background pressures, temperatures, densities and deposited energies that are relevant to pin-to-pin electrode configurations. The advective and diffusive time scales postulated are based on a broad parameter space in Π_1 and Π_2. However, throughout the numerical study, there was an important limitation with respect to

the maximum energy that could be deposited. Thermodynamic properties employed yield significant errors above ≈ 5000 K. From values reported in experimental studies, the lineic energy deposited in the gap can be as high as 1 mJ/mm, which is larger than any of the energies tested in this study by at least a factor of 3. The relationships established in this dissertation can be tested against numerical simulations at higher energies implementing more robust thermodynamic models.

Additional numerical simulations should also be conducted to stride across the transition from the diffusive to the toroidal regime at a variety of Reynolds and Prandtl numbers. This would allow providing a quantitative boundary between toroidal and diffusive regimes. Finally, all numerical simulations are executed with parabolic pins with a constant radius of curvature. The generality of the theory proposed should be assessed against simulations with varying radius of curvature, and alternative pin shapes that are used in experimental configurations.

8.4.2 Multi-pulse effects

In this dissertation, the duration of the acoustic phase, the magnitude of the axial component of velocity induced by the expansion, and the width of the kernel of hot gases generated by a single nanosecond discharge pulses are characterized in depth. An extension of this analysis should be applied to multi-pulse discharges with equivalent energies (e.g., four 200 μJ pulses compared to a single 800 μJ pulse). It is unclear whether by the end of sequence of multiple discharge pulses, the velocity induced would be larger, smaller, or approximately the same. The temperature distribution is also shown to affect the spatial structure of the plasma channel. It is

also unclear if over multiple pulses, the width of the discharge channel would widen or narrow due to non-uniform temperature distribution left behind by the previous pulse, and if there is in fact a cumulative effect. In the toroidal collapse regime, the streamer path and the structure of the conducting channel are significantly altered past the first pulse, requiring a new analysis.

8.4.3 Three-dimensional effects

In this dissertation, although the computational framework handles three-dimensional configurations, all cases were axisymmetric. In reality, pin-to-pin discharges occur in flows with stratified temperature fields. Small fluctuations in the temperature field create pockets of higher and lower reduced electric field that alter the path of the streamer and impact the location where the energy is deposited. This three-dimensional energy deposition is likely to have an impact on the induced velocity, and characteristic diffusive length scales. While this dissertation has established a computational framework amenable to characterizing these effects and mechanisms, the analysis would necessarily include additional parameters for describing turbulent transport. The computational framework developed and demonstrated in this dissertation is capable of supporting these simulations over time scales of several hundred micro-seconds.

Appendices

Appendix A

Internal energy fractions

The calculation of the internal energy fractions for each species was calculated in the same way as Ref. [31], where the full details were provided in private correspondence with the authors. For the calculation of the various internal energy contributions we make a distinction between species at ground state A and excited species A^*. For species at ground state, the internal energy u_k is equal to the internal energy in the chemical energy channel $u_{k,\text{chem}}$. In our mechanism, the excited species are either vibrationally excited, electronically excited, or ionized, and therefore each species contributes to a maximum of two energy channels. The internal energy of each excited species u^* is calculated as the sum of the associated ground species and the excited state

$$u^* = u_{\text{ground}} + u_{\text{exc.channel}}. \tag{A.1}$$

Let us illustrate the calculation of internal energy components with a few examples. Let us begin with excited state $N_2(A^3\Sigma)$, with an internal energy of 6.17 eV and its associated ground state N_2 has an internal energy ≈ 0 at reference conditions. Then

$$u^* = u_{\text{ground}} + u_{\text{exc.channel}} = 0.0 + u_{\text{exc}} = u_{\text{exc}}, \tag{A.2}$$

contributing purely to the electronic excitation energy channel. Similarly species N_2(v=1) has an internal energy of 0.2889 eV, and its associated ground state N_2 has an internal energy ≈ 0 at reference conditions. Then

$$u^* = u_{\text{ground}} + u_{\text{exc.channel}} = 0.0 + u_{\text{vib}} = u_{\text{vib}}, \tag{A.3}$$

contributing purely to the vibrational excitation energy channel.

The key distinction is for excited radicals such as the important O(^{1}D) species with an internal energy of 4.55 eV at reference conditions, and its associated ground state O has a nonzero internal energy at reference conditions of 2.583 eV. Then

$$u^* = u_{\text{ground}} + u_{\text{channel}} = (2.58/4.55)u_{\text{ground}} + (1.97/4.55)u_{\text{exc.channel}} = 0.57u_{\text{chem}} + 0.43u_{\text{exc}}, \tag{A.4}$$

contributing to two different energy channels. It is emphasized that in reality, the internal energy of an excited species is not equal to the sum of the internal energy of the associated ground species and the excitation energy (as discussed in Ref. [1]), but this approximation is deemed accurate enough for the calculation of energy deposition channels. A summary of the computed internal energy channel fractions at reference conditions (1 atm, 300 K) is presented in Fig. A.1.

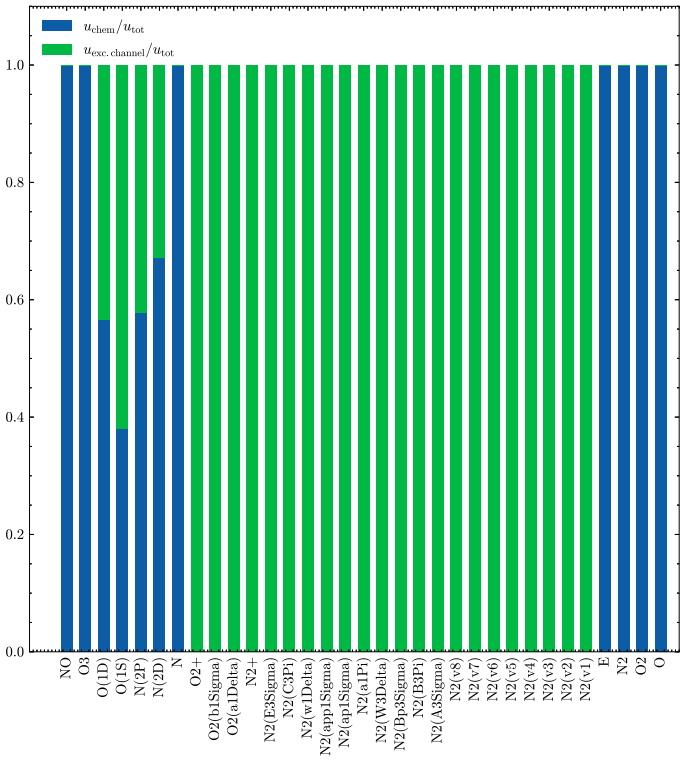

Figure A.1: Example internal energy fractions for all species at reference conditions of 1 atm and 300 K.

We also note that these internal energy fractions are a weak function of the thermodynamic conditions as seen in Fig. A.2. It is a reasonable approximation to calculate these fractions only once at reference conditions, instead of recalculating as the temperature and pressure change. This would come at an increased complexity and computational cost with little benefit.

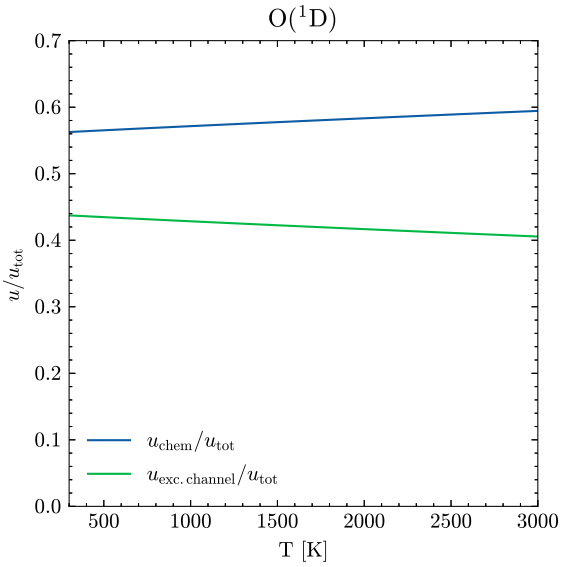

Figure A.2: Variation of the O(^{1}D) internal energy fractions as a function of temperature

Appendix B

Thermodynamic data

The thermodynamic model adopted here is consistent in the sense defined in Ref. [1] as the adiabatic and isobaric equilibrium temperature of ethylene/air mixtures reproduces that obtained with a conventional combustion mechanism, i.e. one that features equilibrium species only. In other words, the thermodynamic model employed in our work yields the correct temperature when the system is in thermal and chemical equilibrium.

Here, the equilibrium temperature at constant enthalpy and pressure is computed for ethylene/air mixtures of varying stoichiometry at 600 K and 0.5 atm with the updated thermodynamic data obtained using the tools provided in Ref. [1] and with thermodynamic data used by our group in previous work [2; 4]. Both sets of results are compared against equilibrium temperatures computed with thermodynamic data in the GriMech 3.0 mechanism [18].

Figure B.1 demonstrates that the errors in the equilibrium temperature associated with thermodynamic data computed with the *shifted enthalpy* method as in Ref. [2] can be significant and calculation of thermodynamic data of vibrationally excited states as discussed in Ref. [1] is essential to recover the correct mixture temperature under conditions of thermal and chemical equilibrium. Although not shown

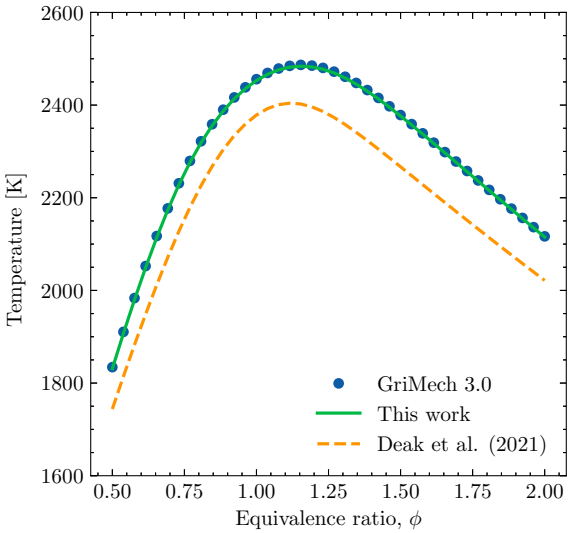

Figure B.1: Equilibrium temperature at constant enthalpy and pressure for ethylene/air mixtures of varying stoichiometry at 600 K and 0.5 atm obtained with the thermodynamic data from this work, thermodynamic data in the GriMech 3.0 mechanism [18], and thermodynamic data from a previous mechanism for plasma assisted combustion proposed by our group [4; 2].

here, we verified that such errors are smaller and less consequential at low gas temperatures and do not affect ignition delay times, which was the objective of the study in Ref. [2]. Regardless, employing consistent thermodynamic models is obviously desirable when calculating rate coefficients of reactions at high temperatures (e.g., to model NO_x emissions), minimizing uncertainties, and comparing results from mechanisms for plasma assisted combustion applications against those from traditional combustion mechanisms.

Appendix C

Effects due to background gas temperature and composition

In general, mean electron energy $\langle\epsilon\rangle$, normalized electron mobility $\mu_e^{\mathrm{e}}N$, and normalized diffusion coefficient $\mathcal{D}_eN$ depend on the composition and temperature of the background gas. In this work, they were calculated with the two-term Boltzmann solver BOLSIG+ for air (21% oxygen and balancing nitrogen by volume) at 300 K and used in all simulations, regardless of gas temperature and composition.

Auxiliary BOLSIG+ solutions with varying ethylene/air mixture stoichiometry (equivalence ratios between 0.6 and 1.4, including pure air) and temperature ($300 \leq T \leq 3000$ K) were obtained in order to explore the impact of the thermochemical state of the background gas on electron properties and results are summarized in Fig. C.1. All simulations used cross-sections from the LXCat database provided in the Supplementary material.

Over a wide range of reduced electric field strengths $10 \leq E/N \leq 2000$ Td, it is apparent that there are only small relative differences within 5% for the mean electron energy $\langle\epsilon\rangle$ and $\mu_e^{\mathrm{e}}N$ and within 10% for $\mathcal{D}_eN$. Although electron properties are more sensitive to the temperature and composition of the background gas for $E/N < 10$ Td, typical values of E/N during the discharge range are above 50 Td.

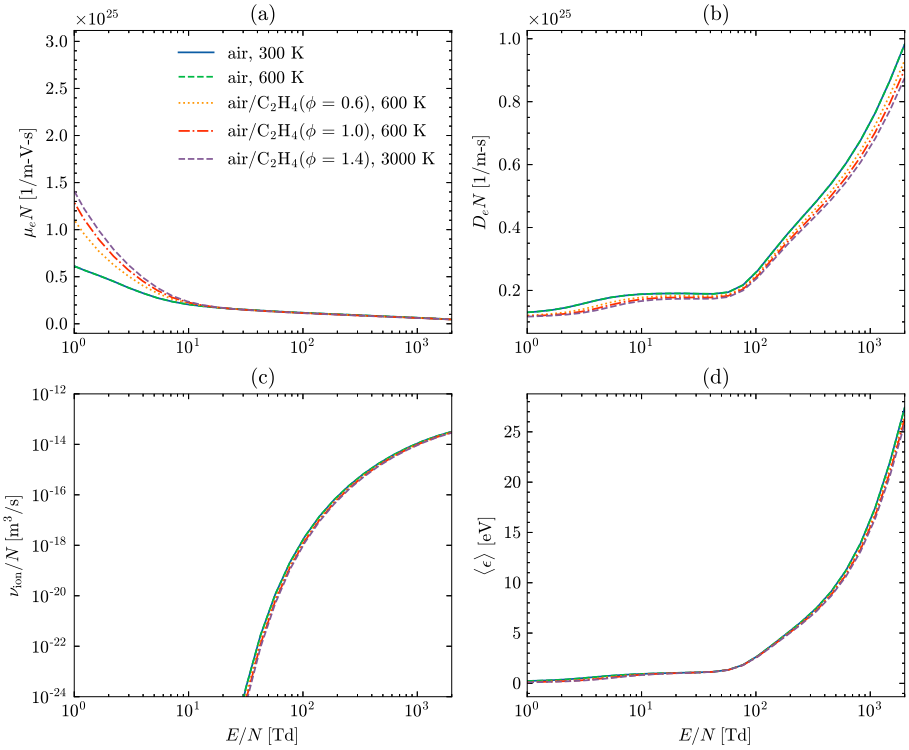

Figure C.1: (a) Normalized electron mobility, (b) normalized electron diffusion coefficient, (c) normalized total ionization frequency (i.e, including the contribution of all ionizing particles in the gaseous mixture), and (d) mean electron energy as a function of the reduced electric field strength E/N. Lines correspond to solutions computed with various combinations of temperature and composition of the background gas.

Appendix D

Electron transport properties

The normalized electron mobility $\mu_e^{\mathrm{e}} N$ and normalized electron diffusivity $\mathcal{D}_e N$ are evaluated using the following functionals:

$$\mu_e^{\mathrm{e}} N = A \exp\left\{ \sum_{n=0}^{8} b_n^{\mu} (\ln T_e)^n \right\}, \tag{D.1}$$

$$\mathcal{D}_e N = A \exp\left\{ \sum_{n=0}^{8} b_n^{\mathcal{D}} (\ln T_e)^n \right\}, \tag{D.2}$$

where T_e is the electron temperature in eV. The functional fits are evaluated during the simulation using coefficients provided in Tab. D.1.

Table D.1: Coefficients of the functional fits for normalized electron mobility $\mu_e^e N$ (Eq. (D.1)) and normalized electron diffusivity $\mathcal{D}_e N$ (Eq. (D.2)). The functional fits assume that T_e is in units of eV.

Normalized mobility $\mu_e^e N$ [1/m-V-s]		Normalized diffusivity $\mathcal{D}_e N$ [1/m-s]	
A	4.02×10^{25}	A	9.42×10^{24}
b_0^μ	-3.408	$b_0^\mathcal{D}$	-1.57
b_1^μ	-0.583	$b_1^\mathcal{D}$	0.328
b_2^μ	0.371	$b_2^\mathcal{D}$	0.118
b_3^μ	-7.842×10^{-3}	$b_3^\mathcal{D}$	4.182×10^{-2}
b_4^μ	-7.737×10^{-2}	$b_4^\mathcal{D}$	-1.046×10^{-2}
b_5^μ	-6.685×10^{-5}	$b_5^\mathcal{D}$	-9.488×10^{-3}
b_6^μ	6.568×10^{-3}	$b_6^\mathcal{D}$	1.154×10^{-4}
b_7^μ	1.132×10^{-4}	$b_7^\mathcal{D}$	5.973×10^{-4}
b_8^μ	-1.568×10^{-4}	$b_8^\mathcal{D}$	6.848×10^{-5}

Appendix E

Rate coefficients for anion reactions

Rate coefficients for R1 and R2 are functions of T_e and T as described in Ref. [71]. The functional form of the forward rate of reaction R1 is

$$k_{\mathrm{R1}} = 1.4 \times 10^{-17} \left(\frac{300}{T_e}\right) \left(\exp \frac{-600}{T}\right) \left(\exp \frac{700(T_e - T)}{T_e T}\right) \ \mathrm{m}^6/\mathrm{s}, \tag{E.1}$$

and a similar functional form is used for the forward rate of reaction R2

$$k_{\mathrm{R2}} = 1.07 \times 10^{-19} \left(\frac{300}{T_e}\right)^2 \left(\exp \frac{-70}{T}\right) \left(\exp \frac{1500(T_e - T)}{T_e T}\right) \ \mathrm{m}^6/\mathrm{s}. \tag{E.2}$$

Rate coefficients for anion reactions R3-R9 in Tab. 4.4 are described by Janev and FIT1 functional forms [61], which were fit to data from Refs. [70; 72]. The Janev form uses a polynomial of the natural logarithm of the electron temperature

$$k_f = A \exp \left(\sum_{n=0}^{8} b_n (\ln X)^n \right), \tag{E.3}$$

while the FIT1 form uses a power series

$$k_f = A \exp \left(\sum_{n=0}^{3} b_n / X^{n+1} \right), \tag{E.4}$$

where X represents either the electron temperature or the reduced electric field strength. Compared to conventional forms of the fits presented in Ref. [61], the

Table E.1: Coefficients for reactions listed in Tab. 4.4. The pre-exponential factor A is in units of m-s. As written here, coefficients b_{0-8} require X in units of eV or Td depending on whether X represents the electron temperature T_e or the reduced electric field strength E/N, respectively.

No.	Fit type	X	A	b_0	b_1	b_2	b_3	b_4	b_5	b_6	b_7	b_8
R3	FIT1	T_e	8.07×10^{-18}	17.86	-61.73	71.80	-28.14	–	–	–	–	–
R4	FIT1	T_e	8.67×10^{-17}	9.20	-36.79	44.45	-18.16	–	–	–	–	–
R5	FIT1	T_e	2.32×10^{-17}	24.89	-71.75	75.25	-27.39	–	–	–	–	–
R6	Janev	T_e	1.58×10^{-17}	-4.79	3.98	-2.62	10.93	-26.14	37.39	-29.76	11.99	-1.90
R7	FIT1	E/N	4.24×10^{-16}	-10.7	1.98	6.16	-4.31	–	–	–	–	–
R8	FIT1	E/N	1.17×10^{-15}	-24.97	11.29	16.89	-15.78	–	–	–	–	–
R9	FIT1	E/N	2.20×10^{-18}	4.22	-12.91	13.33	-5.15	–	–	–	–	–

temperature exponent and activation energy are set to zero (and omitted here) in Eq. (E.3) and Eq. (E.4). The coefficients appearing above are reported in Tab. E.1.

Finally, reactions R10-R13 are represented as modified Arrhenius reactions modeling the recombination of positive and negative ions as

$$\mathrm{A}^- + \mathrm{B}^+ + \mathrm{M} \longrightarrow \mathrm{A} + \mathrm{B} + \mathrm{M}, \tag{E.5}$$

with forward reaction rate reported in Ref. [71] as

$$k_{\mathrm{R10-R13}} = 2 \times 10^{-13}(300/T)^{2.5}\ \mathrm{m}^6/\mathrm{s}. \tag{E.6}$$

Appendix F

Simplifications asssociated with non-thermal electrons

In order to reduce and manage the complexity of the modeling task, two simplifications are adopted in the description of the gas in the presence of non-thermal electrons as typical of high-voltage discharges of nanosecond duration. Firstly, the Local Field Approximation (LFA) is employed, whereby the mean electron energy and related electron temperature are taken to be functions of the local reduced electric field strength E/N. Secondly, a single equation is written for the conservation of the energy of the gaseous system, consisting of all particles, including electrons. Further, closures assume that the gaseous system is one in thermal equilibrium at a common temperature, except for rate coefficients of reactions involving non-thermal electrons and electron transport properties, which are addressed with LFA. The equilibrium temperature is recovered given particle densities, a model for the internal energy of each particle class as a function of temperature, and the internal energy density of the gaseous system, which includes electrons.

Here, we consider a two-fluid/two-temperature (2F/2T) plasma model which defines two separate thermodynamic systems that exchange energy through particle collisions. One system consists of electrons alone and the other includes all remaining

particles, which we shall refer to as "heavy gas" for the remainder of this discussion. The state of the electron gas is uniquely identified by its energy density U_e and the number density of electrons n_e, while that of the heavy gas is identified by energy density U_g and number density vector $\boldsymbol{n}_g$. Thus, one defines an electron temperature T_e based on the electron mean energy $\langle\epsilon\rangle = U_e/n_e = 3k_{\mathrm{B}}T_e/2$ and a corresponding electron gas pressure $p_e = k_{\mathrm{B}}n_eT_e$. Similarly, one defines a heavy gas temperature T_g and pressure $p_g = k_{\mathrm{B}}N_gT_g$. Details of the 2F/2T plasma model are explained in Ref. [2].

The 2F/2T model is undoubtedly more accurate than the one adopted and implemented for the simulation of multi-dimensional nanosecond discharges, albeit more complex and computationally expensive. In order to assess the inaccuracies associated with the models adopted in the proposed discharge simulation framework, we simulate zero-dimensional nanosecond plasma discharges with the 2F/2T model at conditions representative of those in the large scale simulations. We consider two configurations with electric field strengths of 200 and 300 Td and estimate the errors in $\langle\epsilon\rangle$ brought by LFA as well as errors in T_g brought by the modeling choice to solve a single equation for the internal energy of a gaseous system comprising all particles.

As far as the LFA is concerned, Fig. F.1(a) shows $\langle\epsilon\rangle$ from the 2F/2T model and the mean electron energy at the corresponding instantaneous E/N applied to the zero-dimensional reactor interpolated from a BOLSIG+ solution as done in the proposed multi-dimensional discharge simulation framework. It is apparent that the two electron mean energies are very close to each other, with errors below 12.5% throughout the simulation. The data in Fig. F.1(a) support the conclusion that the

LFA does not introduce significant errors in the mean electron energy for plasma discharges considered in this work.

Addressing errors in T_g requires a more complex approach, whereby errors in the heavy gas temperature associated with the newly proposed framework for multi-dimensional simulations are estimated by computing a temperature T_g^* from the 2F/2T model as detailed next. First, we compute $\Delta U_g(t) = U_g(t) - U_g(0)$ and $\Delta U_e = U_e(t) - U_e(0)$, which represent the increase in the internal energy density of the heavy and electron gases, respectively, during the discharge. Second, we compute $U_g^*(t) = U_g(0) + \Delta U_g(t) + \Delta U_e(t)$, which represents the internal energy density of the heavy gas in the limit of all energy gained by the electron gas being attributed to the heavy gas instead. Third, we compute $T_g^*(t)$ from $U_g^*(t)$, the heavy gas number density vector $\boldsymbol{n}_g(t)$, and the electron number density $n_e(t)$. Note that when calculating $T_g^*(t)$ from composition and energy density, electrons are assumed to be at temperature T_g^* also. The relative difference between T_g^* and T_g is taken to represent an error in the heavy gas temperature similar to that associated with the modeling approach used in the proposed novel multi-dimensional plasma modeling framework, i.e., one that features only one internal energy for the combined fluids.

Figure F.1(b) shows T_g and the relative error $e_T = (T_g^* - T_g)/T_g$ as a fraction. The data shown support the conclusion that the error is small and does not exceed 6% or about 80 K, lasting for a few nanoseconds and leading to a slight overestimation of the heavy gas temperature. Such outcome is attributed to the fact that little energy is stored in the electron gas at any time during the discharge as electrons receive large amounts of energy from the electric field, yet they lose nearly all of it

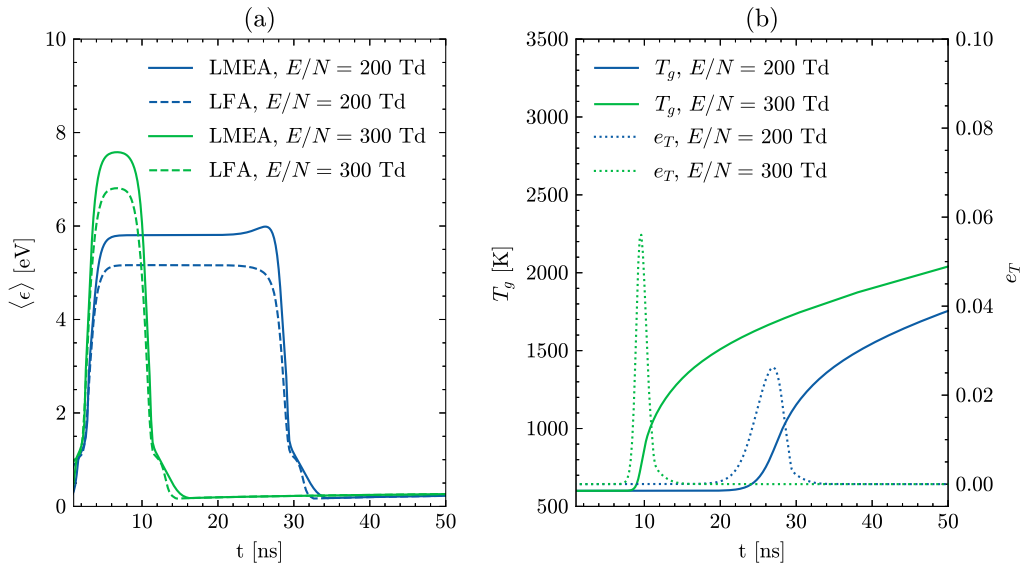

Figure F.1: (a) Mean electron energy defined as $\langle\epsilon\rangle = U_e/n_e$ based on the 2F/2T model and that interpolated from BOLSIG+ solutions given the instantaneous value of E/N. Simulations are carried out at conditions similar to those discussed in Chapter 7 and approximately twice the energy deposition (on a per unit volume basis). The reduced electric field values are $E/N = 200$ and 300 Td for most of the discharge. (b) Temperature T_g and error estimate $e_T = (T_g^* - T_g)/T_g$ as a function of time.

to the heavy gas via inelastic collisions. Moreover, while mean electron energies are elevated and in the range of 5 to 6 eV, the electron number density remains small during plasma discharges of the kind considered in our work.

Appendix G

Isothermal wall analysis

In this section, we provide details concerning the choice of an isothermal wall boundary condition for the electrode as outlined in chapter 5. We begin by providing an estimate of the Biot number of the pin electrode, defined as the ratio of the thermal resistance due to conduction and thermal resistance due to convection. The Biot number is defined as

$$\mathrm{Bi} = hL/k, \tag{G.1}$$

where h is the convective heat transfer coefficient [W/m^2-k], k is the thermal conductivity of the body [W/(m-K)], and L the characteristic length of the geometry considered. For the pin electrode, we will consider only the parabolic section of the tip, where the characteristic length is measured as the ratio of the volume of the body to the heated surface $L = V_{\mathrm{body}}/A_{\mathrm{heated}}$.

From the results presented in chapters 5 and 7 we consistently observe a heated channel with a radius of $\mathcal{O}(r_c)$. We consider the heated area to begin at the pin tip and end at the point at which the radius of the pin is equal to $\approx$ 250-400 μm, resulting in a characteristic length of L between 2 and 4.5 mm. In this analysis, we will assume pin electrodes are made of tungsten, with $k \approx 175$ W/m-K, and that the heat transfer coefficient of air ranges from 10-1000 W/m^2-K. Under natural

convection, the heat transfer coefficient of air is closer to a range of 10 to 25 W/m^2-K, but even using the largest value of 1000 W/m^2-k, the Biot remains below 0.1. The low Biot number of the parabolic section allows for the the use of a lumped capacitance model.

Under the lumped capacitance treatment of the electrode, the temperature of the conductive electrode is approximated by the exponential law

$$T(t) = T_\infty + (T_0 - T_\infty)\exp\{-t/\tau\}, \tag{G.2}$$

$$\tau = \frac{mc_p}{hA_{\text{heated}}}, \tag{G.3}$$

where m and c_p (134 J/kg-K) are the density and heat capacity of the tungsten pin electrode, respectively. Using the density of tungsten (19.3×10^3 kg/m^3) and volume of the pin (approximately 3.1×10^{-9} m^3), we calculate a total mass of 6.06×10^{-5} kg.

In an extreme scenario, we will assume that the pin electrodes are subjected to forced convection in air at temperature T_∞. In Fig. G.1, we plot the pin surface temperature assuming a heat transfer coefficient h of 500 W/m^2-K and different free stream temperatures. It is evident that due to the high conductivity of the pins and their large mass compared to the fluid, the temperature rise is insignificant during the time scales that a meaningful temperature difference is observed between the pin and the heated channel.

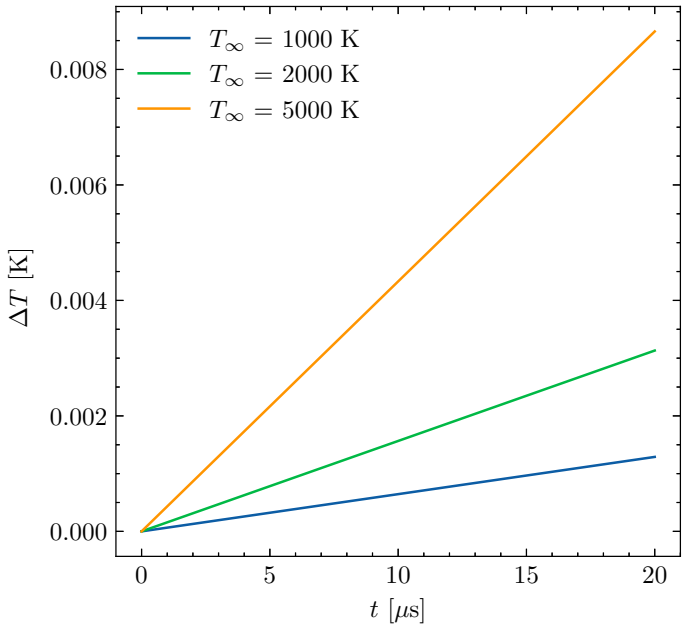

Figure G.1: Change in temperature of the surface of the electrode under forced convection ($h = 500$ W/m^2-K) using a lumped capacitance model and for different free stream temperatures. The change in temperature of the electrode is negligible over the time scales considered in this work.

Appendix H

Fitted surfaces for advective and diffusive time scales

In Chapter 7 we presented equations for dimensionless transit time and diffusive times. To provide estimates of the dimensionless transit and diffusive times in the entire parameter space tested in this study, we fit surfaces to the data computed for the growth of the heated kernel $f(\Pi_1, \Pi_2)$ in terms of the radius of curvature (see Fig. 7.13), and the dimensionless velocity at the end of the acoustic phase $\hat{u}_{z,\max}(\Pi_1, \Pi_2)$ (see Fig. 7.10). The surfaces are fitted using the SciPy library with a piecewise cubic, continuously differentiable (C1), and approximately curvature-minimizing polynomial surface. Surfaces with annotated data points are shown in Figs. H.1 and H.2.

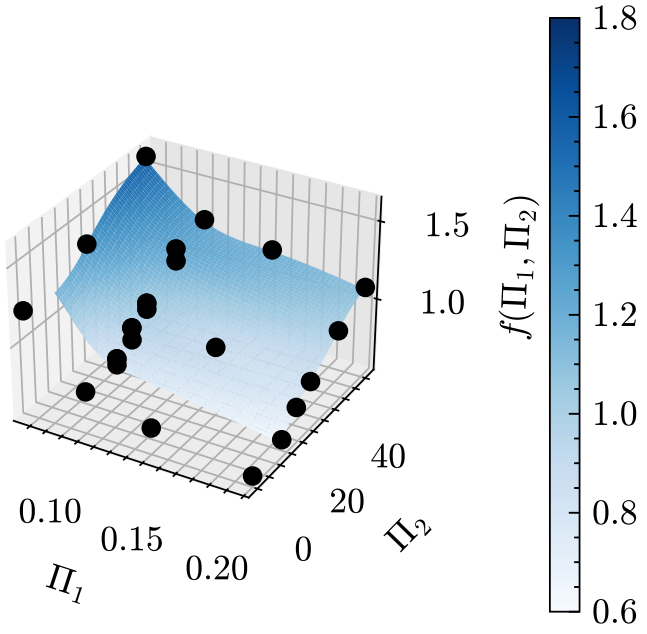

Figure H.1: Surface $f(\Pi_1, \Pi_2)$ fitted to the data for the growth of the heated channel in terms of pin curvature r_c, presented in Fig. 7.13. Data points annotated in black.

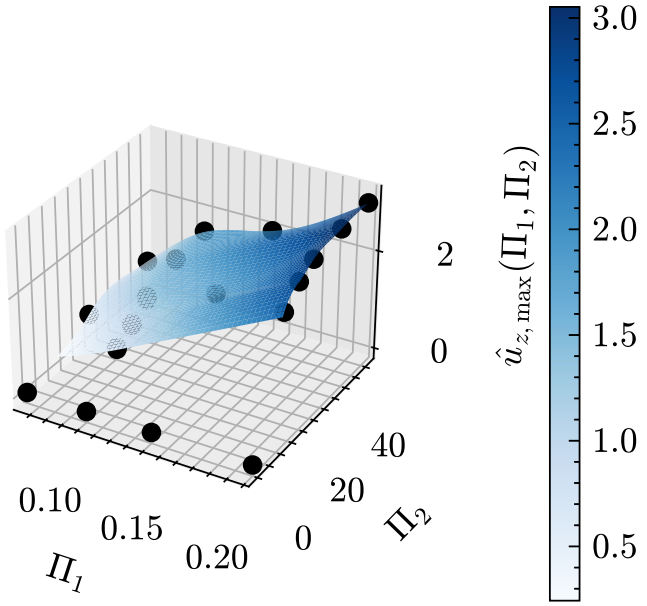

Figure H.2: Surface $\hat{u}_{z,\max}(\Pi_1, \Pi_2)$ fitted to the data for the induced dimensionless velocity at the end of the acoustic phase, presented in Fig. 7.10. Data points annotated in black.

Appendix I

Description of supplementary material

Supplementary data files referenced in this work are summarized in Tab. I.1. Files include thermodynamic data file in NASA format for the reduced air/plasma kinetics mechanism, interpolation table for the mean electron energy as a function of the reduced electric field, and cross section data for the Boltzmann solution in Appendix C. These files are available at `https://dataverse.tdl.org/dataverse/alfredoduartegomez` and also upon request.

Table I.1: File name and description of the supplementary material referenced in this work.

File	Description
S1therm.dat	File with thermodynamic data for each of the species included in the reduced mechanism in NASA format and consistent with CHEMKIN.
S2ENvsMEEtab.dat	Table used to interpolate the value of mean electron energy [in eV] from the value of the reduced electric field [Td], consistent with the local field approximation (LFA) approach.
S3LXCatdata.dat	Cross section data for air and air/ethylene mixtures used to generate the Boltzmann solutions.

Bibliography

[1] T. Hazenberg, J. Janssen, J. van Dijk, and J. van Oijen, *Consistent thermodynamics for plasma-assisted combustion*, Proc. Combust. Inst. 39 (2023), pp. 5541–5549.

[2] N. Deak, A. Bellemans, and F. Bisetti, *Plasma-assisted ignition of methane/air and ethylene/air mixtures: Efficiency at low and high pressures*, Proc. Combust. Inst. 38 (2021), pp. 6551–6558.

[3] A. Bourdon, V. Pasko, N. Liu, S. Célestin, P. Ségur, and E. Marode, *Efficient models for photoionization produced by non-thermal gas discharges in air based on radiative transfer and the helmholtz equations*, Plasma Sources Sci. Technol. 16 (2007), p. 656.

[4] A. Bellemans, N. Kincaid, N. Deak, P. Pepiot, and F. Bisetti, *P-drgep: a novel methodology for the reduction of kinetics mechanisms for plasma-assisted combustion applications*, Proc. Combust. Inst. 38 (2021), pp. 6631–6639.

[5] A. Duarte Gomez, N. Deak, L. Esclapez, M. Day, and F. Bisetti, *Mathematical models and numerical methods for high-fidelity simulation of ignition of reactive mixtures by nanosecond plasma discharges in realistic configurations*, Combust. Theory Model. under review (2024).

[6] *Pelec documentation*, `https://pelec.readthedocs.io/en/latest/index.html`. Accessed: 2022-03-08.

[7] D.Z. Pai, G.D. Stancu, D.A. Lacoste, and C.O. Laux, *Nanosecond repetitively pulsed discharges in air at atmospheric pressure—the glow regime*, Plasma Sources Sci. Technol. 18 (2009), p. 045030.

[8] J.K. Lefkowitz and T. Ombrello, *An exploration of inter-pulse coupling in nanosecond pulsed high frequency discharge ignition*, Combust. Flame 180 (2017), pp. 136–147.

[9] D. Xu, M. Shneider, D. Lacoste, and C. Laux, *Thermal and hydrodynamic effects of nanosecond discharges in atmospheric pressure air*, J. Phys. D Appl. Phys. 47 (2014), p. 235202.

[10] S. Stepanyan, J. Hayashi, A. Salmon, G.D. Stancu, and C.O. Laux, *Large-volume excitation of air, argon, nitrogen and combustible mixtures by thermal jets produced by nanosecond spark discharges*, Plasma Sources Sci. Technol. 26 (2017).

[11] S. Stepanyan, N. Minesi, A. Tibere-Inglesse, A. Salmon, G.D. Stancu, and C.O. Laux, *Spatial evolution of the plasma kernel produced by nanosecond discharges in air*, J. Phys. D: Appl. Phys. 52 (2019).

[12] C. Dumitrache, A. Gallant, N. Minesi, S. Stepanyan, G.D. Stancu, and C.O. Laux, *Hydrodynamic regimes induced by nanosecond pulsed discharges in air: Mechanism of vorticity generation*, J. Phys. D: Appl. Phys. 52 (2019).

[13] M. Castela, B. Fiorina, A. Coussement, O. Gicquel, N. Darabiha, and C.O. Laux, *Modelling the impact of non-equilibrium discharges on reactive mixtures for simulations of plasma-assisted ignition in turbulent flows*, Combust. Flame 166 (2016), pp. 133–147.

[14] X. Mao, H. Zhong, T. Zhang, A. Starikovskiy, and Y. Ju, *Modeling of the effects of non-equilibrium excitation and electrode geometry on h2/air ignition in a nanosecond plasma discharge*, Combust. Flame 240 (2022), p. 112046.

[15] M. Zhelezniak, A.K. Mnatsakanian, and S.V. Sizykh, *Photoionization of nitrogen and oxygen mixtures by radiation from a gas discharge*, High Temp. 20 (1982), pp. 357–362.

[16] G. Naidis, *Modelling of transient plasma discharges in atmospheric-pressure methane–air mixtures*, J. Phys. D Appl. Phys. 40 (2007), p. 4525.

[17] D.L. Rodriguez, M.J. Aftosmis, and M. Nemec, *Formulation and Implementation of Inflow/Outflow Boundary Conditions to Simulate Propulsive Effects*, in *AIAA Aerospace Sciences Meeting* (2018).

[18] G.P. Smith, D.M. Golden, M. Frenklach, N.W. Moriarty, B. Eiteneer, M. Goldenberg, C.T. Bowman, R.K. Hanson, S. Song, J. William C Gardiner, V.V. Lissianski, and Z. Qin, *Gri-mech version 3.0* (1999). URL `http://combustion.berkeley.edu/gri-mech/version30/text30.html`.

[19] S. Barbosa, G. Pilla, D. Lacoste, P. Scouflaire, S. Ducruix, C. Laux, and D. Veynante, *Influence of a repetitively pulsed plasma on the flame stability domain*

of a lab-scale gas turbine combustor, in *Fourth European combustion meeting*. 2009, pp. 1–6.

[20] H. Do, M.A. Cappelli, and M.G. Mungal, *Plasma assisted cavity flame ignition in supersonic flows*, Combust. Flame 157 (2010), pp. 1783–1794.

[21] B. Wolk, A. DeFilippo, J.Y. Chen, R. Dibble, A. Nishiyama, and Y. Ikeda, *Enhancement of flame development by microwave-assisted spark ignition in constant volume combustion chamber*, Combust. Flame 160 (2013), pp. 1225–1234.

[22] D.L. Rusterholtz, D.A. Lacoste, G.D. Stancu, D.Z. Pai, and C.O. Laux, *Ultrafast heating and oxygen dissociation in atmospheric pressure air by nanosecond repetitively pulsed discharges*, J. Phys. D: Appl. Phys. 46 (2013).

[23] A. Starikovskiy and N. Aleksandrov, *Plasma-assisted ignition and combustion*, Prog. Energ. Combust. Sci. 39 (2013), pp. 61–110.

[24] N. Deak, A. Bellemans, and F. Bisetti, *Plasma-assisted ignition of methane/air and ethylene/air mixtures: Efficiency at low and high pressures*, Proc. Combust. Inst. (2020).

[25] S. Lovascio, J. Hayashi, S. Stepanyan, G.D. Stancu, and C.O. Laux, *Cumulative effect of successive nanosecond repetitively pulsed discharges on the ignition of lean mixtures*, Proc. Combust. Inst. 37 (2019), pp. 5553–5560.

[26] K.C. Opacich, J.S. Heyne, J.A. Gray, K. Busby, S.D. Hammack, and T. Ombrello, *Ignition kernel development in a reactive flow for nanosecond-pulsed high-frequency and dc arc discharges*, Combust. Flame 245 (2022).

[27] S.A. Shcherbanev, T. Krzymuski, Y. Xiong, and N. Noiray, *Jetting axial flow induced by nanosecond repetitively pulsed discharges in quiescent ambient air*, J. Phys. D: Appl. Phys. 55 (2022).

[28] L. Cheng, N. Barleon, B. Cuenot, O. Vermorel, and A. Bourdon, *Plasma assisted combustion of methane-air mixtures: Validation and reduction*, Combust. Flame 240 (2022), p. 111990.

[29] T.S. Taneja, P.N. Johnson, and S. Yang, *Nanosecond pulsed plasma assisted combustion of ammonia-air mixtures: Effects on ignition delays and nox emission*, Combust. Flame 245 (2022), p. 112327.

[30] S.P. Bane, J.L. Ziegler, and J.E. Shepherd, *Investigation of the effect of electrode geometry on spark ignition*, Combust. Flame 162 (2015), pp. 462–469.

[31] N. Barléon, L. Cheng, B. Cuenot, and O. Vermorel, *A phenomenological model for plasma-assisted combustion with nrp discharges in methane-air mixtures: Pacmind*, Combust. Flame 253 (2023).

[32] M. Castela, S. Stepanyan, B. Fiorina, A. Coussement, O. Gicquel, N. Darabiha, and C.O. Laux, *A 3-d dns and experimental study of the effect of the recirculating flow pattern inside a reactive kernel produced by nanosecond plasma*

discharges in a methane-air mixture, Proc. Combust. Inst. 36 (2017), pp. 4095–4103.

[33] X. Shao, N. Kabbaj, D.A. Lacoste, and H.G. Im, *A computational study of a laminar methaneâ€"air flame assisted by nanosecond repetitively pulsed discharges*, J. Phys. D: Appl. Phys. 57 (2024), p. 205201.

[34] T.S. Taneja, T. Ombrello, J. Lefkowitz, and S. Yang, *Numerical Investigation of Ignition Kernel Development with Nanosecond Pulsed Plasma in Quiescent and Flowing Mixtures*, in *AIAA SCITECH 2023 Forum*.

[35] T.S. Taneja, T. Ombrello, J. Lefkowitz, and S. Yang, *Large eddy simulation of plasma assisted ignition: Effects of pulse repetition frequency, number of pulses, and pulse energy*, Combust. Flame 267 (2024), p. 113574.

[36] Q. Malé, S. Shcherbanev, M. Impagnatiello, and N. Noiray, *Stabilization of a thermoacoustically unstable sequential combustor using non-equilibrium plasma: Large eddy simulation and experiments*, Proc. Combust. Inst. 40 (2024), p. 105277.

[37] M. Impagnatiello, Q. Malé, and N. Noiray, *Acoustic scattering of a sequential combustor controlled with non-equilibrium plasma: A numerical study*, Proc. Combust. Inst. 40 (2024), p. 105389.

[38] N. Barleon, L. Cheng, B. Cuenot, O. Vermorel, and A. Bourdon, *Investigation of the impact of nrp discharge frequency on the ignition of a lean methane-air*

mixture using fully coupled plasma-combustion numerical simulations, Proc. Combust. Inst. (2022).

[39] X. Mao, H. Zhong, Z. Wang, T. Ombrello, and Y. Ju, *Effects of inter-pulse coupling on nanosecond pulsed high frequency discharge ignition in a flowing mixture*, Proc. Combust. Inst. 39 (2023), pp. 5457–5464.

[40] E.S. Garzon, C. Mehl, and O. Colin, *Modeling of spark ignition in gaseous mixtures using adaptive mesh refinement coupled to the thickened flame model*, Combust. Flame 248 (2023).

[41] N.E. Deak, *Development and application of high-performance framework for high-fidelity simulations of plasma-assisted ignition of hydrocarbon fuels using nanosecond pulse discharges*, Ph.D. diss., The university of Texas at Austin, 2022.

[42] R.J. Kee, F.M. Rupley, and J.A. Miller, *Chemkin-ii: A fortran chemical kinetics package for the analysis of gas-phase chemical kinetics*, Tech. Rep., Sandia National Labs., Livermore, CA (USA), 1989.

[43] A.C. Hindmarsh, P.N. Brown, K.E. Grant, S.L. Lee, R. Serban, D.E. Shumaker, and C.S. Woodward, *Sundials: Suite of nonlinear and differential/algebraic equation solvers*, ACM Trans. Math. Softw. 31 (2005), pp. 363–396.

[44] Z.S. Eckert, *Energy transfer in non-equilibrium reacting gas flows: Applications in plasma assisted combustion and chemical gas lasers*, Ph.D. diss., The Ohio State University, 2018.

[45] N. Popov and S. Starikovskaia, *Relaxation of electronic excitation in nitrogen/oxygen and fuel/air mixtures: fast gas heating in plasma-assisted ignition and flame stabilization*, Prog. Energ. Combust. Sci. 91 (2022), p. 100928.

[46] I. Shkurenkov and I.V. Adamovich, *Energy balance in nanosecond pulse discharges in nitrogen and air*, Plasma Sources Sci. Technol. 25 (2016), p. 015021.

[47] A. Lo, A. Cessou, P. Boubert, and P. Vervisch, *Space and time analysis of the nanosecond scale discharges in atmospheric pressure air: I. gas temperature and vibrational distribution function of n2 and o2*, J. Phys. D: Appl. Phys. 47 (2014), p. 115201.

[48] A. Brisset, F. Guichard, A. Cessou, and P. Tardiveau, *Energy relaxation and heating in the afterglow of high electric field ns-discharges in ambient air using spontaneous raman scattering*, Plasma Sources Sci. Technol. 30 (2021), p. 035013.

[49] S.B. Pope, *Gibbs function continuation for the stable computation of chemical equilibrium*, Combust. Flame 139 (2004), pp. 222–226.

[50] A. Bourdon, Z. Bonaventura, and S. Celestin, *Influence of the pre-ionization background and simulation of the optical emission of a streamer discharge in preheated air at atmospheric pressure between two point electrodes*, Plasma Sources Sci. Technol. 19 (2010), p. 034012.

[51] A. Sharma, V. Subramaniam, E. Solmaz, and L.L. Raja, *Fully coupled modeling*

of nanosecond pulsed plasma assisted combustion ignition, J. Phys. D Appl. Phys. 52 (2018), p. 095204.

[52] A. Zhang, R. Scarcelli, T. Wallner, D. Breden, A. Karpatne, L.L. Raja, I. Ekoto, and B. Wolk, *Numerical investigation of nanosecond pulsed discharge in air at above-atmospheric pressures*, J. Phys. D Appl. Phys. 51 (2018), p. 345201.

[53] J. Kim, V. Gururajan, R. Scarcelli, S. Biswas, and I. Ekoto, *Modeling nanosecond-pulsed spark discharge and flame kernel evolution*, J. Energy Resour. Technol. 144 (2022).

[54] T. Poinsot and D. Veynante, *Theoretical and numerical combustion*, 3rd ed., CERFACS, Toulouse, France, 2012.

[55] J.P. Boeuf and L.C. Pitchford, *Electrohydrodynamic force and aerodynamic flow acceleration in surface dielectric barrier discharge*, J. Appl. Phys. 97 (2005), p. 103307.

[56] T. Coffee and J. Heimerl, *Transport algorithms for premixed, laminar steady-state flames*, Combust. Flame 43 (1981), pp. 273–289.

[57] D. Breden, L.L. Raja, C.A. Idicheria, P.M. Najt, and S. Mahadevan, *A numerical study of high-pressure non-equilibrium streamers for combustion ignition application*, J. Appl. Phys. 114 (2013), p. 083302.

[58] D. Bouwman, J. Teunissen, and U. Ebert, *3d particle simulations of positive air–methane streamers for combustion*, Plasma Sources Sci. Technol. 31 (2022), p. 045023.

[59] R.D. Hudson, *Critical review of ultraviolet photoabsorption cross sections for molecules of astrophysical and aeronomic interest*, Rev. Geophys. 9 (1971), pp. 305–406.

[60] W. Vincenti and C. Kruger, *Introduction to physical gas dynamics*, Krieger, 1975.

[61] R.J. Kee, J.A. Miller, and T.H. Jefferson, *CHEMKIN: A general-purpose, problem-independent, transportable, FORTRAN chemical kinetics code package*, Tech. Rep. SAND80-8003, Sandia National Laboratories, 1980.

[62] J. Han, M. Belhi, F. Bisetti, and S.M. Sarathy, *Numerical modelling of ion transport in flames*, Combust. Theory Model. 19 (2015), pp. 744–772.

[63] G.V. Naıdis, *Effects of nonlocality on the dynamics of streamers in positive corona discharges.*, Tech. Phys. Lett. 23 (1997), p. 493.

[64] N. Liu and V.P. Pasko, *Effects of photoionization on propagation and branching of positive and negative streamers in sprites*, J. Geophys. Res. Space Phys. 109 (2004).

[65] G. Hagelaar and L. Pitchford, *Solving the boltzmann equation to obtain electron transport coefficients and rate coefficients for fluid models*, Plasma Sources Sci. Technol. 14 (2005), p. 722.

[66] S. Pancheshnyi, S. Biagi, M. Bordage, G. Hagelaar, W. Morgan, A. Phelps, and L. Pitchford, *The lxcat project: Electron scattering cross sections and swarm parameters for low temperature plasma modeling* 398 (2012), pp. 148–153, cross sections downloaded from `https://www.utexas.edu` on Jan 1, 2024.

[67] J. Prager, U. Riedel, and J. Warnatz, *Modeling ion chemistry and charged species diffusion in lean methane–oxygen flames*, Proc. Combust. Inst. 31 (2007), pp. 1129–1137.

[68] N. Aleksandrov and E. Anokhin, *Low-energy electron attachment and detachment in vibrationally excited oxygen*, J. Phys. D: Appl. Phys. 42 (2009), p. 225210.

[69] A. Ponomarev and N. Aleksandrov, *Monte carlo simulation of electron detachment properties for ions in oxygen and oxygen: nitrogen mixtures*, Plasma Sources Sci. Technol. 24 (2015), p. 035001.

[70] A. Ponomarev and N. Aleksandrov, *Monte carlo simulation of negative ion kinetics in air plasmas in a time-varying electric field*, J. Phys. D Appl. Phys. 53 (2019), p. 055203.

[71] I. Kossyi, A.Y. Kostinsky, A. Matveyev, and V. Silakov, *Kinetic scheme of the non-equilibrium discharge in nitrogen-oxygen mixtures*, Plasma Sources Sci. Technol. 1 (1992), p. 207.

[72] A. Ionin, I. Kochetov, A. Napartovich, and N. Yuryshev, *Physics and engi-*

neering of singlet delta oxygen production in low-temperature plasma, J. Phys. D Appl. Phys. 40 (2007), p. R25.

[73] R. Barker, K. Becker, U. Kogelschatz, and K. Schoenbach, *Non-Equilibrium Air Plasmas at Atmospheric Pressure*, first edition. ed., Series in Plasma Physics, CRC Press, Boca Raton, FL, 2004.

[74] J. Bittencourt, *Fundamentals of plasma physics*, Springer Verlag, 2004.

[75] D. Whitfield, *Three-dimensional unsteady Euler equations solution using flux vector splitting*, in *17th Fluid Dynamics, Plasma Dynamics, and Lasers Conference*.

[76] J. Blazek, *Computational fluid dynamics principles and applications / J. Blazek.*, 2nd ed., in *Computational fluid dynamics principles and applications*, chap. 8, Elsevier, Amsterdam ; (2005), pp. 271–302.

[77] O. Desjardins, G. Blanquart, G. Balarac, and H. Pitsch, *High order conservative finite difference scheme for variable density low mach number turbulent flows*, J. Comput. Phys. 227 (2008), pp. 7125–7159.

[78] V. Gorin, A. Kudryavtsev, J. Yao, C. Yuan, and Z. Zhou, *Boundary conditions for drift-diffusion equations in gas-discharge plasmas*, Phys. Plasmas 27 (2020), p. 013505.

[79] A. Phelps, *The diffusion of charged particles in collisional plasmas: free and ambipolar diffusion at low and moderate pressures*, J. Res. Natl. Inst. Stan. 95 (1990), p. 407.

[80] P. Chantry, A. Phelps, and G. Schulz, *Theory of electron collision experiments at intermediate and high gas densities*, Phys. Rev. 152 (1966), p. 81.

[81] N.E. Deak, *Development and application of a high-performance framework for high-fidelity simulations of plasma-assisted ignition of hydrocarbon fuels using nanosecond pulsed discharges*, Ph.D. diss., The University of Texas at Austin, 2022.

[82] F. Tholin and A. Bourdon, *Simulation of the stable 'quasi-periodic'glow regime of a nanosecond repetitively pulsed discharge in air at atmospheric pressure*, Plasma Sources Sci. Technol. 22 (2013), p. 045014.

[83] M. Berger and A. Giuliani, *A state redistribution algorithm for finite volume schemes on cut cell meshes*, J. Comput. Phys. 428 (2021), p. 109820.

[84] P. Messina, *The exascale computing project*, Comput. Sci. Eng. 19 (2017), pp. 63–67.

[85] H. Sitaraman, S. Yellapantula, M.T.H. de Frahan, B. Perry, J. Rood, R. Grout, and M. Day, *Adaptive mesh based combustion simulations of direct fuel injection effects in a supersonic cavity flame-holder*, Combust. Flame 232 (2021), p. 111531.

[86] M.S. Day and J.B. Bell, *Numerical simulation of laminar reacting flows with complex chemistry*, Combust. Theory Model. 4 (2000), pp. 535–556.

[87] A. Nonaka, J. Bell, M. Day, C. Gilet, A. Almgren, and M. Minion, *A deferred correction coupling strategy for low mach number flow with complex chemistry*, Combust. Theory Model. 16 (2012), pp. 1053–1088.

[88] L. Esclapez, M. Day, J. Bell, A. Felden, C. Gilet, R. Grout, M.H. de Frahan, E. Motheau, A. Nonaka, L. Owen, B. Perry, J. Rood, N. Wimer, and W. Zhang, *Pelelmex: an amr low mach number reactive flow simulation code without level sub-cycling*, J. Open Source Softw. 8 (2023), p. 5450.

[89] N.E. Deak, A.J. Duarte, L. Esclapez, M. Day, and F. Bisetti, *High-fidelity simulations of plasma-assisted oxidation of hydrocarbon fuels using nanosecond pulsed discharges*, in *AIAA SCITECH 2023 Forum*.

[90] A. Duarte, N. Deak, and F. Bisetti, *Validation of a fully-coupled three-dimensional low-temperature plasma and reactive Navier Stokes solver*, in *AIAA Scitech 2024 Forum*. 2024.

[91] R. Menikoff and B.J. Plohr, *The riemann problem for fluid flow of real materials*, Rev. Mod. Phys. 61 (1989), p. 75.

[92] P.L. Ventzek, T.J. Sommerer, R.J. Hoekstra, and M.J. Kushner, *Two-dimensional hybrid model of inductively coupled plasma sources for etching*, Appl. Phys. Lett. 63 (1993), pp. 605–607.

[93] X. Wang, A. Patel, S. Bane, and A. Shashurin, *Experimental study of atmospheric pressure single-pulse nanosecond discharge in pin-to-pin configuration*, J. Appl. Phys. 130 (2021).

[94] S. Adams, C. Dumitrache, and C. Murray, *Gas density evolution and recirculation after a nanosecond pulsed discharge: experimental and computational results*, Exp. Fluids 64 (2023).

[95] A. Komuro, K. Takahashi, and A. Ando, *Numerical simulation for the production of chemically active species in primary and secondary streamers in atmospheric-pressure dry air*, J. Phys. D: Appl. Phys. 48 (2015).

[96] T.M. Ombrello, C.D. Carter, C.J. Tam, and K.Y. Hsu, *Cavity ignition in supersonic flow by spark discharge and pulse detonation*, Proc. Combust. Inst. 35 (2015), pp. 2101–2108.

[97] A. Duarte Gomez, N. Deak, and F. Bisetti, *Jacobian-free newton–krylov method for the simulation of non-thermal plasma discharges with high-order time integration and physics-based preconditioning*, J. Comput. Phys. 480 (2023), p. 112007.

[98] A. Zhang, R. Scarcelli, T. Wallner, D. Breden, A. Karpatne, L.L. Raja, I. Ekoto, and B. Wolk, *Numerical investigation of nanosecond pulsed discharge in air at above-atmospheric pressures*, J. Phys. D: Appl. Phys. 51 (2018).

[99] T. Huiskamp, *Nanosecond pulsed streamer discharges part i: Generation, source-plasma interaction and energy-efficiency optimization*, Plasma Sources Sci. Technol. 29 (2020), p. 023002.

[100] B. Singh, R.L. K, P. Vlachos, and S.P. Bane, *Shock generated vorticity in spark discharges*, J. Phys. D: Appl. Phys. 54 (2021).

[101] B. Singh, L.K. Rajendran, P.P. Vlachos, and S.P. Bane, *Two regime cooling in flow induced by a spark discharge*, Phys. Rev. Fluids 5 (2020).

[102] S. Shen, E. Rempe, W. Senior-Tybora, and J.K. Lefkowitz, *Destructive inter-pulse coupling in nanosecond-pulsed high-frequency discharge ignition: Effect of hydrodynamic regimes*, Proc. Combust. Inst. 40 (2024), p. 105445.

[103] S. Pancheshnyi, M. Nudnova, and A. Starikovskii, *Development of a cathode-directed streamer discharge in air at different pressures: experiment and comparison with direct numerical simulation*, Phys. Rev. E 71 (2005), p. 016407.

[104] D. Bouwman, J. Teunissen, and U. Ebert, *3d particle simulations of positive air–methane streamers for combustion*, Plasma Sources Sci. Technol. 31 (2022), p. 045023.